School of Mathematical Sciences
Queensland University of Technology

Fractional models in space for diffusive processes in heterogeneous media with applications in cell motility and electrical signal propagation

Nicole Cusimano

Masters by Coursework in Mathematics (Italy)
Bachelor Degree in Mathematics (Italy)

A thesis submitted for the degree of Doctor of Philosophy in the Science and Engineering Faculty, Queensland University of Technology according to QUT requirements

Principal Supervisor: Prof. Kevin Burrage
Associate Supervisor: Dr. Pamela Burrage

2015

Abstract

Fractional calculus, that is, calculus involving derivatives and integrals of non-integer order, was considered for many years from a purely abstract mathematical perspective. However, in the last few decades, fractional operators have been used as modelling tools in a variety of practical disciplines (such as physics, engineering, chemistry, rheology, economics) due to their success in reproducing solution behaviours that significantly deviate from that typically obtained with standard models, as in the case of anomalous diffusion. The interest in fractional operators linked to practical applications is increasingly growing, however, there are still fundamental issues and implementation aspects that have to be addressed for a rigorous implementation of these operators in a wider variety of problems. Important considerations involve for example the restriction of the non-local definition of the operators to bounded domains and the role played by the boundary conditions.

In this thesis we focus our attention on reflecting boundary conditions, essentially extending the concept of standard homogeneous Neumann boundary conditions to non-local problems. We derive a discrete representation of the space-fractional operator embedding reflecting boundary conditions on a finite one-dimensional domain and formulate a theorem providing the analytic expression of its spectrum. We then compare this operator with the one obtained with the matrix transfer technique when standard homogenous Neumann boundary conditions are considered, and show the equivalence of their spectrum in the limit, as the number of discretisation points approaches infinity.

Justified by the above theoretical considerations we adopt the spectral definition of the fractional Laplacian on insulated bounded domains in order to obtain a space-fractional modification of some models of interest for two particular applications (one in biology and one in electrophysiology). We then use the spectral decomposition method to compute their solution in both the standard and fractional case, and analyse how the fractional component affects the solution of these models.

In particular, in the space-fractional modification of the Fisher-Kolmogoroff model for cell migration on an insulated bounded domain we see that solutions evolving as travelling waves in the standard case no longer advance with constant shape and speed in the fractional case. In fact, we observe an acceleration of the solution profile towards the stable steady state of the system

that translates mathematically into the exponential advancing of the level sets of the fractional solution. Inspired by in vivo experimental recordings of the speed of advancing neural crest-derived cells in the gut of mice embryos, we then propose a variable order fractional modification of the model with the aim of characterising the migration pattern observed in different regions of the domain with different values of the fractional order.

Finally, we consider the space-fractional modification of two examples of excitable media models, namely the Fitzhugh–Nagumo and the Beeler–Reuter monodomain models. In one spatial dimension, the same electrical stimulus applied to the system in the standard case and generating a travelling pulse moving through the domain away from the stimulus site, in the fractional case still produces a travelling pulse with shape dictated by the particular cell model used. However, as the fractional order decreases, we observe a reduction in the conduction velocity (and hence a later depolarization of any given point in space), a slight decrease in the action potential peak (for the Beeler-Reuter model also a slightly more pronounced early depolarization phase), and increasing dispersion of the action potential duration as the travelling pulse moves away from the stimulus site. In two-spatial dimensions, we study two different operators introducing non-locality on an insulated rectangular domain: the sum of two one-dimensional fractional Laplacians with reflecting boundary conditions in each spatial dimension (allowing us to consider also different fractional orders in the two spatial directions), and a spectral definition for the two-dimensional fractional Laplacian as a whole. As the level of non-locality in the problem increases (and the fractional orders of the two operators decrease), the same type of qualitative changes found in the one-dimensional case is seen here in the solution. However, we observe differences in the curvature of the travelling pulse front between the two options. Furthermore, if different fractional orders are used for the first option in different directions, even under the assumption of isotropic conductivity values, the temporal evolution of the two-dimensional travelling pulse is not symmetric with respect to the two directions and a faster advancing is observed along the direction characterised by the higher fractional order.

Statement of Original Authorship

The work contained in this thesis has not been previously submitted to meet requirements for an award at this or any other higher education institution. To the best of my knowledge and belief, the thesis contains no material previously published or written by another person except where due reference is made.

SIGNED:

DATE: 7 May 2015

Acknowledgements

To my principal supervisor, Prof. Kevin Burrage, thank you for believing in my abilities and giving me the amazing opportunity of being a student here at QUT under your supervision. This great experience would have not been possible without you and I am incredibly grateful for all the support you gave me over the past three years.

To Prof. Ian Turner, thank you very much for always finding some time to listen to me talking about my work (often during your lunch breaks) and for the countless times you have helped me with useful suggestions and discussions.

To Dr. Pamela Burrage, thank you for regularly meeting me while Kevin was overseas (allowing me to keep being productive and focused), and for always offering valuable feedback on my work.

To Dr. David Kay from the Department of Computer Science of the University of Oxford, a special thank you for defining the initial framework for the understanding of reflecting boundary conditions on finite domains, for having me as member of the "reflecting boundary team", and for the exchange of ideas that eventually brought to the development of the main theoretical part of this thesis.

To the many friends who offered smiles, comforting words, and bore with my grumpiness, especially in the last few months of my PhD. Thanks heaps!!!

Finally, to my family (whom I miss so much), the biggest thank you of all! All I have achieved is because of you. Because you are awesome! Ve voio ben!!!!! Tantononononon.

Nicole Cusimano

May 2015

Contents

List of Figures

List of Tables

Terminology and Units

Name	Description
ODE	Ordinary Differential Equation
PDE	Partial Differential Equation
MOL	Method of Lines
FK	Fisher–Kolmogoroff
HH	Hodgkin–Huxley
FHN	Fitzhugh–Nagumo
BR	Beeler–Reuter
MTT	Matrix Transfer Technique
CTRW	Continuous Time Random Walk
GME	Generalised Master Equation
SE	Standard Error
AP	Action Potential
APD	Action Potential Duration
pdf	probability density function
cm	centimetre
μm	micrometre
h	hour
msec	millisecond
μA	microampere
μF	microfarad
mS	millisiemens
mV	millivolt

Chapter 1

Introduction

This chapter outlines the context and the motivations behind the research presented in this thesis, the main objectives of this work and finally an overview of the content presented in each of the chapters of the manuscript.

1.1 Context and motivation

The theoretical ideas behind fractional calculus, that is, calculus involving derivatives and integrals of non-integer order, can be seen as having their roots a few centuries ago. In fact, as reported by Ross [70], it was soon after the concepts of standard calculus were introduced that the famous mathematicians Leibniz and De L'Hôpital exchanged some ideas on whether it was possible to extend the concept of derivative $\frac{d^n y}{dx^n}$ to have a meaning in the case $n = \frac{1}{2}$.

These ideas became the object of many debates and studies in the Nineteenth Century and eventually lead to the formalisation and development of the theory known today as fractional calculus (see for example [72] and [68]). For many years the interest in these concepts was purely abstract and fractional calculus was studied from an entirely theoretical perspective. As stated by Machado et al. [50], "Only since the Seventies, the fractional calculus has been the object of specialized conferences and treatises. [...] Until recent times, fractional calculus was considered as a rather esoteric mathematical

theory without applications, but in the last (few) decade(s) there has been an explosion of research activities on the application of fractional calculus to very diverse scientific fields" ranging from physics ([60], [43], [71], [57], [73]) to finance and economics ([56], [74]), from hydrology and fluid dynamics in porous media ([5], [27], [49], [16]) to medicine and physiology ([51], [30], [12]).

Among all successful implementations of fractional operators we focus our attention on the use of fractional reaction-diffusion models for the description of phenomena characterised by the so-called anomalous diffusion [58]. Anomalous diffusion typically occurs when the system in which the transport phenomena is observed is characterised by a degree of complexity and heterogeneity that significantly alters the standard laws of diffusion. The alterations caused by the presence of such inhomogeneities cannot be ignored mathematically when formulating the macroscale equation describing the phenomena observed. In fact, spatial interconnectivity pathways and temporal correlations have been shown to impose a number of constraints on transport processes that cannot be accounted for with standard reaction-diffusion equations but can be well captured by using the tools provided by fractional calculus. Fractional reaction-diffusion models are typically obtained by substituting the integer order derivatives of the differential equation describing the problem by a non-integer counterpart and depending on the derivatives chosen, the resulting models can be fractional in time or space (or both).

The motivation for the research in this thesis is that we would like to analyse how the solutions of some standard reaction-diffusion models of practical interest are affected when a space-fractional component is introduced in the model, under the assumption that the diffusion process observed does not take place in a standard homogeneous environment but rather occurs in complex structures characterised by a high degree of heterogeneity and interconnectivity. Specifically, we aim to develop mathematical space-fractional models able to represent some important features observed in *in vivo* experiments of colonisation of the gut of mice embryos by neural crest-derived

cells, and in the propagation of electrical signals in highly heterogeneous media such as neural or cardiac tissue. In fact, for these two specific applications, experimental measurements and results from biological and physiological simulations exhibit characteristics that significantly deviate from that typically observed with standard reaction-diffusion models. Hence, for the work presented in this thesis we decide to focus on examples of reaction-diffusion models for cell migration in biology and electrical signal propagation in electrophysiology, and study the space-fractional modification obtained by replacing the second order differential operator in space with a suitable differential operator of non-integer order.

There are however a number of challenges related to the implementation of space-fractional modifications of models for practical applications. For example, when looking for the definition of a space-fractional differential operator, one immediately notices that there is no universal definition and different options are available instead (see for example [42]). These definitions are generally not equivalent (especially when more than one spatial dimension is considered) and fractional operators are typically defined on unbounded domains, whereas in most applications of practical interest the phenomenon observed is restricted to finite domains. This is a major issue that deserves particular attention. Considering bounded domains in fact requires the introduction of boundary conditions for the model. These boundary conditions in standard problems do not present a challenge due to the local character of the solution. However, in non-local problems in space, where the value of the solution at a given point depends on the solution behaviour on the entire space, it is intuitive to understand that the introduction of a boundary sensibly modifies the non-local operators (otherwise defined on unbounded domains) and these modifications must be properly incorporated in the model, if a correct solution for the problem is sought. The typical approach considered in many practical cases is to assume homogeneous Dirichlet boundary conditions, that is, to assume that the solution vanishes along the entire boundary of the spatial domain. This assumption significantly simplifies the problem. In fact, as we shall see in greater detail later on in the thesis, stan-

dard homogeneous Dirichlet boundary conditions can be trivially extended to non-local problems on finite domains by simply assuming that the solution to the fractional problem is equal to zero everywhere outside of the confined domain of interest.

However, due to the variety of boundary conditions that can arise in practical situations, we identify the need of extending the applicability of space-fractional models beyond the simplest case of homogeneous Dirichlet boundary conditions so that the applicability of non-local operators can be tested on a wider class of practical problems. Among the other options available for standard boundary value problems, we believe that from the mathematical point of view the case of homogeneous Neumann boundary conditions is probably the easiest to be considered next. In fact, the practical interpretation of these boundary constraints as insulating conditions for the considered domain, gives us an intuitive concept that can help us understand the role that these conditions must play on the solution of the model in both the standard and the non-local cases.

Before being able to implement fractional formulations of the practical problems of interest (that are in fact coupled in the standard case to homogeneous Neumann boundary conditions), we recognize the need of developing a firmer theoretical framework for the rigorous formalisation of our non-local modifications. Wanting to address some fundamental issues of non-local models, we decide to first consider fractional operators in space in an abstract mathematical setting and focus on modelling aspects related to the restriction of their definition to finite insulated one-dimensional domains and the role of properly incorporating the right description of the boundary conditions in the problem formulation.

Our aim is then to compare some alternatives and to use these results to develop the correct formulation of the space-fractional modifications of the above-mentioned applications. The particular requirements of the practical applications in our object of study also serve as starting points for the dis-

cussion of other theoretical aspects, such as the possibility of implementing space-fractional operators with a variable fractional order and the generalisation of our one-dimensional considerations to two (or more) spatial dimensions.

One final aspect we consider in order to reach our original goal is the implementation of suitable numerical strategies to compute the solution of the space-fractional modifications of the models of interest. Probably the most used numerical approach is the generalisation of the method of lines for standard reaction-diffusion models, in which the discrete operator resulting from the spatial discretisation process is modified in order to account for nonlocality. However, this method seems to translate inevitably into the use of dense discrete operators and into heavier computational requirements of the solution strategy, if compared to the classical standard case.

Other alternatives are available in the literature and in this thesis we specifically focus on the implementation of a spectral decomposition method (similar to the one presented by Bueno–Orovio et al. [11]) for the practical applications of interest, in order to exploit a full diagonalisation of the problem and hence reduce the computational effort typically related to the use of dense discretisation matrices. The spectral decomposition method, allowing us to obtain an exact solution in the case of the space-fractional diffusion equation, must be adapted in the practical problems studied due to the presence of a reaction term. Exact integration in time is in general not possible anymore and a suitable temporal integration scheme must be introduced. Moreover, in the case of excitable media models, due to the higher modelling complexity compared to the cell migration model considered, the spectral expansion of the solution (accounting for the high heterogeneity assumption made on the spatial domain) must be embedded into a more global solution strategy, thus increasing the challenges related to the numerical implementation.

1.2 Objectives of the thesis

The specific objectives of the research work presented in this thesis are listed below.

Derivation of a matrix representation of the space-fractional operator obtained from the finite-difference Grünwald–Letnikov approach and embedding reflecting boundary conditions.

The research presented in this thesis contains an important theoretical component. As mentioned in Section 1.1, we specifically focus our attention on the role played by homogeneous Neumann boundary conditions on finite one-dimensional domains in the standard case and consider the extension of this concept to the non-local framework. The idea of an insulated boundary as a reflecting condition for non-local operators, as introduced for the semi-infinite case by Krepysheva et al. [45], is of fundamental importance for our results. In this manuscript, we revisit the derivations made in [45] and subsequently by Néel et al. in [65] for the formulation of a continuous operator on an insulated finite interval in one spatial dimension. Reflecting boundary conditions are embedded at both ends and the final result presented in [65] is reformulated with the introduction of a suitable "sawtooth" function. This reformulation allows us to provide a discrete approximation of the considered continuous operator and to obtain a characterisation of our result by analysing the spectrum of this matrix representation.

Investigation and clarification of the relationship between the discrete reflection operator and the discrete operator obtained via the matrix transfer technique when standard homogeneous Neumann boundary conditions are considered.

One of the strategies often used in the implementation of the solution of space-fractional models with homogeneous Dirichlet boundary conditions is given by the matrix transfer technique, originally proposed by Ilić et al. [34]. In [34] and [35], the authors also propose an extension of the method to

other types of homogeneous boundary conditions, including standard homogeneous Neumann boundary conditions. After performing some numerical simulations of simple test problems we observed that a very similar behaviour could be obtained when the numerical solution was computed with the discrete reflection operator (that is, the discrete non-local operator embedding reflecting boundary conditions) and with the matrix transfer technique coupled to homogeneous Neumann boundary conditions. Hence, our second aim is to compare the discrete operator based on the reflection strategy pioneered by Krepysheva et al. [45] and the discretisation approach given by the matrix transfer technique with homogeneous Neumann boundary conditions to see whether it is possible to establish a relationship of some kind between the two approaches.

Suitable formulation of the restriction of the fractional Laplacian operator on an insulated finite one-dimensional domain $[0, L]$.

The space-fractional modification of a given reaction-diffusion problem is obtained by simply replacing the standard differential operator in space with a non-integer counterpart. Due to its probabilistic interpretation in terms of an ensemble of particles undergoing a specific type of continuous time random walk (see details in Section 2.3 and Chapter 4), we are particularly interested in using in our practical applications the so-called fractional Laplacian [72]. However, the fractional Laplacian is normally defined on the entire space $\mathbb{R}$ and therefore, a suitable restriction of its definition must be considered for finite domains. Assuming that both boundaries of the finite one-dimensional interval $[0, L]$ are insulated, our next aim is to provide a suitable description of this operator in order to correctly model the space-fractional problems of interest and then compute their solution.

Formulation and solution of the space-fractional modification of the Fisher–Kolmogoroff equation on an insulated finite interval using the spectral decomposition method.

Studying the effect of the fractional modification of the Fisher–Kolmogoroff equation on its solution is certainly not a novel idea of this work (see for example [22], [23], [75]). However, for this application the original contribution of this thesis consists of the modelling assumptions behind the space-fractional formulation of the model, the definition of the non-local operator incorporating the correct description of the boundary conditions (deriving from a rigorous mathematical analysis - see Chapter 4) and a new numerical strategy for the computation of the solution of the fractional Fisher–Kolmogoroff model based on the spectral decomposition method. We also propose a modification of the problem with variable fractional order and implement its solution after discussing the motivations behind the interest in such an extension, highlighting the theoretical challenges related to the formulation of a non-local operator in this particular form.

Formulation and solution of the space-fractional modification of the Fitzhugh–Nagumo and Beeler–Reuter monodomain models on an insulated finite interval and on an insulated rectangular domain via the spectral decomposition method.

The interest in studying fractional modifications of excitable media models is very recent and to our knowledge the only example available in the literature to date for the case of excitable media models of cardiac tissue is the one proposed by Bueno–Orovio et al. in [12]. The high complexity of excitable media models for the study of electrical pulse propagation in the heart or the brain is already a challenge from the computational point of view in the standard case and the idea of introducing an additional source of complexity by considering a space-fractional modification of the problem might be discouraging and seem unnecessary. However, there are valid physiological reasons (related to the highly heterogeneous nature of the medium considered and the number of scales on which such a heterogeneity is manifested)

that justify questioning the reliability of the assumptions behind the continuous standard formulation of these models, especially in pathological cases. Moreover, comparison of the numerical results produced by space fractional models and experimental data proposed in [12] shows that non-local models are able to reproduce many important features of experimental results more closely than classical standard diffusion models. Therefore, both these considerations suggest that space-fractional operators might offer new insight into these electrophysiological mechanisms and motivate our interest in the topic. In this thesis we consider two simplified models of electrical pulse propagation through neural and cardiac tissue, respectively, and study their non-local modification on a regular insulated domain in one and two spatial dimensions.

1.3 Thesis outline

Chapter 2 – Background and literature review

The purpose of this chapter is to provide a full mathematical description of the reaction-diffusion models we consider in the rest of the thesis, present some classical numerical techniques typically used to compute the solution of standard reaction-diffusion models, and finally provide a more detailed background on non-local operators, elaborating on the various aspects outlined in Section 1.1. In particular, we provide specific definitions of space-fractional operators, examples of numerical strategies used for their discretisation and restate the challenges and issues related to the implementation of these operators for practical applications.

Chapter 3 – Results in the standard diffusion case

Before moving on to the space-fractional modification of the models of interest, in this chapter we describe in detail how the spatial and temporal discretisation strategies presented in Chapter 2 are typically combined in order to obtain suitable solution strategies for each of the problems of interest in the standard case. For each application we also provide a set of numerical

results. The particular aim of the simulations presented is to show the main characteristics of the standard solution of the considered applications and to validate some relevant theoretical results. The first half of the chapter is dedicated to cell migration models, whereas the second half presents different examples of standard excitable media models.

Chapter 4 – Boundary conditions for non-local problems

This chapter contains the fundamental theoretical component of the thesis. Here we consider space-fractional operators in an abstract setting and focus on the important role played by boundary conditions on finite domains. After introducing the concept of reflecting boundary conditions we derive a discrete representation of the reflection operator. We then formulate a theorem providing the analytic expression of the spectrum of such a discrete operator and a substantial part of the chapter is dedicated to the proof of this result. A discussion on the comparison between different discrete and continuous operators follows the theorem. A section dedicated to the implementation and validation of the results obtained by studying the solution of some test numerical simulations concludes the chapter.

Chapter 5 – Space-fractional Fisher–Kolmogoroff model

The theoretical results obtained in Chapter 4 are used here to provide the space fractional formulation of the cell migration model of interest and compute its solution. Comparison of the solution of the model in the standard and fractional cases is possible by introducing the concept of level sets. Inspired by some practical considerations, we then propose a space-fractional modification of the Fisher–Kolmogoroff model with variable fractional order and conclude the chapter with a discussion on the results obtained.

Chapter 6 – Space fractional excitable media models

This chapter is dedicated to the implementation and computation of the solution of space-fractional modifications of excitable media models. In particular, we consider either the monodomain Fitzhugh–Nagumo model or the

monodomain Beeler–Reuter model, and modify their formulation by introducing a suitable non-local operator in space. We begin by presenting the details of the numerical methodology used in order to compute the solution in the fractional case and then provide a set of simulation results. We then discuss different options for the introduction of non-locality in two-dimensional models and provide corresponding extensions to the excitable media models considered. We also provide some simulation results for these fractional models in two spatial dimensions and conclude the chapter with a discussion on our findings.

Chapter 7 – Conclusions

In this final chapter we restate the main objectives of the thesis, discuss how these objectives were addressed, and highlight the outcomes of the work presented. We conclude the chapter by suggesting possible extensions, improvements and future directions of research.

Chapter 2

Background and literature review

In this chapter, we introduce the sets of equations describing the standard models for the practical applications considered in the rest of the thesis and provide references to their original formulations or to the work of other authors who performed detailed studies on these models. We then outline some classical numerical strategies that are used in order to compute approximations of the solutions of these models. Finally, we introduce the concept of space-fractional models, focusing on two particular definitions of these types of non-local operators. We provide references to some of the numerical methods available in the literature to obtain numerical solutions to space-fractional problems and raise some important issues related to their implementation.

2.1 Applications

The models presented in this section are reaction-diffusion equations describing cell migration (involving one or two species in one spatial dimension) and signal propagation in excitable media (in both one and two spatial dimensions). We give a brief description of each model, summarize some of the main results established for these problems, and provide references for a

more detailed description and analysis of the original works.

2.1.1 Cell migration

Cell migration is the process describing the movement of cells that typically occurs in response to particular chemical or mechanical signals and aims to maintain or develop specific functions in multicellular organisms. Wound healing, tumor formation, immune response and embryogenesis are all examples of how a population of cells might invade regions of tissue not yet occupied by that particular cell population.

The Fisher–Kolmogoroff model

The Fisher–Kolmogoroff equation [28] is a milestone in the study of travelling wave phenomena. This model is the simplest example in which the coupling of diffusion and reaction kinetics generates travelling wave solutions. A one-dimensional reaction-diffusion equation for a concentration (or population) $u(x,t)$ generally has the form

$$\frac{\partial u}{\partial t} = D\,\frac{\partial^2 u}{\partial x^2} + g(u), \tag{2.1}$$

where D is the constant diffusion coefficient and $g(u)$ represents the kinetics. As stated by Murray [62], it is part of the classical theory of linear parabolic equations that there are no physically realistic travelling wave solutions for (2.1) when $g(u) = 0$. However, when $g(u) \neq 0$, depending on the analytical form of the reaction term, the model can exhibit travelling waves and this can lead to a change in u very much faster than the one that would be observed with a pure diffusional process.

The one-dimensional Fisher–Kolmogoroff equation

$$\frac{\partial u}{\partial t} = D\,\frac{\partial^2 u}{\partial x^2} + k\;u(1-u), \tag{2.2}$$

in which D and k are positive parameters, is the simplest example of a

nonlinear reaction-diffusion partial differential equation (PDE) involving a single species.

The model, originally proposed in 1937 by Fisher [28] as a deterministic version of a stochastic model for the spatial spread of advantageous genes, is also the natural extension of the well known logistic growth population model, when the population disperses via linear diffusion.

When studying (2.2), it is often convenient to nondimensionalise the problem by introducing the new variables

$$t^* = k\ t \quad \text{and} \quad x^* = x \left(\frac{k}{D}\right)^{1/2}. \tag{2.3}$$

Omitting the asterisks for the sake of simplicity, equation (2.2) can be rewritten in its dimensionless form as

$$\frac{\partial u}{\partial t} = \frac{\partial^2 u}{\partial x^2} + u(1-u). \tag{2.4}$$

For the dimensionless model we consider values of $t > 0$ and the domain for the spatial variable is assumed to be the interval $[0, L]$. Due to the biological context from which this equation is generated, the solution u has to be non-negative $\forall(x,t)$ in the domain of definition.

In order to complete the formulation of the problem we consider equation (2.4) with homogeneous Neumann boundary conditions[1], that is,

$$\left.\frac{\partial u}{\partial x}\right|_{x=0} = 0 \quad \text{and} \quad \left.\frac{\partial u}{\partial x}\right|_{x=L} = 0, \tag{2.5}$$

and initial condition defined by

$$u(x,0) = u_0(x) = \begin{cases} 1 & x < x_1 \\ e^{-\xi(x-x_1)} & x \geq x_1 \end{cases} \tag{2.6}$$

[1]Also called zero-flux boundary conditions.

for a fixed $x_1 \in (0, L)$. This particular type of initial condition is chosen as it allows us to obtain analytical results for the travelling wave speed of the solution and we will test these results using our numerical simulations in Chapter 3. Different values of the parameter ξ enable the leading front of the initial concentration u_0 to decay exponentially with a variable rate.

As shown by Murray [62], equation (2.4) in the spatially homogeneous case has two steady states $u = 0$ and $u = 1$, that are unstable and stable, respectively. Therefore, when we look for travelling wavefront solutions such that $0 \leq u \leq 1$ and of the form $u(x, t) = U(z)$ with $z = x - ct$ where c is the dimensionless wave speed, it can be proved that the following relation must hold:

$$c \geq c_{\min} = 2. \tag{2.7}$$

Kolmogoroff et al. [44] proved that if $u_0(x)$ has compact support, then the solution $u(x, t)$ of equation (2.4) evolves to a travelling wavefront solution $U(z)$ with $z = x - ct$. Another important result provided in [62] is related to the so-called dispersion relation. Indeed, it is possible to prove that if

$$u(x, 0) \sim a\ e^{-\xi x} \quad \text{as} \quad x \to \infty, \tag{2.8}$$

where a and ξ are arbitrary positive constants, then the asymptotic wave speed of the travelling wave solution is

$$c = \xi + \frac{1}{\xi} \quad \text{if} \quad 0 < \xi \leq 1 \quad \text{and} \quad c = 2 \quad \text{if} \quad \xi \geq 1. \tag{2.9}$$

Finally, an additional particular initial condition for which the asymptotic value of c is known is given by

$$u_0(x) = \frac{1}{[1 + (\sqrt{2} - 1)e^{x/\sqrt{6}}]^2}. \tag{2.10}$$

Indeed, it can be proven analytically that the travelling wave solution

$$U(z) = \frac{1}{[1 + a\ e^{z/\sqrt{6}}]^2}, \tag{2.11}$$

for all positive values of the constant a, has a wave speed $c = 5/\sqrt{6}$ (see [62] for details of the proof).

Cell migration model with two interacting species

The second model considered is an extension of the Fisher–Kolmogoroff equation proposed by Simpson et al. in [77] and [78]. This model describes the invading process of neural crest-derived cells during the early stages of development in the gut of chick embryos. It was developed with the aim of reproducing different scenarios obtained from chick-quail graft experiments *in vitro*. These grafts were made in order to study properties of cell migration and proliferation of cells located in different positions with respect to the advancing wave front during the invasion process. The model involves two interacting species, namely the donor and the host cell population densities along the longitudinal axis of the gut, and can therefore be considered a one-dimensional model in space.

In particular, under the assumption of linear diffusion, the system of two one-dimensional PDEs first described in [77] and obtained from the conservation of mass equations can be rewritten for $x \in [0, L]$ and $t > 0$ in the following dimensionless form:

$$\begin{cases} \dfrac{\partial u}{\partial t} &= D\ \dfrac{\partial^2 u}{\partial x^2} + k\ u\ (1 - u - v) \\ \\ \dfrac{\partial v}{\partial t} &= \dfrac{\partial^2 v}{\partial x^2} + v\ (1 - u - v). \end{cases} \tag{2.12}$$

In equation (2.12), $u(x,t)$ and $v(x,t)$ are the donor and host dimensionless population densities. Parameters $D = D_u/D_v$ and $k = k_u/k_v$ represent the relative diffusion coefficient and the relative mitotic index, respectively.

The dimensionless results can be converted to real units (denoted here by a tilde on top) by scaling the dimensionless variables according to the following set of equations:

$$\tilde{t} = \frac{t}{k_v}, \quad \tilde{x} = \sqrt{\frac{D_v}{k_v}}x, \quad \tilde{u} = Cu, \quad \tilde{v} = Cv, \tag{2.13}$$

where C represents the carrying capacity constraining the total cell density $\tilde{u} + \tilde{v}$, that is, $\tilde{u} + \tilde{v} \leq C$.

The boundary conditions considered for this model are once again Neumann conditions. In particular, according to the work of Simpson et al. [77], we implement homogeneous Neumann boundary conditions for both species at both ends of the spatial interval. Therefore, we assume

$$\left.\frac{\partial u}{\partial x}\right|_{x=0} = \left.\frac{\partial u}{\partial x}\right|_{x=L} = 0 \qquad \text{and} \qquad \left.\frac{\partial v}{\partial x}\right|_{x=0} = \left.\frac{\partial v}{\partial x}\right|_{x=L} = 0. \tag{2.14}$$

The initial condition of the model is given in the form

$$\begin{bmatrix} u(x,0) \\ v(x,0) \end{bmatrix} = \begin{bmatrix} u_0 \\ v_0 \end{bmatrix}, \tag{2.15}$$

where the vector $[u_0, v_0]^T$ defines the particular type of tissue graft we want to simulate. Figure 2.1 graphically illustrates the three initial conditions considered in [77] and represents three possible graft scenarios:

- Case 1: the donor tissue is grafted into the invaded region (rostral to the host advancing front);
- Case 2: the donor tissue is grafted into the invading region (coinciding with the host advancing front);
- Case 3: the donor tissue is grafted into the uninvaded region (caudal to the host advancing front).

Differently from the case of the FK equation, this second cell migration

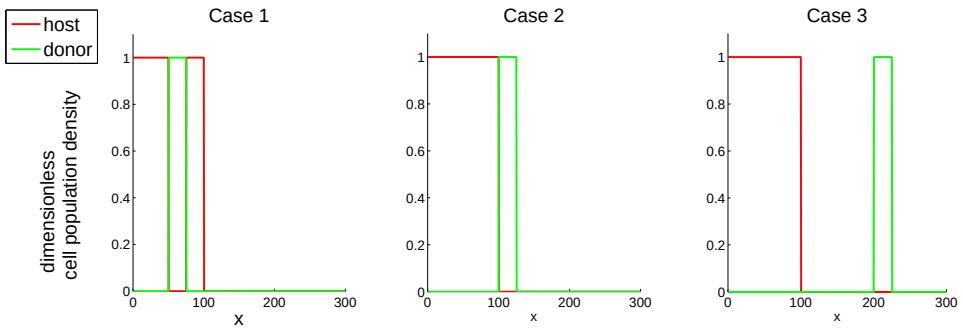

Figure 2.1: *Three different types of graft.*

model will not be considered in the space-fractional setting but only in the standard case (that is, only in its original formulation, not involving any fractional component) in Chapter 3. In fact, we introduce this model because the results proposed in its original formulation [77] were obtained under the assumption that $D = k = 1$ in equation (2.12). However, similarly to that done by Murray [62] for the FK equation or by Trewenack and Landman [81] for a model of invasion by precursor and differentiated cells (see [81] for details on the model description and explanation of these terms), we were able to extend some important considerations on the wave speed of the solutions corresponding to the three initial conditions studied by Simpson et al. [77] to the case of $D, k \geq 1$.

2.1.2 Excitable media

Another class of models considered in this thesis concerns the study of a different aspect of cellular activity, namely the generation and propagation of electrical signals.

A biological cell can be thought of as a collection of sub-structures (organelles) embedded in a fluid called cytosol and separated from the external environment by the cell membrane. The cell membrane consists of a double layer of phospholipid molecules containing aggregates of proteins, some of which span the entire lipid bilayer and form pores (called channels) that can open and close and therefore play a fundamental role in the transport

of substances across the membrane. This membrane is selectively permeable and acts as a barrier to the flow of water and the free flow of ions (such as sodium Na^+ or potassium K^+) so that concentration differences of these ions are maintained in the intracellular and extracellular environment. Concentration differences are vital for cell survival and maintenance of the cellular volume. The creation of a potential difference across the cellular membrane is one of the main consequences of these ion concentration differences and the semi-permeability of the cellular membrane. In fact, since the environments separated by the cell membrane are characterised by different ion concentrations, there is a flow of ions down their concentration gradient. However, semi-permeability allows the passage of certain ion species and prevents the movement through the membrane of ions with opposite charge resulting in a buildup of charge across the membrane. This charge imbalance in turn generates an electric field that opposes the tendency of ions to further move through the membrane and so the potential difference is maintained. Given a particular ion species S, the potential value that exactly balances the diffusion of S and the electric field generated by its movement across the cellular membrane is called the Nernst equilibrium potential or reversal potential.

At rest, the cell membrane can be represented as a simple RC (resistor-capacitor) circuit model where the resistor represents the effect of ion channels on the flow of currents across the membrane and the capacitor reflects the fact that the cellular membrane separates charge. The capacitance C_m of any insulator is defined as the ratio of the charge Q across the capacitor to the voltage potential V necessary to hold that charge, that is, $C_m = Q/V$. Provided that C_m is constant, the capacitive current $\frac{dQ}{dt}$ can then be written as $C_m \frac{dV}{dt}$. Applying the principle of conservation of charge to the RC circuit we obtain that the sum of the ionic and the capacitative currents must be zero[2], that is,

$$C_m \frac{dV}{dt} + I_{\text{ion}} = 0, \tag{2.16}$$

[2]In case of an externally applied current I_{appl}, that is, when the cellular membrane is not at rest, the sum of the capacitive current and the ionic current must equal the external source. Therefore, on the right-hand side of equation (2.16) we would have I_{appl} instead of zero.

where $V = V_i - V_e$ is the difference between the intracellular and the extracellular potential, namely, the transmembrane potential.

The study of the dynamics of the cellular transmembrane potential, involves determining a particular expression for the ionic current I_{ion} in terms of V. Since different types of cells have different ion channels, there is no universal expression for the ionic current. Measurements of the current-voltage relations (that provide the expression of the current as a function of the voltage) are complicated by the fact that ion channels can open, or close, in response to changes in the membrane potential. The simplest example of current-voltage relation is given by the following linear function. Considering the movement of an ion S across a membrane, the transmembrane current (positive outwards) of S can be expressed as $I_S = g_S(V - V_S)$, where g_S is the membrane conductance to the ion S and V_S is the Nernst equilibrium potential of S.

The current through a population of channels does not only depend on the current-voltage relation of a single open channel but also on the proportion of open channels in that population. Being the basis for electrical excitability, the opening and closing of ionic channels in response to changes in the membrane potential is of fundamental importance in neurophysiology.

The simplest way to describe the evolution in time of the proportion of open channels is based on the assumption that each ionic channel can exist in either a closed state C or an open state O and that the rate of conversion from one state to another is dependent on the voltage:

$$C \underset{\beta(V)}{\overset{\alpha(V)}{\rightleftarrows}} O.$$

If w denotes the proportion of channels in the open state (and consequently $1-w$ is the proportion of closed channels), the governing differential equation for w is

$$\frac{dw}{dt} = \alpha(V)(1 - w) - \beta(V)w. \tag{2.17}$$

An alternative way to formulate the above ODE for w is

$$\tau_w(V)\frac{dw}{dt} = w_\infty(V) - w,$$

where

$$w_\infty(V) = \frac{\alpha(V)}{\alpha(V) + \beta(V)}$$

represents the steady-state value of w, and

$$\tau_w(V) = \frac{1}{\alpha(V) + \beta(V)}$$

is the time-constant of approach to the steady-state.

A possible generalization of the above model is obtained by assuming that the channel is made of multiple identical subunits, each of which can be in either the closed or open state, and the channel is open, or conducting, only when all subunits are open. Sometimes, in order to describe the dynamics of a population of ion channels exhibiting a more complex behaviour, each channel is considered to be made of multiple subunits of two different types: the first type activates the channel while the second one inactivates it.

When an electrical stimulus is applied to a cell, the transmembrane potential quickly increases (depolarization) and moves away from the equilibrium value, also called the resting potential. In non-excitable cells, such as epithelial cells, when the applied current is removed, the transmembrane potential immediately returns to its resting state (repolarization), independently from the strength of the current applied. On the contrary, excitable cells are characterised by the fact that if the applied stimulus is strong enough to push their transmembrane potential above a certain threshold level, once the stimulus is removed the potential does not immediately return to rest but rather undergoes a large excursion before eventually reaching the resting state. The very quick depolarization and the subsequent much slower repolarization observed in the transmembrane potential of excitable cells is known as action potential.

The most important work in the study of generation and propagation of signals is the one made by Hodgkin and Huxley [31], who developed the first quantitative model of propagation of an electrical signal along a squid giant axon[3].

Due to the fundamental role played by the Hodgkin-Huxley model in electrophysiology, we outline here its main characteristics and point out some important considerations that led to the development of its analytical formulation. For a more detailed analysis of the model and its derivation, the reader is referred to Hodgkin and Huxley's original work [31] and references therein.

In the squid giant axon (as in many neural cells) the principal ionic currents are the sodium Na^+ current and potassium K^+ current. All other currents are small in comparison to these two and in the Hodgkin-Huxley model they are combined together into the so-called leakage current (denoted by the subscript L). Experimental data suggest that the instantaneous current-voltage relations of open Na^+ and K^+ channels in the squid giant axon are approximately linear. Therefore, from the electrical circuit model for the cell membrane we obtain

$$C_m \frac{dV}{dt} = -g_{\mathrm{Na}}(V - V_{\mathrm{Na}}) - g_{\mathrm{K}}(V - V_{\mathrm{K}}) - g_{\mathrm{L}}(V - V_{\mathrm{L}}) + I_{\mathrm{appl}}, \qquad (2.18)$$

where I_{appl} is the applied current and for $S = \mathrm{Na}, \mathrm{K}, \mathrm{L}$, g_S is the membrane conductance to S and V_S is the Nernst equilibrium potential.

Equation (2.18) can be rewritten in the form

$$C_m \frac{dV}{dt} = -g_{\mathrm{eff}}(V - V_{\mathrm{eq}}) + I_{\mathrm{appl}},$$

where $g_{\mathrm{eff}} = \frac{1}{g_{\mathrm{Na}}+g_{\mathrm{K}}+g_{\mathrm{L}}}$ and $V_{\mathrm{eq}} = (g_{\mathrm{Na}}V_{\mathrm{Na}} + g_{\mathrm{K}}V_{\mathrm{K}} + g_{\mathrm{L}}V_{\mathrm{L}})/g_{\mathrm{eff}}$. V_{eq} is the membrane resting potential and it is a balance between the reversal potentials

[3] An axon is the long threadlike extension of a nerve cell that conducts nerve impulses from the cell body.

for the three ionic currents.

If $R_m = 1/g_{\text{eff}}$ is the passive membrane resistance and $\tau_m = C_m R_m$ is the time constant for the equation (on the order of 1 msec as reported by Keener and Sneyd [39]), for a steady applied current the membrane potential should quickly equilibrate to $V = V_{\text{eq}} + R_m I_{\text{appl}}$. This is indeed what is observed from experimental data when the applied current is small. However, for larger applied currents the response is quite different and this difference is due to the fact that conductances are not constant but rather depend on the voltage.

The development of the voltage clamp was fundamental in the study of the conductances. The voltage clamp fixes the membrane potential (usually by a rapid step from one voltage to another) and then measures the current that must be supplied in order to hold the voltage constant. Since the supplied current must equal the transmembrane current[4], the voltage clamp provides a way to measure the transient transmembrane current that results. As the voltage can be stepped from one level to another and kept constant, the voltage clamp eliminates any voltage changes and allows measurements of the conductances as functions of time only.

Hodgkin and Huxley were able to separate the total ionic current into its constituent parts and obtain from the experimental data the complete time courses of both I_{Na} and I_{K}. The assumption of linear current-voltage relations then allowed them to obtain the time courses of the conductances from

$$g_{\text{Na}} = \frac{I_{\text{Na}}}{V - V_{\text{Na}}} \quad \text{and} \quad g_{\text{K}} = \frac{I_{\text{K}}}{V - V_{\text{K}}}.$$

Their observations on the response of g_{Na} and g_{K} to a step increase or decrease in the membrane potential can be summarised as follows:

- with fixed voltages, the conductances are time-dependent;
- following a step increase in V, g_{K} slowly increases over time in a sig-

[4] V held constant means that $\frac{dV}{dt} = 0$.

moidal fashion and finally reaches a steady state (the time constant and the final level depend both on the step increase in V);

- following a step decrease in V, g_{K} simply decreases and approaches zero exponentially;

- g_{Na} exhibits a more complex behaviour. In fact, following a step increase in V, g_{Na} first increases and then decreases again, all at the same fixed voltage.

Hodgkin and Huxley realized that to obtain ordinary differential equations (ODEs) for the potassium and sodium conductances, in agreement with the behaviour observed from experimental data, it was easier to rewrite these conductances in terms of powers of suitable secondary variables that satisfy first order differential equations. In particular,

$$g_{\mathrm{K}} = \bar{g}_{\mathrm{K}} n^4,$$

where $\bar{g}_{\mathrm{K}}$ is constant and $n(t)$ is called the K^+ activation variable and satisfies

$$\tau_n(V)\frac{dn}{dt} = n_\infty(V) - n.$$

The fourth power was chosen because it was the smallest exponent giving acceptable agreement with experimental data (and not for physiological reasons). Values of τ_n and n_∞ can be obtained by fitting the experimental data. Similarly,

$$g_{\mathrm{Na}} = \bar{g}_{\mathrm{Na}} m^3 h,$$

where $\bar{g}_{\mathrm{Na}}$ is constant, $m(t)$ and $h(t)$ are called the Na^+ activation and inactivation variables, respectively, and satisfy first order ODEs of the form

$$\tau_m(V)\frac{dm}{dt} = m_\infty(V) - m,$$

$$\tau_h(V)\frac{dh}{dt} = h_\infty(V) - h.$$

Once again, the values of τ_m, m_∞, τ_h and h_∞ can be obtained by fitting

experimental data, and the use of two different variables is justified by the fact that experimental data suggested there were two processes at work: one that turns on the sodium current and one that turns it off. The secondary variables n, m and h are also called gating variables.

The gating equations of the Hodgkin-Huxley model can also be derived by assuming that each K^+ channel consists of four "n" subunits each of which can either be open or closed. If the gates operate independently, then the channel conductance is proportional to n^4, where n satisfies the simple two-state channel model. A similar conclusion can be made for the Na^+ channels with conductance being proportional to m^3h, under the assumption that each channel consists of three "m" gates and one "h" gate where m and h obey the equation of the two-state channel model.

The particular dynamics of the gating variables and the analytical form of the steady-state variables and time constants as functions of the voltage determines the opening and closing of different ion channels on different timescales. At rest, the transmembrane potential V is at its equilibrium value V_{eq} and when a small electrical stimulus is applied and then removed, the perturbed potential quickly re-equilibrates to its resting value. However, when the strength of the applied current pushes the Na^+ activation variable above a certain threshold value, it triggers an action potential. The increase in m generates an inward Na^+ current that quickly brings the transmembrane potential close to V_{Na}. Instead of reaching a new equilibrium level, the potential is affected by the difference in time constants of the gating variables and the fact that at this point the sodium current is inactivated. At about the same time, n is activated producing an outward current of K^+, driving the potential below its resting value, toward V_{K}. However, when V is below its resting value, n decreases and the potential eventually returns to its resting state V_{eq}. Since also the Na^+ inactivation variable h gradually returns to its resting state, the sodium channels can be re-activated and a new cycle can commence.

An example of action potential for the Hodgkin-Huxley (HH) model and the corresponding behaviour of the three gating variables is given in Figure 2.2 and Figure 2.3.

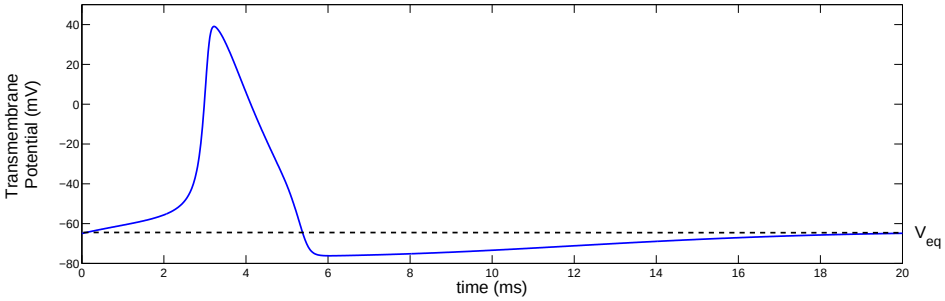

Figure 2.2: *Example of action potential generated by the HH model. The solution behaviour depicted was obtained with the routine ODE solver ode15s in MATLAB®. The parameter values for the model are taken from Keener and Sneyd [39], the potential is assumed to be at rest at the beginning of the simulation and the applied current is* $I_{appl} = 5\,\mu\text{A}\cdot\text{cm}^{-2}$.

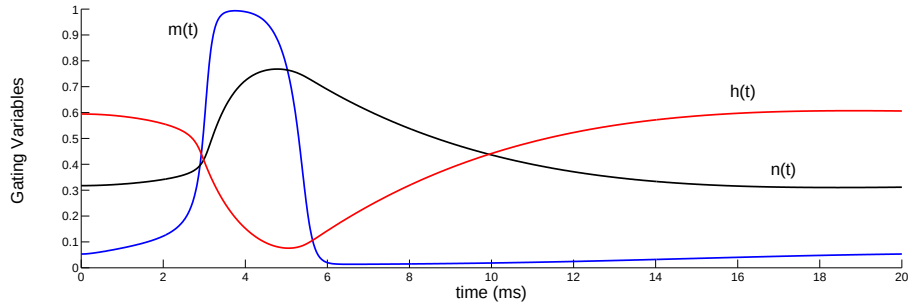

Figure 2.3: *The evolution in time of the gating variables* n, m *and* h, *corresponding to the action potential depicted in Figure 2.2. The initial values are set to* $n_\infty(V_{eq})$, $m_\infty(V_{eq})$ *and* $h_\infty(V_{eq})$, *where* $V_{eq} = -65\,\text{mV}$ *is the resting potential resulting from the parameter values considered by Keener and Sneyd [39].*

The HH model is a milestone in the study of excitable systems and many variations on the theme have been developed during the past 50 years, some of which are mathematical simplifications of the model presented above while others are elaborations or extensions of this model. These modifications

consider, for example, more sophisticated ways of modelling the ionic currents involved in the process, or aim at modelling excitability of different types of cells (not simply neurons), or include spatial dependence in the model and study how an electrical stimulus propagates through a medium made of excitable cells.

In this thesis we consider two specific models describing the variations in the transmembrane potential of a single excitable cell (of two different types) when an electrical stimulus is applied to the cell: the **Fitzhugh–Nagumo** (FHN) model (as proposed in [79]) and the **Beeler–Reuter** (BR) model (originally introduced in [6]). The FHN model still refers to the transmembrane potential of nerve cells and was developed as a simplification of the HH model so that the resulting system of equations was easier to analyze mathematically but still retained many of the qualitative features characterising the original model. On the other hand, the BR model consists of a more elaborate system of equations that was developed in the study of the action potential of ventricular myocardial fibres and therefore describes the behaviour of the excitable cells that constitute cardiac muscle.

The main structure of both models is similar and consists of a system of ODEs describing the evolution in time of the transmembrane potential v of a single excitable cell and the evolution of a system of suitable secondary variables used in the description of the ionic currents involved in the problem. The equation for the transmembrane potential v in both models has the form

$$C_m \frac{dv}{dt} = -I_{\text{ion}} + I_{\text{appl}}, \tag{2.19}$$

where as usual C_m is the cell membrane capacitance, I_{ion} is the ionic current and I_{appl} is an applied electrical stimulus used to trigger an action potential of the cell. The specification of the analytic expression of the ionic current depends on the particular model considered and provides the coupling between the transmembrane potential v and the gating variables of the model.

The Fitzhugh–Nagumo model

The Fitzhugh–Nagumo model [79] has two variables: the transmembrane potential v, also called the excitation variable, and the recovery variable w. When a current is applied to the cell, v rapidly moves away from its resting state. In order to reproduce the action potential observed for excitable cells, we must introduce in the model the variable w so that when the electrical stimulus is removed, the effect of w allows the transmembrane potential to return to its resting state and complete the cycle. As presented in [79], after rescaling both variables in order for the transmembrane potential to assume realistic values during the action potential and expressing both variables v and w in the units of mV, the system of ODEs describing the model can be written as follows:

$$\begin{cases} C_m \dfrac{dv}{dt} &= -I_{\text{ion}} + I_{\text{appl}} \\ \\ \dfrac{dw}{dt} &= b(v - v_{\text{rest}} - c_3 w). \end{cases} \tag{2.20}$$

In particular, the ionic current I_{ion} for the model has the following form:

$$I_{\text{ion}}(v, w) = \frac{c_1}{v_{\text{amp}}^2}(v - v_{\text{rest}})(v - v_{\text{th}})(v - v_{\text{peak}}) + \frac{c_2}{v_{\text{amp}}}(v - v_{\text{rest}})w, \tag{2.21}$$

where the resting potential is denoted by v_{rest}, v_{peak} is the peak potential, $v_{\text{amp}} = v_{\text{peak}} - v_{\text{rest}}$ and $v_{\text{th}} = v_{\text{rest}} + a\ v_{\text{amp}}$ is the so-called threshold potential. In system (2.20) and equation (2.21), the parameters a, b, c_1, c_2 and c_3 are all non-negative constants and can be adjusted to simulate different cell types. The values of the parameters used in the formulation of the model provided in [79] are given in Table 2.1. Currents are expressed in $\mu\text{A}\cdot\text{cm}^{-2}$, voltages in mV and time is in msec.

The initial condition for system (2.20) is generally given by $[v_0, w_0]^T = [v_{\text{rest}}, 0]^T$. By applying an external current at $t = t_1$ for a certain interval of time, that is, by defining $I_{\text{appl}}(t) > 0$ for $t \in [t_1, t_2] \subseteq [0, t_f]$, the electrical stimulus perturbs the potential v moving it away from its equilibrium value

C_m	1 μF$\cdot$cm^{-2}	a	0.13 (-)
v_{rest}	-85 mV	b	0.013 msec^{-1}
v_{peak}	40 mV	c_1	0.26 mS$\cdot$cm^{-2}
v_{th}	-68.75 mV	c_2	0.1 mS$\cdot$cm^{-2}
v_{amp}	125 mV	c_3	1 (-)

Table 2.1: *Parameter values for the Fitzhugh–Nagumo model as given in [79].*

v_{rest}. If I_{appl} is sufficiently strong, the potential of the excitable cell does not return immediately to its resting value but rather undergoes a slow and large excursion (an action potential) before returning to the steady state v_{rest}.

As previously mentioned, the role of the variable w is crucial for the completion of the cycle. In fact, in absence of the recovery variable and the interaction term involving both v and w in I_{ion}, once triggered by a sufficiently strong applied current, the potential v would approach the equilibrium value v_{peak} (also called the excited steady state) and would remain there indefinitely. A thorough description of the interaction between the excitation and the recovery variables can be found in [39]. Figure 2.4 is an example of an action potential for this model.

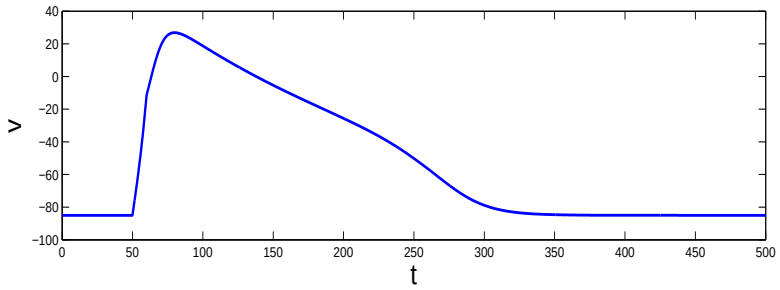

Figure 2.4: *Action potential for the FHN model (2.20) with* $t \in [0, 500]$*, initial condition* $[v_0, w_0]^T = [v_{rest}, 0]^T$*,* $I_{appl}(t) = 10\,\mu\text{A}\cdot\text{cm}^{-2}$ *for* $t \in [50, 55]$ *and all parameter values set as in Table 2.1. Time is expressed in* msec*,* v *is given in* mV*.*

The Beeler–Reuter model

A similar behaviour is observed for a more complex model proposed for ventricular muscle cells: the Beeler–Reuter model [6]. In this case, the ionic current is the sum of four different components and according to the original formulation of the model [6], it can be written as follows:

$$I_{\text{ion}} = I_{\text{Na}} + I_{\text{K}} + I_x + I_s, \tag{2.22}$$

where I_{Na} is the current carried by sodium

$$I_{\text{Na}} = (4m^3hj + 0.003)(v - 50),$$

I_{K} and I_x are the potassium currents defined, respectively, by

$$I_{\text{K}} = 1.4\frac{\exp(0.04(v+85)) - 1}{\exp(0.08(v+53)) + \exp(0.04(v+53))} + 0.07\frac{v+23}{1-\exp(-0.04(v+23))},$$

$$\text{and} \qquad I_x = 0.8\ x\frac{\exp(0.04(v+77)) - 1}{\exp(0.04(v+35))},$$

and I_s is the current of calcium given by

$$I_s = 0.09\ d\ f(v + 82.3 + 13.0287\ln(10^{-7}c)).$$

The six variables m, h, j, d, f and x are the gating variables of the model and $c = 10^7[\text{Ca}]_i$ describes the intracellular calcium concentration and has been scaled to simplify the notation. In the equations above, all currents are in $\mu\text{A}\cdot\text{cm}^{-2}$, v is in mV, the six gating variables are dimensionless, and $[\text{Ca}]_i$ is in mole per litre ($\text{mole}\cdot\text{l}^{-1}$).

As in the case of the FHN model, we assume the cell membrane capacitance to be $C_m = 1\,\mu\text{F}\cdot\text{cm}^{-2}$. The BR model consists of a system of eight ODEs. However, due to the similar form of the six equations describing the evolution in time of the six gating variables, we reformulate the model only in terms

of the following three equations:

$$\begin{cases} \dfrac{dv}{dt} &= -I_{\text{ion}} + I_{\text{appl}} \\ \dfrac{dg}{dt} &= \alpha_g(v)(1-g) - \beta_g(v)g \\ \dfrac{dc}{dt} &= 0.07(1-c) - I_s \end{cases} \tag{2.23}$$

where the second equation describes the evolution in time of the gating variable g $(= m, h, j, d, f, x)$ and the functions α_g and β_g of the transmembrane potential v represent the channel opening and closing rates for the particular gating variable g to which the equation is referring to. Independently of g, that is, for all six gating variables, both α_g and β_g have the form

$$\frac{C_1 \exp(C_2(v - v_*)) + C_3(v - v_*)}{1 + C_4 \exp(C_5(v - v_*))}, \tag{2.24}$$

where the values and the units of the constants involved are specified in Table 2.2. These values are taken from the original work of Beeler and Reuter [6]. The rate constants α_g and β_g are all in msec^{-1} and time is in msec.

An example of action potential for this model is given in Figure 2.5. Note that in this case the shape of the action potential is characterised by a peak, a small concavity called the early depolarization phase and a notch[5] followed by a much slower repolarization phase compared to the one characterizing the FHN model.

Spatially dependent models

The cell models considered so far describe how an electrical stimulus may affect the transmembrane potential of a single excitable cell. However, our

[5]These are typical characteristics observed in action potentials of cardiac cells and cannot be obtained with the FHN model.

	C_1 msec^{-1}	C_2 mV^{-1}	C_3 $\text{mV}^{-1}\cdot\text{msec}^{-1}$	C_4 msec^{-1}	C_5 mV^{-1}	v_* mV
α_m	0	–	1	-1	-0.1	-47
β_m	40	-0.056	0	0	–	-72
α_h	0.126	-0.25	0	0	–	-77
β_h	1.7	0	0	1	-0.082	-22.5
α_j	0.055	-0.25	0	1	-0.2	-78
β_j	0.3	0	0	1	-0.1	-32
α_d	0.095	-0.01	0	1	-0.072	5
β_d	0.07	-0.017	0	1	0.05	-44
α_f	0.012	-0.008	0	1	0.15	-28
β_f	0.0065	-0.02	0	1	-0.2	-30
α_x	0.0005	0.083	0	1	0.057	-50
β_x	0.0013	-0.06	0	1	-0.04	-20

Table 2.2: *Parameter values for the Beeler–Reuter model as given in [6].*

aim is to observe how an electrical signal might propagate throughout a domain composed of excitable cells, such as neural or cardiac tissue. Therefore, we extend these cell models by introducing a spatial domain and defining the potential as a function of both time and space. As stated by Clayton et al. [19], "models of cardiac tissue electrophysiology encode information about excitability at the cell level and electrical conduction at the tissue level to enable quantitative description of action potential propagation". The same idea is still valid in the context of models of electrical propagation through neural tissue. These spatially dependent models can be either discrete or continuous and both have their own strengths and weaknesses. In this thesis we only focus on continuous models. In particular, the spatially varying models considered here are two typical mathematical approaches used in the simulation of cardiac tissue.

The first model we introduce is known as the **bidomain model** [19] and is developed under the assumption that cardiac tissue can be viewed as a composite medium composed of intracellular and extracellular domains. Under certain assumptions, the equations of the bidomain can be significantly simplified leading to the second model object of our study: the **monodomain**

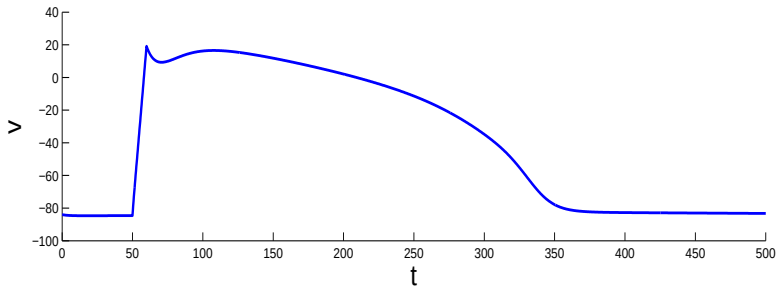

Figure 2.5: *Action potential for the BR model (2.23) with* $t \in [0, 500]$*, initial condition* $[v_0, m_0, h_0, j_0, d_0, f_0, x_0, c_0]^T = [-85, 0, 1, 1, 0, 1, 0, 1]^T$*,* $I_{appl}(t) = 25\,\mu\text{A}\cdot\text{cm}^{-2}$ *for* $t \in [50, 55]$ *and all parameter values set as in Table 2.2. Time is expressed in* msec*,* v *is given in* mV*.*

model [19]. Even though there are major limitations in terms of reproducing realistic phenomena, the monodomain model still captures essential features of the tissue response to electrical stimulation and due to its relative simplicity, for some studies this model offers advantages from both the analytical and numerical point of view.

The bidomain equations

As described in detail in [19] and [40], the mathematical formulation of the bidomain model is obtained by assuming that the spatial domain is composed of intracellular and extracellular domains, that both domains are continuous and overlapping but separated by the cell membrane. In each domain the corresponding potential must be viewed at each point as a quantity averaged over a small volume. Let u_e and u_i denote the extracellular and intracellular potentials, respectively. The transmembrane potential previously introduced is then defined as $v = u_i - u_e$.

The bidomain model can be formulated either in terms of u_i and u_e as a coupled system of two degenerate nonlinear parabolic partial differential equations (PDEs) as shown for example in [66] or [67], or in the equivalent (and probably more popular) parabolic-elliptic formulation in terms of v and u_e

as follows:

$$\begin{cases} \nabla \cdot (M_i \nabla (v + u_e)) &= \chi \left(C_m \dfrac{\partial v}{\partial t} + I_{\text{ion}} \right) - I_i^{(\text{vol})} \\ \nabla \cdot (M_i \nabla v) + \nabla \cdot ((M_i + M_e) \nabla u_e) &= -I_{\text{tot}}^{(\text{vol})}, \end{cases} \tag{2.25}$$

where M_i and M_e are the conductivity tensors in the two domains (intracellular and extracellular), C_m is the cell membrane capacitance, I_{ion} the ionic current, χ the membrane surface to volume ratio, $I_i^{(\text{vol})}$ the intracellular stimuli per unit volume and $I_{\text{tot}}^{(\text{vol})} = I_i^{(\text{vol})} + I_e^{(\text{vol})}$, where $I_e^{(\text{vol})}$ is the extracellular stimuli per unit volume. In the literature it is common to formulate the bidomain equations by setting $I_{\text{tot}}^{(\text{vol})} = 0$. However, as pointed out by Pathmanathan et al. [66], setting $I_{\text{tot}}^{(\text{vol})} = 0$ "does not correspond to zero extracellular stimulus. Instead, it corresponds to choosing $I_e^{(\text{vol})} = -I_i^{(\text{vol})}$, that is, to applying an extracellular stimulus at each point in space where an intracellular stimulus is applied, with a magnitude equal and opposite to the intracellular stimulus".

System (2.25) is the consequence of assumptions on insignificant time variations in the electrical field, balance in charge accumulation at each point and conservation laws for the total current (for a thorough description of the derivation of these two equations see for example [19] or [79]). Conductivities are all expressed in $\text{mS}\cdot\text{cm}^{-1}$, χ is in cm^{-1} and the unit used for the spatial variable is cm.

To complete the formulation of the problem we must specify the boundary conditions for v and u_e. Once again, following [66], we have that appropriate boundary conditions for the problem are given by the specification of current applied across the boundary

$$\begin{aligned} n \cdot (M_i \nabla (v + u_e)) &= I_i^{(\text{surf})}, \\ n \cdot (M_e \nabla u_e) &= I_e^{(\text{surf})}, \end{aligned} \tag{2.26}$$

where n represents the outward pointing unit normal vector to the tissue and $I_i^{(\text{surf})}$ and $I_e^{(\text{surf})}$ are the intracellular and extracellular currents per unit

area applied across the boundary. The conductivities M_i and M_e reflect the anisotropic properties of the cardiac tissue and the fact that the heart muscle is composed of sheets of fibres. Therefore, in general these tensors vary throughout the heart depending on the orientation of the fibres and the sheets. However, since in this thesis we do not aim to reproduce the electrophysiological activity of the entire organ but rather consider only small slabs of tissue, we can adopt a slight simplification by assuming that these conductivity tensors are diagonal matrices and their entries characterise for both domains the conductivity properties of the tissue in each spatial direction.

Note on applied currents

There are important considerations to be made in terms of consistency and well-posedness of the problem when applied currents are considered in the bidomain model. The reader is referred to the work of Pathmanathan et al. [66] for a detailed description of these issues. In Chapter 4, when considering numerical simulations of excitable media models we will outline some of these considerations and according to [66] highlight the assumptions behind the particular choice of applied stimuli we will use in our simulations.

The monodomain equation

Under the assumption that the anisotropy of the intracellular and extracellular spaces is the same, that translates into the assumption of proportionality of the conductivities in the two domains, i.e., $M_e = \lambda M_i$ with $\lambda \in \mathbb{R}$, it is possible to reduce system (2.25) to the following scalar equation known as the monodomain model:

$$\frac{\lambda}{1+\lambda}\nabla \cdot (M_i \nabla v) = \chi \left(C_m \frac{\partial v}{\partial t} + I_{\text{ion}} \right) - I^{(\text{vol})}, \tag{2.27}$$

where $I^{(\text{vol})}$ is a stimulus current. The boundary conditions (2.26) in turn reduce to

$$n \cdot (M_i \nabla v) = I^{(\text{surf})}. \tag{2.28}$$

The hypothesis of proportionality for the conductivities is a great simplification. As stated in [79], "measurements of intracellular and extracellular conductivities contradict this assumption, and it is difficult to specify the parameter λ so as to obtain the closest approximation of the physiological conductivities". However, due to its simplicity, numerical computations of the solution of this model are usually not very computationally expensive. Moreover, as reported by Clayton et al. [19], "if there is no injection of current into the extracellular space, descriptions of action potential propagation provided by monodomain and bidomain models are close to each other even under the condition of unequal anisotropy ratio in the extracellular and intracellular spaces". Therefore, under certain assumptions the monodomain formulation still reflects the main features of the cardiac tissue response and will be used as a starting point in the study proposed in this thesis.

2.2 Numerical techniques

We now provide some background to the numerical methods used to compute the numerical solution of the models of cell migration and excitable media presented in Section 2.1. The main features of spatial discretisation and temporal integration strategies or the alternative spectral approach methods for the solution of a given PDE in one and two spatial dimensions are outlined in this section.

2.2.1 The method of lines and the finite-difference scheme

One of the classical approaches used in the numerical solution of partial differential equations is the so-called **method of lines** (MOL). Typically, in a physical problem, the independent variables considered are space and time. In this thesis, we only consider PDEs that are first order in time and (in the standard case) second order in space. Their solution requires the specification of some auxiliary conditions that in our applications will be of the following type:

- An **initial condition** for the time variable t. The value of the dependent variable(s) is specified at an initial time $t = t_0$ and then evolves in time and space according to the equations of the problem for values of t on a specified finite interval of the form $[t_0, t_f]$.

- **Boundary conditions** in space. The value of the dependent variable(s) or its (their) first order derivatives in space (or a combination of both) are specified along the boundary of the spatial domain considered.

The main idea behind the MOL is to first discretise in space the equations of a given model by replacing all the space derivatives with algebraic approximations and then use a suitable integration algorithm to obtain the solution of the resulting system of ODEs. In fact, after spatial discretisation, the only independent variable remaining for the problem is time and numerical methods for the solution of initial value systems of ODEs can be used to compute an approximate solution of the original PDE (or system of PDEs).

The spatial discretisation technique we will focus on for all the models considered in this thesis is the **finite-difference method** [1]. To illustrate our methodology let us consider a test equation in one spatial dimension and outline the main points of this numerical technique.

For $x \in [a, b]$ and $t \in [t_0, t_f]$, let us consider the one-dimensional parabolic equation for the dependent variable $u(x, t)$ given by

$$\frac{\partial u}{\partial t} = \frac{\partial^2 u}{\partial x^2}. \tag{2.29}$$

Let us assume that equation (2.29) is coupled with homogeneous Neumann boundary conditions at both ends of the spatial interval, that is,

$$\left.\frac{\partial u}{\partial x}\right|_{x=a} = 0 \quad \text{and} \quad \left.\frac{\partial u}{\partial x}\right|_{x=b} = 0, \tag{2.30}$$

and let $u(x, t_0) = u^{(0)}(x)$ be a given initial condition for the problem[6].

Let us divide the interval $[a, b]$ into a mesh with $N + 1$ equally spaced nodes $x_i = a + i\ h_x$ for $i = 0, 1, \ldots, N$, where $h_x = (b - a)/N$ is the uniform mesh size. Let $u_0(t), u_1(t), \ldots, u_N(t)$ represent the approximations of the solution at the nodes of the spatial grid. The second order finite-difference approximation of $\frac{\partial^2 u}{\partial x^2}$ at a given node x_i of the mesh is defined by

$$\left.\frac{\partial^2 u}{\partial x^2}\right|_{x=x_i} \approx \frac{u_{i+1}(t) - 2u_i(t) + u_{i-1}(t)}{h_x^2}. \tag{2.31}$$

We notice that for the internal nodes of the mesh, that is, when the index $i = 1, \ldots, N - 1$, approximation (2.31) is well defined and involves the approximation of the solution at the particular node considered, x_i, and at its two neighbouring nodes, x_{i-1} and x_{i+1}. However, in order to be able to use the above approximation at both ends of the spatial interval, we must define the value of $u_{-1}(t)$ and $u_{N+1}(t)$, respectively.

Since the boundary conditions of the problem involve $\frac{\partial u}{\partial x}$, we can introduce in our spatial grid two fictitious points (located at x_{-1} and x_{N+1}) and consider the second order finite-difference approximation of the first order derivative in space at both ends of the spatial interval given by

$$\left.\frac{\partial u}{\partial x}\right|_{x=x_0} \approx \frac{u_1(t) - u_{-1}(t)}{2h_x} \quad \text{and} \quad \left.\frac{\partial u}{\partial x}\right|_{x=x_N} \approx \frac{u_{N+1}(t) - u_{N-1}(t)}{2h_x}. \tag{2.32}$$

By rearranging the expressions of (2.32) we can rewrite $u_{-1}(t)$ and $u_{N+1}(t)$ only in terms of approximations of the solution or of its first order derivative in space at nodes of the spatial discretisation of $[a, b]$ as follows:

$$u_{-1}(t) \approx u_1(t) - 2h_x \left.\frac{\partial u}{\partial x}\right|_{x=x_0} \quad \text{and} \quad u_{N+1}(t) \approx 2h_x \left.\frac{\partial u}{\partial x}\right|_{x=x_N} + u_{N-1}(t). \tag{2.33}$$

[6]To avoid confusion between the subscript typically used to identify the initial condition and the index "0" denoting the solution approximation at the node of the spatial mesh $x = x_0$, in this section we use a subscript and label the initial condition $u^{(0)}$.

In particular, in the case of homogeneous Neumann boundary conditions, approximation (2.33) reduces to

$$u_{-1}(t) \approx u_1(t) \quad \text{and} \quad u_{N+1}(t) \approx u_{N-1}(t). \tag{2.34}$$

By substituting these values in the approximation of the second order derivative at the boundary nodes we avoid the problem of having to define the solution approximation at points outside of the spatial domain and obtain

$$\left.\frac{\partial^2 u}{\partial x^2}\right|_{x=x_0} \approx \frac{2u_1(t) - 2u_0(t)}{h_x^2}, \tag{2.35}$$

and

$$\left.\frac{\partial^2 u}{\partial x^2}\right|_{x=x_N} \approx \frac{2u_{N-1}(t) - 2u_N(t)}{h_x^2}. \tag{2.36}$$

Let $\mathbf{u}(t) = [u_0(t), u_2(t), \ldots, u_N(t)]^T$. From the finite-difference approximations defined above, equation (2.29) can be approximated by a system of ODEs in the sole variable t of the form

$$\mathbf{u}'(t) = A\ \mathbf{u}(t), \tag{2.37}$$

where A is the tridiagonal matrix of coefficients defined as follows, containing also the information on the boundary conditions of the problem[7]:

$$A = \frac{1}{h_x^2}\begin{bmatrix} -2 & 2 & & & & & \\ 1 & -2 & 1 & & & & \\ & 1 & -2 & 1 & & & \\ & & \ddots & \ddots & \ddots & & \\ & & & 1 & -2 & 1 & \\ & & & & 2 & -2 & \end{bmatrix}. \tag{2.38}$$

[7]Different boundary conditions lead to different matrix approximations of the operator. Sometimes, in the case of homogeneous Neumann boundary conditions, only a first order finite-difference approximation of the first order spatial derivative is used at the boundary nodes. Despite the lower order of approximation at the boundaries, this choice leads to a symmetric discretisation matrix and symmetry is often a desirable property when efficient numerical strategies for the solution of the resulting system of ODEs are sought.

A similar spatial discretisation strategy can be applied in the presence of a reaction term and for higher spatial dimension problems.

For example, let us consider the following example of reaction-diffusion equation on a rectangular domain $\Omega = [X_a, X_b] \times [Y_a, Y_b]$ for $t \in [t_0, t_f]$:

$$\frac{\partial u}{\partial t} = \Delta u + g(u), \tag{2.39}$$

where Δ represents the Laplacian differential operator and $g(u)$ is a given (and possibly nonlinear) reaction term. Let us consider zero-flux boundary conditions along the entire boundary $\partial\Omega$ and assume that the initial condition $u(x, y, t_0) = u^{(0)}(x, y)$ is provided.

In two spatial dimensions, the Laplacian operator Δ is defined as

$$\Delta = \frac{\partial^2}{\partial x^2} + \frac{\partial^2}{\partial y^2}. \tag{2.40}$$

In order to discretise in space our model via finite-differences, we consider a uniform spatial grid in both dimensions with mesh sizes $h_x = (X_b - X_a)/N_1$ and $h_y = (Y_b - Y_a)/N_2$, respectively, resulting in a number $N_1 + 1$ of nodes along the x direction and $N_2 + 1$ along the y direction. Let the indices $i = 0, \ldots, N_1$, $j = 0, \ldots, N_2$ and let $u_{i,j}$ represent the approximation of the solution at the node (x_i, y_j) of the spatial grid. Then, by applying the one-dimensional finite-difference approach to each spatial dimension we obtain

$$\Delta u\Big|_{(x,y)=(x_i,y_j)} \approx \frac{u_{i+1,j} - 2u_{i,j} + u_{i-1,j}}{h_x^2} + \frac{u_{i,j+1} - 2u_{i,j} + u_{i,j-1}}{h_y^2}. \tag{2.41}$$

To avoid the use of two indices and to build a vector in which each index corresponds to a different node of the two-dimensional grid, we introduce a node order favouring the direction in which we have the smaller number of nodes[8]. For example, if we decide to number the nodes along the y direction, we obtain the result shown in Figure 2.6.

[8]As a result, the sparse matrix of the spatial discretisation will have a narrower band which is an important feature when solving linear systems.

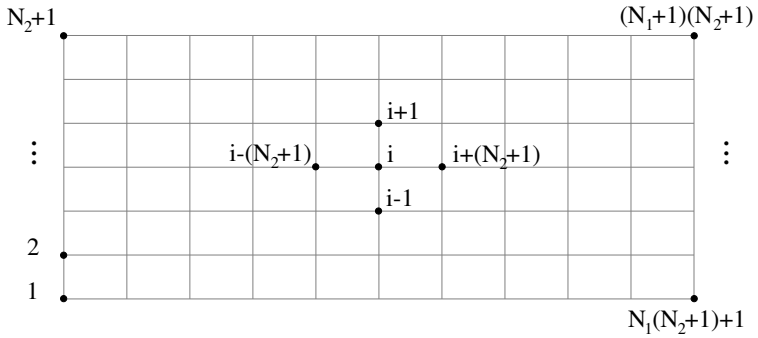

Figure 2.6: *Node order for the two-dimensional rectangular grid with nodes numbered along the columns.*

Let $i = 1, 2, \ldots, (N_1 + 1)(N_2 + 1)$ be the index denoting a particular node $(x, y)_i$ of the rectangular spatial grid and u_i the corresponding approximation of the solution. For all the internal nodes of the rectangular grid, the second order central difference approximation of the finite-difference method becomes

$$\Delta u\Big|_{(x,y)_i} \approx \frac{u_{i-(N_2+1)} - 2u_i + u_{i+(N_2+1)}}{h_x^2} + \frac{u_{i-1} - 2u_i + u_{i+1}}{h_y^2}. \tag{2.42}$$

As shown by Figure 2.6, we observe that the approximation of Δu at a node $(x, y)_i$ depends on the approximation of the solution at that particular node and at its four immediate neighbouring grid points (corresponding to the indices $i - (N_2 + 1)$, $i - 1$, $i + 1$ and $i + (N_2 + 1)$ for this particular choice of node order). These five points are typically called the five-point stencil of the i-th node in the grid.

Along all four sides of the rectangular domain Ω, we see that some of the points in the five-point stencil of the boundary nodes lay outside of Ω and hence do not correspond to any node of our two-dimensional grid. Similarly to the one-dimensional case, we exploit the information provided by the boundary conditions of the problem (in this case zero-flux in each spatial dimension) and rewrite $\Delta u|_{(x,y)_i}$ only in terms of the approximation of the solution at nodes of the two-dimensional grid.

As in the one-dimensional case, from these finite-difference approximations we obtain the coefficients of the matrix A of the spatial discretisation. In this case, A is a block tridiagonal matrix, that is, it has the following block structure:

$$A = \begin{bmatrix} B_1 & C_1 & & & \cdots & & 0 \\ A_2 & B_2 & C_2 & & & & \\ & \ddots & \ddots & \ddots & & & \vdots \\ & & A_k & B_k & C_k & & \\ \vdots & & & \ddots & \ddots & \ddots & \\ & & & & A_{N_1} & B_{N_1} & C_{N_1} \\ 0 & & \cdots & & & A_{N_1+1} & B_{N_1+1} \end{bmatrix}, \tag{2.43}$$

where the only non-zero blocks are on the lower diagonal, main diagonal and upper diagonal. In particular, for our discretisation each B_k is a square tridiagonal block of size $N_2 + 1$, whereas A_k and C_k are diagonal blocks of size $N_2 + 1$ for all k. As a result, the matrix A is very sparse and only has five non-zero diagonals at most.

After spatial discretisation, the problem can be written once again as a system of ODEs for the vector of solution approximations $\mathbf{u} \in \mathbb{R}^{(N_1+1)(N_2+1)}$ in the form

$$\mathbf{u}'(t) = A\ \mathbf{u}(t) + \mathbf{g}(\mathbf{u}(t)), \tag{2.44}$$

where the number of nodes (and therefore the length of the vector $\mathbf{u}(t)$) corresponds to the number of discretisation points of the two-dimensional spatial grid, A is the discretisation matrix (the structure of which depends on the spatial dimension, the discretisation approach used and the way spatial nodes are numbered) including the information provided by the boundary conditions, and $\mathbf{g}(\mathbf{u}(t))$ is the vector obtained by spatial discretisation of the reaction or source term (and it typically is a function of $\mathbf{u}(t)$).

All previous considerations can be easily adapted in the presence of a diffusion coefficient (or tensor in more than one spatial dimension) by suitably

modifying the matrix A.

2.2.2 Finite-element and finite-volume methods

Finite-difference methods are not the only possible numerical strategy used to approximate the solution of partial differential equations. Finite-element methods (FEMs) and finite-volume methods (FVMs) are very widely used and each of these numerical techniques has particular features that might be desirable in the solution of specific PDE problems.

As presented in the review of numerical methods for nonlinear PDEs by Tadmor [80], "FEMs offer great flexibility in modelling problems with complex geometries and, as such, they have been widely used in science and engineering as the solvers of choice for structural, mechanical, heat transfer, and fluid dynamics problems." After dividing the spatial domain into a set of non-overlapping polyhedrons (determining the structured or unstructured spatial grid of the problem), the approximate solution is computed in terms of piecewise polynomial basis functions, typically "polynomials of low degree with minimal requirement of continuity across the interfaces of the elements." On the other hand, FVMs are used to compute the solution approximation on the same type of structured or unstructured spatial grid, but "FV schemes are realized in terms of cell averages, where one ends up with a piecewise constant approximation". Moreover, "similar to finite-elements methods, FV approximations are defined throughout the computational domain, and unlike finite-difference methods, they are not limited to discrete point values. In contrast to FE methods, however, the FV approximations need not be smooth across the edges of the cells. They are therefore suitable to simulate problems with large gradients and, in particular, the spontaneous formation of jump discontinuities in nonlinear conservation laws."

There are a number of advantages and disadvantages in the use of each method previously mentioned and in many applications *ad-hoc* numerical strategies combining these methods are often developed based on the specific problem considered and the requirements in terms of overall accuracy of the

solution, stability, robustness and efficiency of the solver.

2.2.3 Temporal integration and the semi-implicit Euler method

After spatial discretisation of a given PDE (or system of PDEs), we must apply a suitable numerical technique to the resulting system of ODEs in order to obtain the evolution in time of the solution approximation at the nodes of our spatial mesh. There is a vast literature on the solution of ODE systems and once again, the choice of a suitable solver for a given problem depends on accuracy, stability and efficiency requirements.

The concept of accuracy defines how well the solution of a given numerical scheme approximates the exact solution of the considered problem and it is typically the result of two important properties of the numerical method: consistency and stability. Consistency means that the local truncation error[9] at each time step is sufficiently small so that the global error (error accumulated from the beginning of the simulation) goes to zero as the step size of the method goes to zero.

Stability on the other hand, can be classified in different ways. For example, a method is called zero-stable when to a small perturbation in the data of the problem corresponds a comparably small change in the numerical solution produced by the scheme. However, the concept of stability is also related to the asymptotic behaviour of the numerical solution produced with a given step size. We talk in this case of A-stability and this property can be studied by applying the numerical method to a test equation of the form $\mathbf{y}' = \lambda\mathbf{y}$. In fact, a method is A-stable if applied to the test equation it generates bounded numerical solutions for all positive step sizes and for all values of $\lambda \in \mathbb{C}$ with negative real part. Stability is strongly related to the nature of the ODE system to which the numerical scheme is applied and for many

[9]The error between the exact solution at a given time point and the value computed at the same time point by applying the numerical scheme to the exact solution.

problems stability is much more of a constraint than accuracy. It is the case of stiff ODEs.

There is no universal mathematical definition of stiffness and as mentioned by Iserles [38] "it is perhaps more informative to adopt an operative (and slightly vague) designation" of an ODE system. Stiffness typically arises in practice whenever the phenomenon modelled by the ODE system represents processes characterised by significantly different time scales. For some problems, such as linear ODE systems, a very good indicator of stiffness is the ratio of the modulus of the largest and the smallest eigenvalues of the Jacobian of the right-hand side of the system. In fact, if the ratio is large, it is typically safe to assume that the problem is stiff. ODE systems arising from spatial discretisation of PDEs are another example of large stiff systems where the stiffness is artificially introduced in the problem via the discretisation process.

When evaluating the performance of numerical methods in producing the solution of stiff systems, the concept of stability comes back into play and an important distinction arises between explicit and implicit schemes. In fact, explicit methods suffer from significant step size restrictions in the case of stiff problems and unless the step size is taken to be extremely small, the corresponding solution produced by the explicit numerical scheme will be unstable.

On the other hand, implicit schemes were developed in order to remedy these stability issues. The implicit nature of these schemes in fact allows us to exploit the stiff character of the problem and build a stable approximation of the solution with a much larger step size compared to the one allowed by explicit methods. Therefore, the extra computational cost required for the implementation of an implicit method is quickly compensated by the less heavy computational requirements to achieve a prescribed accuracy, due to the use of a much larger temporal step. Only implicit methods can be A-stable but not all implicit schemes have this property. For example, one can

show that all A-stable linear multistep methods have order two or less[10]. However, the requirement of a weaker property called A(α)-stability[11] is often acceptable for the solution of many problems and higher order implicit Runge–Kutta methods satisfying this property exist.

Depending on the software used to compute the numerical solution one might also have access to a number of built-in solvers that can be directly applied (or easily adapted) to the solution of a given problem. The numerical simulations presented in this thesis have all been produced with MATLAB® software.

MATLAB® offers a variety of ODE solvers each of which has its own strengths and might be preferable under different circumstances. Most of the ODE systems considered in this thesis are stiff systems resulting from the spatial discretisation of reaction-diffusion PDEs. Therefore, for our numerical simulations we will, where possible, use the MATLAB® solver **ode15s** that integrates stiff systems of ODEs (on a specified time interval and for a given initial condition) automatically adapting the time step size so that a prescribed accuracy is preserved. However, for some applications, the solution of the discretised system of ODEs is only part of the problem and implementing automatic integration over the entire time interval is not possible. For these applications we will consider different integration strategies depending on the characteristics of the particular problem studied.

One of these strategies is the so-called **semi-implicit Euler method** [4]. As suggested by its name, this integration approach is a combination of the well-known explicit and implicit Euler methods [41]. In particular, for the integration in time of a system of the form (2.44), where the right-hand side is the sum of a linear term and a function of $\mathbf{u}(t)$ (that in our applications is typically nonlinear), we introduce a temporal grid for the time interval $[t_0, t_f]$ and let Δt_k denote the size of the k-th temporal step. At each time step,

[10]This result is known as second Dahlquist barrier (see for example Butcher[13]).

[11]Note that the parameter α used in the name of this stability property has no relationship with the fractional index denoted by α in this thesis. See Butcher [13] for more details regarding the definition of this stability property.

we use a backward difference approximation for the time derivative, treat the linear component of the right-hand side implicitly and the reaction term explicitly (under the assumption that the stiffness in the system arises from the linear component). As a result, at each time step k we must solve the equation

$$\frac{\mathbf{u}^{k+1} - \mathbf{u}^k}{\Delta t_k} = A\ \mathbf{u}^{k+1} + \mathbf{g}(\mathbf{u}^k), \tag{2.45}$$

that in turn can be written as the following linear system:

$$(I - \Delta t_k\ A)\ \mathbf{u}^{k+1} = \mathbf{u}^k + \Delta t_k\ \mathbf{g}(\mathbf{u}^k), \tag{2.46}$$

where I represents the identity matrix.

Depending on the particular problem considered and the characteristics of the matrix on the left-hand side of equation (2.46), we will provide additional details and comments on how the solution of the linear system is computed.

2.2.4 The spectral method

An alternative approach to the MOL considered in this thesis is the so-called **spectral method** (see for example [9] or [80]). This strategy is based on the spectral decomposition of the differential operator in space and builds the analytical solution of the problem by exploiting the knowledge of the eigenvalues and eigenfunctions of that particular operator. In this thesis, we will consider the spectral approach to obtain the solution of space-fractional models. However, to illustrate the generic idea behind the method, we consider it here in the standard case (that is, when the second order derivative in space is used).

Let us consider once again the standard one-dimensional heat equation (2.29) on a finite spatial interval $[a, b]$, coupled with homogeneous Neumann boundary conditions at both ends of the interval and satisfying a given initial condition $u(x, t_0) = u_0(x)$. By using separation of variables we obtain that the

continuous one-dimensional Laplacian[12], $-\frac{\partial^2}{\partial x^2}$, with the above given boundary conditions has a complete set of orthonormal eigenfunctions $\{\varphi_j\}$ with corresponding eigenvalues λ_j, that is,

$$\left(-\frac{\partial^2}{\partial x^2}\right)\varphi_j = \lambda_j \varphi_j,$$

where for $j = 0, 1, 2, \ldots$

$$\lambda_j = \left(\frac{j\ \pi}{b-a}\right)^2 \quad \text{and} \quad \varphi_j(x) = \sqrt{\frac{2}{b-a}}\cos\left(\frac{j\pi(x-a)}{b-a}\right). \tag{2.47}$$

Using a Fourier series for $t \in [t_0, t_f]$, the analytic solution of the heat equation on $[a, b]$ can be expressed in terms of the eigenvalues and eigenfunctions of equation (2.47) as follows:

$$u(x,t) = \sum_{j=0}^{\infty} \hat{u}_j(t)\varphi_j(x) = \sum_{j=0}^{\infty} \hat{u}_j(t_0)e^{-\lambda_j(t-t_0)}\varphi_j(x), \tag{2.48}$$

where

$$\hat{u}_j(t_0) = \int_a^b u_0(x)\ \varphi_j(x)\ dx.$$

A similar approach can be considered when a generic diffusion coefficient D is used (not necessarily equal to one) and in the presence of a source term $g(u)$, that is, when the considered problem is in the form

$$\frac{\partial u}{\partial t} = -D\left(-\frac{\partial^2}{\partial x^2}\right)u + g(u).$$

In this case we introduce a temporal discretisation of the interval $[t_0, t_f]$ with time steps $\Delta t_k = t_{k+1} - t_k$. Let $u^k(x)$ denote the approximation of the solution at $t = t_k$. By applying the semi-implicit Euler method, to obtain $u^{k+1}(x)$ from $u^k(x)$, at each time step k we must solve an equation of the

[12]The choice of the negative sign is justified by the fact that we want the spectrum of the operator to be non-negative.

form

$$\frac{u^{k+1}(x) - u^k(x)}{\Delta t_k} = -D\left(-\frac{\partial^2}{\partial x^2}\right) u^{k+1}(x) + g(u^k(x)). \tag{2.49}$$

However, due to the orthogonality of the basis functions, each of the Fourier coefficients evolves independently from the others and hence the solution at t_{k+1} can be expressed as

$$u(x, t_{k+1}) = \sum_{j=0}^{\infty} \hat{u}_j^{k+1} \varphi_j(x), \tag{2.50}$$

where

$$\hat{u}_j^{k+1} = \frac{1}{1 + D\lambda_j \Delta t_k} \left[\hat{u}_j^k + \Delta t_k \ \hat{g}_j(u^k(x))\right],$$

$$\hat{u}_j^k = \int_a^b u^k(x)\varphi_j(x) \ dx,$$

and $\hat{g}_j$ is the j-th Fourier coefficient of the reaction term, that is,

$$\hat{g}_j(u) = \int_a^b g(u)\varphi_j(x) \ dx.$$

On a rectangular domain in two spatial dimensions, if $\{\varphi_i\}$, $\{\phi_j\}$ represent the sets of orthonormal eigenfunctions of the one-dimensional Laplacian coupled with suitable boundary conditions in each spatial direction, and $\{\lambda_i\}$, $\{\mu_j\}$ are the corresponding sets of eigenvalues, then by separation of variables we obtain that the set of eigenfunctions of the two-dimensional Laplacian is $\{\varphi_i\phi_j\}$ and the corresponding set of eigenvalues is $\{\lambda_i + \mu_j\}$, that is,

$$(-\Delta)\varphi_i(x)\phi_j(y) = \left(-\frac{\partial^2}{\partial x^2} - \frac{\partial^2}{\partial y^2}\right) \varphi_i(x)\phi_j(y) = (\lambda_i + \mu_j)\varphi_i(x)\phi_j(y).$$

Therefore, we can still use the Fourier decomposition for the two-dimensional solution and have that $\forall t \in [t_0, t_f]$ and $\forall (x, y) \in \Omega$

$$u(x, y, t) = \sum_{j=0}^{\infty} \sum_{i=0}^{\infty} \hat{u}_{ij}(t)\varphi_i(x)\phi_j(y), \tag{2.51}$$

where $\hat{u}_{ij}(t)$ is the Fourier coefficient corresponding to the particular combination of indices i, j.

2.3 Non-local models in space

We conclude this chapter with a section dedicated to space-fractional models. Here we introduce some concepts and issues related to the use and the interpretation of these types of non-local models. We also provide references and briefly outline the main ideas behind the implementation of the solution of non-local models in space and how the techniques described in Section 2.2 can be adapted in these non-standard cases.

2.3.1 Definitions

Given a standard reaction-diffusion model, the corresponding fractional modification in space or time (or both) is obtained by simply substituting the integer power derivatives of the standard PDE formulation with a differential operator of non-integer order. In this thesis we only consider space-fractional reaction-diffusion models.

From the purely mathematical point of view, fractional operators have been developed to generalize the ideas of traditional calculus to the case of non-integer order derivatives and integrals. The interest in these kinds of models is however not only theoretical. In fact, the observation of experimental data in many different fields reveals the existence of anomalous transport processes that no longer exhibit Gaussian profiles and therefore, cannot be described via Fick's second law. In many complex systems the time dependence of the mean squared displacement of particles deviates from the linear case (characterising Brownian diffusion) and rather grows non-linearly in time, for example following a power law pattern in the form $\langle (\Delta x)^2 \rangle \sim t^\alpha$, for some positive index $\alpha \neq 1$.

Following the terminology used by Metzler and Klafter [58], if $0 < \alpha < 1$, the

observed transport phenomenon is identified as being subdiffusive, whereas for $1 < \alpha < 2$, the diffusion process is an example of superdiffusion.

The derivation of the standard diffusion equation describing Brownian motion as limiting behaviour of a random walk can be embedded in the more general framework of Continuous Time Random Walks (CTRWs) that allows us to account for a wider range of transport phenomena (including anomalous diffusive processes) and to derive a generalised diffusion equation of fractional order.

An example of superdiffusive behaviour is obtained when considering an ensemble of particles undergoing Lévy flights, that is, a particular type of CTRWs described by a jump probability density function with finite characteristic waiting times and diverging jump length variance.

The fractional diffusion equation in terms of the concentration of particles $u(x,t)$ obtained in this case has the form

$$\frac{\partial u}{\partial t} = -(-\Delta)^{\alpha/2} u,$$

where $(-\Delta)^{\alpha/2}$ for $\alpha \in \mathbb{C} \setminus \{0\}$ is the so-called fractional Laplacian defined on $\mathbb{R}^n$ ($n \in \mathbb{N}$) in terms of the multidimensional Fourier transform $\mathcal{F}$ and its inverse $\mathcal{F}^{-1}$ (see for example Samko et al. [72]) as

$$(-\Delta)^{\alpha/2} f = \mathcal{F}^{-1} |x|^{\alpha} \mathcal{F} f. \tag{2.52}$$

To obtain explicitly the expression of $(-\Delta)^{\alpha/2} f$ in terms of the function f itself, one has to go back to the theory originally developed by Riesz [69] that defines $(-\Delta)^{\alpha/2} f$ for $\alpha > 0$ as an hypersingular integral, called the Riesz fractional derivative, obtained as the inverse of the Riesz potential with kernel

$$\mathcal{K}_{\alpha}(x) = \frac{\Gamma(\frac{n-\alpha}{2})}{2^{\alpha}\ \pi^{n/2}\ \Gamma(\frac{\alpha}{2})}\ |x|^{\alpha-n},$$

with $x \in \mathbb{R}^n$ and $\alpha - n \neq 0, 2, 4, \ldots$ (for more details see, for example, [42]).

In one spatial dimension ($x \in \mathbb{R}$), Yang [84] proved the equivalence of the definition of the fractional Laplacian in terms of its Fourier transform introduced above (i.e., $-(-\Delta)^{\alpha/2} f = -\mathcal{F}^{-1}|x|^{\alpha}\mathcal{F}f$) and the non-local operator $\frac{\partial^{\alpha}}{\partial|x|^{\alpha}}$ introduced by Gorenflo and Mainardi [29] as the Riesz–Feller operator and defined as the weighted sum of two one-sided Riemann–Liouville fractional derivatives as follows:

$$\frac{\partial^{\alpha}}{\partial|x|^{\alpha}} := -[c_{+}^{\alpha} I_{+}^{-\alpha} + c_{-}^{\alpha} I_{-}^{-\alpha}], \tag{2.53}$$

where $c_{+}^{\alpha} = c_{-}^{\alpha} := \frac{1}{2\cos(\pi\alpha/2)}$ and

$$\begin{aligned} I_{+}^{-\alpha} f(x,t) &:= \frac{1}{\Gamma(2-\alpha)} \frac{\partial^2}{\partial x^2} \int_{-\infty}^{x} \frac{f(y,t)}{(x-y)^{\alpha-1}} dy, \\ I_{-}^{-\alpha} f(x,t) &:= \frac{1}{\Gamma(2-\alpha)} \frac{\partial^2}{\partial x^2} \int_{x}^{\infty} \frac{f(y,t)}{(y-x)^{\alpha-1}} dy. \end{aligned} \tag{2.54}$$

On bounded one-dimensional domains $[a, b]$, under the assumption of homogeneous Dirichlet boundary conditions for the function f, one can define the extension

$$\bar{f}(x) := \begin{cases} f(x) & \text{on } (a,b) \\ 0 & \text{on } \mathbb{R} \setminus (a,b), \end{cases}$$

and still obtain the formal equivalence

$$-(-\Delta)^{\alpha/2} \bar{f} = \frac{\partial^{\alpha}}{\partial|x|^{\alpha}} \bar{f}.$$

However, for all other types of boundary conditions, it is still not clear how to restrict and interpret the above operator definitions and therefore proof of their equivalence (or non-equivalence) is not available. Moreover, if we consider the natural extension of the Riesz–Feller operator on $\mathbb{R}^n$ defined as

$$\mathcal{R}^{\alpha} := \frac{\partial^{\alpha}}{\partial|x_1|^{\alpha}} + \frac{\partial^{\alpha}}{\partial|x_2|^{\alpha}} + \cdots + \frac{\partial^{\alpha}}{\partial|x_n|^{\alpha}}, \tag{2.55}$$

the equivalence between the two formulations clearly no longer holds and

even greater care must be taken when considering finite domains $\Omega \subset \mathbb{R}^n$.

An alternative definition of the fractional Laplacian on bounded domains was proposed by Ilić et al. [34], [35]. In this case the non-local operator is defined by exploiting the knowledge of the eigenfunctions and eigenvalues expansion of the corresponding standard operator with given homogeneous boundary conditions. In particular, the definition given in [35] is as follows: suppose the Laplacian $(-\Delta)$ has a complete set of orthonormal eigenfunctions $\{\varphi_n\}$ corresponding to eigenvalues $\{\lambda_n^2\}$ on a bounded region $\mathcal{D}$, i.e., $(-\Delta)\varphi_n = \lambda_n^2\varphi_n$ on $\mathcal{D}$; $\mathcal{B}(\varphi) = 0$ on $\partial\mathcal{D}$, where $\mathcal{B}(\varphi)$ is one of the standard three homogeneous boundary conditions. Let

$$\mathcal{F}_\gamma = \left\{ f = \sum_{n=1}^{\infty} c_n\varphi_n, \quad c_n = \langle f, \varphi_n \rangle \;\middle|\; \sum_{n=1}^{\infty} |c_n|^2 |\lambda_n|^\gamma < \infty, \quad \gamma = \max(\alpha, 0) \right\},$$

then, for any $f \in \mathcal{F}_\gamma$, $(-\Delta)^{\alpha/2}$ is defined by

$$(-\Delta)^{\alpha/2} f = \sum_{n=1}^{\infty} c_n \lambda_n^\alpha \varphi_n.$$

In the literature we often observe authors being loose with the definition of the fractional Laplacian and making interchangeable use of different operators in their applications. Clearly boundary conditions play a fundamental role in practical problems and a unified theory on how to deal with generic types of boundary conditions is still missing. When considering non-local operators (naturally defined on $\mathbb{R}^n$), the introduction of a boundary sensibly modifies the operator and it is intuitive to see that one cannot simply specify the value of the solution (or its derivative) locally at the boundary.

2.3.2 Some issues

In light of all the considerations made so far, it is clear that when dealing with non-local models in space we encounter a number of different modelling issues that must be addressed if we want to use these operators as a valid modelling tool. As previously mentioned, fractional derivatives are generally

defined on all of $\mathbb{R}^n$ but in order to use these operators in models for practical applications we need to restrict their definition on bounded domains. It is essential to consider suitable boundary conditions for the problem and even more importantly to model correctly these conditions to obtain the right numerical approximation of the solution. Moreover, particular care must be taken in the numerical methodology used to compute the solution of the model. There are a number of different fractional order differential operators that can be employed to obtain a space-fractional modification of a standard model. Depending on the non-local operator used, it is then very important to consider the correct approach to approximate the given fractional order derivative.

Alongside these modelling issues, there are various computational issues that have to be taken into consideration when computing the numerical solution for a given fractional problem. For example, as we will see in detail when dealing with particular examples in Chapter 4, when using the method of lines, it is known that the non-locality of the fractional operators introduces a higher level of complexity. In fact, when the fractional power α is not equal to two, the discretization matrix involved in the linear system of ODEs obtained after spatial discretisation loses its sparsity and becomes dense. This obviously results in a much higher computational cost of the spatial discretisation. Furthermore, depending on the characteristics of the problem and the regularity or irregularity of the spatial domain considered, the computational performance and scalability of different numerical approaches (such as finite-difference, finite-element and finite-volume methods) to a specific problem might be significantly different and suggest the use of a particular strategy instead of others.

2.3.3 Numerical methods

Since the only difference between the standard and the non-local models in space considered in this thesis is the fact that the second order differential operator has been substituted with a non-integer counterpart, in the numer-

ical solution of the fractional problems it is natural to still use the method of lines and compute the solution approximation by first discretising the problem in space and then solving the resulting system of discretised ODEs in time. Here we present two different numerical strategies used to discretise in space a given non-local operator (that are essentially based on the two different definitions of the space-fractional operator previously introduced) and restate some of the issues related to the restriction of non-local models to finite domains.

The Grünwald–Letnikov approximation

The first numerical strategy considered is the **shifted Grünwald–Letnikov** finite-difference scheme [55] for the approximation of the Riesz–Feller fractional operator $\frac{\partial^\alpha}{\partial|x|^\alpha}$ introduced in equation (2.53).

Let us consider the space-fractional model

$$\frac{\partial u}{\partial t} = \frac{\partial^\alpha u}{\partial |x|^\alpha}, \tag{2.56}$$

for values of $x \in \mathbb{R}$ and $t \in [t_0, t_f]$, with a given initial condition $u_0(x)$.

The shifted Grünwald–Letnikov approach on a one-dimensional uniform spatial grid with mesh size h_x and nodes $x_i = i\,h_x$, for $i \in \mathbb{Z}$, gives

$$\left.\frac{\partial^\alpha u}{\partial |x|^\alpha}\right|_{x=x_i} = \frac{1}{2|\cos(\pi\alpha/2)|}\frac{1}{h_x^\alpha}\sum_{j=0}^{\infty}(-1)^j\binom{\alpha}{j}(u_{i-1+j} + u_{i+1-j}), \tag{2.57}$$

where u_i denotes the approximation of the solution u at the spatial node x_i. The way such a numerical strategy is adapted in the case of finite domains is by no means trivial. In fact, once again, on bounded domains the implementation of the boundary conditions considered for the problem is crucial.

We note that, if we look for a solution v of equation (2.56) on the one-dimensional finite interval $[a, b]$ and assume homogeneous Dirichlet boundary

conditions at both ends of the spatial interval, namely, for all $t \in [t_0, t_f]$

$$v(a,t) = 0 \quad \text{and} \quad v(b,t) = 0,$$

we can extend the solution v to all of $\mathbb{R}$ by defining its extension u to be identically equal to zero on the complement of the finite domain considered, that is,

$$u(x,t) = \begin{cases} v(x,t) & \forall x \in [a,b] \\ 0 & \forall x \notin [a,b]. \end{cases}$$

In doing so, the solution $u(x,t)$ satisfies the fractional equation (2.56) on all of $\mathbb{R}$ and we can therefore apply the approximation (2.57) to discretise the problem in space and compute the numerical solution to our problem. Due to the constraint imposed on u outside of the interval $[a,b]$, we notice that whenever the indices in the sum on the right-hand side of formula (2.57) refer to the approximation of the solution at a spatial node outside of the considered finite interval, the corresponding term in the sum is zero. Therefore, the approximation of $\frac{\partial^\alpha u}{\partial |x|^\alpha}$ at a given node $x = x_i$ reduces to a finite sum that can be written in terms of the approximations of the solution u only at the internal nodes of $[a,b]$. Since $u = v$ on the considered finite interval, we then obtain that the problem can be reformulated simply in terms of the solution v and its approximations at the internal nodes of the finite domain.

The treatment of all other types of boundary conditions is not so straightforward. In Chapter 4, we introduce a numerical strategy that extends the work made on semi-infinite domains by Krepysheva et al. [45] and describes how the implementation of the Grünwald–Letnikov formula (2.57) can be adjusted on finite intervals so that the solution to the fractional problem satisfies the right formulation of boundary conditions that generalises the concept of standard homogeneous Neumann boundary conditions.

We will also consider the two-dimensional extension of the non-local Riesz–Feller operator and the generalisation of the above numerical approach.

Spectral decomposition and Matrix Transfer Technique

The second numerical approach presented here is based on the work originally proposed by Ilić et al. [34], [35]. The strategy developed in these papers is essentially an operational method for the discretisation in space of the fractional model

$$\frac{\partial u}{\partial t} = -D(-\Delta)^{\alpha/2}u, \tag{2.58}$$

and the transformation of equation (2.58) into a system of ODEs. This method, known as the **matrix transfer technique** (MTT), is based on the assumption that the continuous fractional Laplacian $(-\Delta)^{\alpha/2}$ on a one-dimensional bounded domain can be approximated by some discrete operator defined via its spectral decomposition. Although promising numerical results are provided for the test problems considered in [34] and [35], rigorous mathematical proof of the validity of the proposed approach is missing.

As we will discuss in more detail in the operator theory remarks of Section 4.4 based on the work by Hutson et al. [33], given a continuous function g and a compact self-adjoint operator T, the function $g(T)$ can be defined in terms of the spectrum $\sigma(T)$ of the operator so that essentially we obtain $\sigma(g(T)) = g(\sigma(T))$. Under suitable restrictions on the functional space $\mathcal{H}$ in which the solution u of the problem (2.58) is sought, the standard continuous one-dimensional Laplacian on a finite domain, for example, with homogeneous Dirichlet boundary conditions, is indeed a compact self-adjoint operator. In particular, $(-\Delta)$ has a complete set of orthonormal eigenfunctions $\{\varphi_j\}_0^\infty$ and corresponding eigenvalues $\{\lambda_j^2\}_0^\infty$ such that, for all j,

$$(-\Delta)\varphi_j = \lambda_j^2 \varphi_j.$$

Hence, given a sufficiently regular function u, we can represent $(-\Delta)u$ as follows:

$$(-\Delta)u = \sum_{j=0}^{\infty} \lambda_j^2 \, \hat{u}_j \, \varphi_j,$$

where $\hat{u}_j := \langle u, \varphi_j \rangle$ represents the inner product of the solution u and the j-th

eigenfunction φ_j in the functional space $\mathcal{H}$ in which the problem is defined. The spectral definition of $g(-\Delta)$, for a continuous function g, gives

$$g(-\Delta)u = \sum_{j=0}^{\infty} g(\lambda_j^2)\, \hat{u}_j\, \varphi_j, \tag{2.59}$$

provided that the series on the right-hand side of this expression converges (and hence considering such an object is reasonable).

The MTT considers the particular case of $g(-\Delta) = (-\Delta)^{\alpha/2}$ and aims at building a discrete approximation of the expression (2.59) in a finite-dimensional subspace of $\mathcal{H}$. The strategy can be summarized as follows. Let us denote by A the positive semidefinite matrix[13] of the spatial discretisation of the differential operator $(-\Delta)$ obtained either with a finite-difference or finite volume approach and including the information on the particular type of boundary conditions considered for equation (2.58) on the finite interval of interest. Equation (2.58) can then be rewritten as the ODE system

$$\mathbf{u}'(t) = -DA^{\alpha/2}\mathbf{u}(t), \tag{2.60}$$

where the fractional power of the matrix A is defined as

$$A^{\alpha/2} := V\Lambda^{\alpha/2}V^{-1}\,, \tag{2.61}$$

where $A = V\Lambda V^{-1}$ is a diagonalisation of A (that is, Λ is the diagonal matrix of the eigenvalues and V the matrix of the corresponding eigenvectors). Note that the outlined methodology can be easily extended to the case of multiple spatial dimensions without altering the structure of the numerical procedure but simply considering the right sets of eigenfunctions and eigenvalues as done in [85] and [86].

Relation (2.61) allows us to explicitly compute $A^{\alpha/2}$. An explicit implementation of the solution to the discretised system of ODEs (2.60) requires only

[13] A matrix A is positive semidefinite if an only if all eigenvalues of A are non-negative - see Anton and Rorres [3].

the computation of a matrix function vector product $f(A)\mathbf{u}$ where f is a suitable function of $A^{\alpha/2}$ (see for example [48]). On the other hand, an implicit implementation requires the solution of a linear system of equations at each time step, involving the fractional power of a matrix on the left-hand side. However, iterative approaches can be used to reduce this to a set of matrix function products again - see Burrage et al. [14], Yang et al. [87], Moroney and Yang [61].

A slightly different approach is the one proposed by Bueno–Orovio et al. [11] that exploits the knowledge of the spectrum of the fractional Laplacian operator (as proposed in the continuous case by Ilić et al. [35]) but rather develops a spectral representation of the solution of the problem instead of making use of the MTT. In particular, the solution is computed following the spectral method introduced in Section 2.2, this time with the set of eigenfunctions and eigenvalues obtained by the spectral decomposition of the fractional Laplacian described above.

Chapter 3

Results in the standard diffusion case

In this chapter we consider the two main applications and the standard models proposed in Chapter 2, and present a set of numerical results describing in detail the specific methodology used for each problem. For the cell migration models the aim will be to present the typical solution behaviour observed for a given set of parameters and initial conditions and to validate the theoretical results on the wave speed of the solution reported in Section 2.1. Moreover, in Section 3.2, under some particular assumptions we will obtain an extension of the dispersion relation for the cell migration model with two interacting species and validate our result with some numerical simulations. The second half of the chapter will be dedicated to excitable media models. After presenting the various aspects of the methodology used to compute the numerical solution of these models, in Section 3.3 we will provide both one-dimensional and two-dimensional results replicating the particular solution behaviour observed for this class of models.

3.1 Cell migration models

Let us start by considering the dimensionless FK equation (2.4) on a finite interval $[0, L]$ coupled with homogeneous Neumann boundary conditions. In

order to compute the solution of the problem for $t \in [0, t_f]$, we apply the MOL strategy described in Section 2.2 and discretise the spatial interval into a uniform grid of $N+1$ nodes $x_0 = 0 < \cdots < x_i < \cdots < x_N = L$ and use fictitious points at the boundaries to obtain the finite-difference approximation of the solution at the boundary points.

As a result of the spatial discretisation process we transform the problem of solving the FK PDE into the one of finding a solution of a nonlinear system of ODEs of the form

$$\begin{cases} \mathbf{u}'(t) &= A\ \mathbf{u}(t) + \mathbf{g}(\mathbf{u}(t)) \\ \mathbf{u}(0) &= \mathbf{u}_0, \end{cases} \tag{3.1}$$

where $\mathbf{u}(t) = [u_0(t), \ldots, u_N(t)]^T$ is the vector of the approximations of the solution on the spatial grid, $A \in \mathbb{R}^{(N+1)\times(N+1)}$ is the matrix generated by the spatial discretization of $\frac{\partial^2}{\partial x^2}$ (as given in equation (2.38)), $\mathbf{g}(\mathbf{u})$ is the vector corresponding to the nonlinear term involved in the FK PDE (that is, the vector of components $u_i(1-u_i)$ for $i = 0, 1, \ldots, N$) and $\mathbf{u}_0$ is the vector obtained evaluating the initial condition at each node of the spatial grid.

For a given initial condition, the numerical solution of the model is generated with the MATLAB® ODE solver **ode15s**. The choice of the time step is made automatically in order to preserve a given level of accuracy for the solution[1]. However, it is possible to force the solver to provide the solution at specific time points. We usually require the solution to be provided on a uniform temporal grid with fixed time step Δt so that it is possible to plot it at regular intervals of time.

In order to speed up the computation, we provide as input to the considered ODE solver the explicit form of the Jacobian matrix J of the right hand side of the ODE given in (3.1). Note that its explicit form is not difficult to compute since it is given by $J = A + G$, where A is the constant matrix

[1]The absolute and relative tolerances for this solver are set by default equal to 10^{-6} and 10^{-3}, respectively.

generated by the spatial discretisation and $G = G(\mathbf{u})$ is the Jacobian matrix of the nonlinear term $\mathbf{g}(\mathbf{u})$. In particular, for the FK equation, since $G_{ij} = \frac{\partial \mathbf{g}_i}{\partial \mathbf{u}_j} \neq 0$ only when $j = i$, G is simply a diagonal matrix with diagonal elements $G_{ii} = 1 - 2u_i$.

3.1.1 Wave speed results for the FK model

Let $[0, 200]$ be the dimensionless spatial interval of interest for the following simulations. The set of results proposed here consists of the numerical validation of known analytical results on the travelling wave speed of the solution of the FK equation for three different types of initial condition.

In our numerical simulations we consider the following initial conditions:

- Option 1. u_0 given by equation (2.6) with $x_1 = 10$ and $\xi = 10$. As previously mentioned in Section 2.1.1, x_1 is the point of the spatial interval where the function u_0 defined in equation (2.6) starts its exponential decay and ξ is the parameter defining the rate of decay of u_0. With this choice of parameters for the initial condition, from the theoretical result (2.9) we expect the asymptotic value $c = 2$ for the wave speed of the solution.

- Option 2. u_0 given by equation (2.6) with $x_1 = 10$ and $\xi = 0.5$. In this case, as a result of the dispersion relation (2.9), the asymptotic value of $c = 0.5 + 1/0.5 = 2.5$ is expected for the wave speed.

- Option 3. u_0 as described by (2.10), which leads to a solution with wave speed $c = 5/\sqrt{6} \approx 2.0412$.

For each of these three simulations, we compute the wave speed of our numerical solution following the procedure described by Landman et al. [47]. Note that since the numerical approximation of the solution is provided as a set of discrete values, a linear interpolation scheme is used at each time step n in order to locate the position x_n of the front as shown by Figure 3.1. In our simulations, since the solution lies in the interval $[0, 1]$, we track the

position of the point corresponding to $u = 0.5$. Once such a position for the front is known over successive time intervals, we define the wave speed for $t \in [t_n, t_{n+1}]$ to be

$$c_n = \frac{x_{n+1} - x_n}{\Delta t}. \tag{3.2}$$

We observe that the succession c_n converges for large n to a finite value but the speed of convergence varies with initial conditions and parameter values. Therefore, the domain length must be chosen sufficiently large if the convergence is slow, as stated in [47]. In our simulations we define the numerical value of the wave speed c_{num} by averaging the values of c_n computed for the last 500 time iterations over the time interval $[0, t_f]$ considered.

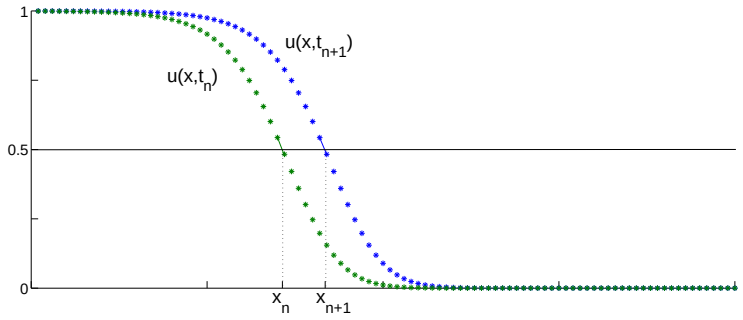

Figure 3.1: *Location of the positions x_n and x_{n+1} to be used in the wave speed computation (3.2).*

The following table summarizes our numerical results.

initial condition	c_{exact}	c_{num}
Option 1 ($\xi = 10$)	2	1.9886
Option 2 ($\xi = 0.5$)	2.5	2.5044
Option 3	$5/\sqrt{6}$	2.0458

The first column of the table refers to the particular initial condition considered, the second column contains the theoretical value of the travelling wave speed and in the last column we report the wave speed value c_{num} calculated from our numerical simulations. For all three initial conditions we observe

that c_{num} is consistent with the expected value c_{exact}.

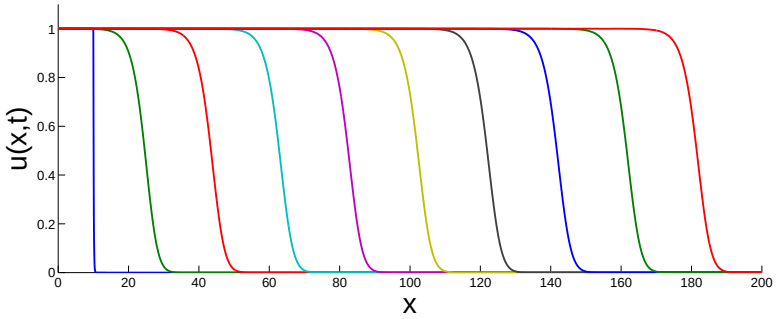

Figure 3.2: *Travelling wave solution for the FK equation (2.4).*

Figure 3.2 depicts the evolution in time of the numerical solution $u(x,t)$ obtained for equation (2.4) in the spatial interval $[0, 200]$ with uniform mesh size $h_x = 0.05$ and for $t \in [0, 90]$. This choice of mesh size results in a number of nodes $N + 1 = 4001$. The initial condition considered is given by (2.6) where the value of ξ is set equal to 10. The solution is plotted at regular intervals of $\Delta t = 10$ and it is evident how the travelling wavefront moves towards the right end of the spatial interval with constant wave speed.

Analogous qualitative behaviour of the numerical solution can be observed for all the other initial conditions previously considered (and previously indicated as Option 2 and Option 3).

3.2 The cell migration model with two interacting species

In this section, we will start by replicating some simulation results and remarks on the wave speed of the model for cell migration proposed by Simpson

et al. [77] with two interacting species defined by

$$\begin{cases} \dfrac{\partial u}{\partial t} &= D\ \dfrac{\partial^2 u}{\partial x^2} + k\ u(1-u-v) \\ \\ \dfrac{\partial v}{\partial t} &= \dfrac{\partial^2 v}{\partial x^2} + v(1-u-v), \end{cases} \tag{3.3}$$

where D and k are positive constants representing the relative diffusion coefficient and the relative mitotic index, respectively. We will then extend the analysis of the wave speed for the particular initial conditions considered by Simpson et al. [77] in the more general case of $D, k \geq 1$ and study the dependence of the wave speed on these two parameters.

For this model the same one-dimensional finite-difference approach considered for the FK model is used to discretise the diffusive terms in system (3.3), that is, the second order derivatives in space of both species ($\frac{\partial^2 u}{\partial x^2}$ and $\frac{\partial^2 v}{\partial x^2}$). Let $\mathbf{u} = [u_0, \ldots, u_N]^T$ and $\mathbf{v} = [v_0, \ldots, v_N]^T$ be the vectors approximating the donor and host cell densities at the nodes of the spatial mesh. As a consequence of the discretisation process the system (3.3) can be rewritten as

$$\mathbf{w}' = B\ \mathbf{w} + \mathbf{g}(\mathbf{w}), \tag{3.4}$$

where

$$\mathbf{w} = \begin{bmatrix} \mathbf{u} \\ \mathbf{v} \end{bmatrix}, \qquad B = \begin{bmatrix} D\,A & 0 \\ 0 & A \end{bmatrix}, \tag{3.5}$$

with $A \in \mathbb{R}^{(N+1)\times(N+1)}$ being the matrix of the spatial discretization of the second order derivative on the one-dimensional grid (defined as in equation (2.38)), the scalar D is the previously introduced relative diffusion coefficient and $\mathbf{g}(\mathbf{w})$ is the vector corresponding to the discretized kinetic term. In particular, the first $N+1$ components of $\mathbf{g}(\mathbf{w})$ have the form $k\ u_i(1-u_i-v_i)$ and the remaining $N+1$ components are given by $v_i(1-u_i-v_i)$.

Once again, to obtain the numerical solution of system (3.4) we use the MATLAB® solver **ode15s** and provide the solver with the explicit form of

the Jacobian matrix J in order to speed up the computation. Note that J is still the sum of two matrices, $J = B + G$, where B is the constant matrix defined in equation (3.5) and $G = G(\mathbf{w})$ is a block diagonal matrix that can be easily computed due to the particular form of the discretized kinetic term. In fact, $G_{ij} \neq 0$ only when $j = i$ and $|i - j| = N + 1$.

3.2.1 Replication of solution behaviour results

The first set of simulations we report here replicates the main results proposed in [77] under the assumption of linear diffusion and for initial conditions representing the three types of graft introduced in Section 2.1.1 as Case 1, Case 2 and Case 3, respectively. Let $[0, 300]$ be the dimensionless spatial interval, $h_x = 0.25$ the mesh size and $[0, 60]$ the temporal interval. As stated in [77], since "extensive historical experiments suggest that neural crest cells from chick and quail animal models behave indistinguishably in chick-quail grafting experiments", and also that under the particular conditions considered in [77] "it is reasonable to assume that the parameters governing a particular function would be the same for both cell types". This implies that the donor and host cells have equal diffusivity and equal mitotic index. Therefore, we initially set $D = k = 1$.

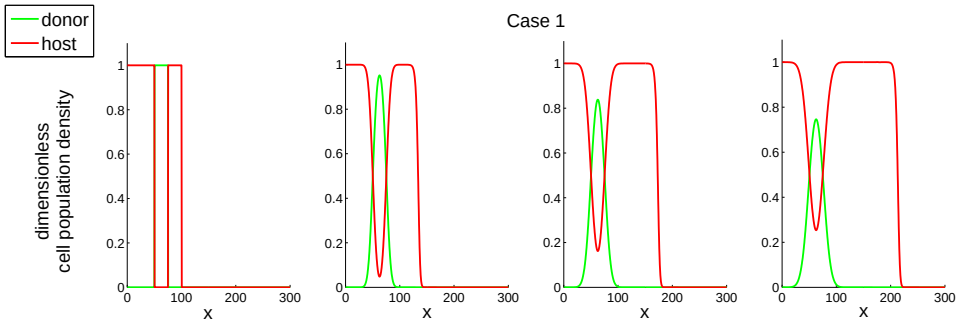

Figure 3.3: *Numerical solution for Case* 1 *at* $t = 0, 20, 40, 60$.

Figure 3.3 shows the evolution of the numerical solution of the model when the initial condition corresponds to Case 1. As we can see, the host cells at the leading edge are located adjacent to regions of gut tissue still unoccupied by the considered cell types (both concentrations are indeed zero for $x > 100$).

As a consequence, host cells migrate into this region and proliferate to reach the carrying capacity whereas donor cells are placed behind the front and therefore do not have the opportunity to proliferate.

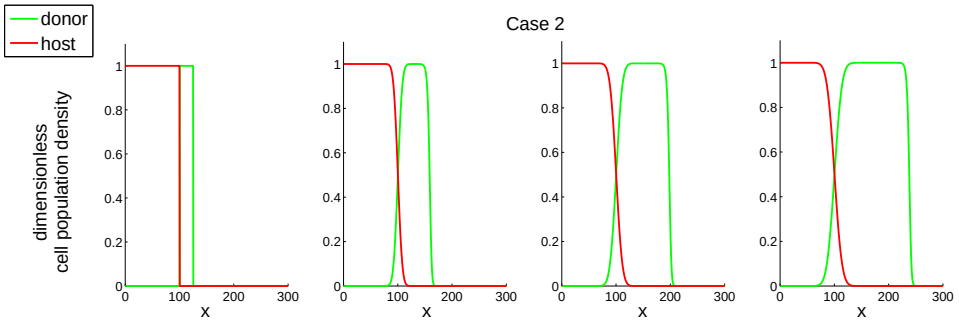

Figure 3.4: *Numerical solution for Case* 2 *at* $t = 0, 20, 40, 60$.

From Figure 3.4 it is evident that, when the initial condition of the model corresponds to Case 2, the travelling wave solution originates from the donor cell density. Indeed, in this scenario, the host cells are the ones behind the front and therefore do not have the chance to proliferate. On the other hand, donor cells migrate caudally into unoccupied regions of gut tissue and proliferate to reach the carrying capacity.

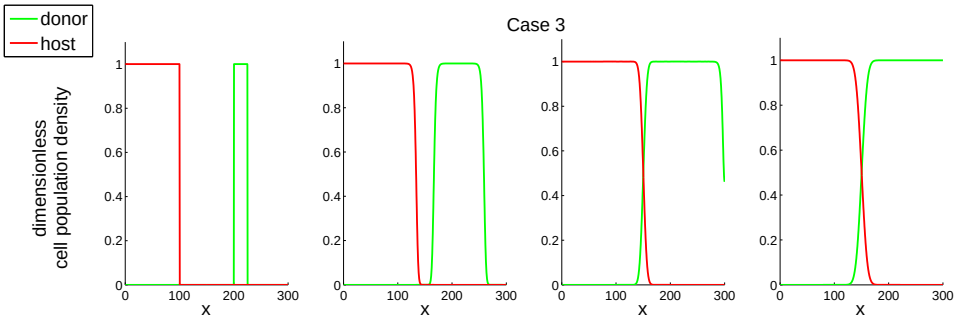

Figure 3.5: *Numerical solution for Case* 3 *at* $t = 0, 20, 40, 60$.

Finally, in Figure 3.5 we report the evolution of the numerical solution when the donor tissue is grafted into the uninvaded region of gut tissue. As we can see, when the simulation starts, both cell types can migrate into unoccupied regions of tissue. In particular, we observe a migration 'to the right' (in the caudal direction) for host cells and an expansion in both directions (rostral

and caudal) for donor cells. However, when the front of host cells migrating in the caudal direction encounters the front of donor cells moving rostrally, these two invading waves stop and the only moving front remaining is the travelling wave of donor cells migrating towards the caudal end of the gut.

3.2.2 Stability analysis and travelling waves

Consider the system of PDEs (3.3). The corresponding spatially homogeneous system has equilibria $(0,0)$ and $(\tilde{u}, 1-\tilde{u})$ for any $\tilde{u} \in [0,1]$, which are unstable and stable, respectively. In our study, we saw that the value of $\tilde{u}$ depends on the initial condition considered. In particular, for the three types of grafts considered by Simpson et al. [77], $\tilde{u} = 0$ in Case 1 and $\tilde{u} = 1$ in both Case 2 and Case 3.

In terms of the travelling wave speed, note that if $D = k = 1$, by defining $p = u + v$ and adding together the two PDEs of system (3.3), we obtain for the new variable p the FK equation

$$\frac{\partial p}{\partial t} = \frac{\partial^2 p}{\partial x^2} + p(1-p), \tag{3.6}$$

that exhibits travelling wave solutions with minimum wave speed $c_{\min} = 2$.

Let us consider now the general case, assuming that the parameters D and k are not necessarily both equal to one, and let us look for travelling wave solutions moving from the left to the right of our spatial interval, that is, $u(x,t) = U(z)$ and $v(x,t) = V(z)$ with $z = x - ct$, where $c > 0$ is the travelling wave speed.

In the new notation, system (3.3) becomes

$$\begin{cases} -cU' &= DU'' + k\,U(1-U-V) \\ -cV' &= V'' + V(1-U-V). \end{cases} \tag{3.7}$$

By introducing the new variables $W = U'$ and $Z = V'$, such a system can be

rewritten in turn as a system of four ODEs of the first order as follows:

$$\begin{cases} U' &= W \\ V' &= Z \\ W' &= \frac{1}{D}(-cW - k\,U(1-U-V)) \\ Z' &= -cZ - V(1-U-V). \end{cases} \tag{3.8}$$

System (3.8) has the following steady states in the (U, V, W, Z) phase space:

- $(0, 0, 0, 0)$ corresponding to the region ahead of the wavefront and therefore also called the uninvaded steady state;
- $(\tilde{U}, 1-\tilde{U}, 0, 0)$, for $\tilde{U} \in [0, 1]$, corresponding to the region behind the wavefront, namely the invaded steady state.

We look for travelling wave solutions such that

$$\begin{array}{lll} (U, V, W, Z) \to (0, 0, 0, 0) & \text{for} & z \to -\infty \\ (U, V, W, Z) \to (\tilde{U}, 1-\tilde{U}, 0, 0) & \text{for} & z \to +\infty. \end{array} \tag{3.9}$$

Note that if we want to replicate numerically the particular type of grafts considered by Simpson et al., that is, the grafts in which an entire slice of host tissue is replaced by donor cells, the three cases of initial conditions previously introduced qualitatively represent all the possible scenarios. From the numerical results given in Section 3.2.1, we can see that when the graft type considered corresponds to a graft of donor tissue in the invaded region (Case 1), the steady state of the spatially homogeneous system in terms of donor and host cell concentrations is $(0, 1)$. On the other hand, when the initial condition represents a graft of donor cells at the front or in the uninvaded region (Case 2 and Case 3 respectively), we see from numerical experiments that the steady state is $(1, 0)$. Hence, for the invaded steady state $(\tilde{U}, 1-\tilde{U}, 0, 0)$ we focus here only on the analysis of the two particular cases $\tilde{U} = 1$ and $\tilde{U} = 0$.

The Jacobian matrix of system (3.8) is

$$J = \begin{bmatrix} 0 & 0 & 1 & 0 \\ 0 & 0 & 0 & 1 \\ \frac{k}{D}(-1+2U+V) & \frac{k}{D}U & -\frac{c}{D} & 0 \\ V & -1+U+2V & 0 & -c \end{bmatrix}. \tag{3.10}$$

Therefore, the eigenvalues at the invaded steady state $(\tilde{U}, 1-\tilde{U}, 0, 0)$ are given by the roots of

$$\det \begin{bmatrix} -\lambda & 0 & 1 & 0 \\ 0 & -\lambda & 0 & 1 \\ \frac{k}{D}\tilde{U} & \frac{k}{D}\tilde{U} & -(\frac{c}{D}+\lambda) & 0 \\ 1-\tilde{U} & 1-\tilde{U} & 0 & -(c+\lambda) \end{bmatrix} = 0 \tag{3.11}$$

and so are the roots of the characteristic polynomial

$$-\lambda \underbrace{\left[-\lambda\left(\frac{c}{D}+\lambda\right)(c+\lambda) + (1-\tilde{U})\left(\frac{c}{D}+\lambda\right) + \frac{k}{D}\tilde{U}(c+\lambda)\right]}_{q(\lambda)} = 0. \tag{3.12}$$

If $\tilde{U} = 1$, the polynomial $q(\lambda)$ becomes

$$q(\lambda) = \left[-\lambda\left(\frac{c}{D}+\lambda\right) + \frac{k}{D}\right](c+\lambda), \tag{3.13}$$

therefore, the four eigenvalues are:

$$\lambda_1 = 0, \quad \lambda_2 = -c < 0 \quad \text{and} \quad \lambda_{3,4} = \frac{1}{2}\left[\frac{c}{D} \pm \sqrt{\left(\frac{c}{D}\right)^2 + 4\frac{k}{D}}\right]. \tag{3.14}$$

Since k and D are both positive, the eigenvalues λ_3 and λ_4 are both real but with opposite sign and hence, the steady state $(\tilde{U}, 1-\tilde{U}, 0, 0)$ is a saddle.

Similarly, when $\tilde{U} = 0$, the polynomial $q(\lambda)$ becomes

$$q(\lambda) = [-\lambda(c+\lambda)+1]\left(\frac{c}{D}+\lambda\right), \tag{3.15}$$

and the eigenvalues are:

$$\lambda_1 = 0, \quad \lambda_2 = -\frac{c}{D} < 0 \quad \text{and} \quad \lambda_{3,4} = \frac{1}{2}[c \pm \sqrt{c^2+4}]. \tag{3.16}$$

Once again, the steady state $(\tilde{U}, 1-\tilde{U}, 0, 0)$ turns out to be a saddle.

On the other hand, for the uninvaded steady state $(0,0,0,0)$ the eigenvalues are the roots of

$$\det \begin{bmatrix} -\lambda & 0 & 1 & 0 \\ 0 & -\lambda & 0 & 1 \\ -\frac{k}{D} & 0 & -(\frac{c}{D}+\lambda) & 0 \\ 0 & -1 & 0 & -(c+\lambda) \end{bmatrix} = 0. \tag{3.17}$$

The characteristic equation can be rewritten as

$$[\lambda(c+\lambda)+1]\left[\lambda\left(\frac{c}{D}+\lambda\right)+\frac{k}{D}\right] = 0, \tag{3.18}$$

and therefore the eigenvalues are:

$$\lambda_{1,2} = \frac{1}{2}[-c \pm \sqrt{c^2-4}] \quad \text{and} \quad \lambda_{3,4} = \frac{1}{2}\left[-\frac{c}{D} \pm \sqrt{\left(\frac{c}{D}\right)^2 - 4\frac{k}{D}}\right]. \tag{3.19}$$

Given our assumptions of positivity of the speed c and the parameters D and k, all four eigenvalues here have negative real parts, ensuring the stability of the steady state. However, in order to guarantee physically realistic travelling wave solutions, we require stability of the steady state in a non-oscillatory manner, i.e., the wave speed must satisfy the following constraints:

$$c \geq 2 \quad \text{and} \quad c \geq 2\sqrt{kD}. \tag{3.20}$$

Note that, when D and k are both greater than one, the condition $c \geq 2\sqrt{kD}$ dominates (being the more restrictive), therefore, the minimum wave speed expected in this case is $c_{\min} = 2\sqrt{kD}$.

3.2.3 Extension of the dispersion relation

Following the analysis of the wave speed dependence on the initial condition performed by Murray [62] for the FK equation, we obtain similar results for our particular model.

Noting that at the leading edge, that is, when $(u, v) = (0, 0)$, both u and v are small, we can neglect the second order terms and consider the following linearisation of system (3.3):

$$\begin{cases} \dfrac{\partial u}{\partial t} &= D\,\dfrac{\partial^2 u}{\partial x^2} + k\,u \\[2ex] \dfrac{\partial v}{\partial t} &= \dfrac{\partial^2 v}{\partial x^2} + v. \end{cases} \tag{3.21}$$

Let us assume $D, k \geq 1$ and focus on the first species. Consider an initial condition

$$u_0(x) \sim Ae^{-ax} \quad \text{as} \quad x \to +\infty, \tag{3.22}$$

with a and A positive constants, and look for travelling wave solutions of the form

$$u(x,t) = Ae^{-a(x-ct)}. \tag{3.23}$$

By substitution of the expression (3.23) in the equation for the donor species in the leading edge linearisation system (3.21), we find the following extension of the dispersion relation (2.9):

$$ca = Da^2 + k, \quad \text{from which} \quad c = Da + \frac{k}{a}. \tag{3.24}$$

Note that equation (3.24) is independent from the value of the constant A. Moreover, $c = c_{\min}(= 2\sqrt{kD})$ if and only if $a = \sqrt{k/D}$. For all other values of $a > 0$ we have $c > c_{\min}$.

Consider now $\min\{e^{-ax}, e^{-\sqrt{k/D}\ x}\}$ for x large and positive. If

$$a < \sqrt{\frac{k}{D}}, \quad \text{then} \quad e^{-ax} > e^{-\sqrt{k/D}\ x}, \tag{3.25}$$

and so the wave speed $c > c_{\min}$ and it is given by the relation (3.24). On the other hand, if $a > \sqrt{k/D}$ then

$$e^{-ax} < e^{-\sqrt{k/D}\ x}, \tag{3.26}$$

that is, the solution is bounded above by the one having wave speed equal to $c_{\min}$. Therefore, the asymptotic speed of the travelling wave solution must be $c = c_{\min}$.

To sum up, we showed that if $D, k \geq 1$ and a travelling wave solution for the species u evolves from an initial condition $u_0 \sim Ae^{-ax}$ as $x \to +\infty$, then the asymptotic travelling wave speed is given by

$$c = \begin{cases} Da + \frac{k}{a} & \text{if} \quad 0 < a \leq \sqrt{\frac{k}{D}} \\ \\ 2\sqrt{kD} & \text{if} \quad a > \sqrt{\frac{k}{D}}. \end{cases} \tag{3.27}$$

In what follows we consider $x \in [0, 300]$ and focus on the initial condition of Case 2, that is,

$$u_0 = \begin{cases} 1 & 100 < x \leq 125 \\ 0 & \text{elsewhere} \end{cases} \quad \text{and} \quad v_0 = \begin{cases} 1 & x \leq 100 \\ 0 & \text{elsewhere.} \end{cases} \tag{3.28}$$

In this case the stable steady state of the spatially homogeneous system is $(\tilde{u}, 1-\tilde{u}) = (1, 0)$ and the stability analysis of the spatially dependent model allows us to obtain some bounds on the value of the parameters D and k in order for the model to exhibit physically realistic traveling wave solutions in the donor species u. Due to the particular initial condition considered, the host species is already at its equilibrium value for $x > 100$ and therefore its solution profile does not evolve to a travelling wave for $D, k \geq 1$.

We now use this particular initial condition to validate the extension of the dispersion relation given in equation (3.27). For a piecewise constant initial condition for u our analysis predicts an asymptotic value of the wave speed equal to $c_{\min} = 2\sqrt{kD}$ because in this case u_0 can be seen as Ae^{-ax} with a arbitrarily large. Once again in the simulations we compute c_{num} by tracking (with linear interpolation) at each time step n the position x_n of the front corresponding to the value $u = 0.5$. The estimate of the wave speed c is then obtained as described in Section 3.1.1 for the simulations of the FK equation.

By setting the dimensionless time interval equal to $[0, 60]$, the spatial mesh size $h_x = 0.25$ and considering a spatial interval sufficiently large in order to be able to track the evolution of the front in the whole time interval (e.g., $L = 300$, 400, 500 or 600, depending on the value of the parameters D and k considered), we obtain the following values of c_{num}:

- $D = k = 1$ (FK equation, $c_{\min} = 2$), $c_{\text{num}} = 1.9811$;
- $D = k = 2$ ($c_{\min} = 4$), $c_{\text{num}} = 3.9927$;
- $D = k = 3$ ($c_{\min} = 6$), $c_{\text{num}} = 6.0036$;
- Variable D, $k = 1.5$ ($c_{\min} = \sqrt{6D}$), c_{num} as in Figure 3.6 on the left (red);
- $D = 1.5$, variable k ($c_{\min} = \sqrt{6k}$), c_{num} as in Figure 3.6 on the right (red).

Figure 3.6 exhibits the results obtained in the case of a fixed value of $k = 1.5$ and variable D (left plot) and for a fixed value of $D = 1.5$ and variable k (right plot). Both plots show the comparison between the numerical values of the travelling wave speed c_{num} (red) and the theoretical values of $c_{\min}$ (blue) as a function of the variable parameter. The numerical approximations reflect well the theoretical results and it is evident how the dependence of the wave speed from the parameters is proportional to their square root.

In order to validate the other analytical results found, that is, the ones obtained in the case of an initial condition u_0 for the donor species behaving

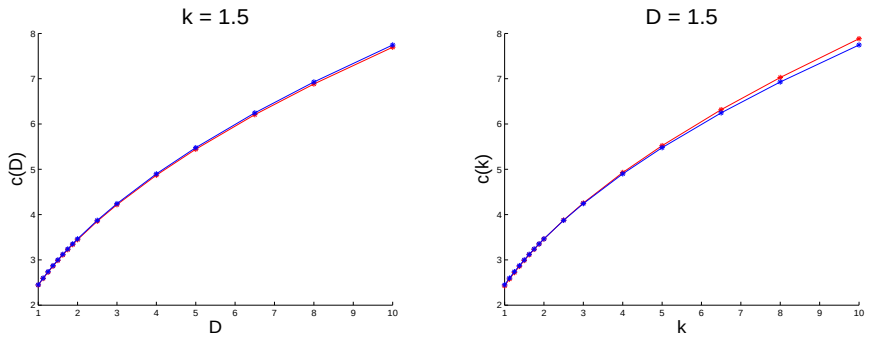

Figure 3.6: *Theoretical wave speed (blue) and numerical wave speed (red) as functions of the parameters D and k when the initial condition for both u and v is as given by (3.28).*

asymptotically as Ae^{-ax} with $0 < a \leq \sqrt{k/D}$, we consider the following test initial condition:

$$u_0 = \begin{cases} 0 & x \leq 100 \\ 1 & 100 < x \leq 125 \\ e^{-ax} & x > 125. \end{cases} \tag{3.29}$$

As in the previous case, v_0 is set as in equation (3.28).

Let $k = 1$ be fixed and consider the initial condition u_0 where the parameter a in the exponential decay is $a = 0.5$. In this case, using the theoretical result given by (3.27), we obtain that the dependence of the wave speed c from the parameter D is

$$c = \begin{cases} \frac{D}{2} + 2 & \text{if} \quad 0.5 \leq \sqrt{\frac{1}{D}} \quad (\Leftrightarrow D \leq 4) \\ \\ 2\sqrt{D} & \text{if} \quad 0.5 > \sqrt{\frac{1}{D}} \quad (\Leftrightarrow D > 4). \end{cases} \tag{3.30}$$

Therefore, here we expect the dependence of the speed to be linear for values of $D \leq 4$ and proportional to the square root of D when $D > 4$.

On the other hand, by fixing $D = 1$ and always considering the initial condition of equation (3.29), where the parameter determining the exponential

decay is now $a = 2$, the dependence of the wave speed c from k becomes

$$c = \begin{cases} 2 + \frac{k}{2} & \text{if} \quad 2 \leq \sqrt{k} \quad (\Leftrightarrow k \geq 4) \\ \\ 2\sqrt{k} & \text{if} \quad 2 > \sqrt{k} \quad (\Leftrightarrow k < 4). \end{cases} \tag{3.31}$$

Hence, contrary to that obtained for c as a function of D, here we expect the dependence of the speed to be linear for $k \geq 4$ and proportional to the square root of k for values of $k < 4$. Note that the value of a is here chosen equal to $a = 2$ instead of $a = 0.5$ as in the previous case, simply because with this choice we can consider the same set of values for the variable parameters k and D and observe a change of behaviour at the same critical point, that is, at $D = k = 4$.

The comparison between theoretical results and numerical estimations for all the parameter values considered here is represented graphically in Figure 3.7. Once again the red dots represent the numerical values for the travelling wave speed c_{num} and the blue dots the theoretical values obtained from the extended dispersion relation (3.27) in the two cases.

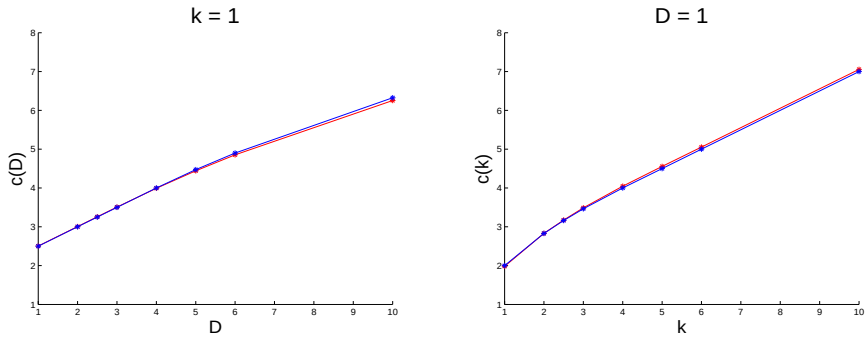

Figure 3.7: *Wave speed as a function of D and k when u_0 is given as in (3.29) and v_0 is as in (3.28).*

Clearly the numerical results proposed only consider specific combinations of D, k and the parameter a of exponential decay in the initial condition (3.29). However, as we can see from Figure 3.7, there is almost perfect agreement

between the theoretical values of the wave speed and the ones calculated from our numerical experiments. A similar result is expected for all other combinations of $D, k \geq 1$ and $a > 0$.

3.3 Solution of excitable media models

In this section we focus on models for the second application object of study in this thesis, namely electrophysiology. We describe in detail the methodology used to obtain the numerical solution of the excitable media models introduced in Chapter 2 and provide a set of results in both one and two spatial dimensions in the standard diffusion case. These results are obtained under different conductivity assumptions and by using different combinations of the spatial formulations and the ionic current models introduced in Section 2.1.2. We start by describing the numerical strategy in the bidomain case and then simply outline how this methodology is adapted in the simpler monodomain case.

By coupling a cell model (such as the FHN model or the BR model of Section 2.1.2) with the bidomain formulation for spatial propagation of the electrical stimulus, the resulting electrophysiological model can be written as

$$\chi \left(\frac{\partial v}{\partial t} + I_{\text{ion}}(v, \mathbf{z}) \right) - \nabla \cdot (M_i \nabla (v + u_e)) = I_i^{(\text{vol})} \tag{3.32}$$

$$\nabla \cdot (M_i \nabla v) + \nabla \cdot ((M_i + M_e) \nabla u_e) = -I_{\text{tot}}^{(\text{vol})} \tag{3.33}$$

$$\frac{d\mathbf{z}}{dt} = \mathbf{f}(v, \mathbf{z}), \tag{3.34}$$

where v is the transmembrane potential, u_e is the extracellular potential, $\mathbf{z}$ is a vector of variables and concentrations (e.g., the recovery variable w for the FHN model or the gating variables and the calcium concentration for the BR model), I_{ion} is the ionic current determined by the cell model considered, χ is the cell surface to volume ratio, M_i and M_e are conductivity tensors,

$I_i^{(\mathrm{vol})}$ and $I_{\mathrm{tot}}^{(\mathrm{vol})}$ are applied stimuli, and $\mathbf{f}$ is a suitable vector-valued function whose expression depends on the particular cell model considered.

For all our simulations we assume that no current crosses the boundaries of the spatial domain and therefore consider the above system (3.32)–(3.34) coupled with the following boundary conditions:

$$\begin{aligned} n \cdot (M_i \nabla (v + u_e)) &= 0 \\ n \cdot (M_e \nabla u_e) &= 0. \end{aligned} \tag{3.35}$$

Noting that u_e only appears in the equations (3.32), (3.33) and the boundary conditions (3.35) through its gradient, we know that the solution for u_e is only defined up to a constant and therefore the above system of PDEs must satisfy some compatibility constraints in order to have any solution. These compatibility constraints are expressed in terms of the applied stimuli as described in detail by Pathmanathan et al. [66]. Following their approach, we specify a non-zero extracellular current and choose it equal in magnitude to $I_i^{(\mathrm{vol})}$ but with opposite sign (i.e., $I_e^{(\mathrm{vol})} = -I_i^{(\mathrm{vol})}$) so that the total current in the volume $I_{\mathrm{tot}}^{(\mathrm{vol})} = 0\,\mu\mathrm{A}\cdot\mathrm{cm}^{-3}$. In doing so, the compatibility constraint is satisfied and the above singular problem is well posed.

At this point we must choose a suitable temporal and spatial discretisation strategy to compute the numerical solution of the problem. We know that a fully explicit discretisation in time is simple to code but the time step that produces a stable approximation of the solution suffers from stability constraints. On the other hand, the time step that can be used with an implicit discretisation is typically much larger but noting that the ionic current in the PDE (3.32) depends on the solution of the stiff ODE system (3.34) governing the time evolution of all the additional variables involved in the cell model, the fully implicit approach would require the simultaneous solution of (3.32), (3.33) and (3.34). Especially for large scale simulations, in more than one spatial dimension and with fine meshes, the fully implicit approach would result in the solution of a very large nonlinear system at each time step which can be extremely expensive from the computational point of view and

therefore, this is not the approach generally used in practice. A much more common choice [66], [19], [83] is to consider a semi-implicit time discretisation method for the PDE system in which the diffusion term is treated implicitly and the reaction term explicitly as presented in Section 2.2.3. At each time step this allows us to obtain the updated value of the transmembrane potential from the solution of the PDE system and this value can then be used in the ODE system so that most of the ODEs involved in system (3.34) become linear. The use of the implicit Euler scheme for linear ODEs is not an issue and most of the gating variables can be updated directly even though an implicit scheme is implemented. Therefore, only a small nonlinear system needs to be solved at each time step. This strategy is the one we adopt in our simulations and it is based on the work proposed by Whiteley [83].

A more detailed description of the method can be summarized as follows. The temporal interval of interest is discretised and v, u_e and $\mathbf{z}$ are computed as functions of x at discrete times $t_0 = 0 < t_1 < \cdots < t_{N_t} = t_f$. Let the k-th temporal step be $\Delta t_k = t_{k+1} - t_k$ and

$$v^k := v(x, t_k), \qquad u_e^k := u_e(x, t_k) \quad \text{and} \quad \mathbf{z}^k := \mathbf{z}(x, t_k). \tag{3.36}$$

After discretising the spatial domain with the finite-difference method[2], at each time iteration, the updated value of v, u_e and $\mathbf{z}$ is computed in two steps.

Step 1: Given v^k, u_e^k and $\mathbf{z}^k$ at each node of the spatial mesh, we first solve the bidomain equations by using the semi-implicit Euler method, that is we evaluate the spatial derivatives at time t_{k+1} and the I_{ion} term at time t_k. We

[2]There is no restriction on the method used for the spatial discretisation process and the same algorithm can be implemented for example with a finite-volume discretisation in space.

hence look for the solution of

$$\begin{cases} \dfrac{v^{k+1}-v^k}{\Delta t_k} &= \frac{1}{\chi}A_i\ v^{k+1} + \frac{1}{\chi}A_i\ u_e^{k+1} - I_{\text{ion}}(v^k,\mathbf{z}^k) + \frac{1}{\chi}I_i^{(\text{vol})} \\ \\ 0 &= A_i\ v^{k+1} + A_{i+e}\ u_e^{k+1}, \end{cases} \tag{3.37}$$

where A_i and A_{i+e} are the matrices of the spatial discretisation of the differential operators (including the effect of the constant χ and the conductivities M_i and $M_i + M_e$, respectively). By rearranging the terms in both equations and by rescaling the second equation by $-\Delta t_k/\chi$, system (3.37) can be rewritten as a linear system involving a symmetric sparse block matrix on the left hand side of the equation as follows:

$$\begin{bmatrix} I - \frac{\Delta t_k}{\chi}\ A_i & -\frac{\Delta t_k}{\chi}\ A_i \\ \\ -\frac{\Delta t_k}{\chi}\ A_i & -\frac{\Delta t_k}{\chi}\ A_{i+e} \end{bmatrix} \begin{bmatrix} v^{k+1} \\ \\ u_e^{k+1} \end{bmatrix} = \begin{bmatrix} b^k \\ \\ \bar{0} \end{bmatrix}, \tag{3.38}$$

where, in standard notation, I is the identity matrix, $\bar{0}$ is the zero vector and

$$b^k := v^k - \Delta t_k\ I_{\text{ion}}(v^k,\mathbf{z}^k) + \frac{\Delta t_k}{\chi}\ I_i^{(\text{vol})}.$$

Step 2: Once the solution of the system (3.38) is known, i.e., v^{k+1} and u_e^{k+1} have been computed, we use the value of v^{k+1} at each point of the mesh in the spatial discretization of (3.34). We then obtain the updated value $\mathbf{z}^{k+1}$ by solving this stiff nonlinear system of ODEs with the implicit Euler scheme:

$$\frac{\mathbf{z}^{k+1}-\mathbf{z}^k}{\Delta t_k} = \mathbf{f}(v^{k+1},\mathbf{z}^{k+1}). \tag{3.39}$$

As previously mentioned, for many electrophysiological problems, and in particular for the ones considered in this thesis, the particular form of most components of the vector-valued function $\mathbf{f}$ can be exploited in order to get a further uncoupling of the problem and an increase in the efficiency of the algorithm. In fact, the ODE governing the recovery variable in the FHN model and each of the six ODEs governing the gating variables of the BR

model, can be expressed in terms of the generic component z_i of $\mathbf{z}$ as

$$\frac{dz_i}{dt} = f_i(v, z_i), \qquad \text{where} \quad f_i = a_i(v) + b_i(v)\ z_i. \tag{3.40}$$

Given v^{k+1}, at each time step k, due to the linear dependence of f_i on the variable z_i, the use of the implicit Euler method leads to

$$z_i^{k+1} = \frac{z_i^k + \Delta t_k\ a_i(v^{k+1})}{1 - \Delta t_k\ b_i(v^{k+1})}. \tag{3.41}$$

Therefore, we are able to compute z_i^{k+1} directly and as a consequence, the size of the nonlinear system to be solved in order to obtain the updated $\mathbf{z}^{k+1}$ can be significantly reduced[3]. As suggested by Whiteley in [83], to solve such a system and obtain the remaining values of $\mathbf{z}^{k+1}$ we use the well-known Newton method.

Note that when the spatial model considered is the monodomain formulation, the approach remains the same but this time system (3.37) reduces to

$$\frac{v^{k+1} - v^k}{\Delta t_k} = \frac{1}{\chi}\frac{\lambda}{1+\lambda} A_i\ v^{k+1} - I_{\text{ion}}(v^k, \mathbf{z}^k) + \frac{1}{\chi} I^{(\text{vol})}, \tag{3.42}$$

that in turn can be rewritten as a linear system:

$$\left(I - \Delta t_k \frac{1}{\chi}\frac{\lambda}{1+\lambda} A_i\right)\ v^{k+1} = b^k, \tag{3.43}$$

where this time

$$b^k := v^k - \Delta t_k\ I_{\text{ion}}(v^k, \mathbf{z}^k) + \frac{\Delta t_k}{\chi}\ I^{(\text{vol})}.$$

[3]In the particular case of the FHN model, the recovery variable is the only component of the vector $\mathbf{z}$. Hence, with this strategy, we are able to avoid having to solve a nonlinear system of equations. When the BR model is considered, out of the seven components of $\mathbf{z}$, only the evolution of the calcium concentration is governed by a nonlinear ODE. Therefore, by using the proposed strategy we are still able to significantly reduce the size of the nonlinear system to be solved in order to obtain the update $\mathbf{z}^{k+1}$.

A note on the singularity of the problem

The singularity of the problem in terms of u_e being defined up to a constant translates (after spatial discretisation) into the matrix on the left-hand side of equation (3.38) being singular. A singular linear system $Bx = z$ has no solution unless the right-hand side vector z is in the range of B, that is, $z \in \mathcal{R}(B)$. Using basic linear algebra results [3] we know that the range of a matrix, $\mathcal{R}(B)$, coincides with the orthogonal complement of its left-hand null space, $\mathcal{N}(B^T)^\perp$. Therefore, the singular linear system has no solution unless

$$z \in \mathcal{R}(B) = \mathcal{N}(B^T)^\perp, \tag{3.44}$$

that is, $z \cdot y = 0$ for all vectors y such that $B^T y = 0$. If the compatibility constraint (3.44) is satisfied, then the singular linear system has infinitely-many solutions that can be obtained by adding to any particular solution x a linear combination of vectors in the non-trivial null space of the singular matrix B. In the particular case of the linear system (3.38), the singularity comes from the matrices A_i and A_{i+e}. Since in our finite-difference approximation we use a centered (second-order) approximation of the first order derivative along the entire boundary to discretise homogeneous Neumann boundary conditions, we obtain that A_i and A_{i+e} are not symmetric and therefore, the left-hand null space of each of these matrices is different from the corresponding right-hand null space (that is, $\mathcal{N}(A_i^T) \neq \mathcal{N}(A_i)$ and $\mathcal{N}(A_{i+e}^T) \neq \mathcal{N}(A_{i+e})$). However, we can show that

$$\mathcal{N}(A_i) = \mathcal{N}(A_{i+e}) = \text{span}\{\bar{e}\}, \tag{3.45}$$

where $\bar{e}$ is the unit vector $\bar{e} = [1, 1, \ldots, 1]^T$ and

$$\mathcal{N}(A_i^T) = \mathcal{N}(A_{i+e}^T) = \text{span}\{\bar{w}\}, \tag{3.46}$$

where $\bar{w}$ is a vector depending on the dimension of the spatial domain considered. In particular, if we consider a one-dimensional domain, then $\bar{w}$ can be written as $\bar{w} = [1, 2, 2, \ldots, 2, 1]^T$, whereas in the case of a rectangular domain with $N_1 + 1$ nodes along the horizontal axis, $N_2 + 1$ nodes along the

vertical axis and assuming that the nodes are numbered along the columns to obtain the spatial discretisation of the second order differential operators in space, then the vector $\bar{w}$ can be written as $\bar{w} = [\bar{w}_0, \bar{w}_1, \ldots, \bar{w}_{N_1}]^T$ where each of the $N_1 + 1$ subvectors $\bar{w}_0, \bar{w}_1, \ldots, \bar{w}_{N_1}$ has $N_2 + 1$ components and is equal to

$$\bar{w}_i = \begin{cases} [1, 2, 2, \ldots, 2, 1]^T & \text{when } i = 0 \text{ or } i = N_1 \\ \\ [2, 4, 4, \ldots, 4, 2]^T & \text{when } i = 1, 2, \ldots, N_1 - 1. \end{cases}$$

Consequently, due to the non-singularity of the submatrix $I - \frac{\Delta t_k}{\chi} A_i$, we obtain that the right-hand and left-hand null spaces of the block matrix B on the left-hand side of equation (3.38) are as follows:

$$\mathcal{N}(B) = \text{span}\left\{ \begin{bmatrix} \bar{0} \\ \bar{e} \end{bmatrix} \right\} \quad \text{and} \quad \mathcal{N}(B^T) = \text{span}\left\{ \begin{bmatrix} \bar{0} \\ \bar{w} \end{bmatrix} \right\},$$

where $\bar{0}$ is the zero vector and $\bar{e}$ and $\bar{w}$ are the vectors defined in equations (3.45) and (3.46).

Returning to condition (3.44), the singular linear system $Bx = z$ has no solution unless $z \cdot y = 0$ for all $y \in \mathcal{N}(B^T)$. Since the left-hand null space of B is spanned by a single vector, the compatibility condition can be written in terms of the inner product of the right-hand side of the singular linear system (3.38) and the vector spanning $\mathcal{N}(B^T)$ as

$$\begin{bmatrix} b^k \\ \bar{0} \end{bmatrix}^T \cdot \begin{bmatrix} \bar{0} \\ \bar{w} \end{bmatrix} = 0.$$

Due to the position of the zero entries in these two vectors, we observe that the compatibility condition is always satisfied.

Knowledge of the vectors spanning the left-hand and the right-hand null spaces of B can be also used in the actual solution of the linear system. In fact, if $\mathcal{N}(B) = \text{span}\{\bar{u}\}$ and $\mathcal{N}(B^T) = \text{span}\{\bar{v}\}$, then rather than solving

the singular linear system $Bx = z$ we can build the nonsingular matrix $B_{\text{shift}} = B + \bar{v}\bar{u}^T$ and solve $B_{\text{shift}}x = z$ instead[4].

3.3.1 Numerical simulations

When coupled with the monodomain equation in one spatial dimension, both the FHN and the BR models exhibit travelling wave phenomena for sufficiently strong values of the applied current. In this section, we present the results of different simulations in which we combine the FHN and the BR model with either the monodomain or the bidomain equations. In particular, we focus on how the action potential generated by a sufficiently strong applied current propagates throughout the considered one-dimensional or two-dimensional domain under different diffusivity assumptions.

For our one-dimensional simulations, the size of the spatial domain was chosen large enough so that it is possible to observe the wave phenomena and the advance of the entire excitation pulse within the domain considered for all $t \in [0, t_f]$. However, we recognize that this approach is limited to the study performed in this thesis because, depending on the cell model used and the consequent width in space of the generated travelling pulse, we might be forced to consider unrealistically large domains to follow the entire wave phenomena. In practice, to measure how the electrical stimulus propagates in time throughout a given domain, the approach used is to record the value of the transmembrane potential at various points of the domain and observe how these values change in time. For example, in a one-dimensional model we could simply apply the stimulus at one end of the domain and record the variations observed in the transmembrane potential at the other end of the spatial interval as a function of time. Similarly, on a rectangular two-dimensional grid, we could apply the stimulus on one side or a corner of the domain and observe the evolution in time of the transmembrane potential at the nodes located on the opposite side of the rectangle or at each of its

[4]Since $z \in \mathcal{R}(B) = \mathcal{N}(B^T)^\perp$ the two linear systems $Bx = z$ and $B_{\text{shift}}x = z$ have the same set of solutions. Besides, the fact that B_{shift} is nonsingular allows the use of traditional methods to compute the solution of the linear system.

three remaining corners to see, for example, whether the stimulus propagates faster along a particular direction.

As we shall see, our choice of model parameters for the BR model results in a travelling pulse with width much larger than the one generated by the considered FHN model and therefore, the domain size that would be required to follow in time the evolution of the pulse generated by the BR cell model is much larger than the one required for the FHN model. In order to reduce the computational load in obtaining the solution of the BR model in the two-dimensional case, we follow the common approach and study the solution by observing the changes in the transmembrane potential at some given nodes of our rectangular domain.

The simulations considered in this section are:

- In one spatial dimension (on a finite interval):
  - FHN monodomain model;
  - BR monodomain model.
- In two spatial dimensions (on a rectangular domain):
  - FHN monodomain model. Stimulus on one side;
  - FHN monodomain model. Stimulus in one corner. Isotropy;
  - FHN monodomain model. Stimulus in one corner. Anisotropy;
  - FHN bidomain model. Stimulus in one corner. Anisotropy;
  - BR monodomain model. Stimulus on one side;
  - BR monodomain model. Stimulus in one corner. Isotropy;
  - BR monodomain model. Stimulus in one corner. Anisotropy;
  - BR bidomain model. Stimulus in one corner. Anisotropy.

The aim of this section is to observe how the qualitative bahaviour of the solution to the considered models changes when different cell models and different formulations for the spatial propagation are combined. Furthermore,

we want to present different strategies that can be used for the visualisation of these results and especially in the two-dimensional case, highlight the typical approaches used to produce and compare simulation results. For this reason, not much attention is given to quantitative results. Once the modelling parameters were set (typically equal to sensible values[5] found in the literature for the considered problems), the choice of the applied stimulus strength, the region to which the stimulus was applied, the size of the spatial domain and the length of the temporal interval were all the result of some test simulations and were chosen so that the visualisation and comparison of the results of interest was possible. The mesh size and the temporal time step were simply chosen small enough to guarantee the correct behaviour of the numerical solution[6]. In the bidomain case and for all two-dimensional simulations involving the BR cell model, in order to be able to use the same mesh size adopted in the other simulations and providing the correct qualitative behaviour of the solution, we decided to consider a smaller spatial domain and hence reduce the otherwise very heavy computational requirements of the numerical strategy.

For all the simulations presented in this section, the spatial variable (in each spatial dimension) and the temporal variable are always expressed in units of cm and msec, respectively. However, in order to simplify the notation, we omit these units in describing the details of our simulations and the temporal and spatial intervals considered, while specifying only the units for the remaining simulation parameters.

One-dimensional simulations

In one spatial dimension we only consider the monodomain equation and set the parameters λ and C_m of equation (2.27) to be $\lambda = 1$ and $C_m = 1\,\mu\mathrm{F}\cdot\mathrm{cm}^{-2}$. We then assume $\chi = 2000\,\mathrm{cm}^{-1}$ and $M_i = 3\,\mathrm{mS}\cdot\mathrm{cm}^{-1}$. When the cell model

[5] Of the right order of magnitude.

[6] Larger mesh sizes would result in the applied stimulus not triggering any excitation wave and larger time steps would not produce a good temporal resolution of the action potential produced.

considered is the FHN model, let $x \in [0, 5]$, $h_x = 0.025$, $t \in [0, 500]$, $\Delta t = 0.25$, and let the initial condition be $[v_0, w_0]^T = [v_{\text{rest}}, 0]^T$ on the entire spatial domain. By applying an electrical stimulus $I^{(\text{vol})} = 5 \cdot 10^5\, \mu\text{A}\cdot\text{cm}^{-3}$ to the left end of the interval at $t = 10$ for five milliseconds, we obtain that the solution profile of v evolves in time as shown by Figure 3.8. Here we plot the solution at constant time intervals of 25 msec.

The electrical stimulus triggers an action potential and due to the spatial dependence introduced in the model, we observe that the solution profile advances towards the right end of the spatial interval with constant shape and speed as time increases. This example of a travelling wave solution is different from that observed for the FK equation, where the wave profile is given by a transition between different steady states. In fact, here the wave corresponds to a change in the potential that starts and ends at the same value. Therefore, in this case, instead of being called a travelling front the excitation wave is typically referred to as a **travelling pulse**.

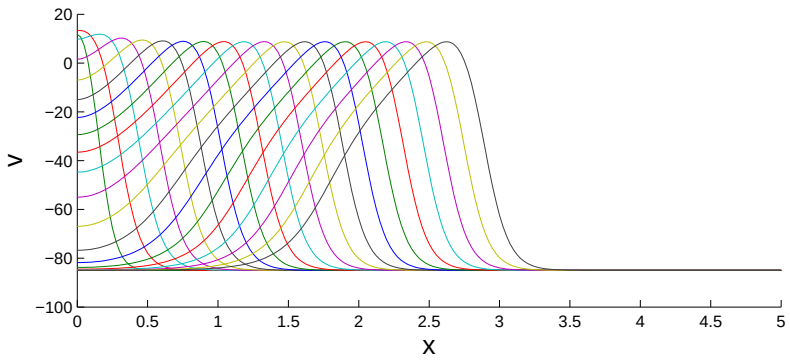

Figure 3.8: *Solution profile of v as a function of x in the FHN monodomain model. The parameters for the FHN model are given in Table 2.1.*

A travelling pulse can be observed also when the monodomain equation is combined with the BR model but in this case the shape of the pulse recalls the one observed in Figure 2.5 for the action potential of the BR cell model. To obtain the solution profile shown by Figure 3.9, we consider again $t \in [0, 500]$, $\Delta t = 0.25$ and $h_x = 0.025$ but we set the spatial interval to be $[0, 20]$ so that

it is possible to have a better visualisation of how the pulse moves in time. The potential v and all the other variables involved in the BR model are initially set equal to $[v_0, m_0, h_0, j_0, d_0, f_0, x_0, c_0]^T = [-85, 0, 1, 1, 0, 1, 0, 1]^T$ at each point of the spatial mesh and a stimulus $I^{(\text{vol})} = 5 \cdot 10^5\, \mu\text{A}\cdot\text{cm}^{-3}$ is applied to the left end of the spatial interval at $t = 10$ for five milliseconds.

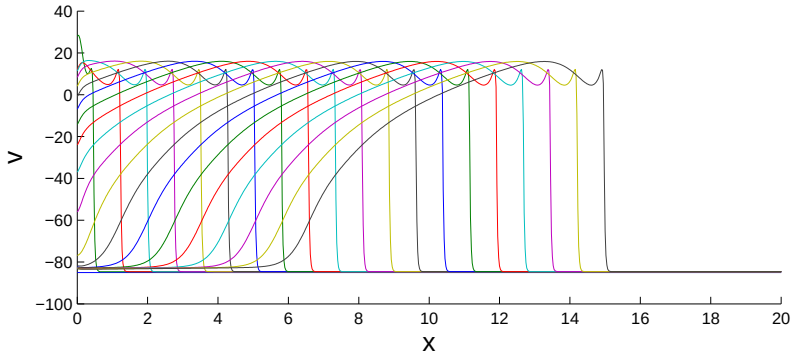

Figure 3.9: *Solution profile of v as a function of x in the BR monodomain model. The value of the parameters for the BR model are given by Table 2.2.*

Two-dimensional simulations

For the models of signal propagation in excitable media we also consider two-dimensional numerical simulations on a rectangular domain $\Omega = [0, L_x] \times [0, L_y]$. As mentioned in Chapter 2, in this thesis we ignore the contribution to the diffusivity tensor due to fibre rotations and simply assume that fibres are parallel to one of the axes of our two-dimensional domain. Therefore, the diffusion tensor can be simply written as a diagonal matrix

$$M = \begin{bmatrix} M_x & 0 \\ 0 & M_y \end{bmatrix}, \tag{3.47}$$

where M_x and M_y are the conductivities of the tissue along the two axes. In the context of cardiac tissue simulations, if we assume for example that the fibres are aligned with the x-axis, then M_x and M_y represent the tissue conductivities in the direction of the fibres and in the direction orthogonal to the fibres, respectively. We initially assume $M_x = M_y$ and in this case

the problem is referred to as **isotropic**. We then modify this assumption and obtain the more general case in which diffusion of the electrical signal is facilitated along one of the two spatial directions. In this case, i.e., when $M_x \neq M_y$, the problem is typically referred to as **anisotropic**.

For both the FHN and the BR models we assume that initially the transmembrane potential is at its resting value at each point of the rectangular spatial grid and that the initial condition for the other variables involved in both cell models is constant on the entire domain Ω. The value of these constants is set to be equal to the initial condition used in the corresponding one-dimensional simulations.

In order to generate an action potential we apply an electrical current that is now a function of t and both x and y. As in the one-dimensional examples, we define the applied current as non-zero for a short temporal interval $[t_a, t_b] \subset [0, t_f]$ on a small region $\bar{\Omega}$ of the domain. We consider two different cases:

- $\bar{\Omega}_{\text{side}} = \{(x, y) \in \Omega \mid x = 0\}$, that is, the electrical stimulus is applied on the left side of the rectangular domain;
- $\bar{\Omega}_{\text{corner}} = [0, \bar{x}] \times [0, \bar{y}]$ with $\bar{x} < L_x$ and $\bar{y} < L_y$, that is, the current is applied on a rectangular region located in the corner of the domain surrounding the origin.

We present our results for the two-dimensional simulations starting with the FHN cell model coupled with the monodomain equation. Once again we assume that the parameters λ, C_m and χ of equation (2.27) are equal to $\lambda = 1$, $C_m = 1\,\mu\text{F}\cdot\text{cm}^{-2}$ and $\chi = 2000\,\text{cm}^{-1}$. We initially consider the isotropic case and set $M_x = M_y = 3\,\text{mS}\cdot\text{cm}^{-1}$ (values taken from [79]).

Let $\Omega = [0, 5] \times [0, 5]$, $h_x = h_y = 0.05$, $t_f = 500$ and $\Delta t = 0.25$. By applying the stimulus $I^{(\text{vol})} = 5 \cdot 10^5\,\mu\text{A}\cdot\text{cm}^{-3}$ at $t = 10$ for five milliseconds on the side $\bar{\Omega}_{\text{side}}$ of the domain, the current triggers an action potential and generates a travelling pulse that advances in the x direction. Because the strength of

the applied current is uniform along the side $\bar{\Omega}_{\text{side}}$ and independent of y, we observe the same behaviour for all values of y (see Figure 3.10).

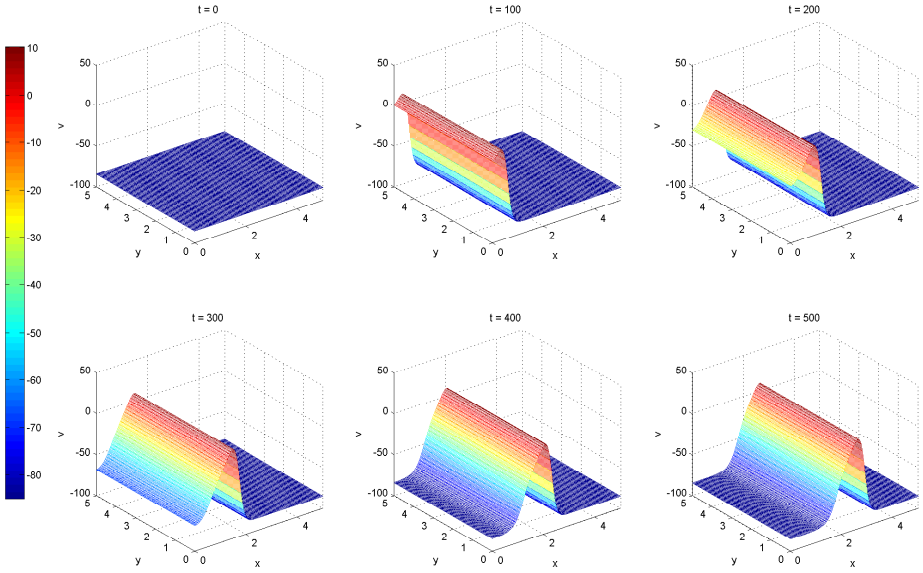

Figure 3.10: *Evolution in time of the solution to the two-dimensional FHN monodomain model with electrical stimulus applied on* $\bar{\Omega}_{side}$*. The solution is plotted at equal time intervals of* 100 msec*.*

The same evolution of the solution profile is obtained in the anisotropic case if we consider $M_y \neq M_x$, for example, $M_y = 1\,\text{mS}\cdot\text{cm}^{-1}$ (value taken from [79]), while keeping $M_x = 3\,\text{mS}\cdot\text{cm}^{-1}$. In fact, once again stimulation of the left side of the rectangle simply induces an action potential that travels in the x direction and therefore its advance in time is only affected by M_x and not by the diffusivity in the orthogonal direction.

On the other hand, if we consider the same set of modelling and numerical parameters but apply the current on $\bar{\Omega}_{\text{corner}}$ with $\bar{x} = \bar{y} = 0.25$, the difference between the isotropic and anisotropic cases becomes evident. When the problem is isotropic, the generated pulse advances equally in both directions as shown by Figure 3.11.

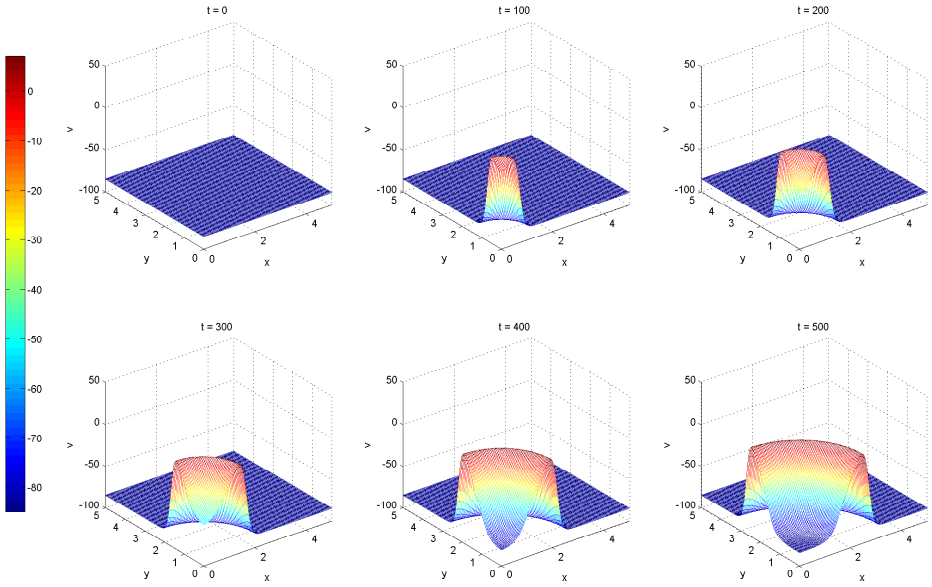

Figure 3.11: *Evolution in time of the solution to the two-dimensional FHN monodomain model with electrical stimulus applied on* $\bar{\Omega}_{corner}$ *in the isotropic case. The solution is plotted at equal time intervals of* 100 msec.

However, if we assume that the problem is anisotropic and therefore consider different values for the conductivities M_x and M_y, the generated pulse still travels in both directions but it advances faster in the direction corresponding to the higher conductivity value. For example, if $M_x = 3\,\text{mS}\cdot\text{cm}^{-1}$ and $M_y = 1\,\text{mS}\cdot\text{cm}^{-1}$, the generated pulse travels faster along the x direction as shown by Figure 3.12.

The difference between the isotropic case and the anisotropic case can be easily visualised by comparing the transmembrane potential surface at the same time point. In Figure 3.13 we consider a projection onto the xy-plane of the last plot of Figure 3.11 and the last one in Figure 3.12, both representing the value of the transmembrane potential on the rectangular domain at $t = 500\,\text{msec}$ (in the isotropic and anisotropic cases, respectively). By observing the location on the spatial mesh of the dark red colour corresponding to the peak of the pulse, we clearly observe that the anisotropy assumption

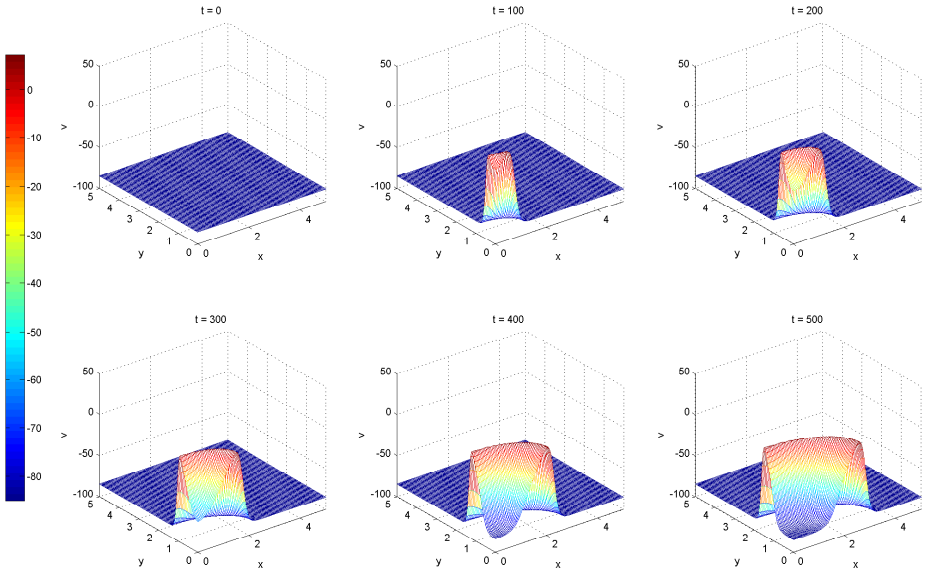

Figure 3.12: *Evolution in time of the solution to the two-dimensional FHN monodomain model with electrical stimulus applied on* $\bar{\Omega}_{corner}$ *in the anisotropic case. The solution is plotted at equal time intervals of* 100 msec.

results in an asymmetric advance of the pulse with respect to the two spatial directions, whereas the advancing of the pulse is clearly asymmetric in the anisotropic case.

To conclude the set of simulations for the FHN cell model, we now consider it in the bidomain setting with uniform diffusivity tensors for the intracellular and extracellular domains defined respectively as (conductivity values taken from [79])

$$M_i = \begin{bmatrix} 3 & 0 \\ 0 & 1 \end{bmatrix} \quad \text{and} \quad M_e = \begin{bmatrix} 2 & 0 \\ 0 & 1.65 \end{bmatrix}. \tag{3.48}$$

Let $\Omega = [0, 2.5] \times [0, 2.5]$, $h_x = h_y = 0.05$, $t \in [0, 400]$ and $\Delta t = 0.25$. By applying an electrical stimulus $I_i^{(\mathrm{vol})} = 5 \cdot 10^5\, \mu\mathrm{A}\cdot\mathrm{cm}^{-3}$ on the corner of the domain surrounding the origin $\bar{\Omega}_{\mathrm{corner}} = [0, 0.25] \times [0, 0.25]$ at $t = 10$ for five milliseconds, we obtain the evolution of the transmembrane potential given in Figure 3.14.

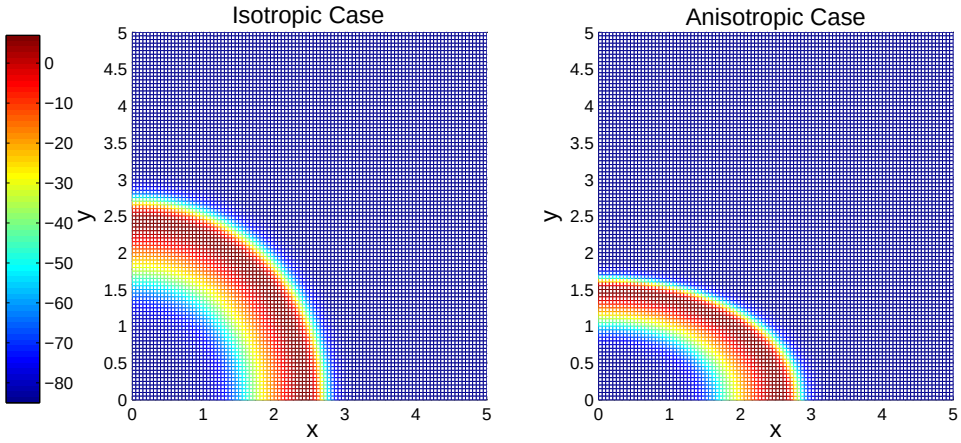

Figure 3.13: *Comparison of the isotropic and the anisotropic cases. The transmemebrane potential surface produced at* $t = 500$ *by the FHN monodomain model in the two cases with the same set of simulation parameters is projected onto the two-dimensional spatial grid used in both simulations. At each node of the grid, the corresponding value of the transmembrane potential is given by the provided colour bar.*

Once again the differences in the diffusivity tensors produce a faster advancing of the pulse in one of the two orthogonal spatial directions. In the particular case depicted in Figure 3.14, we easily see that the x-axis is the preferred direction.

Similar qualitative results can be observed when the spatial models (monodomain and bidomain) are coupled with the BR cell model. This time, however, the action potential triggered by the applied electrical stimulus has the particular shape determined by the BR ionic model. As observed in the one-dimensional case, if we wanted to observe the movement of the entire BR action potential, we would have to consider a much larger spatial domain. Considering a very large spatial domain is however unnecessary if our aim is to observe how the stimulus propagates in space[7]. Here we simply fix the size of the spatial domain to be $\Omega = [0, 2.5] \times [0, 2.5]$ and to have an idea of how the solution of the model evolves in time, we plot the projection

[7]As previously stated, enlarging the domain was simply used as a visualisation tool in our one-dimensional simulations but it is not the approach commonly used in practical applications.

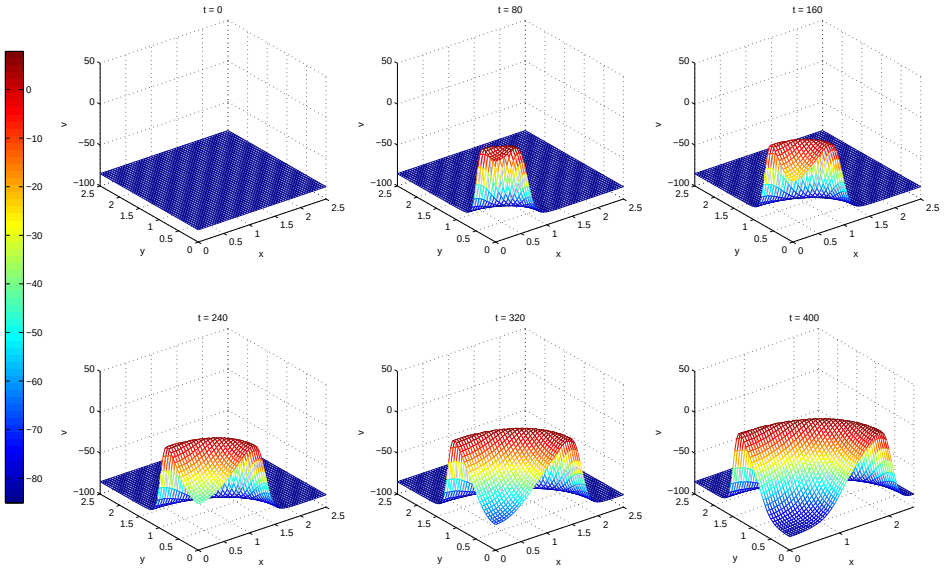

Figure 3.14: *Evolution in time of the solution to the two-dimensional FHN bidomain model with electrical stimulus applied on* $\bar{\Omega}_{corner}$. *The solution is plotted at equal time intervals of* 80 msec.

of the transmembrane potential onto the xy-plane at different time points. Moreover, to better understand and visualise our results, at each time step of the simulation we store the value of v at specific points in space away from the site where the electrical stimulus is applied. We then plot the result as a function of time so that we can see when the travelling pulse reaches the particular points considered and how the transmembrane potential of these points changes in time.

In the first three simulations we consider the BR monodomain model and compute the solution for $t \in [0, 400]$ with $\Delta t = 0.25$ and $h_x = h_y = 0.025$. If an electrical stimulus $I_i^{(\text{vol})} = 10^5\,\mu\text{A}\cdot\text{cm}^{-3}$ is applied to the left side of the rectangular domain at $t = 10$ for five milliseconds, in either the isotropic case ($M_x = M_y = 3\,\text{mS}\cdot\text{cm}^{-1}$) or the anisotropic case ($M_x = 3\,\text{mS}\cdot\text{cm}^{-1}$, $M_y = 1\,\text{mS}\cdot\text{cm}^{-1}$), the generated pulse travels in the positive x direction as shown by Figure 3.15. To facilitate the visualisation of the results at a

given time point t we consider the projection of the transmembrane potential surface v onto the xy-plane. The actual value of v at each node of the spatial grid used in the computation is given by the corresponding colour in the colour bar.

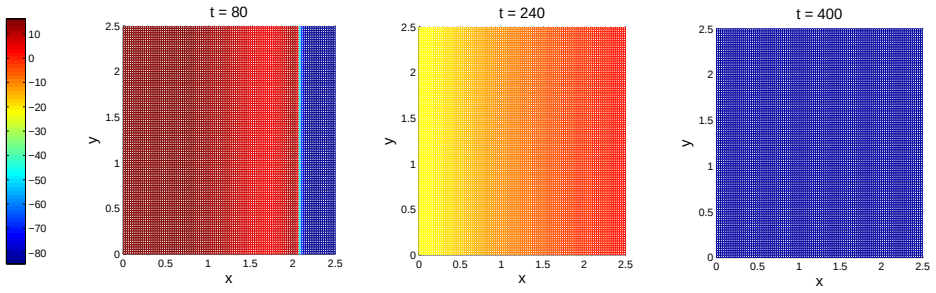

Figure 3.15: *Projection of the transmembrane potential surface onto the xy-plane at* $t = 80, 240, 400$ msec *for the BR monodomain model when the electrical stimulus is applied to the left side of the rectangular spatial domain.*

According to the colour bar of Figure 3.15, we see that applying a stimulus along the left side of the rectangular domain generates a pulse that advances in time along the x-axis but is invariant with respect to the y coordinate. The steep front and the slow recovery phase characteristic of the BR ionic model are clearly visible from the first projection of the numerical solution in Figure 3.15. At $t = 80$, only a small section on the right hand side of the domain is still at rest (blue nodes) while most of the domain has been depolarized and therefore is coloured in various shades of red. A very narrow transition region separates the nodes at rest from nodes corresponding to a much higher transmembrane potential value corresponding to the steep front of the BR pulse (quick depolarization). As time increases, the transmembrane potential at all nodes of the rectangular region goes through the entire action potential (the slow recovery phase is clearly visible from the gradual change of colours observed at $t = 240$), eventually returning to the resting state in the entire domain (all nodes are blue at $t = 400$).

For the same simulation we also consider the point $P_1 = (2.5, 0) \in \Omega$, that is, the bottom right corner of the rectangular domain, and in Figure 3.16

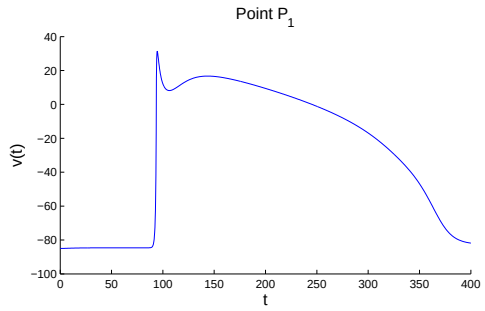

Figure 3.16: *Evolution of the transmembrane potential at* $P_1 = (2.5, 0) \in \Omega$ *obtained with the BR monodomain model when the electrical stimulus is applied to the left side of the rectangular domain.*

we plot the evolution of v at that particular point as a function of time. As we clearly see, the point P_1 is initially at its resting state and remains at rest for a certain time interval also after the electrical stimulus is applied (at $t = 10$). However, once reached by the travelling pulse, the point P_1 is quickly depolarized and the transmembrane potential at that point changes in time following the typical pattern of an action potential generated by the BR cell model (peak followed by the early repolarization phase and then by a notch and a slow recovery phase), eventually returning to the resting value.

When the electrical stimulus $I^{(\mathrm{vol})} = 10^5\,\mu\mathrm{A}\cdot\mathrm{cm}^{-3}$ is applied at $t = 10$ for five milliseconds to the corner $\bar{\Omega}_{\mathrm{corner}} = [0, \bar{x}] \times [0, \bar{y}]$ with $\bar{x} = \bar{y} = 0.25$, as observed for the FHN model, the difference between the isotropic and the anisotropic cases becomes evident. We run both simulations for $t \in [0, 400]$ with the same set of simulation parameters and plot the projection of the v surface onto the xy-plane at $t = 80, 240, 400\,\mathrm{msec}$.

In this case, we see from Figure 3.17 that the evolution in time of the travelling pulse is symmetric with respect to both spatial coordinates. As depicted at $t = 80$, the advancing front is now an arc of circumference rather than a straight line but once again it presents the main characteristics of the BR action potential pulse. In particular, the blue region (nodes at rest) and the wide red region (corresponding to depolarized nodes) are separated by a

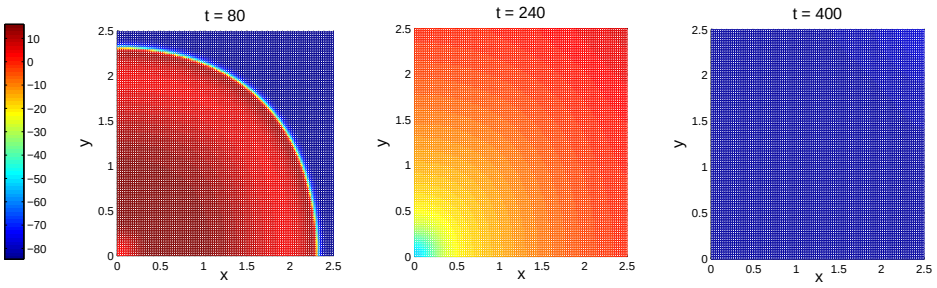

Figure 3.17: *Projection of the transmembrane potential surface onto the xy-plane at* $t = 80, 240, 400\,\text{msec}$ *for the BR monodomain model when the electrical stimulus is applied in a small rectangular region of the domain surrounding the origin in the isotropic case.*

very narrow transition area identifying the steep advancing front of the BR pulse. As time increases, the transmembrane potential at all nodes of the domain goes through the full action potential. After the quick depolarization, the slow recovery phase also affects all nodes having radial symmetry with respect to the origin (as shown by the gradual colour change at $t = 240$). Eventually, starting from the bottom left corner of the rectangular domain, the transmembrane potential at all nodes returns to the resting value and the grid returns to being all coloured in blue.

For this simulation we consider two points $P_1 = (2.5, 0)$ and $P_2 = (0, 2.5)$ in the domain, that is, the bottom right and top left corners of Ω, respectively, and in Figure 3.18 we plot the evolution of the corresponding transmembrane potential as a function of time.

As shown by both Figure 3.17 and Figure 3.18, in the isotropic case the evolution in time of the travelling pulse is symmetric in both spatial directions. On the other hand, when the anisotropic diffusion tensor is used ($M_x = 3\,\text{mS}\cdot\text{cm}^{-1}$, $M_y = 1\,\text{mS}\cdot\text{cm}^{-1}$), the stimulus $I^{(\text{vol})} = 10^5\,\mu\text{A}\cdot\text{cm}^{-3}$ applied at $t = 10$ for five milliseconds on $\bar{\Omega}_{\text{corner}}$ generates an action potential that moves faster in the direction associated with the higher diffusivity value.

As depicted in Figure 3.19 we see that the applied stimulus still generates

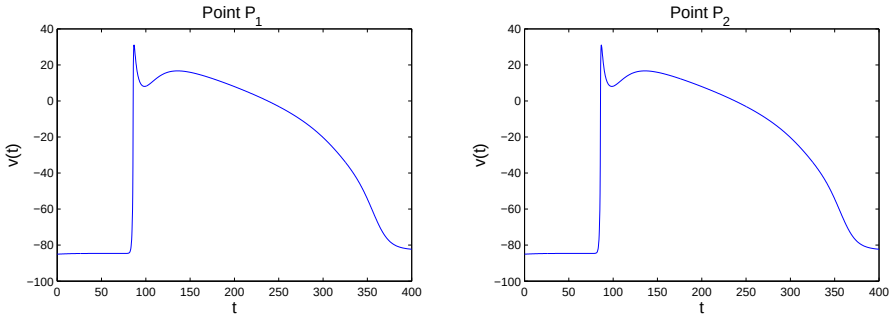

Figure 3.18: *Evolution of the transmembrane potential at* $P_1 = (2.5, 0)$ *and* $P_2 = (0, 2.5)$ *obtained with the BR monodomain model when the electrical stimulus is applied in a small rectangular region of the domain surrounding the origin in the isotropic case.*

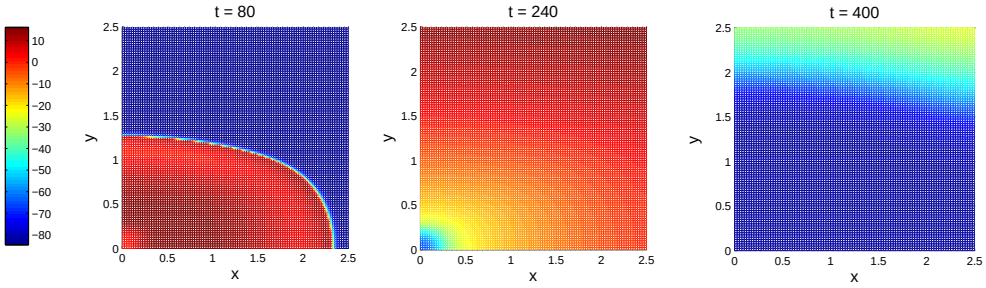

Figure 3.19: *Projection of the transmembrane potential surface onto the xy-plane at* $t = 80, 240, 400$ msec *for the BR monodomain model when the electrical stimulus is applied in a small rectangular region of the domain surrounding the origin in the anisotropic case.*

an action potential with the typical characteristics dictated by the BR cell model and propagating through the domain in both spatial directions. However, the use of different diffusivities in the diagonal diffusion tensor results in an asymmetric advancing of the generated curved front. In this particular case, the assumption of $M_x > M_y$ produces a faster advancing of the pulse along the x-axis rather than in the y direction. Once again, the transmembrane potential at all the nodes of the spatial domain passes through an entire action potential, but due to the differences in the diffusion tensor, the travelling pulse does not advance with radial symmetry with respect to the origin anymore. Having chosen M_x as in the isotropic case shown by

Figure 3.17 and $M_y < M_x$, we obtain that the time required for the entire domain to return back to rest is now longer than in the previous case. In fact, at $t = 400$ there is still an area along the upper side of the domain that has not completed the recovery phase.

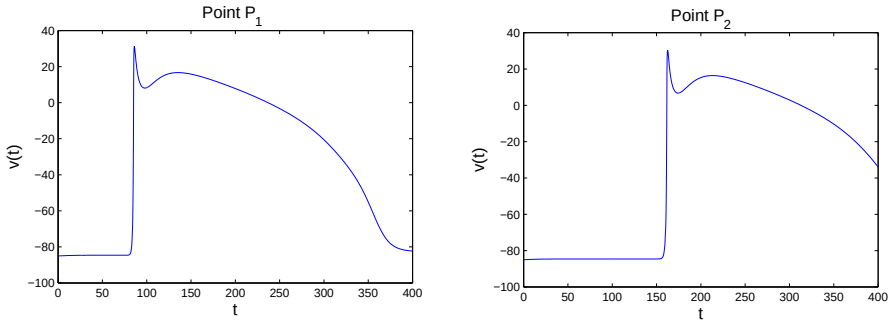

Figure 3.20: *Evolution of the transmembrane potential at* $P_1 = (2.5, 0)$ *and* $P_2 = (0, 2.5)$ *obtained with the BR monodomain model when the electrical stimulus is applied in a small rectangular region of the domain surrounding the origin in the anisotropic case.*

The asymmetric advancing due to the anisotropic assumption is also evident when comparing the evolution in time of v at P_1 and P_2, namely the bottom right and top left corners of Ω, as reported by Figure 3.20. In fact, P_1 is the first of these two points to be depolarized and its potential, during the considered time interval, $[0, 400]$, passes through an entire action potential before eventually returning to rest. On the other hand, P_2 is depolarized at a later time point and by the end of the considered particular simulation, that is, at $t = 400$, it has not gone through the entire action potential, still being in the middle of the recovery phase.

We conclude this section by running one simulation of the BR bidomain model on the spatial domain $\Omega = [0, 2.5] \times [0, 2.5]$ for $t \in [0, 400]$ with mesh sizes $h_x = h_y = 0.025$ and time step $\Delta t = 0.25$. The considered intracellular stimulus, now $I_i^{(\mathrm{vol})} = 10^5\, \mu\mathrm{A}\cdot\mathrm{cm}^{-3}$, is once again applied on the corner $\bar{\Omega}_{\mathrm{corner}} = [0, 0.25] \times [0, 0.25]$ at $t = 10$ for five milliseconds. The diffusivity tensors in the intracellular and extracellular domains are as in

equation (3.48). We report in Figure 3.21 the projection onto the xy-plane of the solution obtained at $t = 80, 240, 400$ msec.

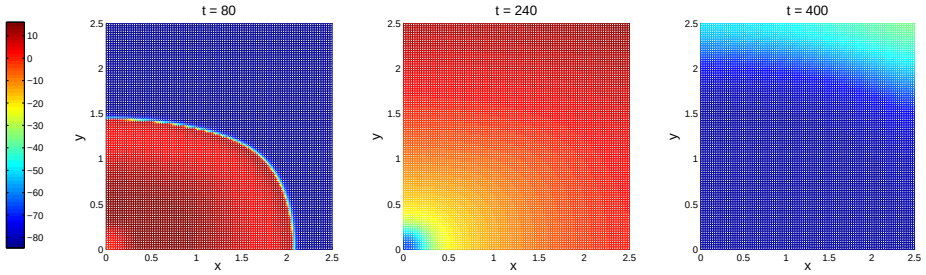

Figure 3.21: *Projection of the transmembrane potential surface onto the xy-plane at* $t = 80, 240, 400$ msec *for the BR bidomain model. The electrical stimulus is applied in a small rectangular region of the domain surrounding the origin.*

As for the monodomain model, when the electrical stimulus is applied to the region surrounding the origin, also for the BR bidomain model the anisotropic assumption results in an asymmetric advancing of the BR pulse throughout the domain. Having a higher diffusivity along the x-axis in both the intracellular and extracellular diffusion tensors determines this axis as the preferential direction for the front advance.

As stated by Bourgault and Pierre [8], "the bidomain model is quite popular for its physiological foundation and relevance whereas the monodomain model simply is a heuristic approximation of the previous one, lacking this physiological foundation but providing computational facilities". As a conclusion of their study [8], they showed that the discrepancy between the two formulations[8] in the continuous case is very small (of the order of 1% in terms of relative error on the activation time) and typically the amount of error due to the discretisation used in even higher. Clearly the discrepancy between the formulations is accentuated as the actual conductivities devi-

[8]In their monodomain formulation the conductivity tensor used in the PDE is defined as the harmonic mean of the intracellular and extracellular conductivity tensors of the corresponding bidomain formulation. This reduces to our formulation under the additional assumption of equal anisotropy ratios.

ate from the assumption behind the monodomain reduction. However, in light of the above considerations we decide that for the purpose of the study proposed in this thesis, the many computational advantages offered by the monodomain model far overcome the need of having a model with a firm physiological foundation. Therefore, throughout the reminder of the thesis, when considering simulations of excitable media models we will simply couple the cell models of interest with the monodomain formulation of spatial propagation.

Chapter 4

Boundary conditions for non-local problems

The interest in non-local operators, especially fractional ones, has substantially increased in recent years due to the success of these types of models in matching experimental data describing transport phenomena characterised by anomalous dynamics.

In the context of space-fractional models, the fractional Laplacian and its probabilistic interpretation in terms of continuous time random walks appear in the description of a large number of physical systems. As shown in Chapter 2, this non-local operator is naturally defined on $\mathbb{R}^n$. However, in practical applications transport processes typically occur on a finite domain and therefore one of the first challenges encountered from the mathematical point of view in the use of the fractional Laplacian is related to the restriction of its definition on a finite domain $\Omega \subset \mathbb{R}^n$ and the well-posedness of the bounded formulation.

In the standard diffusion case, if we consider

$$\begin{cases} \dfrac{\partial u}{\partial t} &= -(-\Delta)u, \\ u(x,0) &= u_0(x) \end{cases} \tag{4.1}$$

with $x \in \Omega \subset \mathbb{R}^n$ and $t > 0$, the specification of a condition at the boundary $\partial\Omega$ for the solution $u(x,t)$ (together with mild regularity assumptions on u and the initial condition u_0) is enough to guarantee that the problem (4.1) is well posed. However, in the non-local case, if we substitute $-\Delta$ in equation (4.1) with its fractional counterpart $(-\Delta)^{\alpha/2}$, specification of a local condition at the boundary is no longer sufficient to obtain a well-posed formulation.

In this chapter we consider the fractional diffusion equation

$$\frac{\partial u}{\partial t} = -(-\Delta)^{\alpha/2} u, \tag{4.2}$$

with $x \in \Omega \subset \mathbb{R}^n$, $t > 0$ and focus our attention on the role of boundary conditions for this non-local problem on finite domains. We begin in Section 4.1 by presenting the case of homogeneous Dirichlet boundary conditions and make some considerations on different types of standard boundary conditions. We then introduce the concept of reflecting boundaries and present the results proposed by Krepysheva et al. [45] for the semi-infinite case and by Néel et al. [65] for the finite one-dimensional cases. In Section 4.2 we derive a discrete representation of the continuous operator embedding reflecting boundary conditions and in Section 4.3 we formulate a theorem providing the analytic expression of the eigenvalues and eigenvectors of such a discrete operator as a function of the number of discretisation points used and the fractional order. Some considerations on the results obtained and the comparison between the discrete reflection operator and the matrix transfer technique follow in Section 4.4. Section 4.5 is dedicated to some numerical simulations and to the comparison of results obtained for the fractional diffusion problem (4.2) under different boundary assumptions.

4.1 Standard and reflecting boundary conditions

The simplest type of boundary conditions that can be considered when studying a boundary value problem of the form (4.1) on a given bounded domain $\Omega \subset \mathbb{R}^n$ is the case of standard homogeneous Dirichlet boundary conditions, that is, the assumption that the solution u is equal to zero along the entire boundary $\partial\Omega$ of the spatial domain:

$$u(x,t) = 0 \qquad \forall x \in \partial\Omega.$$

As previously mentioned, with the simple specification of $u(x,t) = 0$ for all $x \in \partial\Omega$ the corresponding fractional problem (4.2) still remains ill-posed. In order to overcome this problem, the common approach is to define an extension $\bar{u}$ of the function u such that

$$\bar{u}(x,t) = \begin{cases} u(x,t) & \text{when } x \in \Omega \\ 0 & \text{when } x \in \Omega^C := \mathbb{R}^n \setminus \Omega, \end{cases}$$

and consider the unbounded fractional problem

$$\frac{\partial \bar{u}}{\partial t} = -(-\Delta)^{\alpha/2}\bar{u} \tag{4.3}$$

where $(-\Delta)^{\alpha/2}$ is the fractional Laplacian on $\mathbb{R}^n$. Given an extension $\bar{u}_0$ of the initial condition u_0 (equal to zero outside of Ω), the solution $\bar{u}$ of equation (4.3) is computed on $\mathbb{R}^n$ and the solution u to the corresponding bounded problem (4.2) can hence be viewed as the restriction to Ω of the unbounded solution $\bar{u}$.

From the computational point of view, the main advantage of this approach is the fact that the non-locality of the fractional operator is "compensated" by assuming $\bar{u} = 0$ everywhere in the complement of the finite domain Ω. In fact, when introducing a spatial discretisation of the unbounded problem (for example, using the finite-difference method), the approximation of the non-

local term $(-\Delta)^{\alpha/2}\bar{u}$ at a given point of the spatial mesh (see the Grünwald–Letnikov approach in Section 2.3) involves the solution approximation at an infinite number of other nodes. However, due to the assumptions made on $\bar{u}$, the contribution of the solution approximation at all nodes outside of Ω is void. Consequently, the discretised solution can be obtained only in terms of solution approximations at a finite number of points corresponding to the finite number of nodes used to build the spatial grid.

In terms of continuous time random walks and the probabilistic interpretation of the fractional Laplacian, the above strategy used to generalise standard homogeneous Dirichlet boundary conditions is usually referred to as the case of absorbing boundary conditions (as in the terminology used by Zoia et al. [89] or van Milligen et al. [82]). In fact, this case corresponds to the assumption that the particles in the observed ensemble performing the continuous time random walk are removed (or "killed") whenever a jump brings them outside of the considered finite interval.

Whether we are considering a one-dimensional interval or a finite domain in more than one spatial dimension, the same strategy can be applied to generalise the concept of homogeneous Dirichlet boundary conditions and due to its relatively simple interpretation and implementation, this method has been widely used in practice.

The formulation of the fractional diffusion problem (4.2) on bounded domains in presence of nonhomogenous Dirichlet or any other type of boundary conditions is not as simple. In fact, it is fundamental to understand the role of boundary conditions in the problem and how they affect the non-local operator. Different interpretations of the space-fractional problem might also lead to diverse mathematical formulations and therefore, particular care must be taken in the choice of suitable restrictions of the non-local operator.

4.1.1 Reflective boundary conditions

Together with homogeneous Dirichlet boundary conditions, another type of homogeneous conditions that is very often used with standard diffusion models for practical applications involves the specification at the boundary points of the gradient of the solution in the direction normal to the boundary surface. It is the case of homogeneous Neumann boundary conditions, that is,

$$\mathbf{n} \cdot \nabla u = 0 \qquad \forall x \in \partial\Omega, \tag{4.4}$$

where $\mathbf{n}$ is the outward unit vector normal to the surface $\partial\Omega$. Condition (4.4) is also called a zero-flux boundary condition due to the physical interpretation of a fixed normal derivative at the boundary in terms of constant[1] flux of u in and out of the simulation domain. For example, if we think of the heat conduction problem in the standard diffusion case, the imposition of zero-flux conditions at the boundary of the spatial domain corresponds to the assumption of no heat conduction across $\partial\Omega$ and the fact that the domain can be viewed as an insulated medium.

The idea of insulating boundary conditions is at the base of the work proposed by Krepysheva et al. [45] on the concept of reflecting boundaries and the corresponding modification of the unbounded space-fractional operator for the description of anomalous dynamics on a finite one-dimensional domain. Krepysheva et al. [45] follow the approach used by Compte [20] and Metzler et al. [59] on the unbounded domain to obtain a mathematical PDE formulation at the macroscale describing the temporal and spatial evolution of an ensemble of particles performing symmetric α-stable Lévy flights at the microscale. In particular, the authors of [45] consider how such a macroscale formulation could be modified in order to take into account the presence of a reflecting boundary.

These ideas have then been generalised by Néel et al. [65] to the nontrivial case of a finite one-dimensional domain with two reflecting boundaries and by

[1] In this case the constant is zero.

van Milligen et al. [82] who considered a wider class of boundary conditions that has perfectly reflecting boundary conditions[2] and absorbing boundary conditions as particular cases.

In what follows we describe the main ideas proposed by Krepysheva et al. [45] for the semi-infinite case and show how these ideas can be extended when a finite domain is considered and a second reflecting boundary is introduced. Using Continuous Time Random Walks (CTRWs) to derive macroscopic transport equations from microscopic dynamics, we will build a set of macroscopic space-fractional models, based on α-stable symmetric Lévy walks initially on infinite domains, then semi-infinite domains and finally on bounded domains.

For the work presented in the remainder of this section we would like to acknowledge the fundamental contribution of Dr. David Kay from the Department of Computer Science of the University of Oxford. During his visit to the School of Mathematical Sciences of QUT in 2012, he discussed with us some original ideas on the reformulation of reflecting boundary conditions on an insulated one-dimensional finite domain via the introduction of a suitable "sawtooth" function. Dr. Kay's framework for the understanding of reflections on bounded domains and his novel perspective on the topic laid the foundations for a series of discussions on this subject. The refinement of these original ideas and the elaboration of the details of the proposed reformulation eventually resulted in the work we now present.

CTRW on the infinite domain

Let us consider an ensemble of particles performing an α-stable symmetric Lévy walk on the unbounded domain $\mathbb{R}$. Let l and τ_0 be the characteristic space and time scales of the jump length and the waiting times between particle jumps, respectively. Let $\Lambda_l(x, x')dx$ denote the probability that a particle jumps from x' and arrives in $[x, x + dx]$, also known as the transition probability. Then, in the unbounded domain, the probability $P(x, t)dx$ of

[2]This is how van Milligen et al. [82] describe the reflective case considered by Krepysheva et al. [45].

finding a particle in $[x, x+dx]$ at an instant t satisfies the Generalised Master Equation (GME) given by

$$\begin{aligned} P(x,t) &= \delta_{x_0}(x) \int_{t'=t}^{\infty} \psi_{\tau_0}(t')\ dt' + \\ &\qquad \int_{x'=-\infty}^{\infty} \int_{t'=0}^{t} P(x',t') \Lambda_l(x,x') \psi_{\tau_0}(t-t')\ dt'\ dx', \end{aligned} \quad (4.5)$$

where $\psi_{\tau_0}(t) := e^{-t/\tau_0}/\tau_0$ is the Markovian probability density function (pdf) of waiting times T_i between successive jumps, x_0 is the initial starting position of the particles and $\delta_{x_0}(x)$ the Dirac delta function.

Assuming there exists a random variable X such that the jumps X_i are distributed as lX and that the pdf $\phi_1(\cdot)$ of X is a symmetric α-stable Lévy law $p_\alpha(\cdot, 0)$ such that

$$\phi_1(x) \sim |x|^{-(\alpha+1)} \quad \text{for } |x| \to \infty,$$

then the resulting transition pdf satisfies

$$\Lambda_l(x,x') = \phi_l(x-x'), \quad \phi_l(X) := \frac{\phi_1(X/l)}{l}, \quad \phi_1(X) := p_\alpha(X,0),$$

see Metzler and Klafter [58].

CTRW on the semi-infinite domain $[0,+\infty)$ with reflection at $x=0$

If we consider a force field constraining particles to never leave the semi-infinite domain $[0,+\infty)$, then the GME involves an integral over $[0,+\infty)$ instead of $(-\infty,+\infty)$, and equation (4.5) becomes

$$\begin{aligned} P(x,t) &= \delta_{x_0}(x) \int_{t'=t}^{\infty} \psi_{\tau_0}(t')\ dt' + \\ &\qquad \int_{x'=0}^{\infty} \int_{t'=0}^{t} P(x',t') \Lambda_l^+(x,x') \psi_{\tau_0}(t-t')\ dt'\ dx'. \end{aligned} \quad (4.6)$$

The fact that a reflecting boundary is considered at $x=0$ modifies the transition probability and leads to the definition of $\Lambda_l^+(x,x')$.

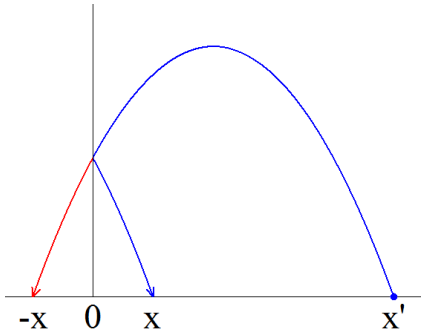

Figure 4.1: *Particle trajectory from x' to x with one reflection. The trajectory of the particle hitting the wall follows the mirror image of the portion of parabola situated on the left-hand side of the wall and ends at x instead of $-x \notin [0, +\infty)$.*

In order to understand how this transition probability is affected by the introduction of a reflecting wall, Krepysheva et al. [45] consider the example of particles jumping in (x, z) coordinates in a uniform force field (with direction z orthogonal to x). At the microscopic level, the introduction of a reflecting boundary at zero affects the parabolic trajectory of particles hitting the wall. When a bouncing particle hits the elastic barrier, the assumption of no energy exchange with the wall results in a change of sign of the x component of the momentum and the trajectory of the particle simply follows the mirror image of the portion of parabola situated on the left-hand side of the wall. Hence, a jump that in absence of the barrier would end at $-x \in (-\infty, 0)$, in the semi-infinite case ends at the point $+x \in (0, +\infty)$ (see Figure 4.1).

The presence of the reflecting wall at the origin can be viewed as the introduction of a symmetric correspondence of arrival points in the unbounded domain of jumps starting at a given $x' \in [0, +\infty)$. In fact, points located at the same distance from the wall can be identified under reflection.

Consequently, a jump from x' to x, with both x' and x in $[0, +\infty)$, can be obtained either directly or via a single bounce off the reflective barrier, and

therefore, the transition probability can be rewritten as

$$\Lambda_l^+(x, x') = \phi_l(x - x') + \phi_l(-x - x').$$

A straightforward representation of this symmetric identification of points introduced by the reflective wall at zero is given by the absolute value $|\cdot|$. Indeed, for a fixed $x \in [0, +\infty)$, the set Y_x of equivalent arrival points can be denoted by

$$Y_x := \{y \in (-\infty, +\infty) \mid |y| = x\},$$

and as previously observed, $Y_x = \{x, -x\}$.

CTRW on the finite domain $[0, L]$

The introduction of a second reflective barrier at a given $x = L > 0$ results in an additional constraint to the movement of particles and can be interpreted as a force field that forces the particles to remain in the finite domain $[0, L]$. In this case, the modified GME involves an integral over $[0, L]$ rather than $[0, +\infty)$ or $(-\infty, +\infty)$, and therefore takes the form

$$\begin{aligned} P(x,t) &= \delta_{x_0}(x) \int_{t'=t}^{\infty} \psi_{\tau_0}(t')\, dt' + \\ &\qquad \int_{x'=0}^{L} \int_{t'=0}^{t} P(x', t') \Lambda_l^L(x, x') \psi_{\tau_0}(t - t')\, dt'\, dx'. \end{aligned} \tag{4.7}$$

Obviously, the introduction of an additional reflecting barrier once again affects the transition probability and leads to the definition of $\Lambda_l^L(x, x')$. In fact, at the microscale, the trajectory of a particle in the uniform force field in (x, z) coordinates can be affected this time also when the particle starts at a given $x' \in [0, L]$ and jumps in the positive direction. Similarly to that observed in the semi-infinite case, if the particle reaches the reflecting wall at $x = L$, it bounces back and its parabolic trajectory follows the mirror image of the portion of parabola located on the right-hand side of the new wall (no energy exchange between particle and wall). Therefore, the introduction of a wall at L results in the additional symmetric identification of points located on both sides of the new reflecting boundary.

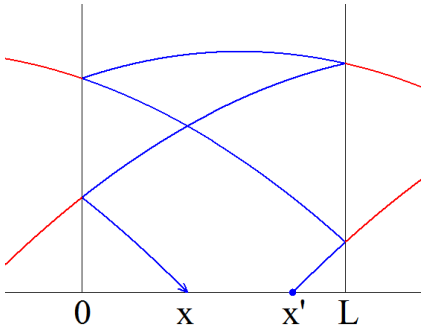

Figure 4.2: *Particle trajectory from x' to x via repeated bounces between the two reflecting walls. Whenever the particle trajectory encounters a reflecting barrier, it follows the mirror image of the portion of parabola located on the other side of that wall.*

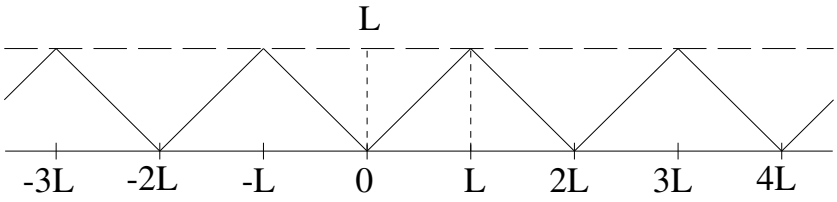

Figure 4.3: *The continuous sawtooth function* $[x]_0^L$.

With two reflecting boundaries, the new scenario of multiple bounces between the walls becomes possible (see Figure 4.2). As suggested by Dr. David Kay from the Department of Computer Science of the University of Oxford, a simple way to represent the resulting identification of points of the unbounded domain with their corresponding $x \in [0, L]$ under reflections is given by the sawtooth function graphically represented in Figure 4.3 and denoted by $[\cdot]_0^L$. Such a function coincides with the absolute value in the interval $[-L, L]$ and it is then extended periodically with period $2L$ to the entire unbounded domain (so that it preserves symmetry about both $x = 0$ and $x = L$).

For a fixed $x \in [0, L]$, let S_x represent the set

$$S_x := \{y \in (-\infty, +\infty) \mid [y]_0^L = x\},$$

that is, the set of points in the unbounded domain that can be identified with $x \in [0, L]$ under repeated reflections between the two boundaries. Due to the symmetry and the periodicity of the sawtooth function, for a fixed $x \in [0, L]$, we obtain

$$S_x = \{x + 2mL, -x + 2mL \mid m \in \mathbb{Z}\}.$$

In light of our previous considerations, a jump from x' to x, with both x' and x in $[0, L]$, can be obtained either directly or via an infinite number of possible multiple bounces between the walls. In particular, in this case the transition probability $\Lambda_l^L(x, x')$ can be rewritten as

$$\Lambda_l^L(x, x') = \sum_{y \in S_x} \phi_l(y - x') = \sum_{m \in \mathbb{Z}} \phi_l(\pm x + 2mL - x').$$

Using simple properties of definite integrals and the two variable substitutions $y_m = x + 2mL$ and $z_m = -x + 2mL$, we now show that the transition probability indeed integrates to one on $[0, L]$. In fact, $\int_{x=0}^{L} \Lambda_l^L(x, x')\, dx$ can be written as

$$\begin{aligned}
&\int_{x=0}^{L} \sum_{m \in \mathbb{Z}} \Big[\phi_l(x + 2mL - x') + \phi_l(-x + 2mL - x')\Big]\, dx \\
= &\sum_{m \in \mathbb{Z}} \left[\int_{y_m = 2mL}^{(2m+1)L} \phi_l(y_m - x')\, dy_m - \int_{z_m = 2mL}^{(2m-1)L} \phi_l(z_m - x')\, dz_m\right] \\
= &\sum_{m \in \mathbb{Z}} \left[\int_{2mL}^{(2m+1)L} \phi_l(x - x')\, dx + \int_{(2m-1)L}^{2mL} \phi_l(x - x')\, dx\right] \\
= &\int_{-\infty}^{+\infty} \phi_l(x - x')\, dx = 1.
\end{aligned}$$

Based on this analysis we can now write down the modified fractional operator on $[0, L]$ that accounts for two reflecting boundaries and generalises the semi-infinite case.

From $[0, L]$ to the unbounded domain and the modified operator

Let us first define the even extension P_E of P with respect to the origin, that is,

$$P_E(x,t) = \begin{cases} P(x,t) & \text{if } x \in [0,L], \\ P(-x,t) & \text{if } x \in [-L,0). \end{cases}$$

Exploiting the symmetry of ϕ_l, we obtain that P_E satisfies the following GME:

$$\begin{aligned} P_E(x,t) &= [\delta_{x_0}(x) + \delta_{-x_0}(x)] \int_{t'=t}^{\infty} \psi_{\tau_0}(t')\ dt' + \\ &\qquad \int_{x'=-L}^{L} \int_{t'=0}^{t} P_E(x',t') \Lambda_{l,E}^{L}(x,x') \psi_{\tau_0}(t-t')\ dt'\ dx', \quad (4.8) \end{aligned}$$

where $\Lambda_{l,E}^{L}(x,x') = \sum_{m\in\mathbb{Z}} \phi_l(x + 2mL - x')$.

By defining on the unbounded domain the periodic extension P_∞ of P_E, that is, the function that coincides with P_E on $[-L, L]$ and is then extended with period $2L$ to the entire $\mathbb{R}$, from equation (4.8) we see that P_∞ satisfies the following GME:

$$\begin{aligned} P_\infty(x,t) &= \sum_{m\in\mathbb{Z}} [\delta_{x_0+2mL}(x) + \delta_{-x_0+2mL}(x)] \int_{t'=t}^{\infty} \psi_{\tau_0}(t')\ dt' + \\ &\qquad \int_{\mathbb{R}} \int_{t'=0}^{t} P_\infty(x',t') \phi_l(x-x') \psi_{\tau_0}(t-t')\ dt'\ dx'. \quad (4.9) \end{aligned}$$

Observe that, if the initial condition for the particles is given by a Dirac distribution located at $x_0 \in [0, L]$, namely $\delta_{x_0}(x)$, the corresponding initial condition in the GME (4.8) for the even extension P_E is given by the sum $\delta_{x_0}(x) + \delta_{-x_0}(x)$ and for the periodic extension P_∞ we obtain all the possibilities given by

$$g_0(x) := \sum_{m\in\mathbb{Z}} [\delta_{x_0+2mL}(x) + \delta_{-x_0+2mL}(x)].$$

The function $g_0(x)$ is clearly an even periodic function of period $2L$ and can

be seen as the sum of two shifted Dirac combs.

Noting that the integral $\int_{t'=t}^{\infty} \psi_{\tau_0}(t')\ dt'$ represents the probability of performing no jump before t, this quantity can be rewritten as $1 - \int_0^t \psi_{\tau_0}(t')\ dt'$. Following the notation introduced in [45], let us denote by $\hat{f}(k)$ and $\tilde{h}(u)$ the Fourier and Laplace transforms of functions $f(x)$ and $h(t)$ of $x \in \mathbb{R}$ and $t \in \mathbb{R}^+$, respectively. From the GME (4.9) we find that in Fourier–Laplace coordinates

$$\hat{\tilde{P}}_\infty(k,u) = \hat{g}_0(k) \left(\frac{1 - \tilde{\psi}_{\tau_0}(u)}{u} \right) + \hat{\tilde{P}}_\infty(k,u)\ \hat{\phi}_l(k)\ \tilde{\psi}_{\tau_0}(u), \tag{4.10}$$

where $\hat{g}_0(k)$ is the Fourier transform of the initial condition $g_0(x)$ and in this particular case is given by

$$\hat{g}_0(k) = \sum_{m \in \mathbb{Z}} [e^{ik(x_0 + 2mL)} + e^{ik(-x_0 + 2mL)}].$$

Using the definition of $\phi_l(x)$ and $\psi_{\tau_0}(t)$, we see that their Fourier and Laplace transforms are given, respectively, by

$$\begin{aligned} \hat{\phi}_l(k) &= e^{-l^\alpha |k|^\alpha} \\ \tilde{\psi}_{\tau_0}(u) &= (\tau_0 u + 1)^{-1}. \end{aligned}$$

Therefore, equation (4.10) can be rewritten as

$$u\hat{\tilde{P}}_\infty(k,u) - \hat{g}_0(k) = \hat{\tilde{P}}_\infty(k,u) \frac{e^{-l^\alpha |k|^\alpha} - 1}{\tau_0}. \tag{4.11}$$

For fixed k and u, in order to obtain the macroscopic behaviour of P_∞, we consider equation (4.11) in the limit $(l, \tau_0) \to (0,0)$ while keeping the ratio l^α/τ_0 constant (namely $l^\alpha/\tau_0 = K_\alpha$). As a result

$$u\hat{\tilde{P}}_\infty(k,u) - \hat{g}_0(k) = -K_\alpha |k|^\alpha \hat{\tilde{P}}_\infty(k,u).$$

Hence, by inverting the transforms we see that for $\alpha \in (1,2]$, P_∞ is the

solution of

$$\begin{cases} \partial_t P_\infty(x,t) &= K_\alpha \, \mathcal{R}_x^\alpha P_\infty(x,t) \\ P_\infty(x,0) &= g_0(x), \end{cases}$$

where ∂_t denotes the partial derivative with respect to the temporal variable t and $\mathcal{R}_x^\alpha$ is used here to indicate the one-dimensional symmetric Riesz–Feller fractional derivative of order α introduced in Section 2.3 as $\frac{\partial^\alpha}{\partial|x|^\alpha}$. On the other hand, in a similar fashion we find that the concentration P on $[0, L]$ evolves according to the equation $\partial_t P(x,t) = K_\alpha \, \mathcal{R}_{x,L}^\alpha P(x,t)$, where $\mathcal{R}_{x,L}^\alpha$ is the restriction of the Riesz–Feller operator to the finite domain and has a modified kernel that takes into account the effect of the two reflecting boundaries, that is,

$$\mathcal{R}_{x,L}^\alpha P(x,t) = \\ \frac{-c_\alpha}{\Gamma(2-\alpha)} \frac{\partial^2}{\partial x^2} \int_0^L \sum_{m\in\mathbb{Z}} \Big[|x-y+2mL|^{1-\alpha} + |x+y+2mL|^{1-\alpha} \Big] P(y,t) \, dy,$$

where, to simplify the expression, we set $c_\alpha := \frac{1}{2\cos(\pi\alpha/2)}$.

4.2 Spatial discretisation of the reflective operator

In this section we show how the traditional Grünwald–Letnikov numerical approach used to approximate $\mathcal{R}_x^\alpha$ on $\mathbb{R}$ can be adapted to produce the same type of approximation for the reflection operator $\mathcal{R}_{x,L}^\alpha$ on $[0, L]$. This approximation will lead to a discrete version of the modified fractional operator that can be expressed in a particular matrix form. After describing how the discrete operator of reflections and the corresponding matrix form are obtained, in Section 4.3 we will study the spectrum of these discrete operators and make a comparison with the spectrum of the discrete and continuous Laplacian operator on $[0, L]$ in the standard case.

As previously seen in equation (2.53) of Section 2.3, in the one-dimensional case the Riesz-Feller operator $\mathcal{R}_x^\alpha$ can be written as the weighted sum of two

one-sided Riemann–Liouville fractional derivatives ($I_+^{-\alpha}$ and $I_-^{-\alpha}$ in equation (2.54)). As reported by Gorenflo and Mainardi [29], on the unbounded domain, if h denotes a small positive step length, the operators $I_+^{-\alpha}$ and $I_-^{-\alpha}$ can be obtained in the limit

$$I_+^{-\alpha} = \lim_{h\to 0} {}_hI_+^{-\alpha} \quad \text{and} \quad I_-^{-\alpha} = \lim_{h\to 0} {}_hI_-^{-\alpha},$$

where ${}_hI_+^{-\alpha}$ and ${}_hI_-^{-\alpha}$ are shifted Grünwald–Letnikov operators defined for $1 < \alpha \leq 2$ (our case of interest) and for any sufficiently smooth function f on $\mathbb{R}$ as follows:

$${}_hI_+^{-\alpha} f(x) := \frac{1}{h^\alpha} \sum_{j=0}^{\infty} (-1)^j \binom{\alpha}{j} f(x - (j-1)h)$$

and

$${}_hI_-^{-\alpha} f(x) := \frac{1}{h^\alpha} \sum_{j=0}^{\infty} (-1)^j \binom{\alpha}{j} f(x + (j-1)h),$$

where $(\omega_j)_0^\infty$ is a sequence of weights defined by $\omega_j := (-1)^j \binom{\alpha}{j}$ for all $j \geq 0$. Note that $\omega_0 = 1$ and $\omega_1 = -\alpha$ is the only negative weight of the entire sequence $(\omega_j)_0^\infty$. Moreover, since in our case of interest $\mathrm{Re}(\alpha) > 0$, the value of the sum of all the weights can be seen from the absolutely converging series $(1+x)^\alpha = \sum_{j=0}^{\infty} \binom{\alpha}{j} x^j$ evaluated at $x = -1$. Therefore,

$$\sum_{j=0}^{\infty} \omega_j = (1-1)^\alpha = 0. \tag{4.12}$$

These properties of the weights are important for some considerations that will be made later on in this chapter.

The above definition of the shifted Grünwald–Letnikov operators leads to a first order accurate approximation of $\mathcal{R}_x^\alpha$ (that is, $O(h)$ as shown by Meerschaert et al. [55]) in the form

$$\mathcal{R}_x^\alpha \approx -[c_\alpha \, {}_hI_+^{-\alpha} + c_\alpha \, {}_hI_-^{-\alpha}].$$

By introducing a uniform mesh of nodes $x_i = i\,h$, with $i \in \mathbb{Z}$, the infinite one-dimensional domain is partitioned into non-overlapping open intervals (x_i, x_{i+1}). At each node x_i, the discrete finite-difference approximations of $I_+^{-\alpha}$ and $I_-^{-\alpha}$ given by the shifted Grünwald–Letnikov approach are

$$I_+^{-\alpha} f\Big|_{x=x_i} \approx {}_h I_+^{-\alpha} f_i = \frac{1}{h^\alpha} \sum_{j=0}^{\infty} \omega_j \; f_{i-j+1}, \tag{4.13}$$

and

$$I_-^{-\alpha} f\Big|_{x=x_i} \approx {}_h I_-^{-\alpha} f_i = \frac{1}{h^\alpha} \sum_{j=0}^{\infty} \omega_j \; f_{i+j-1}, \tag{4.14}$$

where f_i is the approximation of f at the node x_i. Putting together equation (4.13), equation (4.14) and the definition of the Riesz–Feller operator in one spatial dimension (equation (2.54)) we see that when $\alpha \in (1, 2]$, $\forall i \in \mathbb{Z}$,

$$\mathcal{R}_x^\alpha f\Big|_{x=x_i} \approx \frac{-c_\alpha}{h^\alpha} \sum_{j=0}^{\infty} \omega_j \left(f_{i-j+1} + f_{i+j-1} \right), \tag{4.15}$$

where $c_\alpha = \frac{1}{2\cos(\pi\alpha/2)}$. The approximation of $\mathcal{R}_x^\alpha f$ at $x = x_i$ can therefore be seen as a weighted sum of approximations of the function f at all nodes of the spatial discretisation. In particular, for a fixed i, if we consider the value of the indices $i - j + 1$ and $i + j - 1$ when $j = 0, 1, 2, \ldots$ and the corresponding weight ω_j with which the approximations of f appear in equation (4.15), we observe that one sequence of weights $(\omega_j)_0^\infty$ is associated with the function approximations at a sequence of nodes in descending order starting from x_{i+1} (that is, to $x_{i+1}, x_i, x_{i-1}, x_{i-2}, \ldots$) and another sequence of weights is associated in ascending order with nodes starting from x_{i-1} (that is, to $x_{i-1}, x_i, x_{i+1}, x_{i+2}, \ldots$) - see Figure 4.4.

In order to obtain the same type of approximation in the finite case, we observe that the reflection operator $\mathcal{R}_{x,L}^\alpha$ introduced in Section 4.1.1, with a modified kernel representing the effect of two reflecting boundary conditions for the finite domain $[0, L]$, can be rewritten as the sum of two pseudo-

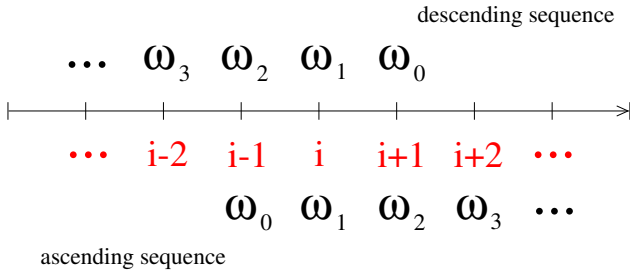

Figure 4.4: *The plot shows how the two sequences of weights* $(\omega_j)_0^\infty$ *are associated with the nodes of the spatial grid (red indices) in the approximation of* $\mathcal{R}_x^\alpha f|_{x=x_i}$ *in equation (4.15) for a fixed* i.

differential operators:

$$\mathcal{R}_{x,L}^\alpha = -[c_\alpha S_+ + c_\alpha S_-].$$

Once again $c_\alpha = \frac{1}{2\cos \pi\alpha/2}$ and for any sufficiently smooth function f on $[0, L]$ we define

$$S_+ f(x) := \frac{1}{\Gamma(2-\alpha)} \partial_x^2 \int_{-\infty}^{x} (x-y)^{1-\alpha}\ f([y]_0^L)\ dy$$

and

$$S_- f(x) := \frac{1}{\Gamma(2-\alpha)} \partial_x^2 \int_{x}^{\infty} (y-x)^{1-\alpha}\ f([y]_0^L)\ dy,$$

with $[\cdot]_0^L$ the continuous sawtooth function introduced in Section 4.1.1. In analogy with the approach proposed for the approximation of $\mathcal{R}_x^\alpha$ on the unbounded domain, if h represents a small step length, then the shifted Grünwald–Letnikov operators can be adapted in order to obtain a sequence of modified Grünwald–Letnikov operators ${}_hS_+$ and ${}_hS_-$ approximating the operators S_+ and S_-, respectively:

$${}_hS_+ f(x) := \frac{1}{h^\alpha} \sum_{j=0}^{\infty} \omega_j\ f([x-(j-1)h]_0^L)$$

$${}_hS_- f(x) := \frac{1}{h^\alpha} \sum_{j=0}^{\infty} \omega_j\ f([x+(j-1)h]_0^L).$$

To obtain the modified finite-difference scheme approximating the reflection operator $\mathcal{R}^{\alpha}_{x,L}$, let us consider a spatial discretisation of the finite domain $[0, L]$ by introducing a uniform mesh of $N+1$ nodes $x_i = i\,h$ where the mesh size is $h = \frac{L}{N}$ and $i = 0, 1, \ldots, N$. Let $f_i \approx f(x_i)$. Using the definitons of ${}_hS_+$ and ${}_hS_-$, the modified scheme approximating $\mathcal{R}^{\alpha}_{x,L}$ at each node x_i of $[0, L]$ (that is, for $i = 0, 1, \ldots, N$) becomes

$$\mathcal{R}^{\alpha}_{x,L} f\Big|_{x=x_i} \approx \frac{-c_\alpha}{h^\alpha} \sum_{j=0}^{\infty} \omega_j \Big(f_{[i-j+1]_0^N} + f_{[i+j-1]_0^N} \Big), \tag{4.16}$$

where $[\cdot]_0^N$ denotes the discrete version of the continuous sawtooth function $[\cdot]_0^L$, that is, the restriction of the continuous sawtooth function $[x]_0^L$ to integer values of the argument x. From equation (4.16) we see that the value of $\mathcal{R}^{\alpha}_{x,L} f$ at a given node of the spatial mesh is approximated in terms of the solution approximation at all the nodes of the interval discretisation. In terms of weights, for i fixed we still have two sequences $(\omega_j)_0^\infty$ that are initially associated with the function approximation at nodes in descending and ascending order (starting from x_{i+1} and x_{i-1}, respectively). However, due to the presence of $[\cdot]_0^N$ in equation (4.16), whenever the sequences reach a boundary node, we can think of them as being "reflected" inside the interval $[0, L]$ and their direction "inverted" so that the weights continue to be associated with the solution approximation at nodes x_k with $k \in \{0, 1, \ldots, N\}$ (see Figure 4.5 for a specific example with $N = 5$ and $i = 3$).

Keeping these considerations in mind we observe that there is a particular relationship between the subsequences of weights associated with each node x_k with $k \in \{0, 1, \ldots, N\}$ in the approximation of $\mathcal{R}^{\alpha}_{x,L} f$ at a given $x = x_i$. Indeed, for a fixed $i \in \{0, 1, \ldots, N\}$, the infinite sum on the right-hand side of equation (4.16) can be rewritten as

$$\sum_{j=0}^{\infty} \omega_j \Big(f_{[i-j+1]_0^N} + f_{[i+j-1]_0^N} \Big) = \sum_{k=0}^{N} M_{ik} f_k,$$

where each M_{ik} is an infinite sum of weights ω_j with indices chosen in suitable

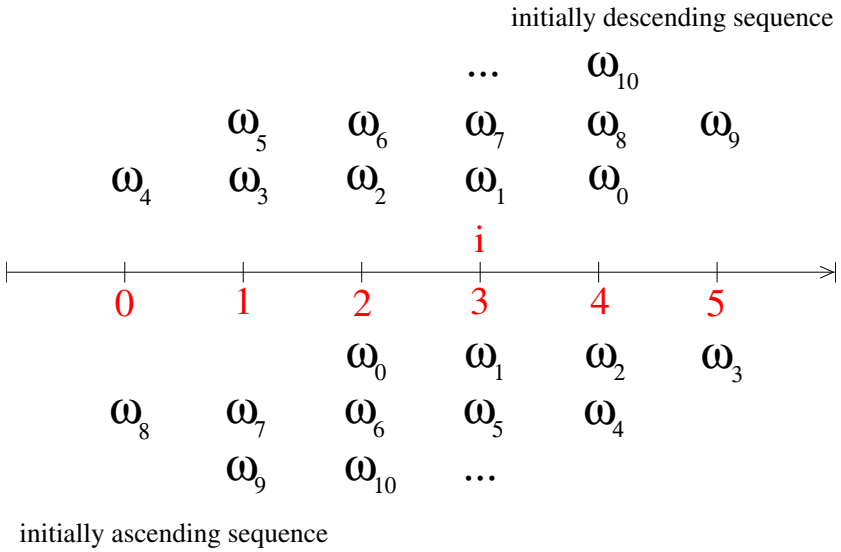

Figure 4.5: *The plot shows how the two sequences of weights* $(\omega_j)_0^\infty$ *are associated with the nodes of a spatial grid (red indices) with* $N = 5$ *in the approximation of* $\mathcal{R}^\alpha_{x,L} f|_{x=x_i}$ *given by equation (4.16) when* $i = 3$.

subsets $W_{i,k} \subset \mathbb{Z}_0^+$ (where $\mathbb{Z}_0^+$ denotes the set of all non-negative integers). In fact, given $i, k \in \{0, 1, \ldots, N\}$,

$$M_{ik} = \sum_{j \in W_{i,k}} \omega_j \quad \text{where} \quad W_{i,k} := \{j \in \mathbb{Z}_0^+ \mid [i+j-1]_0^N = k \text{ or } [i-j+1]_0^N = k\},$$

that is, using the definition of $[\cdot]_0^N$,

$$W_{i,0} = \{j \in \mathbb{Z}_0^+ \mid i + j - 1 = 2mN \text{ or } i - j + 1 = 2mN \text{ for } m \in \mathbb{Z}\},$$

when $k \in \{1, \ldots, N-1\}$,

$$W_{i,k} = \{j \in \mathbb{Z}_0^+ \mid i+j-1 = \pm k+2mN \text{ or } i-j+1 = \pm k+2mN \text{ for } m \in \mathbb{Z}\},$$

and

$$W_{i,N} = \{j \in \mathbb{Z}_0^+ \mid i+j-1 = N+2mN \text{ or } i-j+1 = N+2mN \text{ for } m \in \mathbb{Z}\}.$$

The above relationships can be rewritten in order to obtain an explicit ex-

pression for j in terms of the indices i, k and the integer m. Since we are only interested in expressions resulting in a non-negative integer j (i.e., we want $j \in \mathbb{Z}_0^+$), for i and k given, $i, k \in \{0, 1, \ldots, N\}$, by rearranging the above relationships we can write

$$j = \pm k + 2mN - i + 1 \quad \text{and} \quad j = \pm k + 2mN + i + 1,$$

where we restrict $m \in \mathbb{Z}_0^+$. Note however that if the value of $\pm k - i + 1$ or $\pm k + i + 1$ is negative, we exclude the case $m = 0$ and simply consider $m \in \mathbb{Z}^+$. In other words, we can express each M_{ik} as follows:

$$M_{i0} = \sum_{m=0}^{\infty} \left(\omega_{2Nm-i+1} + \omega_{2Nm+i+1}\right),$$

then for $k = 1, \ldots, N-1$,

$$M_{ik} = \sum_{m=0}^{\infty} \left(\omega_{2Nm+k-i+1} + \omega_{2Nm-k-i+1} + \omega_{2Nm+k+i+1} + \omega_{2Nm-k+i+1}\right),$$

and finally

$$M_{iN} = \sum_{m=0}^{\infty} \left(\omega_{2Nm+N-i+1} + \omega_{2Nm+N+i+1}\right),$$

keeping in mind that when the value of $\pm k - i + 1$ or $\pm k + i + 1$ is negative, we shift all indices in the corresponding sum by $2N$.

Observe that, for i fixed, we have

$$\sum_{k=0}^{N} M_{ik} = 2 \sum_{j=0}^{\infty} \omega_j, \tag{4.17}$$

and using equation (4.12) we conclude that $\sum_{k=0}^{N} M_{ik} = 0$.

In light of all these considerations, if we denote by $\mathbf{f}$ the vector of $N+1$ approximations of $f(x)$ at the $N+1$ nodes of the finite interval $[0, L]$, the spatial

discretisation of $\mathcal{R}^{\alpha}_{x,L}f$ leads to the matrix vector product approximation

$$\mathcal{R}^{\alpha}_{x,L}f \approx \frac{-c_\alpha}{h^\alpha} M\mathbf{f},$$

where h is the uniform mesh size, c_α the usual coefficient and M is the square matrix of size $N+1$ with entries M_{ik} defined above ($i,k \in \{0,1,\ldots,N\}$).

For example, if $N=3$, the subsets $W_{i,k}$ can be written as

$$W_{i,k} = \{j \in \mathbb{Z}_0^+ \mid j = 6m \pm k - i + 1 \text{ or } j = 6m \pm k + i + 1 \text{ with } m \in \mathbb{Z}_0^+\}.$$

Consequently, the entries of the 4×4 matrix M of weights corresponding to this particular case ($N=3$) only involve six (in general $2N$) subseries of the sequence of weights[3]. In order to simplify the notation, let us define the above-mentioned six subseries of weights as

$$\begin{aligned} a &:= \sum_{m=0}^{\infty} \omega_{6m}, & b &:= \sum_{m=0}^{\infty} \omega_{6m+1}, & c &:= \sum_{m=0}^{\infty} \omega_{6m+2}, \\ d &:= \sum_{m=0}^{\infty} \omega_{6m+3}, & e &:= \sum_{m=0}^{\infty} \omega_{6m+4}, & f &:= \sum_{m=0}^{\infty} \omega_{6m+5}, \end{aligned} \tag{4.18}$$

then the 4×4 matrix M of weights can be written as follows:

$$M = \begin{bmatrix} 2b & 2(a+c) & 2(d+f) & 2e \\ a+c & 2b+d+f & a+c+2e & d+f \\ d+f & a+c+2e & 2b+d+f & a+c \\ 2e & 2(d+f) & 2(a+c) & 2b \end{bmatrix}. \tag{4.19}$$

We conclude this section by noting that in the particular case $\alpha = 2$, the only non-zero weights in the sequences $(\omega_j)_0^\infty$ are $\omega_0 = 1$, $\omega_1 = -2$ and $\omega_2 = 1$. Furthermore, the coefficient $c_\alpha = \frac{1}{2\cos(\pi\alpha/2)}$ reduces to $c_\alpha = -1/2$ and as a

[3]As we shall see in greater detail in the next section, these subseries of weights correspond to the shifts $r = 0, 1, 2, \ldots, 2N-1$ in the index j of the sequence of weights.

result the matrix $\frac{-c_\alpha}{h^\alpha}M$ becomes

$$\frac{-c_\alpha}{h^\alpha}M = \frac{1}{h^2}\begin{bmatrix} -2 & 2 & & & & \\ 1 & -2 & 1 & & & \\ & \ddots & \ddots & \ddots & & \\ & & & 1 & -2 & 1 \\ & & & & 2 & -2 \end{bmatrix}. \tag{4.20}$$

Therefore, when $\alpha = 2$, the discretisation matrix obtained with the reflection approach corresponds to the finite-difference approximation of the operator $-(-\Delta)$ on $[0, L]$ coupled with homogeneous Neumann boundary conditions, obtained when the spatial interval is discretised with a uniform mesh of $N+1$ nodes with spacing $h = \frac{L}{N}$ and a second order approximation of the first order derivative is considered at the boundary points, as shown in equation (2.38).

4.3 Spectral decomposition of the discrete reflection operator

Let us now define the matrix $A_\alpha := \frac{c_\alpha}{h^\alpha}M$ for $\alpha \in (1, 2]$, that is, the matrix obtained from the spatial discretisation of the operator $-\mathcal{R}^\alpha_{x,L}$. We observe that A_α is always diagonally dominant and its sign has been chosen so that its diagonal entries are always non-negative[4]. In this section we provide an analytical formulation of the eigenvalues and eigenvectors of the matrix A_α of arbitrary size $N + 1$ given by the number of points used in the finite-difference spatial discretisation of $[0, L]$. A fundamental result found in the literature on the summation of subseries in closed form and a number of well-established properties of trigonometric functions are here introduced in the form of lemmas or remarks and then used to prove the main theorem of the section. The spectral decomposition in the particular case $\alpha = 2$ follows

[4]In fact, the only negative weight in each sequence $(\omega_j)_0^\infty$ is ω_1 and it appears only in the sequences on the main diagonal of M. We also know that $\sum_{j=0}^{\infty}\omega_j = 0$ but in each diagonal entry of M we are only summing over a subset of indices and therefore we always obtain a negative quantity. Since $h^\alpha > 0$ and $c_\alpha < 0$, we then obtain the required property for A_α.

as a corollary of our main theorem.

Note on notation. In previous sections of this chapter (and in the rest of the thesis), we normally use the letter i to refer to a given node x_i of our one-dimensional spatial discretisation. In this section however we prefer to use the letter i to denote the imaginary unit when dealing with complex numbers and to use the index p in order to refer to a particular node of the mesh, avoiding the use of confusing notation.

Theorem 1. ***[Eigenvalues and eigenvectors of the reflection matrix]*** *Let us consider a uniform spatial discretisation of the finite interval $[0, L]$ with $N+1$ nodes $x_p = p\,h$ for $p = 0, 1, \ldots, N$ and spacing $h = \frac{L}{N}$. Let $\alpha \in (1, 2]$ and let A_α be the matrix of reflections obtained with finite-difference approximation of the reflection operator $-\mathcal{R}^\alpha_{x,L}$ with the modified shifted Grünwald–Letnikov approach (as described in the previous section). The analytic form of the $N+1$ eigenvalues μ_j of A_α is then given by*

$$\mu_j = \frac{\left(2\sin\left(\frac{j\pi}{2N}\right)\right)^\alpha}{h^\alpha \cos\left(\alpha\pi/2\right)} \cos\left(\frac{2j + \alpha(N-j)}{2N}\pi\right) \quad \textit{for } j = 0, 1, \ldots, N. \tag{4.21}$$

The corresponding $N+1$ eigenvectors φ_j can be described in terms of their components $\varphi_j^{(p)}$ as follows:

$$\varphi_j^{(p)} = \varphi_j^{(0)} \cos\left(\frac{jp\pi}{N}\right), \quad \textit{for } p = 0, 1, \ldots, N, \tag{4.22}$$

where $\varphi_j^{(0)}$ is a normalisation constant, that is, a constant defined so that $||\varphi_j||_2 = 1$ for all j (where $||\cdot||_2$ denotes the Euclidean norm). In particular,

$$\varphi_j^{(0)} = \begin{cases} \dfrac{1}{\sqrt{N+1}} & \textit{if } j = 0 \textit{ or } j = N, \\ \\ \sqrt{\dfrac{2}{N+2}} & \textit{if } j = 1, 2, \ldots, N-1. \end{cases} \tag{4.23}$$

The spectral decomposition of the reflection operator in the particular case $\alpha = 2$ follows as a corollary.

Corollary 1. *When $\alpha = 2$, the eigenvalues of A_α reduce to*

$$\mu_j = \frac{4}{h^2} \sin^2 \left(\frac{j\pi}{2N} \right) \quad \textit{for } j = 0, 1, \ldots, N. \tag{4.24}$$

Proof. Simply evaluate the expression of the eigenvalues μ_j given by equation (4.21) in the particular case $\alpha = 2$. □

Therefore, as pointed out at the end of Section 4.2, if $\alpha = 2$ we recover the eigenvalues of the square matrix of size $N + 1$ obtained from a finite-difference approximation of the standard Laplacian $(-\Delta)$ on $[0, L]$ coupled with homogeneous Neumann boundary conditions when the spatial interval is discretised with a uniform mesh of $N+1$ nodes with spacing $h = \frac{L}{N}$ and a second order approximation of the first order derivative is considered at both boundary points.

Some preliminary results

In order to simplify the proof of Theorem 1, we now introduce some preliminary lemmas and considerations on the various elements involved in the proof. The first result reported here is a theorem by Chen [17] addressing the following question: let $g(x) = \sum_{m=0}^{\infty} a_m x^m$. Consider a subseries of g, say

$$g_1(x) := \sum_{m \in \mathbb{N}_1} a_m x^m,$$

where $\mathbb{N}_1 \subset \mathbb{N}$ with $\mathbb{N}_1 \neq \emptyset$ and $\mathbb{N}_1 \neq \mathbb{N}$ ($\mathbb{N}$ here is considered inclusive of zero, that is, $\mathbb{N}$ is the set of all non-negative integers). Is there a closed-form expression for the function $g_1(x)$? In [17] we find the following result:

Lemma 1. *Let n be a positive integer and let $z = e^{i\frac{2\pi}{n}}$ be a primitive n-th root of unity. If $g(x) = \sum_{j=0}^{\infty} a_j \, x^j$, then for any integer r, we have*

$$\sum_{j \equiv r \mod n} a_j \, x^j = a_r x^r + a_{r+n} x^{r+n} + \cdots = \frac{1}{n} \sum_{l=0}^{n-1} z^{-lr} \, g(z^l x).$$

Proof. See Chen [17]. □

Observation of the entries of the reflection matrix A_α reveals that the quantities denoted by M_{ik} in the previous section are sums of subseries of the sequence of weights where the indices considered are all equivalent to a certain integer[5] $r \mod 2N$, that is, sums of the form

$$\sum_{m=0}^{\infty} \omega_{2Nm+r} = \sum_{m=0}^{\infty} \binom{\alpha}{2Nm+r} (-1)^{2Nm+r} = \sum_{j \equiv r \mod 2N} \binom{\alpha}{j} (-1)^j,$$

with $r = 0, 1, 2, \ldots, 2N-1$. Therefore, we can apply Lemma 1 with the function $g(x)$ given by

$$g(x) = (1+x)^\alpha = \sum_{j=0}^{\infty} \binom{\alpha}{j} x^j, \tag{4.25}$$

evaluated at $x = -1$, given that $\mathrm{Re}(\alpha) > 0$ ensures convergence of the series (4.25). We hence obtain the following result.

Lemma 2. *Let N be an arbitrary positive integer and for $\alpha \in (1, 2]$ let us consider the sequence $(\omega_j)_0^\infty$ with elements defined by $\omega_j := \binom{\alpha}{j} (-1)^j$, for all j. For $r = 0, 1, 2, \ldots, 2N-1$, let $g_r := \sum_{m=0}^{\infty} \omega_{2Nm+r}$. Then, g_r can be expressed as*

$$g_r = \frac{1}{2N} \sum_{l=0}^{2N-1} e^{-i\frac{lr\pi}{N}} \left(1 - e^{i\frac{l\pi}{N}}\right)^\alpha. \tag{4.26}$$

Proof. Direct consequence of Lemma 1 applied with $n = 2N$, $g(x)$ given by equation (4.25) and evaluated at $x = -1$. □

Note that due to the particular form of the function g considered here, when $l = 0$,

$$\left(1 - e^{i\frac{l\pi}{N}}\right)^\alpha = (1-1)^\alpha = 0.$$

[5] In the notation used in Section 4.2, $r = \pm k - i + 1$ or $r = \pm k + i + 1$, with i referring to the particular row of the matrix of weights considered and k the index referring to the column. Remember that when the value of $r = \pm k - i + 1$ or $r = \pm k + i + 1$ is negative, we interpret it as shifted by $2N$ so that the corresponding index j of the sequence of weights ω_j is still non-negative. Note however that this does not affect the conclusions made in this section because in modular arithmetic the shift $2N$ is congruent to $0 \mod 2N$.

Therefore, g_r can be computed by simply summing over values of the index $l \in \{1, 2, \ldots, 2N-1\}$.

We now provide a list summarising some important trigonometric properties that will play a fundamental role in the proof of the following results and of Theorem 1.

Some trigonometric properties. Other than basic properties of sine and cosine functions and the well-known expressions for sine and cosine of a sum (or difference) of angles, we will use the following properties:

P.1 Given $j \in \{0, 1, \ldots, N\}$, for all k,

$$\cos\left(\frac{jk\pi}{N}\right) = \begin{cases} +\cos\left(\dfrac{j(N-k)\pi}{N}\right) & \text{if } j \text{ is even,} \\ -\cos\left(\dfrac{j(N-k)\pi}{N}\right) & \text{if } j \text{ is odd,} \end{cases}$$

due to the symmetry (antisymmetry) of the cosine function on intervals of length $j\pi$ for j even (odd).

P.2 Given $j \in \{0, 1, \ldots, N\}$, for all l,

$$\cos\left(\frac{jl\pi}{N}\right) = \cos\left(\frac{j(2N-l)\pi}{N}\right),$$

and

$$\sin\left(\frac{jl\pi}{N}\right) = -\sin\left(\frac{j(2N-l)\pi}{N}\right),$$

due to the symmetry of the cosine function and the antisymmetry of the sine function on intervals of length multiple of 2π.

P.3 When $l \in \mathbb{Z}$,

$$e^{il\pi} = e^{-il\pi} = \begin{cases} +1 & \text{if } l \text{ is even,} \\ -1 & \text{if } l \text{ is odd.} \end{cases}$$

P.4 For all θ, $e^{-i\theta} + e^{i\theta} = 2\cos(\theta)$.

P.5 For all $\theta \neq j\pi$ with $j \in \mathbb{Z}$, $\cot(\theta) = \tan\left(\frac{\pi}{2} - \theta\right)$.

P.6 For all θ, $\sin(2\theta) = 2\sin(\theta)\cos(\theta)$.

P.7 For all θ, $\cos(2\theta) = 1 - 2\sin^2(\theta) = 2\cos^2(\theta) - 1$.

We now introduce a definition generalising De Moivre's formula that will be used to compute non-integer powers of complex numbers.

Definition 1. ***[Generalisation of De Moivre's formula]*** *Let $z \in \mathbb{C}$, $z = a + ib$. Then*

$$z^\alpha := R^\alpha e^{i\alpha\theta},$$

where $R = |z| = \sqrt{a^2 + b^2}$ is the modulus of z and $\theta = Arg(z) \in (-\pi, \pi]$ is its principal argument.

In particular, in what follows we will use the fact that

$$\mathrm{Arg}(a + ib) = \begin{cases} \arctan\left(\dfrac{b}{a}\right) & \text{if } a > 0, b > 0, \\ \\ -\arctan\left(\dfrac{|b|}{a}\right) & \text{if } a > 0, b < 0. \end{cases}$$

In light of Definition 1, the following two lemmas provide an explicit expression of the power z^α for complex numbers z expressed in a particular form and will be used later in the main proof.

Lemma 3. *Let N be an arbitrary positive integer and let z be the complex number $z = 1 - e^{i\frac{l\pi}{N}}$ with $l \in \{1, 2, \ldots, N\}$. Then*

$$z^\alpha = \left(2\sin\left(\frac{l\pi}{2N}\right)\right)^\alpha e^{-i\frac{\alpha(N-l)\pi}{2N}}. \tag{4.27}$$

Proof. If $l = N$, z simply becomes $z = 1 - e^{i\pi} = 2$. Hence, $z^\alpha = 2^\alpha$, that corresponds to the value of expression (4.27) when $l = N$. When $l < N$, z

can be written as $z = a + ib$ with

$$a = 1 - \cos\left(\frac{l\pi}{N}\right) > 0 \quad \text{and} \quad b = -\sin\left(\frac{l\pi}{N}\right) < 0.$$

Using the above definition, $z^\alpha := R^\alpha e^{i\alpha\theta}$, where $R = |z| = \sqrt{a^2 + b^2}$ and $\theta = \text{Arg}(z)$. In this particular case, with simple algebraic calculations and thanks to property **P.7**, we find

$$\begin{aligned} R &= \left[\left(1 - \cos\left(\tfrac{l\pi}{N}\right)\right)^2 + \left(-\sin\left(\tfrac{l\pi}{N}\right)\right)^2\right]^{1/2} \\ &= \left[2 - 2\cos\left(\tfrac{l\pi}{N}\right)\right]^{1/2} \\ &= \left[4\sin^2\left(\tfrac{l\pi}{2N}\right)\right]^{1/2} \\ &= 2\sin\left(\tfrac{l\pi}{2N}\right). \end{aligned}$$

On the other hand, to compute the principal argument θ we use the fact that for $a > 0$ and $b < 0$,

$$\theta = -\arctan\left(\frac{|b|}{a}\right) = -\arctan\left(\frac{\sin\left(\frac{l\pi}{N}\right)}{1 - \cos\left(\frac{l\pi}{N}\right)}\right).$$

Using properties **P.6** and **P.7** we can rewrite the ratio $\frac{|b|}{a}$ as $\cot\left(\frac{l\pi}{2N}\right)$ and using property **P.5** we see that

$$\theta = -\arctan\left(\cot\left(\frac{l\pi}{2N}\right)\right) = -\arctan\left(\tan\left(\frac{\pi}{2} - \frac{l\pi}{2N}\right)\right) = -\frac{(N-l)\pi}{2N}.$$

Therefore, we can conclude that also when $l = 1, 2, \ldots, N-1$,

$$z^\alpha = \left(2\sin\left(\frac{l\pi}{2N}\right)\right)^\alpha e^{-i\frac{\alpha(N-l)\pi}{2N}}.$$

□

Lemma 4. *Let N be an arbitrary positive integer and z the complex number $z = 1 - e^{i\frac{(2N-l)\pi}{N}}$ with $l \in \{1, 2, \ldots, N-1\}$. Then*

$$z^\alpha = \left(2\sin\left(\frac{l\pi}{2N}\right)\right)^\alpha e^{i\frac{\alpha(N-l)\pi}{2N}}.$$

Proof. By exploiting property **P.2** with $j = 1$, z can be written as $z = a + ib$ with

$$a = 1 - \cos\left(\frac{l\pi}{N}\right) > 0 \quad \text{and} \quad b = \sin\left(\frac{l\pi}{N}\right) > 0.$$

By applying the same strategy used for the proof of Lemma 3, we obtain that the modulus R of z is once again $R = 2\sin\left(\frac{l\pi}{2N}\right)$, whereas the principal argument θ is now computed using the fact that for $a > 0$ and $b > 0$,

$$\theta = \arctan\left(\frac{b}{a}\right) = \arctan\left(\frac{\sin\left(\frac{l\pi}{N}\right)}{1 - \cos\left(\frac{l\pi}{N}\right)}\right) = \frac{(N-l)\pi}{2N}.$$

□

We now introduce the function $\psi : \mathbb{Z} \to \{0, 1\}$ defined as follows:

$$\psi(j) = \begin{cases} 0 & \text{if } j \text{ is even,} \\ 1 & \text{if } j \text{ is odd.} \end{cases} \tag{4.28}$$

This function will be used in the proof of Theorem 1 to compare the even/odd character of two given indices. In particular, we see that $\psi(j) = \psi(l)$ if the indices j and l are either both even or both odd. Otherwise, $\psi(j) \neq \psi(l)$.

We conclude our list of preliminary results with the following lemma (known in the literature as one of Lagrange's trigonometric identities), providing a simple expression for a finite sum of cosine functions evaluated at integer multiples of the same angle.

Lemma 5. ***[Lagrange's trigonometric identity]*** *Let $\theta \in (0, 2\pi)$, then given a positive integer K,*

$$\sum_{k=1}^{K} \cos(k\theta) = -\frac{1}{2} + \frac{\sin\left(\left(K + \frac{1}{2}\right)\theta\right)}{2\sin\left(\frac{\theta}{2}\right)}. \tag{4.29}$$

Proof. Let us consider the complex number z defined as the following sum:

$$z = 1 + e^{i\theta} + e^{i2\theta} + \cdots + e^{iK\theta}.$$

Using the well-known result on the sum of the first $K+1$ terms of a geometric series we obtain

$$z = \frac{e^{i(K+1)\theta} - 1}{e^{i\theta} - 1}.$$

Factorising the denominator as $e^{i\theta/2}(e^{i\theta/2} - e^{-i\theta/2})$ we see that

$$z = \frac{\left(e^{i(K+1)\theta} - 1\right) e^{-i\theta/2}}{2i\sin(\theta/2)} = \frac{e^{i(K+1/2)\theta} - e^{-i\theta/2}}{2i\sin(\theta/2)}.$$

Multiplying both the numerator and the denominator by i we finally find

$$z = \frac{\sin\left(\left(K + \frac{1}{2}\right)\theta\right) + \sin\left(\frac{\theta}{2}\right) - i\left[\cos\left(\left(K + \frac{1}{2}\right)\theta\right) - \cos\left(\frac{\theta}{2}\right)\right]}{2\sin\left(\frac{\theta}{2}\right)}.$$

By observing that $\mathrm{Re}(z) = \frac{1}{2} + \frac{\sin((K+1/2)\theta)}{2\sin(\theta/2)}$ and $\sum_{k=1}^{K}\cos(k\theta) = \mathrm{Re}(z) - 1$, we can hence conclude that

$$\sum_{k=1}^{K} \cos(k\theta) = -\frac{1}{2} + \frac{\sin\left(\left(K + \frac{1}{2}\right)\theta\right)}{2\sin\left(\frac{\theta}{2}\right)}.$$

□

4.3.1 The proof of our main result

We now proceed by proving Theorem 1.

Proof. Our aim is to show that, for all $j \in \{0, 1, \ldots, N\}$, $A_\alpha \varphi_j = \mu_j \varphi_j$, where

μ_j is defined by equation (4.21) and φ_j is defined as in (4.22). Therefore, if $A_\alpha^{(p)}$ denotes the $(p+1)$-th row of the matrix A_α and $\varphi_j^{(p)}$ the $(p+1)$-th component of the vector φ_j, we must verify that for $p = 0, 1, \ldots, N$,

$$A_\alpha^{(p)} \varphi_j = \mu_j \varphi_j^{(p)}. \tag{4.30}$$

Let us start by considering the case $j = 0$. When $j = 0$, from equations (4.21) and (4.22) we obtain $\mu_0 = 0$ and $\varphi_0 = \frac{1}{\sqrt{N+1}}\,\mathbf{e}$, where $\mathbf{e}$ is the unit vector of $N+1$ components, that is, $\mathbf{e} = [1, 1, \ldots, 1]^T$. We can then simply show that $A_\alpha^{(p)} \varphi_0 = 0$ for all $p \in \{0, 1, \ldots, N\}$. Note that, since φ_0 is a constant vector, $A_\alpha^{(p)} \varphi_0$ can be rewritten as

$$A_\alpha^{(p)} \varphi_0 = \frac{c_\alpha}{h^\alpha \sqrt{N+1}} \sum_{k=0}^{N} M_{pk},$$

where (as in Section 4.2) $c_\alpha = \frac{1}{2\cos(\alpha\pi/2)}$. Using equation (4.17) and the fact that the sum of all weights of the sequence $(\omega_j)_0^\infty$ is equal to zero, that is, $\sum_{j=0}^{\infty} \omega_j = 0$, we find that $A_\alpha^{(p)} \varphi_0 = 0$ and can conclude that $\mu_0 = 0$ and $\varphi_0 = \frac{1}{\sqrt{N+1}}\,\mathbf{e}$ form an eigenpair for the matrix A_α.

Let us now consider the case $j \in \{1, 2, \ldots, N\}$. For a given $p \in \{0, 1, \ldots, N\}$, using the explicit form of the entries of the row $A_\alpha^{(p)}$, the analytic expression of the eigenvalue μ_j and of the components of the eigenvector φ_j, the left-hand side and the right-hand side of equation (4.30) can be rewritten as

$$A_\alpha^{(p)} \varphi_j = \frac{1}{2h^\alpha \cos(\alpha\pi/2)} \sum_{k=0}^{N} M_{pk}\ \varphi_j^{(0)} \cos\left(\frac{jk\pi}{N}\right)$$

and

$$\mu_j \varphi_j^{(p)} = \frac{\left(2\sin\left(\frac{j\pi}{2N}\right)\right)^\alpha}{h^\alpha \cos(\alpha\pi/2)} \cos\left(\frac{2j + \alpha(N-j)}{2N}\pi\right) \varphi_j^{(0)} \cos\left(\frac{jp\pi}{N}\right),$$

respectively. Proving that $A_\alpha^{(p)} \varphi_j = \mu_j \varphi_j^{(p)}$ can then be simplified by multiplying each side of the equation by the non-zero term $h^\alpha \cos(\alpha\pi/2)$ and

dividing each side by $\varphi_j^{(0)}$. Our proof hence reduces to showing that the following result holds for $p = 0, 1, \ldots, N$:

$$\sum_{k=0}^{N} M_{pk} \cos\left(\frac{jk\pi}{N}\right) = 2\left(2\sin\left(\frac{j\pi}{2N}\right)\right)^{\alpha} \cos\left(\frac{2j + \alpha(N-j)}{2N}\pi\right) \cos\left(\frac{jp\pi}{N}\right). \tag{4.31}$$

For a given $j \in \{1, 2, \ldots, N\}$ and $p \in \{0, 1, \ldots, N\}$, we now focus on the sum

$$\sum_{k=0}^{N} M_{pk} \cos\left(\frac{jk\pi}{N}\right), \tag{4.32}$$

and show that it can be rewritten as the expression provided on the right-hand side of equation (4.31).

Using property **P.1**, we combine the terms of the sum (4.32) that have the same absolute value of the cosine function, that is, the term with a given index k and the corresponding one with index $N - k$. In doing so, we must distinguish between three different cases:

I If $N + 1$ is even, then the sum (4.32) consists of an even number of terms and using property **P.1** it can be rewritten as

$$\sum_{k=0}^{\frac{N-1}{2}} \left(M_{pk} \pm M_{p(N-k)}\right) \cos\left(\frac{jk\pi}{N}\right), \tag{4.33}$$

where the sign depends on j being even $(+)$ or odd $(-)$.

II If $N+1$ is odd, then we have an odd number of terms in the sum (4.32) and hence the term corresponding to the index $N/2$, that is, $M_{pN/2} \cos\left(\frac{j\pi}{2}\right)$, must be considered separately. However, we see that

IIa if j is odd, $\cos\left(\frac{j\pi}{2}\right) = 0$ and the sum (4.32) becomes

$$\sum_{k=0}^{\frac{N-2}{2}} \left(M_{pk} - M_{p(N-k)}\right) \cos\left(\frac{jk\pi}{N}\right); \tag{4.34}$$

IIb if j is even,

$$\cos\left(\frac{j\pi}{2}\right) = \begin{cases} +1 & \text{if } j/2 \text{ is still even,} \\ -1 & \text{if } j/2 \text{ is odd.} \end{cases}$$

Therefore, in this case we rewrite the sum (4.32) as

$$\sum_{k=0}^{\frac{N-2}{2}} \left(M_{pk} + M_{p(N-k)}\right) \cos\left(\frac{jk\pi}{N}\right) \pm M_{pN/2}, \tag{4.35}$$

where the sign of the last term depends on $j/2$ being even $(+)$ or odd $(-)$.

Let $g_r := \sum_{m=0}^{\infty} \omega_{2Nm+r}$. When $k = 0$, $\cos\left(\frac{jk\pi}{N}\right) = 1$ and using the expression of the entries of the matrix of weights M given in the previous section, we observe that

$$M_{p0} \pm M_{pN} = g_{-p+1} + g_{p+1} \pm (g_{N-p+1} + g_{N+p+1}).$$

Applying Corollary 2, we then write

$$M_{p0} \pm M_{pN} = \frac{1}{2N} \sum_{l=1}^{2N-1} G_l^{(0)} \left(1 - e^{i\frac{l\pi}{N}}\right)^{\alpha},$$

where

$$G_l^{(0)} := e^{-i\frac{l(-p+1)\pi}{N}} + e^{-i\frac{l(p+1)\pi}{N}} \pm \left(e^{-i\frac{l(N-p+1)\pi}{N}} + e^{-i\frac{l(N+p+1)\pi}{N}}\right).$$

$G_l^{(0)}$ in turn can be rewritten as

$$G_l^{(0)} = e^{-i\frac{l\pi}{N}} \left(e^{i\frac{lp\pi}{N}} + e^{-i\frac{lp\pi}{N}}\right) \left(1 \pm e^{-il\pi}\right).$$

Using property **P.4**, we see that $e^{i\frac{lp\pi}{N}} + e^{-i\frac{lp\pi}{N}} = 2\cos\left(\frac{lp\pi}{N}\right)$. Moreover, using

property **P.3** and the definition of the function ψ given by (4.28), we obtain

$$1 \pm e^{-il\pi} = \begin{cases} 2 & \text{if } \psi(l) = \psi(j), \\ 0 & \text{otherwise.} \end{cases}$$

Therefore,

$$M_{p0} \pm M_{pN} = \frac{1}{2N} \sum_{\substack{l=1 \\ \psi(l)=\psi(j)}}^{2N-1} e^{-i\frac{l\pi}{N}} \left(1 - e^{i\frac{l\pi}{N}}\right)^{\alpha} 4\cos\left(\frac{lp\pi}{N}\right). \tag{4.36}$$

Similar considerations are made when $k > 0$, in order to rewrite the terms $(M_{pk} \pm M_{p(N-k)})\cos\left(\frac{jk\pi}{N}\right)$. In fact,

$$\begin{aligned} M_{pk} \pm M_{p(N-k)} &= g_{k-p+1} + g_{-k-p+1} + g_{k+p+1} + g_{-k+p+1} \\ &\pm (g_{N-k-p+1} + g_{-N+k-p+1} + g_{N-k+p+1} + g_{-N+k+p+1}), \end{aligned}$$

and applying Corollary 2, we see that

$$M_{pk} \pm M_{p(N-k)} = \frac{1}{2N} \sum_{l=1}^{2N-1} G_l^{(k)} \left(1 - e^{i\frac{l\pi}{N}}\right)^{\alpha},$$

where

$$\begin{aligned} G_l^{(k)} &:= e^{-i\frac{l(k-p+1)\pi}{N}} + e^{-i\frac{l(-k-p+1)\pi}{N}} + e^{-i\frac{l(k+p+1)\pi}{N}} + e^{-i\frac{l(-k+p+1)\pi}{N}} \\ &\pm \left(e^{-i\frac{l(N-k-p+1)\pi}{N}} + e^{-i\frac{l(-N+k-p+1)\pi}{N}} + e^{-i\frac{l(N-k+p+1)\pi}{N}} + e^{-i\frac{l(-N+k+p+1)\pi}{N}}\right). \end{aligned}$$

Once again by using property **P.3**, property **P.4** and the definition of ψ, we find that $G_l^{(k)}$ becomes

$$G_l^{(k)} = \begin{cases} e^{-i\frac{l\pi}{N}}\ 8\ \cos\left(\frac{lk\pi}{N}\right)\cos\left(\frac{lp\pi}{N}\right) & \text{if } \psi(l) = \psi(j), \\ 0 & \text{otherwise.} \end{cases}$$

Therefore, when $k = 1, \ldots, \frac{N-1}{2}$ in case **I** or $k = 1, \ldots, \frac{N-2}{2}$ in case **IIa**, then

$(M_{pk} \pm M_{p(N-k)}) \cos\left(\frac{jk\pi}{N}\right)$ becomes

$$\frac{1}{2N} \sum_{\substack{l=1 \\ \psi(l)=\psi(j)}}^{2N-1} e^{-i\frac{l\pi}{N}} \left(1 - e^{i\frac{l\pi}{N}}\right)^{\alpha} 8 \cos\left(\frac{lk\pi}{N}\right) \cos\left(\frac{lp\pi}{N}\right) \cos\left(\frac{jk\pi}{N}\right). \quad (4.37)$$

In case **IIb**, that is, when $N+1$ is odd and j is even, we must add to the sum the term $\pm M_{pN/2}$, with sign depending on $j/2$ being even $(+)$ or odd $(-)$.

$$\pm M_{pN/2} = \pm(g_{N/2-p+1} + g_{-N/2-p+1} + g_{N/2+p+1} + g_{-N/2+p+1}),$$

and using Corollary 2 we obtain

$$\pm M_{pN/2} = \frac{1}{2N} \sum_{l=1}^{2N-1} G_l^{(N/2)} \left(1 - e^{i\frac{l\pi}{N}}\right)^{\alpha},$$

where

$$G_l^{(N/2)} := \pm \left(e^{-i\frac{l(N/2-p+1)\pi}{N}} + e^{-i\frac{l(-N/2-p+1)\pi}{N}} + e^{-i\frac{l(N/2+p+1)\pi}{N}} + e^{-i\frac{l(-N/2+p+1)\pi}{N}}\right).$$

Using property **P.4**, we rewrite $G_l^{(N/2)}$ as

$$G_l^{(N/2)} = \pm 4 \cos\left(\frac{l\pi}{2}\right) \cos\left(\frac{lp\pi}{N}\right) e^{-i\frac{l\pi}{N}}.$$

Recalling that in the case **IIb** j is even by assumption and noting that

$$\cos\left(\frac{l\pi}{2}\right) = \begin{cases} 0 & \text{if } l \text{ is odd,} \\ +1 & \text{if } l \text{ is even and } l/2 \text{ is even,} \\ -1 & \text{if } l \text{ is even and } l/2 \text{ is odd,} \end{cases}$$

we can then conclude that

$$\pm M_{pN/2} = \frac{1}{2N} \sum_{\substack{l=1 \\ \psi(l)=\psi(j)}}^{2N-1} e^{-i\frac{l\pi}{N}} \left(1 - e^{i\frac{l\pi}{N}}\right)^{\alpha} \left(\pm 4 \cos\left(\frac{lp\pi}{N}\right)\right), \quad (4.38)$$

where the sign of the last factor is positive when $\psi(l/2) = \psi(j/2)$ and negative otherwise.

Putting together all previous results (given by (4.36), (4.37) and (4.38)) we hence obtain that for a given $j \in \{1, 2, \ldots, N\}$ and a given $p \in \{0, 1, \ldots, N\}$,

$$\sum_{k=0}^{N} M_{pk} \cos\left(\frac{jk\pi}{N}\right) = \frac{1}{2N} \sum_{l \in T_j} e^{-i\frac{l\pi}{N}} \left(1 - e^{i\frac{l\pi}{N}}\right)^{\alpha} \phi(N, j, p, l), \tag{4.39}$$

where T_j is the set of indices

$$T_j = \{l \in \{1, 2, \ldots, 2N-1\} \mid \psi(l) = \psi(j)\},$$

and the expression of $\phi(N, j, p, l)$ depends on the particular case considered:

- in case **I**,

$$\phi(N, j, p, l) = \left[4 + 8 \sum_{k=1}^{\frac{N-1}{2}} \cos\left(\frac{lk\pi}{N}\right) \cos\left(\frac{jk\pi}{N}\right)\right] \cos\left(\frac{lp\pi}{N}\right);$$

- in case **IIa**,

$$\phi(N, j, p, l) = \left[4 + 8 \sum_{k=1}^{\frac{N-2}{2}} \cos\left(\frac{lk\pi}{N}\right) \cos\left(\frac{jk\pi}{N}\right)\right] \cos\left(\frac{lp\pi}{N}\right);$$

- in case **IIb**,

$$\phi(N, j, p, l) = \left[4 + 8 \sum_{k=1}^{\frac{N-2}{2}} \cos\left(\frac{lk\pi}{N}\right) \cos\left(\frac{jk\pi}{N}\right) \pm 4\right] \cos\left(\frac{lp\pi}{N}\right),$$

  where the sign of the term ± 4 is positive when $\psi(l/2) = \psi(j/2)$ and negative otherwise.

Note that for $l = 1, 2, \ldots, N-1$, $\psi(2N - l) = \psi(l)$. Therefore, if $l \in T_j$, then $2N - l \in T_j$ as well. If in the sum on the right-hand side of equation (4.39)

we add the terms corresponding to these two indices, that is, the one with a given $l \in T_j$, $l < N$, and the one with index $2N - l$, and if we let U_l be this sum, then U_l becomes

$$\begin{aligned} U_l &= e^{-i\frac{l\pi}{N}}\left(1 - e^{i\frac{l\pi}{N}}\right)^{\alpha}\phi(N, j, p, l) + \\ & \quad e^{-i\frac{(2N-l)\pi}{N}}\left(1 - e^{i\frac{(2N-l)\pi}{N}}\right)^{\alpha}\phi(N, j, p, 2N - l). \end{aligned} \tag{4.40}$$

Let R_l denote the modulus of the complex number $z = 1 - e^{i\frac{l\pi}{N}}$. Using the results given by Lemma 3, Lemma 4 and the property **P.2**, we see that $R_l = 2\sin\left(\frac{l\pi}{2N}\right)$, that $\phi(N, j, p, 2N - l) = \phi(N, j, p, l)$ independently from the particular form of the function ϕ, and that the sum (4.40) can be written as

$$U_l = R_l^{\alpha}\left[e^{-i\frac{l\pi}{N}}e^{-i\frac{\alpha(N-l)\pi}{2N}} + e^{i\frac{l\pi}{N}}e^{i\frac{\alpha(N-l)\pi}{2N}}\right]\phi(N, j, p, l). \tag{4.41}$$

Applying property **P.4** on the term between square brackets in (4.41), this becomes

$$U_l = R_l^{\alpha}\ 2\cos\left(\frac{2l + \alpha(N - l)}{2N}\pi\right)\ \phi(N, j, p, l).$$

When $\psi(N) = \psi(j)$, the index $l = N$ also appears in the sum on the right-hand side of equation (4.39). However, since $2N - N = N$, in order to avoid counting the index $l = N$ twice, this case is considered separately. If $l = N \in T_j$, using property **P.3** the corresponding term in the sum on the right-hand side of equation (4.39) (here labelled U_N) simply reduces to

$$U_N = (-1)\ 2^{\alpha}\ \phi(N, j, p, N),$$

where the factors -1 and 2^{α} are actually equal to $\cos\left(\frac{2l+\alpha(N-l)}{2N}\pi\right)$ and R_l^{α} in the particular case $l = N$, respectively.

In light of the above considerations we can rewrite the right-hand side of

equation (4.39) as

$$\frac{1}{2N}\left[\sum_{\substack{l=1\\ l\in T_j}}^{N-1} 2R_l^{\alpha}\cos\left(\frac{2l+\alpha(N-l)}{2N}\pi\right)\ \phi(N,j,p,l)+C(N,j)\right], \qquad (4.42)$$

where $C(N,j)$ is defined as follows:

$$C(N,j)=\begin{cases} -2^{\alpha}\ \phi(N,j,p,N) & \text{if } \psi(N)=\psi(j),\\ 0 & \text{otherwise.}\end{cases}$$

In order to conclude the proof of the theorem and show that for all values of $p\in\{0,1,\ldots,N\}$ expression (4.42) reduces to

$$2\left(2\sin\left(\frac{j\pi}{2N}\right)\right)^{\alpha}\cos\left(\frac{2j+\alpha(N-j)}{2N}\pi\right)\cos\left(\frac{jp\pi}{N}\right), \qquad (4.43)$$

that is, it coincides with the right-hand side of equation (4.31), we will now use Lagrange's trigonometric identity (Lemma 5) and show that for $l\leq N$ such that $l\in T_j$, the following three conditions hold:

- **F1** If $l\neq j$, then $\phi(N,j,p,l)$ is always zero.
- **F2** If $l=j<N$, then

$$\phi(N,j,p,j)=2N\ \cos\left(\frac{jp\pi}{N}\right).$$

- **F3** If $l=j=N$, then

$$\phi(N,N,p,N)=4N\ \cos(p\pi).$$

As a consequence of **F1**, for a given $j\in\{1,2,\ldots,N\}$, we observe that the only non-vanishing term in (4.42) is the one corresponding to $l=j$. Conditions **F2** and **F3**, on the other hand, are used to show that the term corresponding to a given index j in expression (4.39) is actually equal to (4.43)

and therefore equal to the right-hand side of equation (4.31).

By looking at the expression of $\phi(N, j, p, l)$, we see that in all three cases (**I**, **IIa** and **IIb**)

$$\phi(N, j, p, l) = \bar{\phi}(N, j, l) \cos\left(\frac{lp\pi}{N}\right), \tag{4.44}$$

for a suitable function $\bar{\phi}(N, j, l)$. In order to prove **F1**, it is therefore sufficient to show that $\bar{\phi} = 0$ when $l \neq j$. We observe that, independently from the particular case analysed, even though $l \neq j$, we are only considering indices $l \in T_j$, that is, indices l such that $\psi(l) = \psi(j)$. Hence, we can always write $l = j + 2n$ for some integer $n \neq 0$. Furthermore, since $l \neq j$ and both $l, j \in \{1, 2, \ldots, N\}$, we also find that $n \neq N$, $j + n \neq 0$ and $j + n \neq N$.

Using basic trigonometric formulas of the cosine and sine of a sum of angles, we then rewrite the products of cosine functions in the expression of $\bar{\phi}$ as

$$\cos\left(\frac{lk\pi}{N}\right) \cos\left(\frac{jk\pi}{N}\right) = \frac{1}{2}\left[\cos\left(\frac{2nk\pi}{N}\right) + \cos\left(\frac{2(j+n)k\pi}{N}\right)\right],$$

for all values of interest of the index k. As a result, $\bar{\phi}$ in case **I** becomes

$$\bar{\phi} = 4 + 4\sum_{k=1}^{\frac{N-1}{2}} \cos\left(\frac{2nk\pi}{N}\right) + 4\sum_{k=1}^{\frac{N-1}{2}} \cos\left(\frac{2(j+n)k\pi}{N}\right). \tag{4.45}$$

Applying Lemma 5 (Lagrange's identity) to the two sums of equation (4.45) with $\theta_1 = \frac{2n\pi}{N}$ and $\theta_2 = \frac{2(j+n)\pi}{N}$, we obtain

$$\bar{\phi} = 4 - 2 + 2\frac{\sin\left(\left(\frac{N-1}{2} + \frac{1}{2}\right)\theta_1\right)}{\sin\left(\frac{\theta_1}{2}\right)} - 2 + 2\frac{\sin\left(\left(\frac{N-1}{2} + \frac{1}{2}\right)\theta_2\right)}{\sin\left(\frac{\theta_2}{2}\right)}.$$

By noting that

$$\begin{aligned}
\sin\left(\left(\tfrac{N-1}{2} + \tfrac{1}{2}\right)\theta_1\right) &= \sin\left(\tfrac{N\theta_1}{2}\right) = \sin(n\pi) = 0, \\
\sin\left(\left(\tfrac{N-1}{2} + \tfrac{1}{2}\right)\theta_2\right) &= \sin\left(\tfrac{N\theta_2}{2}\right) = \sin((j+n)\pi) = 0,
\end{aligned}$$

we then conclude that in case **I**, when $l \neq j$, $\bar{\phi} = 0$.

In case **IIa**, the same type of considerations and the use of Lemma 5 with the same angles θ_1 and θ_2 leads to the following expression for $\bar{\phi}$:

$$\bar{\phi} = 4 - 2 + 2\frac{\sin\left(\left(\frac{N-2}{2} + \frac{1}{2}\right)\theta_1\right)}{\sin\left(\frac{\theta_1}{2}\right)} - 2 + 2\frac{\sin\left(\left(\frac{N-2}{2} + \frac{1}{2}\right)\theta_2\right)}{\sin\left(\frac{\theta_2}{2}\right)}. \tag{4.46}$$

This time, noting that

$$\begin{aligned}
\sin\left(\left(\tfrac{N-2}{2} + \tfrac{1}{2}\right)\theta_1\right) &= -\cos(n\pi)\sin\left(\tfrac{n\pi}{N}\right), \\
\sin\left(\left(\tfrac{N-2}{2} + \tfrac{1}{2}\right)\theta_2\right) &= -\cos(n\pi)\cos(j\pi)\sin\left(\tfrac{(j+n)\pi}{N}\right),
\end{aligned}$$

we find

$$\bar{\phi} = -2\cos(n\pi)\left[1 + \cos(j\pi)\right]. \tag{4.47}$$

Recalling that in case **IIa**, j is odd by assumption, we see that $\cos(j\pi) = -1$ and consequently expression (4.47) becomes $\bar{\phi} = 0$.

In case **IIb**, we can simply modify equation (4.47) by adding the term ± 4, obtaining

$$\bar{\phi} = \begin{cases} -2\cos(n\pi)\left[1 + \cos(j\pi)\right] + 4 & \text{if } \psi(l/2) = \psi(j/2), \\ -2\cos(n\pi)\left[1 + \cos(j\pi)\right] - 4 & \text{otherwise.} \end{cases} \tag{4.48}$$

In this case, we know by assumption that j is even. Therefore, $1+\cos(j\pi) = 2$ and $\bar{\phi}$ can be rewritten as

$$\bar{\phi} = \begin{cases} -4\cos(n\pi) + 4 & \text{if } \psi(l/2) = \psi(j/2), \\ -4\cos(n\pi) - 4 & \text{otherwise.} \end{cases}$$

Recalling that $l = j + 2n$, we have $l/2 = j/2 + n$. If $\psi(l/2) = \psi(j/2)$, then n must be even and hence $\cos(n\pi) = +1$, leading to $\bar{\phi} = 0$. Otherwise, n must be odd and hence $\cos(n\pi) = -1$, leading once again to $\bar{\phi} = 0$.

In light of all these considerations, we can conclude that for a given index $j \in \{1, 2, \ldots, N\}$, the only non-vanishing term in expression (4.42) is the one corresponding to the index $l = j$. In order to complete our proof, we will

now show that **F2** and **F3** hold.

Let us consider the case $l = j < N$. From equation (4.44) we observe that

$$\phi(N, j, p, j) = \bar{\phi}(N, j, j) \cos\left(\frac{jp\pi}{N}\right),$$

therefore, verifying that **F2** holds simply reduces to showing that when $j < N$, $\bar{\phi}(N, j, j) = 2N$. By assuming that $l = j$, independently from the particular case considered for $\bar{\phi}$, we observe that the products of cosine functions involved in $\bar{\phi}$ become squares of cosine functions. In case **I**, for example,

$$\bar{\phi}(N, j, j) = 4 + 8 \sum_{k=1}^{\frac{N-1}{2}} \cos^2\left(\frac{jk\pi}{N}\right). \tag{4.49}$$

Using property **P.7** we rewrite equation (4.49) as

$$\bar{\phi}(N, j, j) = 4 + 4 \sum_{k=1}^{\frac{N-1}{2}} \cos\left(\frac{2jk\pi}{N}\right) + 4\left(\frac{N-1}{2}\right),$$

and applying Lemma 5 with $\theta = \frac{2j\pi}{N}$ we conclude that

$$\bar{\phi}(N, j, j) = 4 - 2 + 2\frac{\sin\left(\left(\frac{N-1}{2} + \frac{1}{2}\right)\theta\right)}{\sin\left(\frac{\theta}{2}\right)} + 2N - 2 = 2N.$$

A similar strategy and analogous considerations (details omitted) are applied in the remaining two cases to prove that $\bar{\phi} = 2N$. In particular, we use that $j < N$ is assumed to be even in the case **IIa** and odd in the case **IIb**. Clearly, when considering case **IIb**, the additional term ± 4 in the expression of $\bar{\phi}$ is only considered with the positive sign because we assume $l = j$ and hence $\psi(l/2) = \psi(j/2)$ must hold.

Finally, let us assume $l = j = N$. Once again, thanks to the general expression of $\phi(N, j, p, l)$ given by equation (4.44), proving **F3** reduces to showing that

$$\bar{\phi}(N, N, N) = 4N.$$

In case **I**, for example, using that $\cos^2(k\pi) = +1$ for all integers k, $\bar{\phi}(N, N, N)$ becomes

$$\bar{\phi}(N, N, N) = 4 + 8 \sum_{k=1}^{\frac{N-1}{2}} \cos^2(k\pi) = 4 + 8 \left(\frac{N-1}{2} \right) = 4N.$$

Note that the assumption $j = N$ implies that the case **IIa** can now be ignored. In fact, if $N + 1$ is even, $j = N$ cannot be even as well. Therefore, the only case left is **IIb**. Once again using that $\cos^2(k\pi) = +1$ for all integers k and given that $l = j$, the expression of $\bar{\phi}(N, N, N)$ here becomes

$$\bar{\phi}(N, N, N) = 4 + 8 \sum_{k=1}^{\frac{N-2}{2}} \cos^2(k\pi) + 4 = 4 + 8 \left(\frac{N-2}{2} \right) + 4 = 4N.$$

□

4.3.2 The normalisation constant $\varphi_j^{(0)}$

In equation (4.23) of Theorem 1, we provide an explicit expression for the normalisation coefficient $\varphi_j^{(0)}$ of the $N+1$ eigenvectors of the matrix A_α. We now briefly justify that result.

Using the definition of the Euclidean norm $||\cdot||_2$ and looking at the definition of the $N + 1$ components of the eigenvector φ_j for a given $j \in \{0, 1, \ldots, N\}$, the coefficient $\varphi_j^{(0)}$ such that $||\varphi_j||_2 = 1$ is given by

$$\varphi_j^{(0)} = \left[\sum_{p=0}^{N} \cos^2 \left(\frac{jp\pi}{N} \right) \right]^{-1/2}. \tag{4.50}$$

Therefore, if $j = 0$ or $j = N$, equation (4.50) reduces to

$$\varphi_j^{(0)} = \left[\sum_{p=0}^{N} 1 \right]^{-1/2} = \frac{1}{\sqrt{N+1}}.$$

On the other hand, when $j = 1, \ldots, N - 1$, we can simply isolate the term

corresponding to $p = 0$ and use property **P.7** to obtain

$$\begin{aligned}\varphi_j^{(0)} &= \left[1 + \sum_{p=1}^{N} \left(\tfrac{1}{2}\cos^2\left(\tfrac{2jp\pi}{N}\right) + \tfrac{1}{2}\right)\right]^{-1/2} \\ &= \left[1 + \tfrac{1}{2}\sum_{p=1}^{N} \cos^2\left(\tfrac{2jp\pi}{N}\right) + \tfrac{N}{2}\right]^{-1/2}.\end{aligned}$$

By then applying Lemma 5 (Lagrange's identity) with $\theta = \frac{2j\pi}{N}$ on the sum of cosine values we find

$$\varphi_j^{(0)} = \left[1 - \frac{1}{4} + \frac{\sin\left(\left(N + \frac{1}{2}\right)\frac{2j\pi}{N}\right)}{4\sin\left(\frac{j\pi}{N}\right)} + \frac{N}{2}\right]^{-1/2},$$

and since

$$\sin\left(\left(N + \frac{1}{2}\right)\frac{2j\pi}{N}\right) = \sin\left(\frac{j\pi}{N}\right),$$

we can hence conclude

$$\varphi_j^{(0)} = \left[1 + \frac{N}{2}\right]^{-1/2} = \sqrt{\frac{2}{N+2}}.$$

4.4 Some considerations

Observing the result presented in Theorem 1 of Section 4.3, the analytic expression of the eigenvalues of the reflection matrix A_α for $\alpha \in (1, 2]$ can be written for $j = 0, 1, \ldots, N$ as

$$\mu_j = \left[\frac{2}{h}\sin\left(\frac{j\pi}{2N}\right)\right]^{\alpha} \frac{1}{\cos\left(\frac{\alpha\pi}{2}\right)}\cos\left(\frac{2j + \alpha(N-j)}{2N}\pi\right), \tag{4.51}$$

where, using the notation previously introduced, $h = \frac{L}{N}$ is the uniform mesh size of the spatial discretisation of the finite interval $[0, L]$ and $N + 1$ is the total number of spatial nodes used in the mesh (and therefore corresponds to the size of the matrix A_α).

In particular, by looking at expression (4.51), we see that each μ_j can be

thought of as the product $\lambda_j^{\alpha/2}\, q_\alpha$ where

$$\lambda_j = \frac{4}{h^2}\sin^2\left(\frac{j\pi}{2N}\right) \tag{4.52}$$

is the j-th eigenvalue of the matrix A_α in the standard case, that is, the j-th eigenvalue of the discrete Laplacian of size $N+1$ obtained with a finite-difference scheme when second order approximations are used at the boundary nodes, and q_α is the term

$$q_\alpha = \frac{1}{\cos\left(\frac{\alpha\pi}{2}\right)}\,\cos\left(\frac{2j+\alpha(N-j)}{2N}\pi\right). \tag{4.53}$$

With simple analysis arguments, it is straightforward to prove that for a fixed interval $[0, L]$ and a given fractional index α, when $N \longrightarrow \infty$,

$$\lambda_j \longrightarrow \left(\frac{j\pi}{L}\right)^2 \quad \forall j \quad \text{and} \quad q_\alpha \longrightarrow 1.$$

Therefore, when $N \longrightarrow \infty$, for the j-th eigenvalue of A_α we find

$$\mu_j \longrightarrow \left(\frac{j\pi}{L}\right)^\alpha. \tag{4.54}$$

In other words, the limiting result given by (4.54) tells us that the spectrum of the discrete reflection operator A_α asymptotically converges to the fractional power (with exponent $\alpha/2$) of the eigenvalues of the continuous standard Laplacian $(-\Delta)$ on the finite interval $[0, L]$ coupled with homogeneous Neumann boundary conditions at both ends.

Moreover, if we now look at the eigenvectors φ_j and for all j we consider their non-normalised scalar multiple[6] $\tilde{\varphi}_j$, that is, $\tilde{\varphi}_j = 1/\varphi_j^{(0)} \cdot \varphi_j$, by using the definition of the p-th node of the mesh $x_p = p\,h$ and the fact that $h = \frac{L}{N}$,

[6]Clearly for all j, $\tilde{\varphi}_j$ is still an eigenvector corresponding to the j-th eigenvalue μ_j.

the components of each $\tilde{\varphi}_j$ can be rewritten as

$$\tilde{\varphi}_j{}^{(p)} = \cos\left(\frac{jp\pi}{N}\right) = \cos\left(\frac{jx_p\pi}{L}\right) \quad \text{for } p = 0, 1, \ldots, N.$$

Hence, the p-th component of the eigenvector $\tilde{\varphi}_j$ is the function

$$\Phi_j(x) := \cos\left(\frac{jx\pi}{L}\right)$$

evaluated at the p-th node of the spatial mesh used to discretise $[0, L]$ and we observe that the cosine functions Φ_j are in turn the main component of the eigenfunctions of the continuous standard Laplacian $(-\Delta)$ on the finite interval $[0, L]$ coupled with homogeneous Neumann boundary conditions[7].

Therefore, the discrete operator A_α generated from the reflection strategy presented in this chapter can be seen as a finite approximation of the continuous fractional Laplacian defined via its spectral decomposition as proposed, but not proved, by Ilić et al. in [34].

The spectral definition proposed in [34] is a consequence of some fundamental linear operator theory results that can be summarised as follows.

- **Hilbert-Schmidt theorem.** Let $\mathcal{H}$ be a separable Hilbert space and suppose that $T : \mathcal{H} \to \mathcal{H}$ is a compact and self-adjoint operator. Then its eigenfunctions form an orthonormal basis of $\mathcal{H}$.

- **Canonical form for compact self-adjoint operators.** Let $\{\phi_n\}$ be the set consisting of all the eigenfunctions of T and $\{\eta_n\}$ the set of corresponding eigenvalues. Then for all $f \in \mathcal{H}$

$$Tf = \sum \eta_n \langle f, \phi_n \rangle \phi_n, \tag{4.55}$$

  where $\langle \cdot, \cdot \rangle$ denotes the inner product of $\mathcal{H}$.

[7]The actual eigenfunctions being typically equal to Φ_j multiplied by a normalisation coefficient.

- Let T be an unbounded self-adjoint operator on the infinite dimensional separable Hilbert space $\mathcal{H}$. Suppose T has a compact inverse, and let $\{\nu_n\}$ and $\{\phi_n\}$ be the sets of eigenvalues and eigenfunctions of T^{-1}. Then, the eigenvalues of T^{-1} are all non-zero, and $\{\phi_n\}$ is an orthonormal basis for $\mathcal{H}$. With $\eta_n = \nu_n^{-1}$, the sequence (η_n) is infinite and $|\eta_n| \to \infty$ as $n \to \infty$. The spectrum of T is the set $\{\eta_n\}$ and the eigenfunctions of T are the ϕ_n with corresponding eigenvalues η_n.

- **Spectral mapping theorem.** Let T be a compact self-adjoint operator and g a continuous function. Define the operator $g(T)$ by setting

$$g(T)f = \sum g(\eta_n)\langle f, \phi_n\rangle\phi_n. \tag{4.56}$$

  Then $\sigma(g(T)) = g(\sigma(T))$, where $\sigma(\cdot)$ denotes the spectrum of the considered operator.

The second result in the above list cannot be applied directly to the differential operator $T := -\frac{d^2}{dx^2}$ since this particular operator fails to satisfy the compactness requirement, despite being self-adjoint. However, under suitable conditions, T has a compact inverse and therefore, the third result can be used to obtain a spectral decomposition of Tf, for any f in the domain of the operator. For example, if $\mathcal{H} = \mathcal{L}_2(0, L)$ and $T : \mathcal{A} \longrightarrow \mathcal{H}$ is defined as $T = -\frac{d^2}{dx^2}$ with $\mathcal{A}$ the set of functions $f \in \mathcal{H}$ with absolutely continuous first derivative, second derivatives in $\mathcal{H}$ and $f(0) = f(L) = 0$, then T is self-adjoint and its inverse can be defined as the integral operator

$$T^{-1}f(x) = \int_0^L g(x, \xi)f(\xi)d\xi,$$

where $g(x, \xi)$ is the following Green function:

$$g(x, \xi) = \begin{cases} (L - \xi)x/L & 0 \le x \le \xi \le L, \\ (L - x)\xi/L & 0 \le \xi \le x \le L. \end{cases}$$

Proof of T^{-1} being compact (see for example Hutson et al. [33] for details) allows us to conclude that the eigenfunctions of T (the one-dimensional Lapla-

cian on the finite interval $[0, L]$ with homogeneous Dirichlet boundary conditions) form an orthonormal basis and hence any $f \in \mathcal{A}$ can be expressed as a Fourier sine series[8] and Tf can be expressed as in equation (4.55), where ϕ_n are sine functions and η_n the corresponding eigenvalues.

If in the definition of the domain $\mathcal{A}$ we assume homogeneous Neumann conditions, that is, $f'(0) = f'(L) = 0$, we see that the operator T becomes singular in the sense that T is no longer injective. However, it is possible to conclude that the eigenfunctions of this operator (known to be cosine functions always due to separation of variables) still form an orthonormal basis by considering the shifted injective operator $T + aI$ for some constant $a > 0$, where I denotes the identity operator[9].

Using the above results, as proposed by Ilić et al. [34], we can therefore mimic the spectral mapping theorem previously mentioned and define the fractional power of $T = -\frac{d^2}{dx^2}$ for any $f \in \mathcal{A}$ via the spectral decomposition of T as in equation (4.56), where $g(T) = T^{\alpha/2}$, provided that $\sum |\lambda_n^{\alpha/2} \langle f, \phi \rangle|^2 < \infty$. As a consequence we obtain that $\sigma(T^{\alpha/2}) = (\sigma(T))^{\alpha/2}$. Once again, our result on the limiting behaviour of the spectrum of the reflection operator is in agreement with the above spectral definition of $T^{\alpha/2}$ when the continuous Laplacian T on the finite interval $[0, L]$ is coupled with homogeneous Neumann boundary conditions. Hence, as previously stated, the discrete reflection operator can be seen as a discrete approximation of $T^{\alpha/2}$ and used to compute the numerical solution to a space-fractional problem involving $T^{\alpha/2}$ via the method of lines.

The authors of [34] on the other hand do not consider the concept of reflections and in order to compute the numerical solution of a one-dimensional space-fractional problem on $[0, L]$ involving the operator $T^{\alpha/2}$ a different strategy is adopted to approximate the fractional Laplacian: the matrix

[8] It is well-established that the eigenfunctions of the considered T are sine functions and can be computed with the separation of variables technique.

[9] Note that $T + aI$ has the same set of eigenfunctions but they now correspond to the shifted eigenvalues $\lambda_n + a$.

transfer technique (MTT). As reported in Section 2.3, if $\lambda_0, \ldots, \lambda_N$ are the eigenvalues and $\phi_0, \ldots, \phi_N$ the corresponding eigenvectors of the standard discrete Laplacian associated with a particular set of standard homogeneous boundary conditions, the discrete fractional operator of size $N+1$ given by the MTT is simply the matrix defined as VDV^{-1}, where V is the matrix with columns equal to the $N+1$ eigenvectors $\phi_0, \ldots, \phi_N$ and D is the diagonal matrix with diagonal entries equal to the fractional power of the $N+1$ eigenvalues, that is, $D = \mathrm{diag}(\lambda_0^{\alpha/2}, \ldots, \lambda_N^{\alpha/2})$.

Let us denote here by B_α the discrete fractional operator obtained with the MTT in the case of homogeneous Neumann boundary conditions. If we compare the spectrum of the reflection matrix A_α and the spectrum of the operator B_α, we observe that a first difference might arise from the type of finite-difference approximation used at the boundary nodes. In fact, in this thesis we always adopt a second order approximation, whereas the typical approach followed by Ilić et al. [34] is to consider only a first order approximation at the boundary nodes so that the resulting operator is symmetric. However, if in the MTT we adopt a second order approximation of the first order derivative at both ends of the spatial interval, in the standard case $\alpha = 2$, the spectrum and the eigenvectors of both A_α and B_α coincide and provide the well-known eigenpairs of the discrete one-dimensional Laplacian on the finite interval $[0, L]$ coupled with homogeneous Neumann boundary conditions. In the purely fractional case, that is, when $\alpha < 2$, noting that the eigenvalues of B_α are simply defined as the fractional power of the corresponding eigenvalues in the standard case (the λ_j in equation (4.52)), we see that there is a difference between the two spectra and such a difference can be explicitly quantified as the term q_α defined in equation (4.53). However, thanks to the result on the asymptotic behaviour of the eigenvalues μ_j of the reflection matrix (and their factors λ_j and q_α) as $N \longrightarrow \infty$, we find that the spectrum of both these discrete operators (A_α and B_α) converges to the same limit, namely the fractional power of the eigenvalues of the continuous standard one-dimensional Laplacian on the finite interval $[0, L]$ coupled with homogeneous Neumann boundary conditions.

We believe that both the reflection strategy and the MTT are valid approaches, however from what we have seen in this chapter on the construction of the operator A_α, the strength of the reflection strategy consists in giving a meaning to the concept of boundary conditions for the considered fractional operator on the finite interval $[0, L]$. When the MTT is used, in fact, such an interpretation is lost and only boundary conditions for the corresponding standard problem are provided. In light of the previous analysis we hence conclude that the reflection boundary conditions are the appropriate boundary conditions allowing us to complete the mathematical description of a superdiffusive transport phenomenon (in which particles move according to Lévy flights at the microscale) in an insulated one-dimensional finite medium.

However, if we leave the physical interpretation and motivation behind the construction of the two discrete operators and rather focus on computational aspects, we notice that adopting either the reflection technique or the MTT with a large number of nodes for the spatial discretisation (often required for reasons of stability and/or accuracy of the numerical solution) are both very expensive procedures. In fact, at least in principle[10], these methods require the construction of the matrices describing the considered discrete operators and the computation of matrix function vector products involving them. These matrices are no longer characterised by a very high level of sparsity (as for the case of standard diffusion) but rather become dense as soon as $\alpha < 2$, mirroring the fact that the operator is now non-local.

All these considerations, together with the results of our spectrum analysis, suggest the use of an alternative approach for the computation of the solution of the non-local problem on the insulated one-dimensional finite domain, namely the spectral approach, where the eigenvalues are given by the limiting spectrum of A_α when $N \longrightarrow \infty$ and the corresponding eigenfunctions are the normalised continuous versions of the eigenvectors of A_α. This method naturally applies to an operator defined via its spectral decomposition as in [34].

[10]The actual implementation could be considered "matrix free" to a certain extent, if suitable techniques are used to approximate matrix function vector products of the form $f(M)b$.

Moreover, by using the fact that the eigenfunctions of the operator form an orthonormal basis of the Hilbert space on which the operator is considered, this method allows us to obtain a solution to the non-local problem exploiting a fully diagonal representation of the space-fractional operator, bypassing the technical and computational restrictions and difficulties related to the use of the method of lines.

In the following section, after describing the details of implementation of the various strategies considered in this section, we reaffirm the observations and remarks made here by presenting some specific numerical examples, highlighting the strengths and/or weaknesses of each of the proposed methods.

4.5 Implementation details and some numerical simulations

In this section we compute the solution of a space-fractional diffusion problem of the form

$$\frac{\partial u}{\partial t} = -(-\Delta)^{\alpha/2} u, \tag{4.57}$$

on an insulated finite one-dimensional domain $[0, L]$ for values of $t > 0$ and for a given initial condition $u(x, 0) = f(x)$. We choose here to define the initial condition as f instead of the usual u_0 in order to avoid confusion in what follows between the index representing the solution approximation at the node $x = x_0$ of the spatial mesh and the index denoting the initial condition. In particular, we will consider the spatial interval $[0, L] = [0, 1]$ and the initial condition $f(x) = 1 - \cos(2\pi x)$. Our first set of results is based on the method of lines (MOL) and aims at comparing the solution obtained from the use of different discrete operators in the linear ODE resulting from spatial discretisation of equation (4.57).

Let us introduce a spatial mesh of $N + 1$ nodes $x_i = i\,h$ for $i = 0, \ldots, N$, where $h = \frac{L}{N}$ is the uniform mesh size. Let $\mathbf{u}(t) = [u_0(t), \ldots, u_N(t)]^T$ be the vector of solution approximations at the $N + 1$ nodes of the spatial grid.

Equation (4.57) can then be discretised in space and rewritten in the form

$$\begin{cases} \mathbf{u}'(t) &= -\Lambda\,\mathbf{u}(t), \\ \mathbf{u}(0) &= \mathbf{f} \end{cases} \tag{4.58}$$

where Λ is a suitable square matrix of size $N+1$ representing the discrete approximation of the continuous operator $(-\Delta)^{\alpha/2}$ on the insulated finite domain, and $\mathbf{f}$ is the vector obtained by evaluating the initial condition at the nodes of the spatial grid considered. As observed in Section 4.4, the appropriate choice of Λ for the discretisation of the considered problem is given by $\Lambda = A_\alpha$, where A_α is the reflection matrix defined in Section 4.2. However, in our first set of results we also consider other options for the finite operator Λ corresponding to different implementations of the boundary conditions. We then compare the numerical solution of the ODE system (4.58) in the various cases, and show why these other options are not consistent with the assumptions made for the problem (4.57).

The different options for the matrix Λ considered here are all built starting from the shifted Grünwald–Letnikov finite-difference approximation of the one-dimensional fractional operator $\mathcal{R}_x^\alpha = -[c_\alpha I_+^{-\alpha} + c_\alpha I_-^{-\alpha}]$ equivalent to the one-dimensional fractional Laplacian $-(-\Delta)^{\alpha/2}$ on the unbounded domain. We consider the approximation of $I_+^{-\alpha}$ and $I_-^{-\alpha}$ given by the shifted Grünwald–Letnikov operators ${}_hI_+^{-\alpha}$ and ${}_hI_-^{-\alpha}$ defined in equations (4.13) and (4.14), and build a truncated version of them by only considering a finite number of terms in the sums defining ${}_hI_+^{-\alpha}$ and ${}_hI_-^{-\alpha}$. In particular, in the approximation at a given node $x = x_i$ we only consider the terms in the right-hand side of equations (4.13) and (4.14) that involve the solution approximation u_k at a node of the spatial grid of the considered domain $[0, L]$, that is, we ignore all terms with index $k < 0$ or $k > N$. Let us denote ${}_h\bar{I}_+^{-\alpha}$ and ${}_h\bar{I}_-^{-\alpha}$ the newly defined truncated Grünwald–Letnikov operators. The discrete operator corresponding to this truncated Grünwald–Letnikov approximation is then built by noting that $c_\alpha[{}_h\bar{I}_+^{-\alpha} +_h \bar{I}_-^{-\alpha}]u$ at each node $x = x_i$ of the spatial mesh can be written as the coefficient $\frac{c_\alpha}{h^\alpha}$ times the inner product of a suitable vector of weights $\bar{\omega}_i$ and the vector $\mathbf{u}$ of solution

approximations on the given grid. In our first set of numerical simulations we hence consider:

- $\Lambda = A_{\mathcal{D}}$, where for all $i \in \{0, 1, \ldots, N\}$ the $(i+1)$-th row of the square matrix $A_{\mathcal{D}}$ is given by the product of the coefficient $\frac{c_\alpha}{h^\alpha}$ times the row of weights $\bar{\omega}_i$ such that

$$\frac{c_\alpha}{h^\alpha}\,\bar{\omega}_i\,\mathbf{u} = c_\alpha\left[{}_h\bar{I}_+^{-\alpha} +_h \bar{I}_-^{-\alpha}\right] u\Big|_{x=x_i}.$$

  In light of the considerations made at the beginning of this chapter, we expect the discrete operator $A_{\mathcal{D}}$ to produce a numerical solution satisfying homogeneous Dirichlet boundary conditions.

We then consider a second option for Λ obtained by slightly modifying the discrete operator $A_{\mathcal{D}}$ at the boundary nodes. We hence define:

- $\Lambda = A_{\mathcal{N}}$, where for all the internal nodes (that is, for $i = 1, \ldots, N-1$) the corresponding row of the matrix $A_{\mathcal{N}}$ is obtained as in the case $\Lambda = A_{\mathcal{D}}$, whereas the finite-difference scheme adopted at both boundaries and used to determine the solution approximation at the nodes x_0 and x_N is simply given by standard homogeneous Neumann boundary conditions. We could therefore think of the solution of system (4.58) in this case as fractional inside the finite domain and satisfying standard homogeneous Neumann boundary conditions at both ends of $[0, L]$.

Finally we consider the following case:

- $\Lambda = A_\alpha$, where A_α is the reflection matrix defined in Section 4.3. Actually, recalling that the definition of each entry of the reflection matrix A_α involves infinite sums of weights, for practical reasons, we must truncate these sums and only consider a finite number $\bar{m}$ of reflections in the computation of the numerical solution, that is, only integer values of $m \leq \bar{m}$ are used in the definition of the entries M_{ik} of the matrix of weights M such that $A_\alpha = \frac{c_\alpha}{h^\alpha} M$ (see Section 4.2). Let $\bar{A}_{\alpha,\bar{m}}$ be the truncated reflection matrix A_α obtained considering a finite number of

reflections equal to $\bar{m}$. We will now investigate the role of $\bar{m}$ by considering the properties of the solution of equation (4.58) with $\Lambda = \bar{A}_{\alpha,\bar{m}}$ for different values of $\bar{m}$.

To compute the solution of equation (4.58) for a given matrix Λ we use the MATLAB® built-in ODE solver **ode15s** and specify the Jacobian (in this case $J = \Lambda$) of the linear right-hand side of equation (4.58) to improve the performance of the solver. We also provide a uniform time grid as input of **ode15s** so that the adaptive time-step solver explicitly computes the solution at the regular time intervals of interest, allowing us to make some considerations on the output of the various ODE systems by comparing their solutions on the same fixed grid of uniformly spaced time points.

Given the assumption of $[0, L]$ being an insulated medium, the criterion used here to determine if the discrete numerical solution is consistent with the above hypothesis is to verify whether the total mass of the system is preserved in time, that is, whether $\int_0^L u(x,t)\,dx$ is constant as a function of t.

Let u_i^k represent the approximation of the solution $u(x,t)$ at the i-th node of the spatial grid at time $t_k = k\,\Delta t$. By using the trapezoidal rule to approximate the integral of the solution, in terms of the discrete numerical approximation $\mathbf{u}^k = [u_0^k, \ldots, u_N^k]^T$, we obtain that mass is conserved if

$$h \sum_{i=0}^{N} \beta_i \; u_i^k = C \quad \text{for all } k > 0,$$

where C is the constant representing the total mass of the initial condition $\mathbf{f}$, h is the uniform mesh size of the spatial discretisation, and $\beta_0, \ldots, \beta_N$ are the weights of the trapezoidal rule, that is,

$$\beta_0 = \beta_N = \frac{1}{2} \quad \text{and} \quad \beta_i = 1 \quad \forall i \neq 0, N.$$

We hence compute the solution of (4.58) in the time interval $[0, 1]$ for two different values of the fractional order α when Λ is the discrete operator $A_{\mathcal{D}}$, $A_{\mathcal{N}}$ and $\bar{A}_{\alpha,\bar{m}}$ with a number of reflection blocks $\bar{m}$ equal to 1, 10 and 100.

The number of nodes used in the discretisation of the spatial interval $[0, 1]$ is here $N + 1 = 501$.

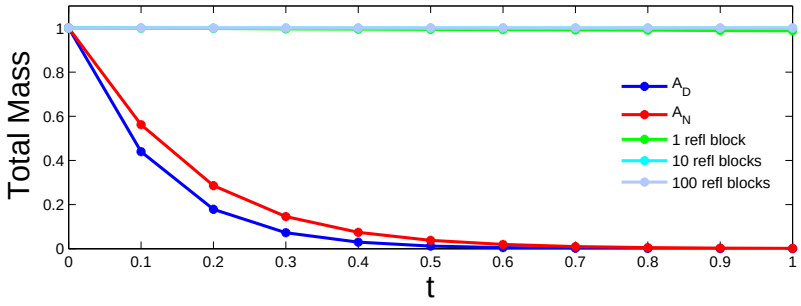

(a) $\alpha = 1.95$

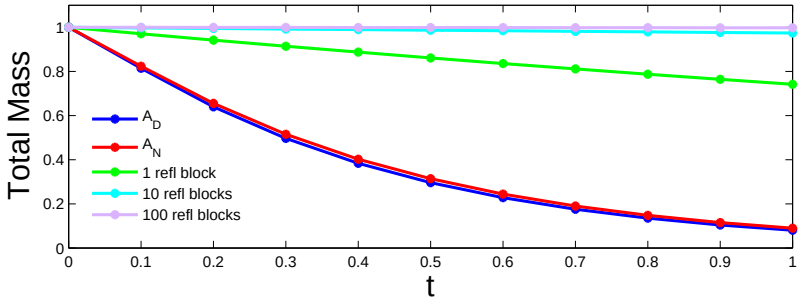

(b) $\alpha = 1.05$

Figure 4.6: *For $t \in [0, 1]$ we compute the solution of the initial value ODE problem (4.58) for different choices of Λ and two different values of α on a grid of $N + 1 = 501$ nodes for the spatial interval $[0, 1]$. Total mass is then computed via the trapezoidal rule and plotted at regular time steps of length $\Delta t = 0.1$ from the discrete solution of system (4.58) when Λ is equal to $A_{\mathcal{D}}$ (blue), $A_{\mathcal{N}}$ (red) or the truncated reflection matrix $\bar{A}_{\alpha,\bar{m}}$ with a number $\bar{m}$ of reflection blocks equal to 1 (green), 10 (cyan), or 100 (lilac). Wrong implementation of the boundary conditions or the use of an insufficient number of reflecting blocks in the truncated approximation of A_α result in mass loss over time.*

In Figure 4.6 we plot the total mass computed by approximating $\int_0^1 u(x, t_k)\, dx$ via the trapezoidal rule at uniform time intervals with $\Delta t = 0.1$ for all the cases considered. It is straightforward to compute analytically the total mass of the specified initial condition and see that $\int_0^1 f(x)\, dx = 1$. As we can see

from Figure 4.6, the use of either the operator $A_{\mathcal{D}}$ or $A_{\mathcal{N}}$ leads to immediate loss of mass and clearly corresponds to the wrong implementation of the boundary conditions for the considered problem. Moreover, as expected, we find that the number of reflecting blocks used in the approximation of the reflection matrix plays an important role. In particular, the number of reflecting blocks to be considered in the approximation in order to guarantee mass conservation varies depending on the value of the parameter α. For example, in the particular case considered in Figure 4.6, when $\alpha = 1.95$ the use of 10 reflecting blocks, that is, computing the solution of system (4.58) with $\Lambda = \bar{A}_{\alpha,10}$ is already sufficient to produce a mass preserving discrete approximation[11]. On the other hand, when $\alpha = 1.05$, considering 10 reflecting blocks is no longer sufficient and the use of a higher number of reflections is required to avoid mass loss over time.

Mass loss over time can also be seen by comparing the evolution in time of the numerical solution in the different cases considered. Figure 4.7 shows the evolution behaviour for a fixed value of α (here taken as $\alpha = 1.95$) when Λ is either equal to $A_{\mathcal{D}}$, $A_{\mathcal{N}}$ or $\bar{A}_{\alpha,100}$.

The solution plotted here at regular time intervals with $\Delta t = 0.04$ depicts the evolution in time of the initial condition (blue line) in the time interval $[0, 0.2]$. The choice of a shorter time interval and the display of only five iterations of the solution profile was simply made to have a better visualisation of what happens in these three cases. Once again we see that the use of the discrete operator $A_{\mathcal{D}}$ produces a numerical solution clearly satisfying homogeneous Dirichlet boundary conditions. Furthermore, the simple modification of this operator at the boundaries, locally introducing standard homogeneous Neumann boundary conditions as in the definition of the operator $A_{\mathcal{N}}$, is still not enough to produce a numerical solution consistent with the initial insulation assumption made on the spatial domain $[0, 1]$. On the other hand, the reflection approach (where the number of reflecting blocks

[11]Note that the cyan and lilac lines in Figure 4.6(a), corresponding to the solution computed with 10 and 100 blocks respectively, are visually indistinguishable.

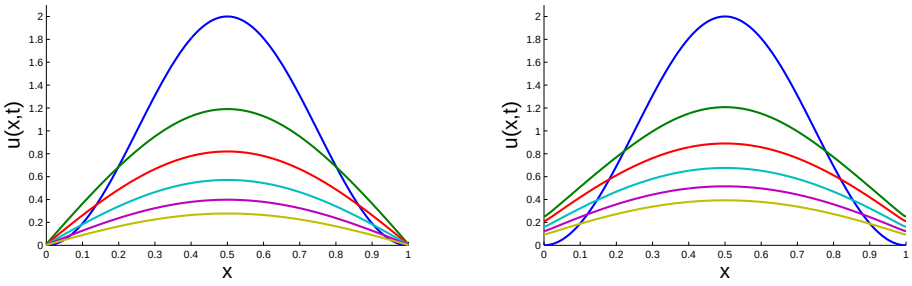

(a) $\Lambda = A_{\mathcal{D}}$ (b) $\Lambda = A_{\mathcal{N}}$

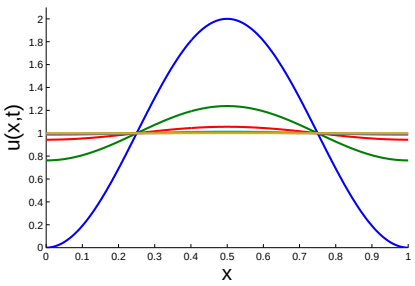

(c) $\Lambda = \bar{A}_{\alpha,100}$

Figure 4.7: *Comparison of the evolution in time of the solution of system (4.58) when* $\Lambda = A_{\mathcal{D}}$, $\Lambda = A_{\mathcal{N}}$ *and* $\Lambda = \bar{A}_{\alpha,100}$. *The value of the fractional parameter is set equal to* $\alpha = 1.95$ *for all three simulations. The solution profiles are computed on a mesh of* $N+1 = 501$ *equally spaced nodes on* $[0, 1]$ *and plotted for* $t \in [0, 0.2]$ *at regular time intervals with* $\Delta t = 0.04$.

considered in the truncated operator is sufficiently high) produces the correct solution behaviour, modelling on $[0, 1]$ non-standard ($\alpha < 2$) particle dynamics at the microscale but still preserving mass in time as shown by Figure 4.7(c).

In our next set of results we only consider the reflection approach and make some remarks on how different values of α affect the behaviour of the solution of (4.58). To do so we compute the solution of our ODE system where $\Lambda = \bar{A}_{\alpha,100}$ on a spatial grid of $N + 1 = 501$ nodes and for $t \in [0, 0.2]$. In Figure 4.8 we plot the solution computed for four different values of α (namely $\alpha = 2$, $\alpha = 1.75$, $\alpha = 1.5$ and $\alpha = 1.25$) at regular time intervals

with $\Delta t = 0.04$.

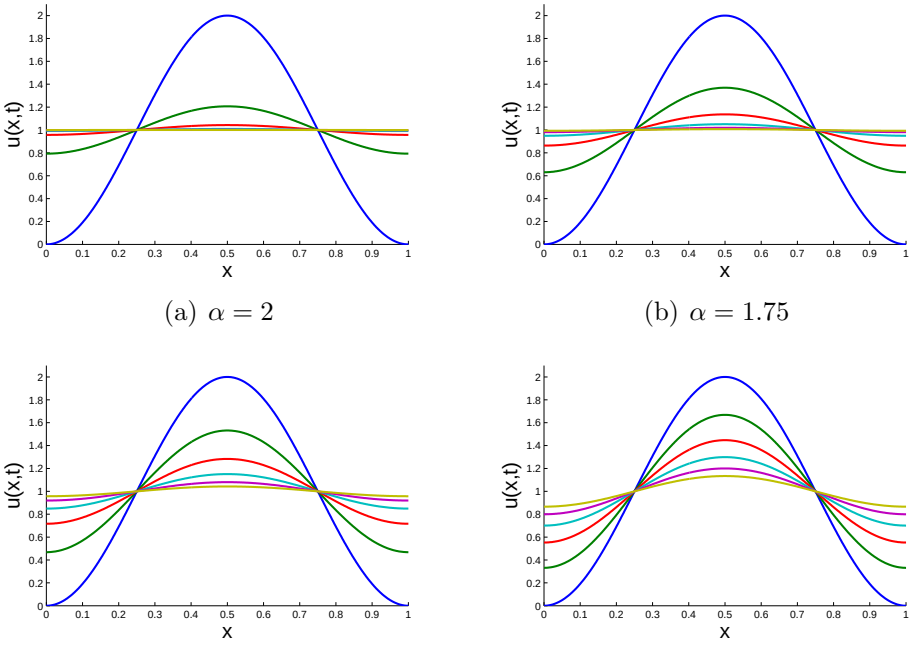

(a) $\alpha = 2$ (b) $\alpha = 1.75$

(c) $\alpha = 1.5$ (d) $\alpha = 1.25$

Figure 4.8: *Comparison of the evolution in time of the solution of system (4.58) when* $\Lambda = \bar{A}_{\alpha,100}$ *for four different values of the parameter* $\alpha \in (1, 2]$. *In all four simulations the solution profiles are computed on a mesh of* $N+1 = 501$ *equally spaced nodes on* $[0, 1]$ *and plotted for* $t \in [0, 0.2]$ *at regular time intervals with* $\Delta t = 0.04$.

As we can see, all solutions evolve towards the same asymptotic solution $u_\infty(x) = 1$ for all x. However, as α decreases, the speed of convergence clearly decreases. These observations can be justified mathematically by considering the exact solution of

$$\begin{cases} \mathbf{u}'(t) &= -A_\alpha\, \mathbf{u}(t), \\ \mathbf{u}(0) &= \mathbf{f}, \end{cases}$$

namely

$$\mathbf{u}(t) = e^{-A_\alpha\, t}\mathbf{f}.$$

The analysis conducted in Section 4.3 allows us to explicitly compute the matrix exponential $e^{-A_\alpha t}$ by exploiting the spectral decomposition of the matrix A_α. Let us define $V = [\varphi_0, \ldots, \varphi_N]$, that is, the matrix with columns φ_j given by the $N+1$ eigenvectors of A_α, and let $D = \text{diag}(\mu_0, \ldots, \mu_N)$ be the diagonal matrix of corresponding eigenvalues so that $A_\alpha = VDV^{-1}$. Fundamental linear algebra results allow us to define $e^{-A_\alpha t}$ as the product

$$e^{-A_\alpha t} = VE(t)V^{-1}, \quad \text{where} \quad E(t) = \text{diag}(e^{-\mu_0 t}, \ldots, e^{-\mu_N t}).$$

As observed in Section 4.3 all the eigenvalues μ_j are real and positive for all $\alpha \in (1, 2]$, except for $\mu_0 = 0$. Therefore, if we consider the asymptotic behaviour (that is, the limit for $t \to \infty$) of the scalar exponential functions we observe that $e^{-\mu_j t} \to 0$ for all $j \neq 0$ and for the zero eigenvalue μ_0 we have $e^{-\mu_0 t} = 1$ for all values of t.

The asymptotic solution vector $\mathbf{u}_\infty := \lim_{t\to\infty} \mathbf{u}(t)$ can hence be computed as

$$\mathbf{u}_\infty = VE_\infty V^{-1}\mathbf{u}^0,$$

where

$$E_\infty := \lim_{t\to\infty} E(t) = \text{diag}(1, 0, \ldots, 0).$$

It is easy to see that $\mathbf{u}_\infty$ does not depend on α and is indeed equal to the constant vector $\mathbf{u}_\infty = [1, 1, \ldots, 1]^T$. Furthermore, if $\mu_j(\alpha)$ denotes the j-th eigenvalue of A_α for a specific value of $\alpha \in (1, 2]$, one can show that if $\alpha_1 < \alpha_2$, then $\mu_j(\alpha_1) < \mu_j(\alpha_2)$ for all $j \neq 0$. Hence, the slower convergence observed numerically is due to the fact that for all $j \neq 0$, as $t \to \infty$, each exponential $e^{-\mu_j(\alpha_1)t}$ approaches zero slower than the corresponding $e^{-\mu_j(\alpha_2)t}$.

In the set of results reported in Figure 4.9, we compare the solution behaviour obtained with the reflection approach and the one obtained via the MTT, that is, using the notation introduced in Section 4.4, when the discrete operator of equation (4.58) is $\Lambda = B_\alpha$. The solution is computed on a spatial mesh of $N + 1 = 501$ nodes for values of $t \in [0, 0.2]$ and plotted at regular time intervals with $\Delta t = 0.02$.

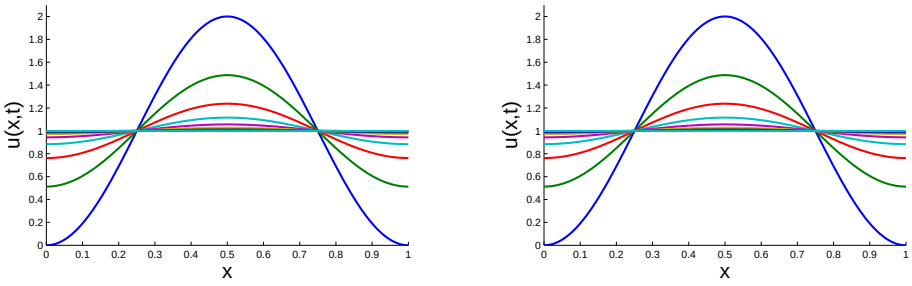

(a) Reflection BCs, $\alpha = 1.95$

(b) MTT, $\alpha = 1.95$

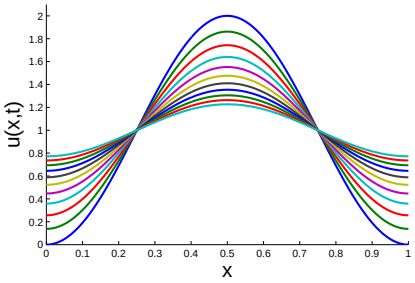

(c) Reflection BCs, $\alpha = 1.05$

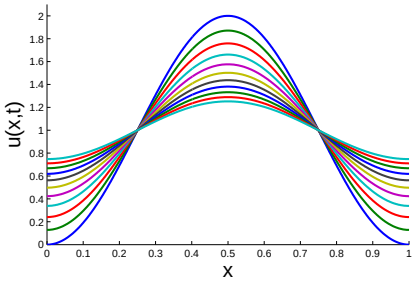

(d) MTT, $\alpha = 1.05$

Figure 4.9: *Comparison of the solution profile obtained from system (4.58) via the reflection approach ((a) and (c)) and via the MTT ((b) and (d)) for two different values of the fractional order* α. *Once again the discrete solution is computed for both methods on a uniform mesh of* $N + 1 = 501$ *spatial nodes in* $[0, 1]$ *and is here plotted for* $t \in [0, 0.2]$ *at regular time intervals of* $\Delta t = 0.02$.

Thanks to the convergence analysis made in the previous section on the spectrum of both these discrete operators (A_α and B_α), we expect the solution of the two models to be quite similar on the fine grid considered. Figure 4.9 validates our previous results and as we can see for both the considered values of α, the numerical solution produced by these two methods evolves in time in a very similar fashion. As previously observed both these discrete methods are valid approaches in determining the solution of equation (4.57) via the MOL. However, due to the asymptotic results obtained from our analytic study in Section 4.4 and due to the computational cost involved in the generation of the matrix A_α (or better a sufficiently accurate truncated version of it) and

B_α, in our applications we consider the use of an alternative approach, based on the spectral definition of the one-dimensional fractional Laplacian: the spectral method, introduced for the standard case in Section 2.2.

To conclude this section on one-dimensional numerical simulations we hence present the implementation details of the spectral method in the fractional case. Recalling that for sufficiently regular functions u the spectral definition of the fractional Laplacian on an insulated finite domain $[0, L]$ is given by

$$(-\Delta)^{\alpha/2} u = \sum_{j=0}^{\infty} \lambda_j^{\alpha/2} \, \hat{u}_j(t) \, \phi_j(x),$$

where $\{\phi_j\}_0^\infty$ is the set of orthonormal eigenfunctions[12] defined as

$$\phi_j(x) = \begin{cases} \frac{1}{\sqrt{L}} & \text{if } j = 0, \\ \\ \sqrt{\frac{2}{L}} \cos\left(\frac{jx\pi}{L}\right) & \text{if } j > 0, \end{cases}$$

$\{\lambda_j\}_0^\infty$ is the set of corresponding eigenvalues $\lambda_j = \left(\frac{j\pi}{L}\right)^2$, and for all j, $\hat{u}_j(t) = \int_0^L u(x,t)\phi_j(x)\,dx$, we can easily derive the analytical solution of equation (4.57) corresponding to a given initial condition $u(x,0) = f(x)$ as

$$u(x,t) = \sum_{j=0}^{\infty} \hat{u}_j(0) e^{-\lambda_j^{\alpha/2} t} \phi_j(x). \tag{4.59}$$

For practical reasons, in the implementation of our numerical solution we notice that the infinite sum in equation (4.59) must be truncated after a sufficiently high number of terms and the integrals $\hat{u}_j$ must be computed. In this particular example, thanks to the specific form of the initial condition, we could compute analytically the exact value of $\hat{u}_j$ for all j. However, in order to present the general strategy that will be used later in the thesis for the case of a generic initial condition f, we choose here to simply approximate

[12]The set $\{\phi_j\}$ forms a basis of the considered Hilbert space of sufficiently regular functions.

each integral $\hat{u}_j$ by using the trapezoidal rule. We therefore introduce a spatial mesh on which an approximation of the solution is computed, use the given nodes to obtain $\hat{u}_j$ and truncate the infinite sum of equation (4.59) after considering a finite number of eigenfunctions equal to the number of discretisation points.

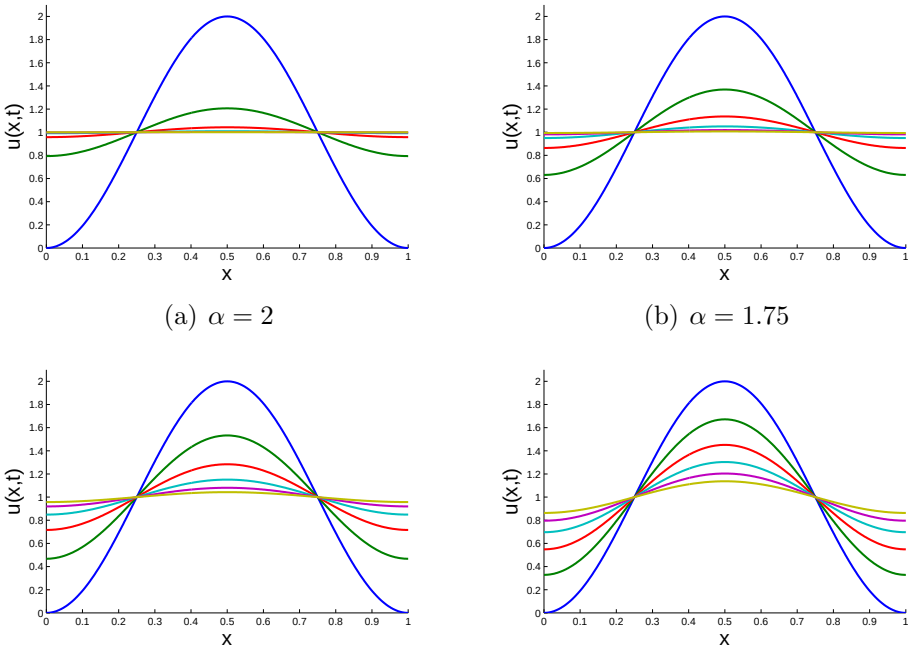

(a) $\alpha = 2$ (b) $\alpha = 1.75$

(c) $\alpha = 1.5$ (d) $\alpha = 1.25$

Figure 4.10: *Effect of different values of the parameter* $\alpha \in (1, 2]$ *on the spectral solution given by equation (4.59). In each case the solution is computed on a spatial grid of* $N+1 = 501$ *uniformly spaced nodes for the finite domain* $[0, 1]$ *and the solution profile is plotted for* $t \in [0, 0.2]$ *at regular time intervals with* $\Delta t = 0.04$.

Figure 4.10 shows the evolution in time of the spectral solution for four different values of the fractional order α. As in the discrete case in which the reflection matrix was considered, we see from our numerical simulations that the asymptotic continuous solution is the constant function $u_\infty(x) = 1$ for all x, and as the value of $\alpha \in (1, 2]$ decreases, the convergence towards u_∞ becomes slower.

Since all eigenvalues λ_j are real and positive, except for $\lambda_0 = 0$, from considerations on the asymptotic behaviour of the exponential functions $e^{-\lambda_j^{\alpha/2}t}$ for $j \neq 0$ similar to what observed in the discrete case, we can conclude that as $t \to \infty$ the only non-vanishing term in the analytic expression (4.59) is the one corresponding to the eigenpair (μ_0, ϕ_0). Therefore, the asymptotic solution $u_\infty(x) := \lim_{t\to\infty} u(x,t)$ can be written as follows:

$$u_\infty(x) = \left[\int_0^L f(x)\phi_0(x)\,dx\right]\phi_0(x) = \frac{1}{L}\int_0^L f(x)\,dx.$$

In the particular case considered, $L = 1$ and $f(x) = 1 - \cos(2\pi x)$. Therefore, we find $u_\infty(x) = 1$ for all $x \in [0, 1]$.

Once again, the slower convergence towards the asymptotic solution as α decreases can be easily justified by the slower convergence to zero of the exponential terms $e^{-\lambda_j^{\alpha/2}t}$. In fact, it is immediate to see that $\forall j \neq 0$, if $\alpha_1 < \alpha_2$, then $\lambda_j^{\alpha_1/2} < \lambda_j^{\alpha_2/2}$.

Moreover, if we consider a fixed value of α and compare the spectral decomposition method with the discrete reflection approach (or the MTT), we obtain a faster convergence towards the asymptotic solution. In fact, given that $\forall j \neq 0$ the j-th eigenvalue $\mu_j^{\alpha/2}$ of the discrete reflection matrix is smaller than the corresponding eigenvalue $\lambda_j^{\alpha/2}$ of the continuous fractional Laplacian, we obtain that each exponential $e^{-\mu_j^{\alpha/2}t}$ approaches zero slower than the corresponding $e^{-\lambda_j^{\alpha/2}t}$ as $t \to \infty$.

Chapter 5

Space-fractional Fisher–Kolmogoroff model

5.1 Motivation

As seen in Chapter 2, standard reaction-diffusion models exhibiting travelling wave solutions with constant wave speed are the classical mathematical approach used to describe wave phenomena in biology. On the other hand, if we consider for example the study of cell motion, the fact that the cell population is moving with constant speed is often used by biologists as an assumption to obtain an estimate of the speed from experimental data [52]. Enteric neural crest cells colonize the embryonic gut and move in the caudal direction (towards the posterior/inferior end of the body) giving rise to the enteric nervous system. From our research and the literature examined, we could see that most of the experimental data available in the context of enteric cell migration is obtained through *in vitro* simulation assays and these data seem to agree well with the constant wave speed assumption (see for example [2] and [78]). However, we believe that considering isolated segments of enteric tissue and recording measurements in this "simplified" setting might affect the complexity and the interactions between different parts of the natural environment in which the process occurs, thus leading to erroneous conclusions.

Measurements of the speed of invasion for the enteric neural crest cell population *in vivo* are often not straightforward. For example, it is not always clear how the advancing front is defined and this may substantially vary between different experiments (see for example [25], [53] and [88]). Lack of information and poor measurements may also lead to wrong interpretations of biological results. For example, in recent *in vivo* experiments [88], the wave speed was determined by measuring the distance between the location of the most caudal cell at the beginning and at the end of the experiment, obviously resulting in a constant estimate of the speed. Moreover, measurements were taken only in the proximal midgut and the distal hindgut (respectively the initial and the final parts of the gut observed in these experiments) due to the impossibility of observing the cell population in the caecum (the pouch between midgut and hindgut) due to its complex geometric structure and the multiple focal planes on which the cell movement occurred. When measurements were taken regularly over shorter intervals of time and with a different strategy, differences in the speed became evident.

Biological data provided by Druckenbrod and Epstein [24] on the pattern and average speed of invasion of the gut in mice embryos can be summarized as follows. Enteric neural crest-derived cells predominantly colonize the gut in the form of strands of connected cells. At E10.5 (day 10.5 in the embryonic stage of mouse development) the front is in the ileum and advances caudally at an average speed of $45\,\mu\mathrm{m}\cdot\mathrm{h}^{-1}(\pm 10.8\,\mathrm{SE}^{1})$ but slows down to $32\,\mu\mathrm{m}\cdot\mathrm{h}^{-1}$ at E11.25 approaching the nascent caecum. At E11.5, for a period of 8 - 12 hours, the enteric neural crest cell population is concentrated at the caecal base and does not migrate forward. A number of single cells break-off from the strands, move fast into the caecal body as isolated cells and after approximately 12 hours begin to extend as short strands towards one another. Successively the initial front invades the caecum and connects with these short strands forming a complete network again. From E11.5 to E12.5 the wavefront advances through the caudal axis of the caecal body at an average speed of $23\,\mu\mathrm{m}\cdot\mathrm{h}^{-1}(\pm 6.3\,\mathrm{SE})$. This value includes the period when the cells

[1]Standard Error.

were paused (from E11.5 to E12.0). Finally, from E12.5 to E13.25, the wavefront moves at an average speed of $30\,\mu\mathrm{m}\cdot\mathrm{h}^{-1}(\pm 7.8\,\mathrm{SE})$ along the caudal axis of the mid-colon. At E13.5 the enteric cells approach the termination of the bowel.

In other words, the *in vivo* experiments reported by Druckenbrod and Epstein [24] showed that enteric neural crest-derived cells initially advance in the form of strands of connected cells but the advancing population regularly pauses at the caecum base and then displays a very different pattern of migration from that found in other more proximal regions. In fact, after a period of pause, a few cells rapidly migrate forward as isolated cells and only successively the remaining cell population colonizes the caecum body and reaches the few advanced isolated cells building again a complex network of strands.

We note that, since there is a pause of the cell population at the caecum base and the speed in the caecal body is computed including the period of pause, the actual value of the average speed in the caecum must be much higher than $23\,\mu\mathrm{m}\cdot\mathrm{h}^{-1}$ and an acceleration from zero up to a maximum speed value must occur. In fact, the average speed $23\,\mu\mathrm{m}\cdot\mathrm{h}^{-1}$ is computed over a time window of about 24 hours (from E11.5 to E12.5) but recordings of the cell population show a pause period of about 12 hours (from E11.5 to E12), that is, almost as long as the time required to colonise the entire caecum body. We can therefore expect the actual average speed over the time frame E12 to E12.5 to be roughly twice the one reported by Druckenbrod and Epstein [24].

The values of the speed obtained from these experiments show that the dynamics of the invasive process reflect particular properties of the gut structure along which the migration occurs and changes according to the location of the front in the domain. In particular, the more complex geometric structure of the caecum and the heterogeneity of the caecal tissue result in an anomalous behaviour of the cell population and therefore, it is evident that a standard reaction-diffusion model cannot capture the main characteristics

of the whole invasion phenomenon *in vivo*.

One way to overcome this limitation could be the introduction of a spatially varying diffusivity but the definition of such a variable diffusion coefficient typically requires extremely detailed information on the connectivity properties of the region in which the anomalous behaviour is observed. The option we present here is of a different nature and is fundamentally based on the use of non-local models in space to capture the heterogeneity of the domain in which the anomalous transport phenomena is observed.

Inspired by the above considerations, in this chapter we start by considering a simple cell migration model, namely the Fisher–Kolmogoroff (FK) model analysed in Chapter 3, and study the effect of the introduction of a space-fractional component with fractional order $\alpha \in (1, 2]$ on the numerical solution corresponding to a given initial condition. The numerical simulations of the fractional modification of the FK model are performed in light of the results provided in Chapter 4. However, the presence of a source term in the fractional FK equation requires the adaptation of the previously introduced spectral method to account for the additional reaction term. We present the space-fractional FK model and the modified spectral approach to compute its solution in Section 5.2. The results of our numerical simulation of the fractional FK equation on a finite one-dimensional interval are then provided in Section 5.3 and a study of the solution properties is undertaken via the introduction of the concept of level sets and the analysis of their location as a function of time. Finally, motivated by the fact that in the practical application considered there seems to be a link between different cell migration patterns and different regions of the gut, in Section 5.4 we propose a possible strategy to model the observed phenomena by developing a fractional model in space with variable order α. The idea behind this approach is that we want to "switch" between fractional diffusion ($\alpha < 2$) and standard diffusion ($\alpha = 2$) in different regions of the spatial domain.

The content of this chapter is based on the ideas we presented in [21] and

essentially follows the main structure of that paper. However, the formulation of the problem and the numerical strategies used have all been changed in light of the theoretical results obtained in Chapter 4. In addition, different considerations and a more detailed discussion on the case of the space-fractional modification with variable order are made.

5.2 The fractional FK model

Our first objective in this chapter is to study the effect of a space-fractional component on the solution of the FK model presented in Chapter 2. Therefore, we start from the dimensionless formulation of the FK model given by equation (2.4) and for $t > 0$ we consider the following PDE problem:

$$\begin{cases} \frac{\partial u}{\partial t} = -(-\Delta)^{\alpha/2} u + u(1-u) \\ u(x,0) = f(x), \end{cases} \tag{5.1}$$

on an insulated one-dimensional domain $[0, L]$ where $f(x)$ is a given initial condition.

For all $\alpha \in (1, 2]$, in accordance with our insulation assumption for the spatial domain, the definition of the non-local operator $(-\Delta)^{\alpha/2}$ is as given in Chapter 4 and can be thought of in terms of the one-dimensional Riesz–Feller operator coupled with reflecting boundary conditions at both ends of $[0, L]$ or, equivalently, in terms of the spectral decomposition of the standard one-dimensional Laplacian operator as shown in Section 4.4. Either way, when $\alpha = 2$, the above PDE reduces to the standard FK equation coupled with homogeneous Neumann boundary conditions at both ends of the spatial domain.

5.2.1 The modified spectral approach

Let $g(u) := u(1-u)$. Using the spectral definition of the fractional Laplacian and wanting to apply the spectral method to compute the solution of equation (5.1), we need now to account for the reaction term $g(u)$ and consider

a spectral decomposition of this term. An analytic form for the exact solution of (5.1) is not available for this particular problem. However, we still compute the solution in the form $u(x,t) = \sum_{j=0}^{\infty} \hat{u}_j(t)\varphi_j(x)$, where $\{\varphi_j(x)\}_0^\infty$ is the set of eigenfunctions of $(-\Delta)^{\alpha/2}$ and thanks to their orthogonality, each coefficient $\hat{u}_j(t)$ can be approximated independently according to the temporal integration scheme chosen.

Let us consider a uniform time grid of points $t_k = k\,\Delta t$ for $k = 0, 1, 2, \ldots$. Let $\hat{u}_j^k$ represent the approximation of the Fourier coefficient $\hat{u}_j(t)$ at $t = t_k$ and let us choose the semi-implicit Euler scheme for the time integration step (in which the nonlinear term $g(u)$ is considered explicitly). We hence obtain that for all $j = 0, 1, 2, \ldots$, the coefficients in the spectral decomposition of the solution at t_{k+1} can be computed as

$$\hat{u}_j^{k+1} = \frac{1}{1 + \lambda_j^{\alpha/2}\Delta t}\left[\hat{u}_j^k - \Delta t\,\hat{g}_j(u^k)\right], \tag{5.2}$$

where $\{\lambda_j\}_0^\infty$ is the set of eigenvalues of the standard Laplacian with standard homogeneous Neumann boundary conditions and $\hat{g}_j(u^k)$ is the j-th Fourier coefficient of the spectral expansion of the source term evaluated at $u^k = u(x, t_k)$, that is,

$$\hat{g}_j(u^k) = \int_0^L g(u(x,t_k))\varphi_j(x)\,dx.$$

Once again, for practical reasons, the numerical solution is computed on a discrete grid of $N+1$ nodes $x_i = i\,h$ for $i = 0, 1, \ldots, N$, where the uniform mesh size is defined as $h = \frac{L}{N}$, the integrals are approximated via the trapezoidal rule on the considered grid, and in the spectral representation of the solution only a finite number of eigenfunctions equal to the number of nodes of the spatial mesh is used.

5.3 Numerical results

We will now use the modified spectral method presented in Section 5.2 to compute the solution of equation (5.1) for a given initial condition in both

the standard case, $\alpha = 2$, and in the purely fractional case, that is, for a fixed value of $\alpha \in (1, 2)$. We then compare the solution behaviour obtained from our simulations and make some connections with analytical results available in the literature.

Let us consider the spatial domain $[0, 50]$ for the non-dimensional variable x and the following initial condition:

$$f(x) = \begin{cases} 1 & \text{if } x \leq 5 \\ e^{-10(x-5)} & \text{if } x > 5. \end{cases} \tag{5.3}$$

Recalling that $\lambda_j = \left(\frac{j\pi}{L}\right)^2$ for $j = 0, 1, 2, \ldots$, and the eigenfunctions $\varphi_j(x)$ are defined as

$$\varphi_j(x) = \begin{cases} \frac{1}{\sqrt{L}} & \text{if } j = 0 \\ \\ \sqrt{\frac{2}{L}} \cos\left(\frac{j\pi x}{L}\right) & \text{if } j > 0, \end{cases}$$

we here define a spatial mesh of $N + 1 = 1001$ nodes $x_i = i\,h$ with uniform spacing $h = 0.05$ and compute the evolution in time of the solution profile via the semi-implicit Euler method on a regular time grid with time step $\Delta t = 0.25$ for values of $t \in [0, 25]$.

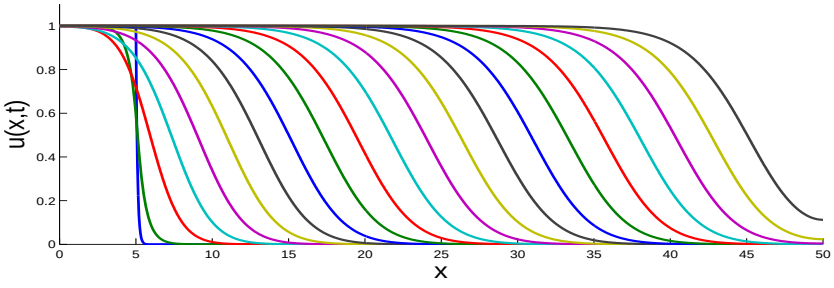

Figure 5.1: *Time evolution of the solution computed via the spectral approach and the semi-implicit Euler method from equation (5.1) when $\alpha = 2$ and the initial condition is as given in equation (5.3). The solution is computed on a uniform mesh of* 1001 *nodes and plotted at regular time intervals of* $\Delta t = 1.25$.

In Figure 5.1 we plot the evolution in time of our truncated spectral solution in the case $\alpha = 2$ at regular time intervals of $\Delta t = 1.25$. As expected, according to the results presented in Chapter 3, in the standard case the exponentially decaying initial condition $f(x)$ given by equation (5.3) evolves in time to a travelling wave solution moving towards the right end of the spatial interval $[0, L]$ with constant shape and speed. In particular, according to the analytic results reported in Chapter 2 (see dispersion relation (2.9)), for this particular initial condition we can show that the value of the front speed is equal to $c = 2$.

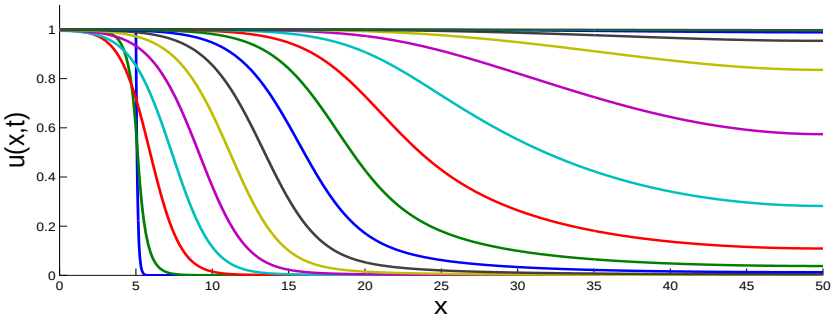

Figure 5.2: *Time evolution of the solution computed via the spectral approach and the semi-implicit Euler method from equation (5.1) when* $\alpha = 1.95$. *The initial condition is once again as given in equation (5.3). The solution is computed on a uniform mesh of* 1001 *nodes and plotted at regular time intervals of* $\Delta t = 1.25$.

On the other hand, if we compute the solution of equation (5.1) in the purely fractional case, that is, for a value of the fractional order $\alpha < 2$, the travelling wave nature of the solution generated by the same initial condition $f(x)$ is completely lost. If we observe Figure 5.2, where the spectral solution has been computed with $\alpha = 1.95$ and plotted at regular time intervals of $\Delta t = 1.25$ (the solution is therefore plotted at the same time points used for the standard case in Figure 5.1), we observe a rapid deformation of the solution profile towards the stable steady state $u = 1$ of the spatially homogeneous system corresponding to the PDE (5.1). More precisely, following the work done by Engler [26], Cabré and Roquejoffre [15], or Schumacher [75], we can

quantify this rapid deformation by introducing the concept of level sets and by tracing their position in time.

5.3.1 Level sets

For a fixed value $s \in (0,1)$, the corresponding level set is defined as the set of positions $x_s(t) \in [0, L]$ such that $u(x_s(t), t) = s$. Graphically, the level set corresponding to a given $s \in (0,1)$ is given by the time dependent set of x-coordinates of the intersection points between the solution $u(x,t)$ and the horizontal line $u = s$.

In Figure 5.3, we use horizontal dashed lines to help us visualize the level sets corresponding to four different values of s, namely $s = 0.1$, $s = 0.4$, $s = 0.5$ and $s = 0.6$. Note that, at a given time point t_k (that is for a fixed solution profile, for example, the green line in the middle of Figure 5.3), if we compare the location $x_s(t_k)$ for different values of s, we find that the lower the value of s is, the more advanced will be the corresponding position (as pointed out by the arrows in Figure 5.3).

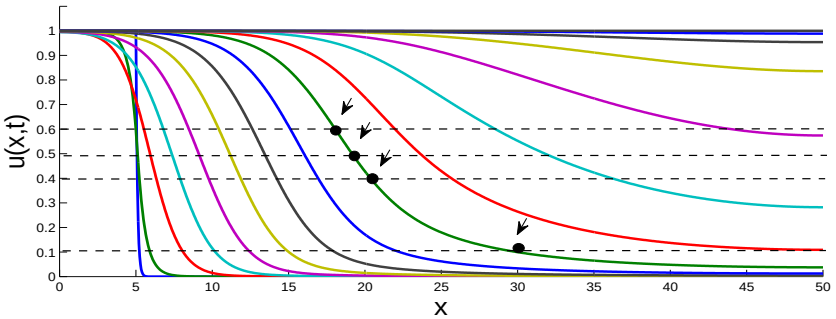

Figure 5.3: *The evolution in time of $x_s(t)$ for $s = 0.1$, $s = 0.4$, $s = 0.5$ and $s = 0.6$ at regular time intervals of $\Delta t = 1.25$ for the solution to the fractional FK model with $\alpha = 1.95$ is given by the x-coordinates of the intersection points between the horizontal dashed lines and each solution profile plotted. As indicated by the arrows, if we compare different level sets at the same time point, we obtain that the lower the value of s, the more advanced will be the corresponding level set position.*

If we trace[2] the position $x_s(t)$ for three different values of $s \in (0,1)$, namely $s = 0.4$, $s = 0.5$ and $s = 0.6$, at each time step t_k of our numerical simulations in both the standard and the fractional cases, and plot these positions as a function of time, we obtain the results shown in Figure 5.4. When $\alpha = 2$, as expected, all level sets advance linearly in time, mirroring the fact that the solution front moves forward with constant shape and speed. However, when $\alpha = 1.95$, the situation is quite different and there is a clear acceleration of each level set towards the right end of the spatial interval.

Note that, since the solution quickly moves towards $u = 1$ and is eventually equal to the steady state on the entire length of the interval, there will be a time point past which it is not possible to trace the considered level set anymore. The smaller the value of s, the sooner the solution will be greater than s on the entire interval. In other words, if $s_1 < s_2$, we expect the position $x_{s_1}(t)$ to reach the right end of the spatial interval $L = 50$ faster than $x_{s_2}(t)$ (as can be seen from Figure 5.4(b)). However, regardless of the particular value of s considered, as we can see from Figure 5.4 the position $x_s(t)$ advances exponentially in time towards the right end of the spatial domain (in agreement with the results by Engler [26] and Cabré and Roquejoffre [15]).

Similar considerations can be made when comparing the solution to the standard problem and the solution to the fractional modification of the model for all other values of $\alpha \in (1,2)$, the only difference being a faster acceleration towards $u = 1$ of each solution profile as the fractional order α decreases.

In the next section of this chapter we aim to develop a model in which a different value of α characterises different regions of the spatial domain.

[2]Given the discrete character of our numerical solution, in order to approximate the location of the considered level sets at each time step of our simulations, we simply use a linear interpolation scheme similar to the one presented in Section 3.1.1 (see Figure 3.1) and used to estimate the wave speed of the advancing front.

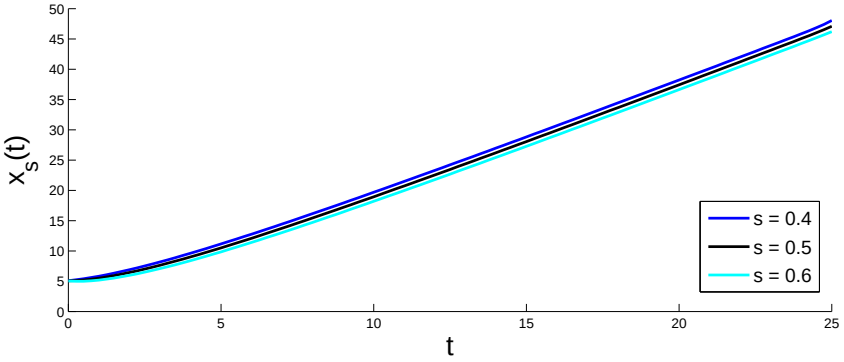

(a) $\alpha = 2$

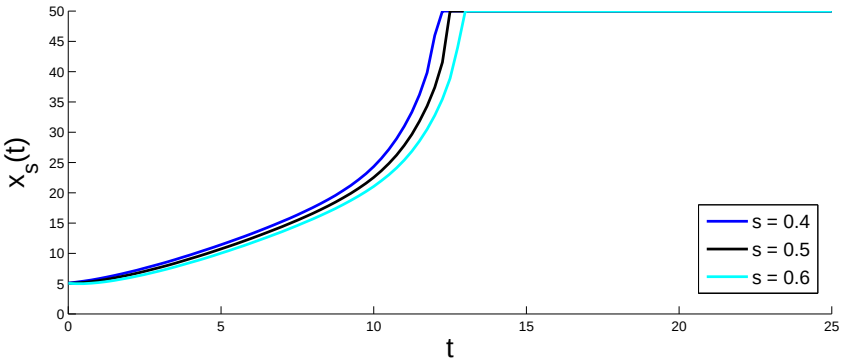

(b) $\alpha = 1.95$

Figure 5.4: *Comparison of the level set evolution in time for three different values of* $s \in (0, 1)$ *in the (a) standard and (b) fractional case.*

5.4 Variable fractional order

Having in mind the particular application considered at the beginning of the chapter and in light of the numerical results obtained for the fractional FK model in the previous section, we aim now at finding a possible way to model, for example, what happens after the pause at the caecum base in the neural crest-derived cell migration process.

If we think of the solution $u(x,t)$ as the neural crest cell concentration at a particular point x along the longitudinal axis of the gut at time t, we want to investigate whether implementing a variation of the fractional FK model with spatially varying α could help us characterise the different behaviour observed in the caecal region and in the subsequent region of the gut.

We therefore reformulate the problem as follows:

$$\begin{cases} \frac{\partial u}{\partial t} = -(-\Delta)^{\alpha(x)/2}u + u(1-u) \\ u(x,0) = f(x), \end{cases} \tag{5.4}$$

where the only difference between (5.1) and (5.4) is in the spatial dependence of the fractional order being now $\alpha = \alpha(x)$. We consider here the one-dimensional spatial interval $[0, 2L]$ with insulating boundary conditions at both ends and assume that the first half of our spatial domain, $[0, L]$, ideally corresponds to the caecum and the second half, $(L, 2L]$, represents the following region of the gut. We are hence interested in investigating the effect of defining $\alpha(x) = \bar{\alpha} < 2$ on $[0, L]$ and $\alpha(x) = 2$ on the rest of the domain.

However, before considering the practical aspects of our numerical simulations, we must discuss how the non-local operator $(-\Delta)^{\alpha(x)/2}$ should be interpreted when $\alpha(x)$ is not constant.

In particular, we discuss here the case of $\alpha(x)$ a piecewise constant function

of the form

$$\alpha(x) = \begin{cases} \alpha_1 & \text{on } \Omega_1 \\ \alpha_2 & \text{on } \Omega_2, \end{cases}$$

where Ω_1 and Ω_2 are non-overlapping intervals such that $\Omega_1 \cup \Omega_2$ is the entire domain Ω. We also assume that the finite one-dimensional spatial domain Ω is insulated so that if $\alpha_1 = \alpha_2 = \alpha$ for all $x \in \Omega$, the definition of the operator $(-\Delta)^{\alpha(x)/2}$ reduces to the one considered so far in this thesis.

When $\alpha_1 \neq \alpha_2$, one could build the solution u of the problem (5.4) on Ω as

$$u(x,t) = u_1(x,t)\chi_1(x) + u_2(x,t)\chi_2(x),$$

where for $i = 1, 2$, χ_i is the characteristic function

$$\chi_i(x) = \begin{cases} 1 & \text{if } x \in \Omega_i \\ 0 & \text{elsewhere,} \end{cases}$$

and u_i is the solution of the PDE

$$\frac{\partial u_i}{\partial t} = -(-\Delta)^{\alpha_i/2} u_i + u_i(1 - u_i)$$

on Ω_i, satisfying the additional conditions $u_1 = u_2$ and $\frac{\partial u_1}{\partial x} = \frac{\partial u_2}{\partial x}$ at the interface between Ω_1 and Ω_2.

This approach has been studied by Ilić et al. [36] in the case $g(u) = 0$, with the definition of the fractional Laplacian essentially given by the matrix transfer technique. However, we notice that the proposed approach presents a number of complications that we would like to avoid in designing the solution methodology that best represents the assumptions made on the considered problem.

For example, we immediately notice that this approach requires the introduction of additional boundary conditions at the interface between the two spatial domains so that the definition of each operator $(-\Delta)^{\alpha_i/2}$ on Ω_i is well-posed. We also observe that assuming either homogeneous Dirichlet or

reflective boundary conditions at the interface would result in the imposition of unwanted additional restrictions to the solutions u_1 and u_2, resulting in an incorrect global solution u.

For example, we have seen in Chapter 4 that imposing reflective boundary conditions at both ends of a finite one-dimensional interval $[0, L]$ corresponds to the assumption of $[0, L]$ being an insulated domain. Therefore, if we imposed reflective boundary conditions at the ends of Ω and at the interface, that is, at both ends of Ω_1 and at both ends of Ω_2, we would end up with two insulated domains and according to this assumption nothing would ever cross the interface. On the other hand, homogeneous Dirichlet boundary conditions at the interface would force the global solution to be always equal to zero at that point. Moreover, they would introduce the additional difficulty of having to deal with two non-local operators with mixed boundary conditions due to the initial insulation assumption made for Ω.

There are of course a number of other options for the boundary conditions that could possibly be considered at the interface and correspond, for example, to non-homogeneous standard boundary conditions. However, our interest lies in solving space-fractional problems[3] and for these types of model a unified and clear definition of the meaning and the implementation of the fractional Laplacian with non-homogeneous boundary conditions has not been developed yet.

We hence believe that a preferable approach to the problem of interest is to consider the action of the spatially varying operator $(-\Delta)^{\alpha(x)/2}$ as a whole on the global solution u and only impose reflective boundary conditions at both ends of the interval Ω, avoiding the issues related to having to provide additional conditions at the interface between subregions.

One final point we make here is that the convenient implementation of a fully diagonal spectral approach for $(-\Delta)^{\alpha(x)/2}$ is clearly possible only when

[3]At least one of the two values α_1 and α_2 in the definition of $\alpha(x)$ is strictly smaller than 2.

the eigenfunction and eigenvalue decomposition of the operator is known and the orthogonality of the eigenfunctions can be exploited in order to obtain a diagonal representation of the operator. We recall that our spectral method is based on the asymptotic result obtained in Section 4.4 for a constant fractional order and the fact that the continuous definition of the fractional Laplacian can be viewed as the limiting case for $N \longrightarrow \infty$ of its finite-difference approximation. However, in the case of a spatially varying α, knowledge of the spectrum of either the discrete or continuous operator is still unknown. Besides, we can guess that care must be taken in considering a number of nodes $N \longrightarrow \infty$ when α is spatially dependent due to the clear dependence of the discrete spectrum on the interplay between the number of nodes considered in the spatial discretisation, their location and the corresponding value of $\alpha(x)$. We therefore stress that, in our understanding, obtaining an asymptotic result similar to the case of a constant α is not so simple.

Although exploiting a spectral decomposition approach might not be possible in this case, defining a discrete approximation of $(-\Delta)^{\alpha(x)/2}$ in terms of the finite-difference approach and using the concept of reflecting boundary conditions still make sense. As we shall see in the following subsection, building such a discrete operator is not difficult and the numerical solution of the discretised problem possesses the main features we are aiming to reproduce with the newly developed model.

In light of the above considerations, to continue with our numerical simulations we here return to the method of lines (MOL) and the shifted Grünwald–Letnikov finite-difference approach for the approximation of the non-local one-dimensional operator $(-\Delta)^{\alpha(x)/2}$ on the insulated finite domain $[0, L]$.

5.4.1 Numerical implementation and results

Let us consider the equation (5.4) on the spatial interval $[0, 2L] = [0, 100]$, with initial condition $f(x)$ defined as in (5.3) and spatially variable fractional

order given as follows:

$$\alpha(x) = \begin{cases} \bar{\alpha} = 1.5 & \text{if } x \in [0, 50] \\ 2 & \text{if } x \in (50, 100]. \end{cases} \tag{5.5}$$

In order to obtain the discrete operator $A_{\alpha(x)}$ approximating $(-\Delta)^{\alpha(x)/2}$ on the insulated domain $[0, 2L]$, we introduce a uniform spatial grid with $N+1$ nodes $x_i = i\,h$ for $i = 0, 1, \ldots, N$, where the mesh size is $h = \frac{L}{N}$. We then use the shifted Grünwald–Letnikov approximation with reflecting boundary conditions at $x = 0$ and $x = 2L$ (as seen in Chapter 4) to approximate $(-\Delta)^{\alpha(x)/2}u$ at each point $x = x_i$ and build the corresponding row in $A_{\alpha(x)}$. At a given node x_i, the value $\alpha_i := \alpha(x_i)$ is a fixed constant (in our example either 1.5 or 2) and we can hence write the approximation of $(-\Delta)^{\alpha_i/2}u\Big|_{x=x_i}$ as the following inner product

$$(-\Delta)^{\alpha_i/2}u\Big|_{x=x_i} \approx A^{(i)}_{\alpha_i}\mathbf{u},$$

where, in the notation of Chapter 4, $A^{(i)}_{\alpha_i}$ indicates the $(i+1)$-th row of the reflection matrix with fractional order α_i, that is, the matrix A_{α_i}, and $\mathbf{u}$ represents the vector of solution approximations at the nodes used in the discretisation of the entire spatial domain, that is, $\mathbf{u}(t) = [u_0(t), u_1(t), \ldots, u_n(t)]^T$. Recall that, for a given $\alpha \in (1, 2]$, the entries of each row of the reflection matrix A_α involve the coefficient $\frac{c_\alpha}{h^\alpha}$ and suitable subseries of the sequence of weights $(\omega_j)_0^\infty$, where $c_\alpha = \frac{1}{2\cos(\alpha\pi/2)}$, h^α is the fractional power of the mesh size h, and each ω_j is defined as $\omega_j = (-1)^j\binom{\alpha}{j}$. Clearly, all these elements depend on the value of α considered.

In the particular case of $\alpha(x)$ defined as in (5.5), if the first $\bar{N}$ nodes belong to $[0, L]$ and the remaining $N+1-\bar{N}$ are in $(L, 2L]$, we obtain that the first $\bar{N}$ rows of the matrix $A_{\alpha(x)}$ coincide with the first $\bar{N}$ rows of the reflection matrix $A_{\bar{\alpha}}$ with $\bar{\alpha} = 1.5$, whereas the remaining $N+1-\bar{N}$ rows are as the last $N+1-\bar{N}$ rows of the discrete operator in the standard case, that is, as in the reflection matrix A_α with $\alpha = 2$. Hence, the discrete operator $A_{\alpha(x)}$

can be viewed as a block matrix

$$A_{\alpha(x)} = \left[\begin{array}{c|c} B & C \\ \hline D & E \end{array}\right], \tag{5.6}$$

where the $\bar{N} \times \bar{N}$ block B and the $\bar{N} \times (N + 1 - \bar{N})$ block C are dense and come from the reflection matrix $A_{\bar{\alpha}}$, the $(N + 1 - \bar{N}) \times \bar{N}$ block D is made of all zeros except for the entry in position $(1, \bar{N})$ set equal to $-\frac{1}{h^2}$ and the square block E of size $N + 1 - \bar{N}$ is a tridiagonal matrix corresponding to the finite-difference discretisation of the standard Laplacian $(-\Delta)$ with a second order approximation of the first order derivative at the boundary point $x_N = 2L$.

By using the above discretisation strategy, equation (5.4) can be then rewritten as a system of ODEs in the following form

$$\begin{cases} \mathbf{u}'(t) = -A_{\alpha(x)}\mathbf{u} + \mathbf{g}(\mathbf{u}) \\ \mathbf{u}(0) = \mathbf{f}, \end{cases} \tag{5.7}$$

where $\mathbf{g}(\mathbf{u})$ is the discretised source term, that is, the vector whose entries are defined as $u_i(t)\,(1 - u_i(t))$ for $i = 0, 1, \ldots, N$, and $\mathbf{f}$ is the discretised initial condition, that is, the vector obtained by evaluating the initial condition $f(x)$ at each node of the spatial mesh.

In order to obtain the temporal evolution of the discrete solution of equation (5.7), we then use the **ode15s** solver in MATLAB® and to improve its performance we provide the explicit form of the Jacobian J of the right-hand side of the considered system of ODEs. In fact, the matrix J is simply given by the sum $J = -A_{\alpha(x)} + G$, where $A_{\alpha(x)}$ is our discrete spatial operator and G is the Jacobian matrix of the source term, that is, the diagonal matrix with entries $G_{ii} = 1 - 2u_i \ \forall i$.

Figure 5.5 depicts the solution behaviour computed for equation (5.4) with $\alpha(x)$ defined as in (5.5) on a spatial grid of $N+1 = 2001$ nodes with uniform spacing $h = 0.05$. The numerical solution is computed for $t \in [0, 25]$ via the

adaptive time step solver **ode15s** in MATLAB®. We require however the solver to provide the solution at a given set of equally spaced time points so that we can observe its evolution in time with constant time steps. In Figure 5.5 we use time intervals of $\Delta t = 1.25$ to plot the solution profile.

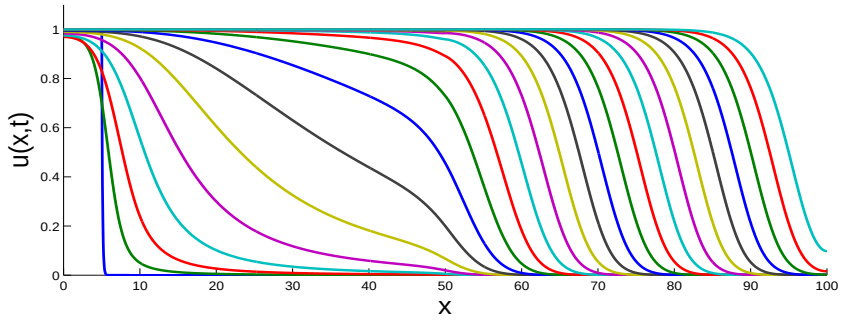

Figure 5.5: *Time evolution of the solution to equation (5.4) with spatially varying fractional order defined by equation (5.5). The solution is computed on a uniform spatial mesh of* $N + 1 = 2001$ *nodes via the MOL (as described in detail in the text) and here plotted at regular time intervals of* $\Delta t = 1.25$.

The consequence of using a spatially varying fractional order is clearly visible on the behaviour of the numerical solution obtained. Indeed, the solution initially moves in a similar fashion to that observed in the previous section, for the purely fractional case. However, the rapid movement of the solution profile towards the stable steady state $u = 1$ is here slowed down as the solution moves closer to the second half of the spatial interval where the dynamics is essentially governed by the standard FK equation. Once the profile enters this region, the effect of the fractional component of the model is not dominant anymore and the solution evolves to a travelling wave moving with constant shape and speed towards the right end of the spatial domain.

The main features of this solution behaviour can be captured by looking at the level sets $x_s(t)$ for $s \in (0, 1)$. In particular, we here focus on $s = 0.5$ and trace the position $x_{0.5}(t)$ for $t \in [0, 25]$ on a uniform grid with constant time step $\Delta t = 0.25$ via linear interpolation of the solution profile produced at

each of the considered time steps[4]. The resulting time evolution is reported in Figure 5.6 and can be successfully related to two important theoretical results available in the literature. In particular, the analysis done by Cabré and Roquejoffre [15] gives an estimate of the level set behaviour for large values of t in the solution of the fractional FK equation with constant fractional order α that in the one-dimensional case and with our notation[5] can be rewritten as

$$x_s(t) \sim e^{\sigma_* t}, \quad \text{where} \quad \sigma_* = \frac{1}{1+\alpha}.$$

On the other hand, the dispersion relation for the standard nondimensional FK equation provides an analytical value of the speed of advance of the front equal to $c = 2$. Therefore, in the standard case we expect each level set to advance in time as $x_s(t) \sim 2t$.

Figures 5.6(a) and 5.6(b) validate these results. Indeed, Figure 5.6(a) shows that the level set initially behaves in agreement[6] with the prediction by Cabré and Roquejoffre [15] for the purely fractional case with order $\alpha = \bar{\alpha}$. Once the level set reaches the second half of the spatial interval, the dynamics of the solution evolution in time changes significantly. As shown by Figure 5.6(b) the advance of $x_s(t)$ becomes in fact linear in time (with gradient $m = 2$), in perfect agreement with the result given by the dispersion relation in the standard case.

We conclude this section by making some comments on the numerical solution obtained and the practical application that inspired the development of our spatially varying fractional FK model.

[4]We specifically ask the adaptive solver to provide the solution on a uniform temporal mesh with $\Delta t = 0.25$.

[5]In [15] the authors actually consider $(-\Delta)^\beta$ on $\mathbb{R}^n$ with fractional order β chosen in the interval $(0, 1)$. Relating β to our definition of a constant fractional order α gives $\alpha = 2\beta$. This simple relationship has been used in obtaining the particular expression of the coefficient σ_* provided.

[6]In the comparison of our numerical solution to the theoretical result proposed in [15] we keep in mind that the non-local operator is here defined on a finite domain rather than $\mathbb{R}^n$ and tracing the considered level set for large values of t might not be possible.

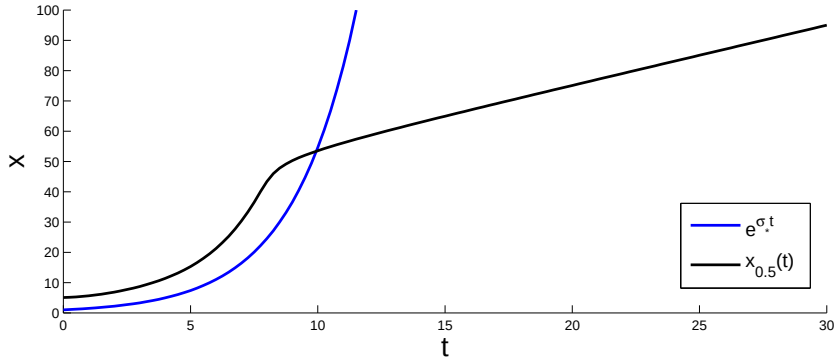

(a) Exp part

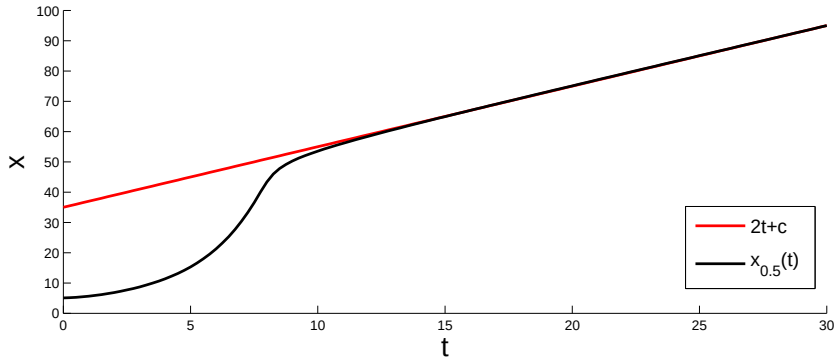

(b) Lin part

Figure 5.6: *Comparison between two fundamental theoretical results and the level set $x_{0.5}(t)$ traced from the solution of the spatially varying model (5.4) with $\alpha(x)$ given by (5.5). The black line in both plots represents $x_{0.5}(t)$. In (a) the level set is plotted together with the exponential function $e^{\sigma_* t}$ where $\sigma_* = \frac{1}{1+\bar{\alpha}}$ and $\bar{\alpha} = 1.5$ as in definition (5.5). In (b) the level set is plotted together with the linear function of time $2t + q$ where the intercept q has been chosen equal to $q = 35$ in order to match the two lines as t approaches the right end of its definition domain.*

If we let the function $u(x,t)$ represent the concentration of neural crest-derived cells along the longitudinal axis of the caecum and the subsequent region of the gut, the solution of our spatially variable model computed via the MOL reflects the main qualitative features emerging from the experimental data provided at the beginning of the chapter and characterising the invasive process observed in the developing intestine of mice embryos after the pause at the caecum base. When $\alpha(x) < 2$, that is, in the first half of our spatial domain, our numerical solution can be linked to the cell migration pattern observed in the caecum body. By looking at the level sets of the solution depicted in Figure 5.5 for different values of s we see a very fast advancing of $x_s(t)$ when we consider a low value of s (corresponding to a low cell concentration) followed by the rapid invasion of the subinterval representing the caecum by the rest of the cell population (high concentration level corresponding to a value of s close to 1). On the other hand, in the second half of the spatial interval, the assumption of a standard reaction-diffusion process results in a modification of the solution behaviour that can be related to the reestablishment of a complete network of strands and a regular advancing of the migrating front once the neural crest-derived cell population leaves the caecum and starts migrating into the following enteric region.

At this stage, due to the lack of more detailed experimental results on the front location and the speed values as functions of time, we are not able to validate our model any further but we believe that the qualitative behaviour of the invasion process after the period of pause at the caecum base is well-captured by our approach.

5.5 Discussion

The variable order fractional model proposed in this chapter is a new approach in the context of cell migration. The key aspect of this modelling approach is the possibility of changing from fractional to standard diffusion in different subintervals of the spatial domain, combining regions characterised by spatial heterogeneity with others where the invasion dynamics agrees with

the constant wave speed assumption. As discussed in Section 5.4, our model provides promising results in terms of reproducing important features of the qualitative behaviour of mouse enteric neural crest invasion *in vivo*. However, in our study we only focus on reproducing the main characteristics of the invasion process after the experimentally observed pause at the caecum base. The main reason behind our choice of focusing only on the specified spatial region and the temporal time frame following the pause at the caecum base is essentially the lack of a clear biological explanation for the alteration of the migrating behaviour observed in the midgut and at the caecum base.

Recent studies [10] seem to link the pause at the caecum base with an inhibitory effect due to some ligands of receptors strongly expressed in the caecum suggesting a chemotaxis effect to be introduced in the model. However, lack of detailed experimental data connecting the two phenomena makes it hard to develop (and especially validate) a model that takes this possible new effect into account.

We stress that the modelling approach presented here is certainly not the only possible way to reproduce the different migration patterns observed in *in vivo* experiments. Furthermore, in the literature we find a number of different modelling approaches that could provide deeper insight in the observed phenomena, such as models incorporating domain growth, for example as in [46] and [76]. Studies on how a subpopulation of embryonic cells travels long distances and responds to tissue growth to accurately reach a target present new interesting insights on the role of heterogeneity in an invading cell population. The fully integrative experimental-modelling approach proposed by McLennan et al. [54] analyses the migratory behaviour of cranial neural crest cells of a living chick embryo and shows that a simple cell chemotaxis model is insufficient to explain their experimental evidence. In order to reproduce a successful invasion of the domain *in silico*, the model was refined by introducing two neural crest cell populations (namely leading and trailing cells) which respond differently to local microenvironmental signals.

In particular, McLennan et al. [54] consider a two-dimensional domain growing in time along the x-axis according to a logistic function. The neural crest cell population has its own migrating ability but at the same time it is dragged along the domain by such growth. In this chapter, we do not consider the two-dimensional extension of the model but rather focus on the effect of a spatially varying fractional order reflecting different spatial connectivity properties of the gut structures in one dimension. We also do not present any model accounting for the effects of domain growth on the solution behaviour. However, we ran a few simulations taking into account both of these aspects and we report here some general considerations, leaving the detailed analysis of these extensions as possible future improvements of the model.

The idea behind a two-dimensional extension is to model the neural crest-derived cell concentration on the gut walls, where the gut is idealised as a long thin cylinder. We can identify our two-dimensional domain with the external surface of this cylinder cut along the gut length (x direction) and therefore model the problem on a long thin rectangle. The one-dimensional initial condition considered in Section 5.3 can be extended in a natural way to the two-dimensional problem by simply defining a uniform behaviour along the y direction (representing the cross-section of the gut). As a result, for a fixed rectangular domain, we observe that the behaviour of the two-dimensional solution (both in the standard diffusion case and in the case of fractional diffusion with variable fractional order $\alpha = \alpha(x)$) preserves the invariance along the y-axis and therefore, for all values of y, the solution profile along x is exactly the same.

Previous studies on gut elongation and cell migration in the standard diffusion case (see Binder et al. [7]) have shown that domain growth has an impact on both cell migration and proliferation and the choice of a particular function (or combination of functions) for the uniform (nonuniform) domain growth is fundamental in determining the solution behaviour.

In our simulations with a uniform growing one-dimensional domain we observe that, already in the standard diffusion case, the advancing front is not linear anymore but it is rather affected by the way the underlying domain elongates and the solution level sets reflect the assumptions made on the particular functional form chosen for $L(t)$ (the temporally dependent right end of the spatial interval). However, the introduction of a space-fractional component with variable order $\alpha(x)$ still produces an acceleration in the advancing of the front in the region where $\alpha(x) < 2$ resulting in a much larger difference in the time dependent position of different level sets in that particular region. Such an acceleration allows the front to rapidly reach a more advanced region of the domain and consequently move towards the end of the growing spatial interval in much shorter times than in the corresponding model with standard diffusion.

In our study we have only considered the case of a uniformly growing one-dimensional domain and made some general considerations for a specific functional form of $L(t)$. We do not exclude the fact that the choice of a different $L(t)$ or the assumption of nonuniform domain growth might produce qualitatively different results. Moreover, we acknowledge that the simultaneous use of a two-dimensional model and the assumption of a growing domain might lead to interesting results because the change in geometry (especially if nonuniform throughout the domain) is likely to affect the solution behaviour and could be responsible for changes in the speed of the advancing cell front.

Chapter 6

Space-fractional excitable media models

6.1 Motivation

Beside cell migration, another important application of mathematical modelling introduced in Chapter 2 and studied in this thesis is the propagation of electrical signals through excitable media. Excitable media models such as those given by equations (2.25) and (2.27) are typical mathematical tools used to reproduce *in silico* the generation and spread of electrical signals across excitable biological tissues. In particular, depending on the characteristics of the cell model used (determining the particular form of the ionic current, the number of gating variables involved and the set of ODEs governing their time evolution), we are able to reproduce the main features of the action potential observed for cells in different types of excitable media.

In this thesis, as seen in Chapters 2 and 3, we focus on two relatively simple cell models capturing the main qualitative features of the action potential that excitable cells undergo in neural tissue (when considering the FHN model) and in cardiac muscle (when using the BR model). The equations derived in both cases to describe electrical propagation in space at a macroscopic level are based on modelling strategies that represent the tissue as

a continuum structure characterised by space average quantities according to the homogenisation principle [32], that is, under the assumption that the complexity of the composite structure observed at the microscale has a negligible effect on the propagation of electrical signals at the macroscale.

In the case of cardiac tissue, as discussed by Clayton in [19], despite being the main assumption behind most of the available cardiac tissue models and having allowed over the years the discovery of many important findings, the use of the homogenisation principle has well-established limitations in representing the heterogeneous tissue microstructure and the effects on modulation of signal conduction due to different levels of heterogeneity. The same type of argument can be extended also to the case of neural tissue, where the applicability of the homogenisation assumption can again be questioned (see for example Nelson et al. [64]), given the high level of inhomogeneity clearly present in the medium.

When heterogeneity and complex connectivity properties characterize the medium in which the transport phenomenon is observed on a very large number of scales (as in the case of cardiac tissue and pulse propagation), space-fractional models have been proposed as an alternative modelling approach. As thoroughly discussed by Bueno–Orovio et al. [12], fractional models in space incorporate multiscale effects of transport processes in complex heterogeneous media and can therefore offer important insight into mechanisms that cannot be investigated via classical standard diffusion modelling techniques. In fact, as reported in [12], "traditional approaches to understand the role of tissue heterogeneity in cardiac conduction have been based on the combination of standard diffusion models with high resolution anatomical reconstructions of tissue structure. [...] Finer anatomical features, such as capillaries or intercellular cleft spaces, would imply, however, the use of anatomical models at submicrometre resolution, which are currently intractable even with the most advanced high-performance facilities. [...] As an alternative, the proposed fractional diffusion models represent a flexible approach to characterize the role of cardiac microstructure in electrical prop-

agation in terms of computational tractability, because spatial discretization is retained at a mesoscopic and not subcellular scale."

The numerical results presented in the work by Bueno–Orovio et al. [12] show good agreement between numerical solutions to space-fractional modifications of standard cardiac models with experimental data and indicate that values of $\alpha < 2$ reproduce many interesting tissue properties.

The promising successful results highlighted above and the challenges related to the use of classical standard diffusion models in handling the presence of heterogeneity on a number of scales in complex media such as the heart or the brain are the core motivations behind the simulation study reported in this chapter. The relative simplicity of the cell models considered for the study and the adoption of a number of modelling simplifications were made in order to contain the problem size and to allow the computation of their solution in a short amount of time (without the need of turning to high performance computers). This work does not intend to produce results that could be directly compared to the ones produced by state-of-the-art models of the heart or the brain. Our aim will rather be the use of one-dimensional and two-dimensional simplified models of electrical pulse propagation in confined regular domains to highlight the consequences and eventual issues related to the implementation and solution of their non-local modifications, laying the foundations for much more complex simulations on a much larger scale.

In this chapter we will combine the methods typically used to solve excitable media problems with the results obtained in Chapter 4 in order to implement a space-fractional modification of the spatially varying FHN and BR models presented in Chapter 2 and investigate how the presence of a non-local operator in space affects the solution of the corresponding standard diffusion model. As in Chapter 3, we will start by considering the simpler case of one-dimensional models. In Sections 6.2 and 6.3, after describing the numerical approach adopted here to compute the one-dimensional solutions, we will provide a set of results highlighting the effect of considering different values

of $\alpha \in (1, 2]$ and the possible numerical and computational challenges related to the use of a particular fractional parameter.

The results obtained in Chapter 4 for $(-\Delta)^{\alpha/2}$ using the concept of reflections have been proved in the one-dimensional case. A generalisation of these ideas to higher dimensions is not trivial and as we shall see in Section 6.4, different methods can be developed to introduce non-locality in space in these settings. The two options proposed will then be used in Section 6.5 to produce some simulation results for the space-fractional modification of the excitable media models of interest in two spatial dimensions. A discussion on the results obtained and on further directions for the proposed study concludes the chapter.

6.2 Solution strategy for space-fractional excitable media models in 1D

As observed in Chapters 2 and 3, when introducing spatial dependence in a given cell model, the classical approach is to consider the bidomain formulation of the model. Under the assumption of proportionality of the diffusion tensors of the intracellular and extracellular domains, such a formulation can be then simplified mathematically and reduced into a form, namely the monodomain formulation, that is much easier to deal with from the numerical point of view.

In this chapter, in both one and two spatial dimensions, we consider the monodomain formulation of the two cell models of interest (that is, FHN and BR) and develop their non-local counterparts by introducing in the monodomain equation a fractional operator in space.

For a given cell model the monodomain formulation of the spatially varying problem on a one-dimensional interval $[0, L]$ and for $t > 0$ can be written as

follows:

$$\begin{cases} \dfrac{\partial v}{\partial t} &= -\dfrac{\lambda}{1+\lambda}\dfrac{M_i}{\chi}\left(-\dfrac{\partial^2 v}{\partial x^2}\right) - I_{\text{ion}}(v, \mathbf{z}) + \dfrac{1}{\chi} I^{(\text{vol})} \\ \\ \dfrac{d\mathbf{z}}{dt} &= \mathbf{f}(v, \mathbf{z}), \end{cases} \tag{6.1}$$

where v is the transmembrane potential, λ is the coefficient of proportionality between the intracellular and extracellular diffusivity tensors, χ is the surface to volume ratio, M_i is the intracellular diffusivity constant[1], I_{ion} is the ionic current of the model, $\mathbf{z}$ is the vector of additional variables associated with the particular cell model considered, $I^{(\text{vol})}$ is the applied stimulus used here to trigger an action potential and $\mathbf{f}$ is the vector-valued function determining the evolution in time of the set of additional variables considered in the vector $\mathbf{z}$ (and therefore clearly depends on the cell model). The system of equations (6.1) is then coupled with suitable boundary conditions and an initial condition for the problem is provided.

Under the hypothesis of $[0, L]$ being an insulated domain, we can introduce the following space-fractional modification of the above model

$$\begin{cases} \dfrac{\partial v}{\partial t} &= -\dfrac{\lambda}{1+\lambda}\dfrac{M_i}{\chi}(-\Delta)^{\alpha/2} v - I_{\text{ion}}(v, \mathbf{z}) + \dfrac{1}{\chi} I^{(\text{vol})} \\ \\ \dfrac{d\mathbf{z}}{dt} &= \mathbf{f}(v, \mathbf{z}), \end{cases} \tag{6.2}$$

where $(-\Delta)^{\alpha/2}$ is the one-dimensional fractional Laplacian defined as in Section 4.4 and incorporating in its spectral definition the effect of reflecting boundary conditions associated with the non-local problem.

In order to compute the solution of the above fractional modification, we follow once again the approach proposed by Whiteley [83] and described in Section 3.3. After introducing a uniform time discretisation, the numeri-

[1]Since the model considered is one-dimensional, the diffusivity tensor simply reduces to a constant.

cal solution is computed at each time step by first solving the PDE for the transmembrane potential (while keeping the value of $\mathbf{z}$ fixed) and then updating the gating variables by using the newly computed value of v. The strategy used to update the vector of additional variables $\mathbf{z}$ is once again as described in Chapter 3 and exploits the fact that for most of these variables, the right-hand side of the corresponding ODE is linear in the considered variable. Therefore, the backward differentiation formula allows us to obtain an unconditionally stable explicit expression of the updated value[2]. The main difference between the strategy presented here and the one used in the standard case of Chapter 3 is that instead of introducing a spatial discretisation of the fractional operator and transforming the PDE of system (6.2) into a system of ODEs, we now exploit the asymptotic result obtained in Section 4.4 and compute the solution of the space-fractional PDE via the modified spectral approach described in Section 5.2 for the solution of the fractional Fisher–Kolmogoroff equation.

The solution v is decomposed as $v(x,t) = \sum_{j=0}^{\infty} \hat{v}_j(t)\varphi_j(x)$, in terms of the eigenfunctions $\{\varphi_j\}$ of the fractional one-dimensional Laplacian $(-\Delta)^{\alpha/2}$ on the insulated domain and the coefficients $\hat{v}_j(t)$ are computed on the given temporal grid of points $t_k = k\,\Delta t$ by using a semi-implicit Euler scheme, that is,

$$\hat{v}_j^{k+1} = \frac{1}{1 + \Delta t \frac{\lambda}{1+\lambda}\frac{M_i}{\chi}\,\lambda_j^{\alpha/2}} \Big[\hat{v}_j^k + \Delta t\,\hat{g}_j(v^k, \mathbf{z}^k)\Big], \tag{6.3}$$

where $\{\lambda_j^{\alpha/2}\}$ is the set of eigenvalues of the non-local operator $(-\Delta)^{\alpha/2}$ and $\hat{g}_j$ is the j-th Fourier coefficient of the spectral expansion of the source term $g(v,\mathbf{z}) := -I_{\text{ion}}(v,\mathbf{z}) + \frac{1}{\chi} I^{(\text{vol})}$ evaluated at v^k and $\mathbf{z}^k$.

Once again for practical reasons the eigenfunction expansion of the solution and the source term are truncated after a finite number of terms and the approximation of the integral coefficients $\hat{v}_j^k$ and $\hat{g}_j^k$ is computed via the trapezoidal rule.

[2]When the right-hand side of the equation is not linear, as in the case of the calcium concentration for the BR cell model, the Newton method is used instead.

We recognize that the trapezoidal rule might not be the best method for the approximation of integrals of the form $\int_a^b r(x)\,\cos(\omega x)\,dx$ when the frequency ω determines a highly oscillatory behaviour of the integrand[3]. To give an idea of the type of problems we could face in using the trapezoidal rule with highly oscillatory integrands we consider the following example involving the eigenfunction of our problem of interest. Recalling that $\varphi_j(x) = \sqrt{\frac{2}{L}}\cos\left(\frac{jx\pi}{L}\right)$ and by introducing a uniform grid of $N+1$ nodes $x_i = i\,h$ with $h = \frac{L}{N}$, we have

$$\varphi_j(x_i) = \sqrt{\frac{2}{L}}\cos\left(\frac{ji\pi}{N}\right) \quad \text{for all } j \geq 0 \text{ and } i = 0, 1, \ldots, N.$$

If $j = 2N$, then $\cos\left(\frac{2Ni\pi}{N}\right) = \cos\left(2i\pi\right) = +1$ for all values of $i \in \{0, \ldots, N\}$. Therefore, the approximation of $\int_0^L \varphi_{2N}(x)\,dx$ via the trapezoidal rule on the given spatial mesh returns the quantity

$$\sqrt{\frac{2}{L}}\,\frac{1}{h}\left[1 + 2\sum_{i=1}^{N}\cos\left(2i\pi\right) + \cos\left(2(N+1)\pi\right)\right] = \sqrt{\frac{2}{L}}\,\frac{2(N+1)}{h},$$

instead of the actual zero value of the integral considered.

In order to avoid this type of approximation issue in our implementation we must hence ensure that the value of $\frac{j}{N}$ does not become too large. However, in order for the truncated expansion of the solution to be sufficiently accurate we might have to consider a large number of eigenfunctions and consequently compute the approximation of $\hat{v}_j^k$ and $\hat{g}_j$ for large values of j.

To bypass the problem while still exploiting the simplicity of implementation of the trapezoidal rule, we simply decide to increase the number $N+1$ of nodes considered for the spatial interval and truncate the eigenfunction expansion after a number of terms equal to the number of nodes. In doing so we note that the ratio $\frac{j}{N} \leq 1$ for all the considered values of j and therefore the frequency of the eigenfunctions remains always contained and the approximation of all the required Fourier coefficients can be made via the

[3]In this case a much more appropriate integration scheme could be given by Filon-type approximations (see for example Iserles [37]).

trapezoidal rule.

6.3 One-dimensional numerical simulations

We now provide a set of simulation results in the one-dimensional case for the space-fractional modification of both the FHN and the BR monodomain models. Independently from the particular cell model considered, the numerical strategy presented in the previous section will be used to compute the solution of system (6.2) for different values of α, while keeping fixed all other parameters. The comparison between solutions obtained for a given ionic model will be made by studying the effect of reducing the parameter α on some important features characterizing the spatial and temporal evolution of the excitation wave in the standard case.

Throughout the chapter we assume that the parameter λ in the monodomain formulation is $\lambda = 1$ (resulting in $\frac{\lambda}{1+\lambda} = 0.5$), the surface to volume ratio is $\chi = 2000\,\mathrm{cm}^{-1}$, the constant diffusivity coefficient is $M_i = 1\,\mathrm{mS}\cdot\mathrm{cm}^{-1}$ and all the functional forms and parameters of the FHN and BR ionic models are given as in Section 2.1.2, Table 2.1 and Table 2.2.

In all simulations we assume that initially the transmembrane potential and all the additional variables are at rest and at $t = 10\,\mathrm{msec}$ an electrical stimulus $I^{(\mathrm{vol})}$ is applied to the left end of the spatial interval for five consecutive milliseconds and then removed.

In all the simulations run for this section we also consider a uniform spatial grid with mesh size $h = 0.004\,\mathrm{cm}$ and a uniform grid in time with time step $\Delta t = 0.01\,\mathrm{msec}$. However, depending on the type of result we want to show, the size of the spatial interval $[0, L]$ and/or the temporal interval $[0, t_f]$ on which the solution is computed might vary.

With the above choice of parameters, in the standard case ($\alpha = 2$), we observe that a stimulus $I^{(\mathrm{vol})} = 10^5\,\mu\mathrm{A}\cdot\mathrm{cm}^{-3}$ triggers for both cell models the

propagation throughout the domain of a travelling pulse with the characteristic shape determined by the considered ionic model (as seen in Section 3.3).

In Figure 6.1 we report the evolution in time of the travelling pulse produced by the considered stimulus when the solution of system (6.2) is computed in the case $\alpha = 2$.

In order to visualise how the entire pulse moves in space from the point of application of the electrical stimulus to the other end of the domain (that is, towards $x = L$), we choose L larger than the characteristic width of the travelling pulse produced by each model with the considered simulation parameters. In particular, we define $L = 2\,\text{cm}$ for the FHN model and $L = 10\,\text{cm}$ in the BR case. Having fixed the spatial mesh size to be $h = 0.004$, these choices of L result in two spatial meshes with $N + 1 = 501$ (FHN) and $N + 1 = 2501$ (BR) nodes, respectively. In both Figure 6.1(a) and Figure 6.1(b) the solution is plotted on the corresponding spatial mesh at regular intervals of 50 msec in time.

The same electrical stimulus applied to the system (6.2) in the case of $\alpha < 2$ still produces a travelling pulse moving towards $x = L$ as time increases and having the same shape determined by the ionic model in the corresponding standard case. The use of $\alpha < 2$ however affects the width of the travelling pulse and the speed of advancing of the moving pulse in space, that is, its conduction velocity. These effects are clearly visible in Figure 6.2 where the solution of system (6.2) is plotted at the same time point $t = \bar{t}\,\text{msec}$ for six different values of the parameter α on the fine mesh of the spatial interval of interest.

The value of $\bar{t}$ was chosen so that in the standard case the depolarization front of the advancing pulse has travelled at least 90% of the total length of the spatial interval considered. In particular, $\bar{t} = 500\,\text{msec}$ in the FHN case and $\bar{t} = 400\,\text{msec}$ for the BR model. The solution of system (6.2) for all other values of α considered was then plotted at the same time point $\bar{t}$ on the same graph.

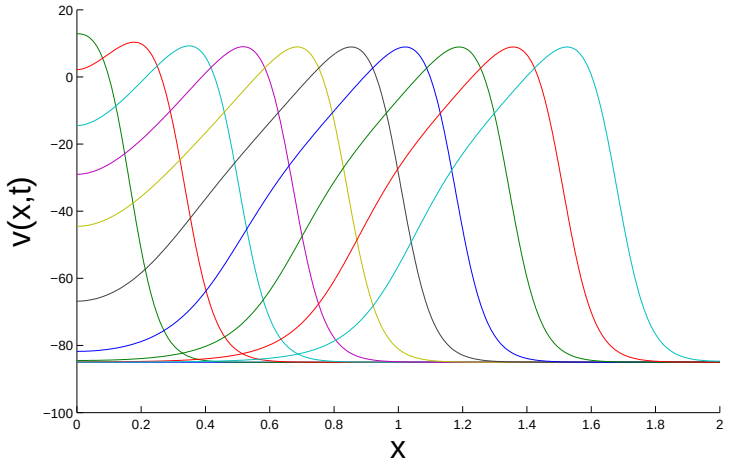

(a) FHN

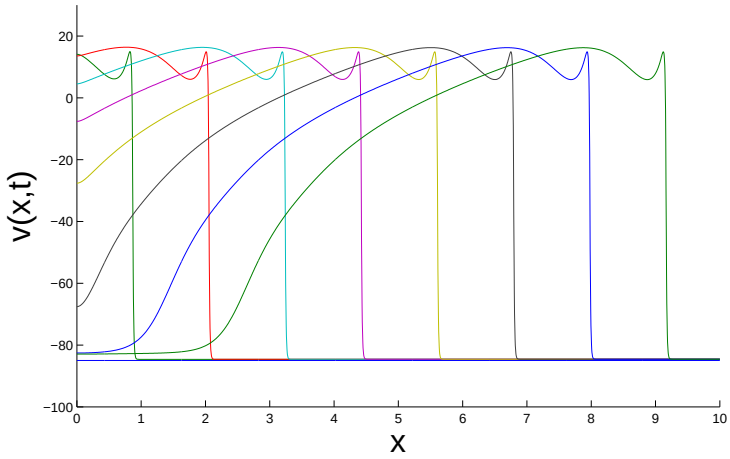

(b) BR

Figure 6.1: *Evolution in time of the solution to the standard one-dimensional monodomain FHN model (a) and the monodomain BR model (b) computed via spectral decomposition of the solution on a spatial grid with uniform spacing* $h = 0.004\,\mathrm{cm}$ *and on a uniform temporal grid with time step of* $0.01\,\mathrm{msec}$. *In both plots the evolution of the transmembrane potential* v *in the considered spatial domain is plotted at regular time intervals of* $\Delta t = 50\,\mathrm{msec}$.

As α decreases we find that the width of the pulse is reduced and the distance covered by the moving wave becomes shorter, intuitively corresponding to a

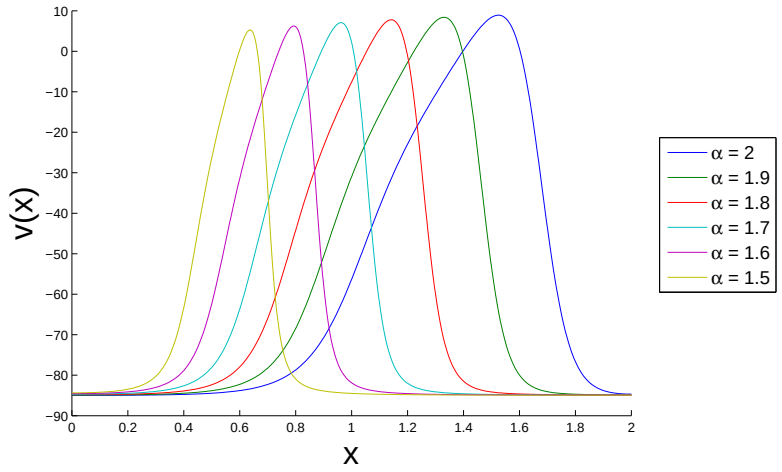

(a) FHN

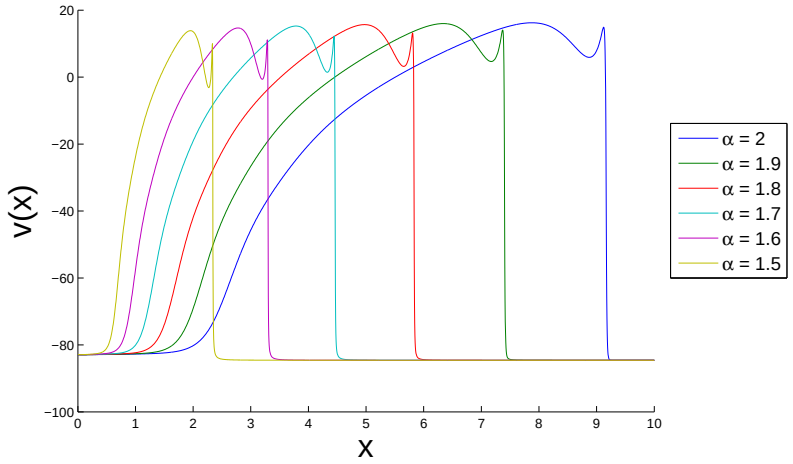

(b) BR

Figure 6.2: *Effect of different values of α on the shape and spatial location of the travelling pulse at a given time point $t = \bar{t}$. The value of the solution on the entire spatial domain and corresponding to the same $\bar{t}$ was then plotted on the same graph in the fractional case for different values of α. $\bar{t} = 500$ msec in the FHN case and $\bar{t} = 400$ msec for the BR model.*

reduction in the conduction velocity (as we shall see later on in this section). We also observe that as α is reduced, the peak of the moving pulse for the FHN ionic model slightly decreases. In the BR case, both the height of

the depolarization peak and of the following notch are slightly reduced as α decreases. Moreover, the minimum of the early repolarization phase (that is, the local minimum of the concavity between the peak and the notch typically observed in the BR pulse) becomes lower for smaller values of the fractional order.

As pointed out in Section 3.3, wanting to follow the propagation in space of the entire pulse might lead to the need of considering unrealistically large spatial intervals, which in turn requires a considerable computational effort to produce the solution approximation due to the large number of nodes involved in the spatial discretisation.

The much more common approach for the study of the solution of excitable media models consists of reducing the size of the spatial domain of interest and tracking the changes in the transmembrane potential as a function of time at selected points in the domain, rather than following the evolution in space of the whole travelling pulse. From now on in this section we will hence consider the spatial domain $\Omega = [0, 2\,\mathrm{cm}]$ for both cell models and observe the differences obtained in the action potential shape and duration at different points of the considered domain.

For example, if we focus on the point $x = 1\,\mathrm{cm} \in \Omega$, record the value of the solution computed at each time step of the numerical simulation at that particular point, and plot these values as a function of time in the standard case we obtain the results shown in Figure 6.3.

The length t_f of the temporal interval on which the entire solution is computed was chosen such that the point $x = 1$ undergoes a complete action potential for each cell model. Therefore, in Figure 6.3(a) we see that $t_f = 800\,\mathrm{msec}$, whereas in Figure 6.3(b) we have $t_f = 500\,\mathrm{msec}$. Once again we find that each action potential has the particular shape determined by the corresponding ionic model.

In Figure 6.3, we also highlight the action potential duration (APD), defined

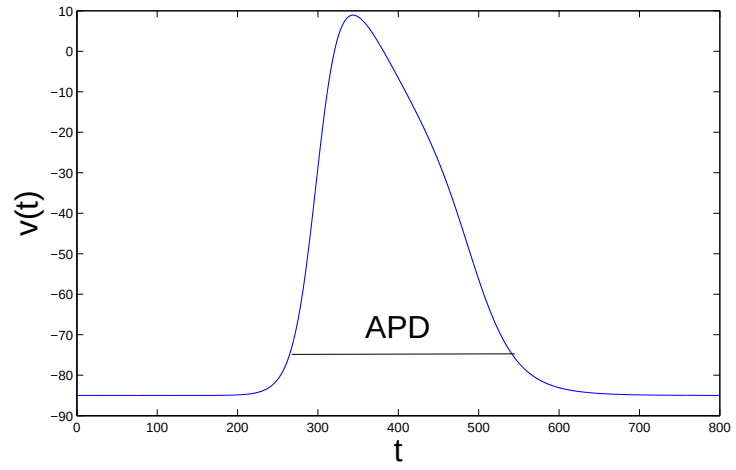

(a) FHN

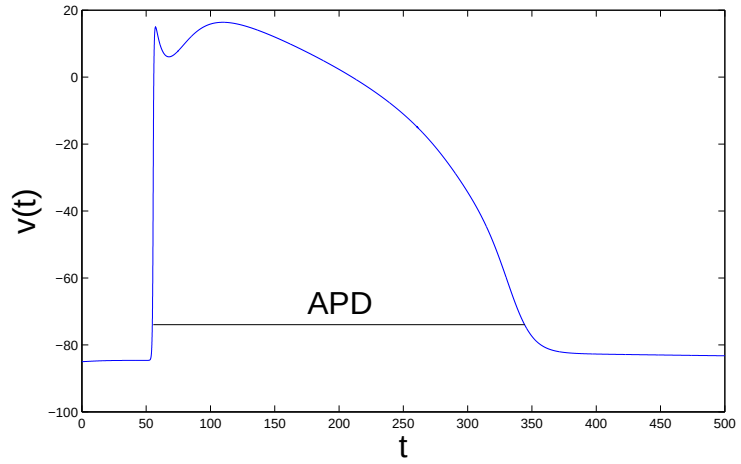

(b) BR

Figure 6.3: *Changes in the transmembrane potential v as a function of time at $x = 1\,\mathrm{cm}$ for the two monodomain models in the standard case. In both cases v starts at the resting state and undergoes a full action potential (AP) in the time interval considered. The differences in the AP shape reflect the characteristics of the particular cell model used. In both graphs the length (in milliseconds) of the horizontal black line depicted inside of the AP profile corresponds to the action potential duration (APD).*

independently from the particular ionic model used as the difference between

the time of repolarization and the time of depolarization at a given point in space. Depolarization time was measured as the time when the voltage reached 10% of its full depolarization. Repolarization time was measured as the time when the voltage repolarized to the same value, that is, the transmembrane potential reached 90% of repolarization to its resting value[4]. In both cases, linear interpolation was used to obtain better resolved time values.

The effect of different values of α on the action potential at $x = 1$ can be clearly seen from Figure 6.4.

As α decreases we observe for both cell models a shift towards the right of the action potential, corresponding to a later depolarization of the same point in space and therefore, indicating once again a smaller conduction velocity. Furthermore, as observed in Figure 6.2, we see here the same qualitative differences in the main features of the action potential shape. As α is reduced, the peak of both the FHN and the BR pulses slightly decreases. Moreover, in the BR case, we obtain a reduction in the local minimum corresponding to the early repolarization phase. A similar comparison can be made for the action potential obtained with different values of α at any other point of the spatial domain reached by the travelling pulse generated by the applied electrical stimulus.

As previously observed for both cell models we see a reduction in the conduction velocity associated with the problem as α decreases. In Figure 6.5 we plot the activation time recorded for fifty equally spaced nodes in the considered domain Ω.

It is immediate to see that the excitation pulse travels linearly in space for all values of α (with very slight deviations from linearity in the FHN case in proximity of the boundary $x = L$) and the conduction velocity for the six values of α considered corresponds to the reciprocal of the gradient of each of

[4]For this reason the considered APD is often called APD_{90} in the electrophysiology literature.

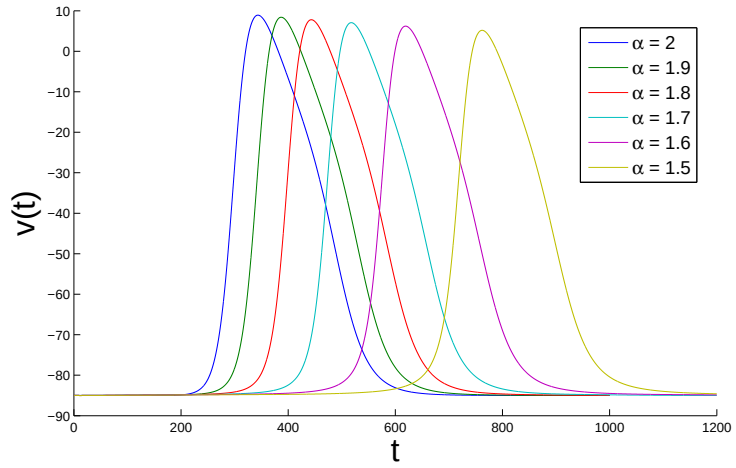

(a) FHN

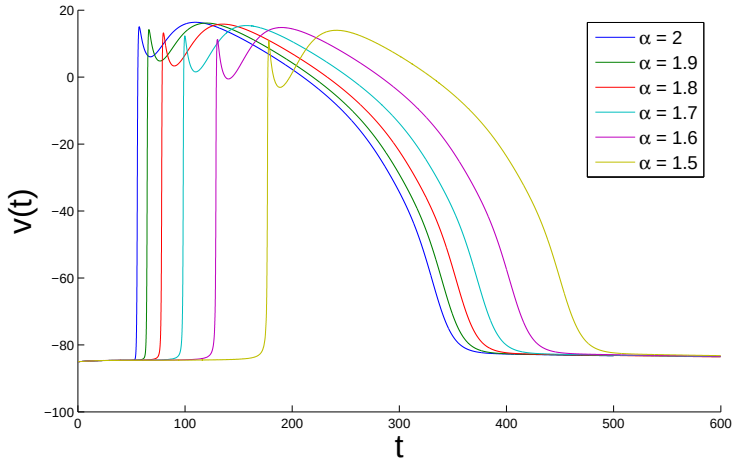

(b) BR

Figure 6.4: *Action potential recorded at* $x = 1\,\text{cm}$ *for the solution of the fractional FHN monodomain model (a) and the fractional BR monodomain model (b) when different values of* α *are considered in system (6.2).*

these straight lines. The specific values of the conduction velocity obtained for our numerical simulations are reported in Table 6.1 for the FHN case and in Table 6.2 for the BR case. As α is reduced, the conduction velocity of the corresponding solution of the monodomain system (6.2) decreases.

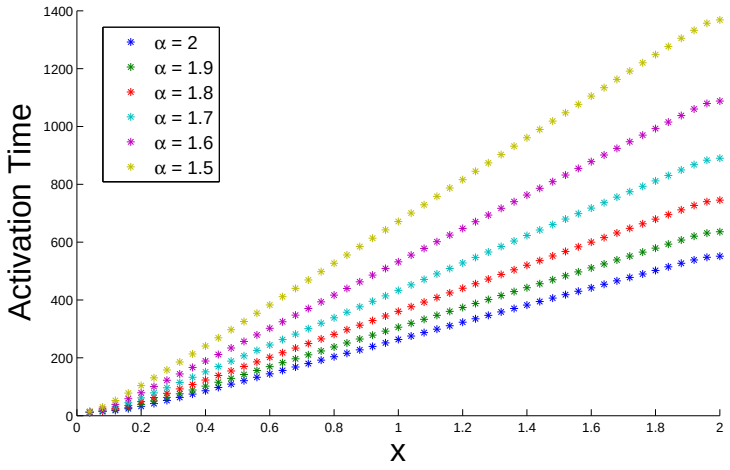

(a) FHN

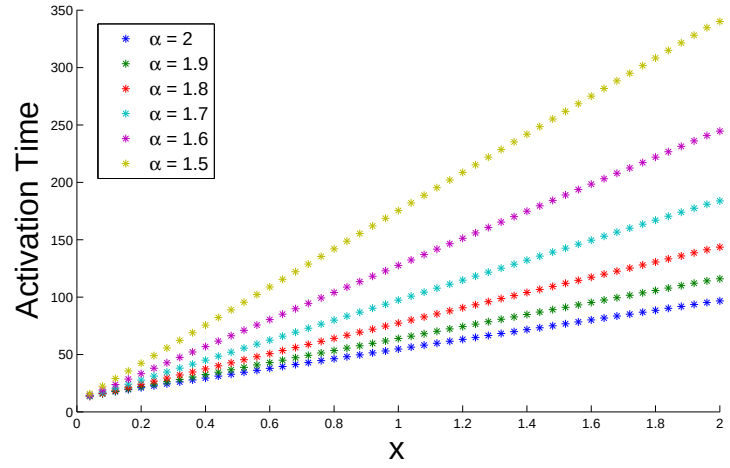

(b) BR

Figure 6.5: *Activation time (*msec*) of fifty equally spaced nodes in* $\Omega = [0, 2]$ *produced by different values of* α *in system (6.2).*

The final set of results we present in this section concerns the APD. Despite the linear advancing of the depolarization front in the domain of interest, one important characteristic observed in standard simulations of excitable media models is the dependence on the domain geometry and the proximity to the boundaries of the advancing of the repolarization front. These spatial variations result in differences of APD across the domain.

FHN	$\alpha = 2$	$\alpha = 1.9$	$\alpha = 1.8$	$\alpha = 1.7$	$\alpha = 1.6$	$\alpha = 1.5$
CV ($\text{cm}\cdot\text{sec}^{-1}$)	3.37	2.94	2.52	2.12	1.74	1.39

Table 6.1: *Conduction velocity (CV) of the FHN action potential for different values of the fractional order α.*

BR	$\alpha = 2$	$\alpha = 1.9$	$\alpha = 1.8$	$\alpha = 1.7$	$\alpha = 1.6$	$\alpha = 1.5$
CV($\text{cm}\cdot\text{sec}^{-1}$)	23.7	19.1	15.0	11.5	8.5	6.0

Table 6.2: *Conduction velocity (CV) of the BR action potential for different values of the fractional order α.*

In Figure 6.6 we report the computed values of the APD on fifty equally spaced nodes across the spatial domain Ω and see how the APD decreases as we move away from $x = 0$, that is, from the point of application of the electrical stimulus.

Despite some quantitative and qualitative differences between the recorded values of the spatially dependent APD of the two cell models (such as a much larger variation in magnitude for the FHN model and a less wavy profile in the BR case), the initial reduction of APD in both models appears to be followed by the adjustment about an almost constant level before dropping significantly in proximity of the boundary $x = L$.

The overall behaviour observed is in agreement with the study by Cherry and Fenton [18] on the spatial distribution of action potential duration in cardiac tissue, in which detailed considerations are made on a number of factors influencing APD changes in the standard case.

In order to compare the effect of different values of the parameter α on the variations produced in APD across the considered domain, we measure the APD dispersion (typically denoted ΔAPD and computed here for a given α as the difference between the value of APD at a given spatial node and the maximum APD value recorded for the same value of α over the entire spatial domain.

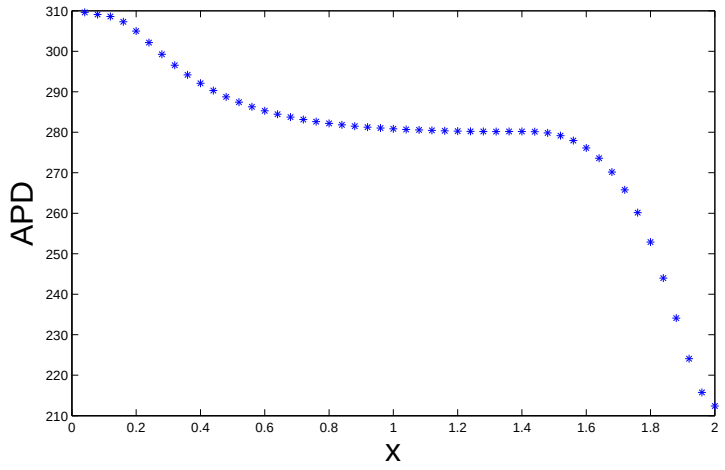

(a) FHN

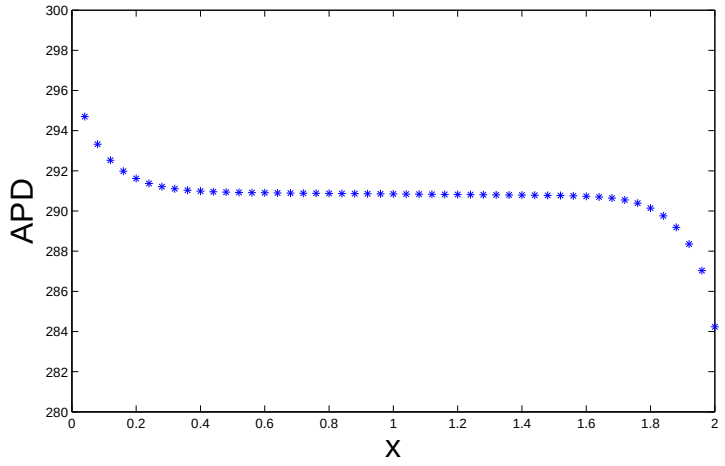

(b) BR

Figure 6.6: *Action potential duration (*msec*) as a function of space recorded at fifty equally spaced nodes in* $\Omega = [0, 2]$ *for the solution of system (6.2) in the standard case (*$\alpha = 2$*).*

As we can see from Figure 6.7, differences in the APD across the spatial interval are present for all values of α. In particular, as α decreases we observe in both cell models an increasingly large dispersion and a more pronounced effect in the dispersion when considering a node in proximity of the boundary $x = L$.

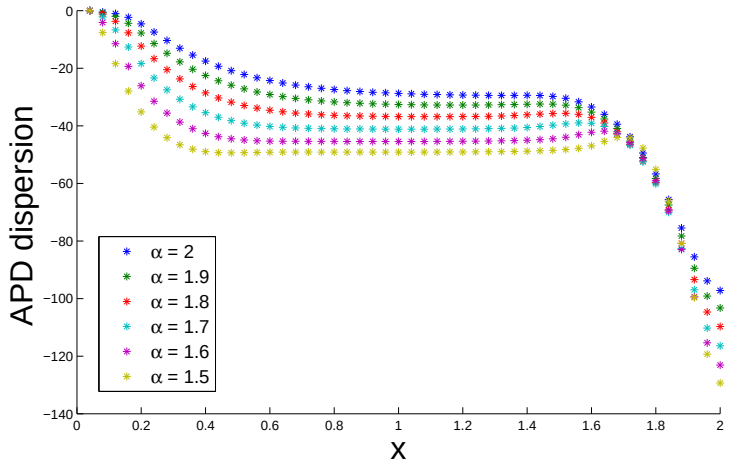

(a) FHN

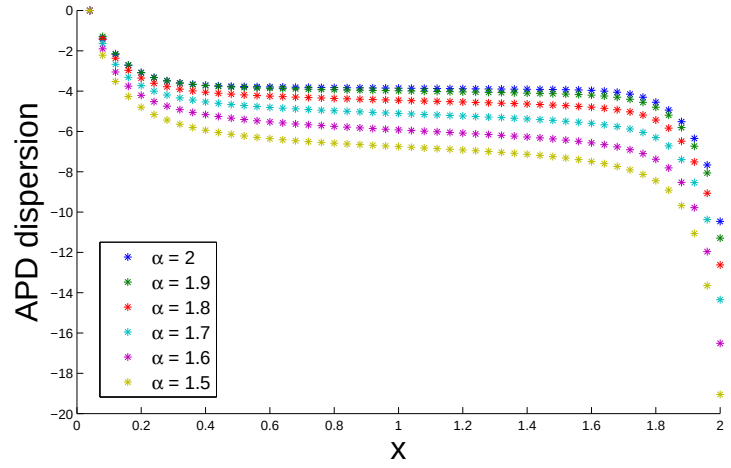

(b) BR

Figure 6.7: *Dispersion of action potential duration (*msec*) computed for the solution of system (6.2) on a uniform grid of fifty nodes in* $\Omega = [0, 2]$ *with different values of* α*.*

As thoroughly described by Cherry and Fenton [18] for a one-dimensional excitable medium in the standard case, "during repolarization most cells find themselves with one neighbor that is more depolarized (farther from the stimulus site) and one neighbor that is more repolarized (closer to the stimulus site); i.e., there is an asymmetry due to the direction of propagation."

However, "at the boundary, this condition does not hold; there is no longer a neighbor that is more depolarized. The loss of the more depolarized neighbor at the boundary increases the repolarizing electrotonic current arising from diffusive coupling, thereby accelerating repolarization and shortening APD."

When $\alpha < 2$, we add to the reflecting nature of the boundary conditions the non-locality of the solution. Hence, as we move closer to the end of the spatial interval, the influence on the solution of the increasing number of more repolarized nodes (closer to the stimulus site) becomes stronger as α decreases, due to the increased non-locality of the space-fractional operator used in the fractional monodomain model of system (6.2).

Even though we choose here to present the dispersion of APD as a function of space, the results reported in Figure 6.7 are in agreement with those proposed by Bueno–Orovio et al. [12] on the inverse AT-APD relationship[5]. In fact, in [12], when compared to the APD dispersion observed experimentally in human, canine and rabbit cardiac tissue, the larger dispersion obtained for fractional models shows a much better fit to the data than the ΔAPD obtained from standard diffusion models. This result (together with some other considerations made in [12]) shows that fractional models are able to capture important features characterising electrical pulse propagation in heterogeneous media better than their standard counterparts, and hence supports the idea that the use of these non-local models might allow us to gain deeper insight into the considered example of transport process.

6.4 The two-dimensional case

So far in this thesis we have only considered the definition of fractional Laplacian $(-\Delta)^{\alpha/2}$ on an insulated finite domain in one spatial dimension. The main reason behind this choice is the fact that the result obtained in Chapter 4 for the asymptotic behaviour of the eigenvalues of the reflection matrix is strictly connected to the definition of reflecting boundary conditions intro-

[5] AT stands for Activation time.

duced in the same chapter.

In the two-dimensional case we could think of repeating the same process by first introducing a discrete mesh, then defining the discrete operator embedding the reflecting conditions, and finally studying the limiting behaviour of the spectrum of this discrete operator. However, the generalisation of the concept of reflecting boundaries to more than one spatial dimension is not so straightforward.

Intuitively, if we return to the interpretation of insulated boundaries as elastic walls reflecting the trajectory of jumping particles inside the domain, we can imagine that the nature of the boundary of a finite two-dimensional (or three-dimensional) domain will play a fundamental role in determining the adjusted trajectory of the jumping particles. Perhaps something could be said about reflections by studying how angles of incidence and angles of reflection affect the trajectory of a moving object hitting the boundary of a regular domain (such as a circle, for example). However, at this stage, in our understanding it is not clear how we could formalize the expression of the probability of a bouncing particle reaching a point x in a given domain Ω, when starting its trajectory at a point $x' \in \Omega$.

Despite the above-mentioned difficulties, thanks to the analysis performed in this thesis and the results obtained for the one-dimensional case, we are still able to make some important considerations for a space-fractional problem on a finite domain in higher dimensions. In particular, in this section and in the following one we will consider two different options for the introduction of non-locality in a two-dimensional model on a rectangular domain Ω, under the assumption that all four sides of the considered rectangle are insulated, and consider their effect on the solution of excitable media models in two spatial dimensions.

The first option we introduce here is based on the definition of the unbounded two-dimensional Riesz-Feller operator, that is, according to the notation in-

troduced in Chapter 2, the operator

$$\mathcal{R}^{\alpha} := \mathcal{R}_x^{\alpha} + \mathcal{R}_y^{\alpha} = \frac{\partial^{\alpha}}{\partial |x|^{\alpha}} + \frac{\partial^{\alpha}}{\partial |y|^{\alpha}}. \tag{6.4}$$

$\mathcal{R}^{\alpha}$ is simply the sum of two unbounded one-dimensional fractional operators and we see that the non-locality is introduced separately in the two spatial dimensions. Once two insulated boundaries are introduced in each direction, for example at $x = 0$, $x = L_x > 0$, $y = 0$, and at $y = L_y > 0$, the concept of one-dimensional reflections can be easily applied to both spatial dimensions independently, resulting in the operator

$$\mathcal{R}_{\Omega}^{\alpha} := \mathcal{R}_{x,L_x}^{\alpha} + \mathcal{R}_{y,L_y}^{\alpha}, \tag{6.5}$$

on the insulated rectangle $\Omega = [0, L_x] \times [0, L_y]$, where $\mathcal{R}_{x,L_x}^{\alpha}$ and $\mathcal{R}_{y,L_y}^{\alpha}$ are one-dimensional reflection operators (defined as in Section 4.1.1) on $[0, L_x]$ and on $[0, L_y]$, respectively.

By essentially using separation of variables and applying the results obtained in Chapter 4 to both $\mathcal{R}_{x,L_x}^{\alpha}$ and $\mathcal{R}_{y,L_y}^{\alpha}$, we find that the eigenvalues of $-\mathcal{R}_{\Omega}^{\alpha}$ (the negative sign is considered in order to ensure non-negativity of the eigenvalues) on the insulated rectangular domain Ω can be expressed as the sum of the eigenvalues of two one-dimensional fractional Laplacians with reflecting boundaries as follows:

$$\left(\frac{j\pi}{L_x}\right)^{\alpha} + \left(\frac{i\pi}{L_y}\right)^{\alpha} \quad \text{for } j, i = 0, 1, 2, \ldots. \tag{6.6}$$

The corresponding eigenfunctions, obtained via separation of variables as well, are products of the form $\varphi_j(x)\,\phi_i(y)$, where φ_j and ϕ_i are the eigenfunctions of the two one-dimensional fractional operators on the insulated $[0, L_x]$ and the insulated $[0, L_y]$, respectively, that is,

$$\varphi_j(x) = \begin{cases} \frac{1}{\sqrt{L_x}} & j = 0 \\ \\ \sqrt{\frac{2}{L_x}} \cos\left(\frac{jx\pi}{L_x}\right) & j \geq 1, \end{cases} \tag{6.7}$$

and similarly

$$\phi_i(y) = \begin{cases} \frac{1}{\sqrt{L_y}} & i = 0 \\ \\ \sqrt{\frac{2}{L_y}} \cos\left(\frac{iy\pi}{L_y}\right) & i \geq 1. \end{cases} \tag{6.8}$$

The second option we consider in this chapter is based on the one-dimensional case and consists of defining a spectral decomposition of the two-dimensional operator $(-\Delta)^{\alpha/2}$ as a whole on the insulated rectangle. We stress that this second option is not grounded on any theoretical result but rather is a speculation on what we would expect to see as a consequence of the extension of the concept of reflections to two spatial dimensions. A proof for this conjecture is however still missing and will therefore require further analysis.

Knowing the analytic expression of the eigenvalues and eigenfuntions of the standard continuous Laplacian $(-\Delta)$ on an insulated rectangle (that is, with homogeneous Neumann boundary conditions), we define the spectral expansion of the corresponding non-local operator by considering as eigenvalues the fractional powers of the standard two-dimensional eigenvalues, that is,

$$\left[\left(\frac{j\pi}{L_x}\right)^2 + \left(\frac{i\pi}{L_y}\right)^2\right]^{\alpha/2} \quad \text{for } j, i = 0, 1, 2, \ldots, \tag{6.9}$$

and as eigenfunctions, the products $\varphi_j(x)\,\phi_i(y)$, where $\varphi_j(x)$ and $\phi_i(y)$ are as in equation (6.7) and in equation (6.8), respectively.

Having at our disposal the spectral decomposition of these two non-local operators and noting the orthonormality of the considered set of eigenfunctions, will allow us to implement a simple extension of the spectral method introduced in the one-dimensional case and to exploit a full diagonalisation of the fractional operator for a faster computation of the solution[6].

[6]Compared for example to a traditional finite difference approach in which the dense matrix representing the non-local operator is involved.

6.4.1 Some considerations on the anisotropic case and on irregular domains

Before presenting some simulation results in order to study the effect of using the proposed operators to introduce non-locality in two-dimensional excitable media problems, we make here some considerations on possible strategies to account for anisotropy in the fractional two-dimensional case.

Excitable tissue is typically anisotropic, that is, it is characterised by different diffusivities along different directions (for example, along, across and orthogonal to the fibres in cardiac tissue, as seen in Chapter 2). In what follows, for the sake of simplicity, we ignore rotational effects and assume that the two-dimensional diffusivity tensor M involved in the formulation of the standard monodomain problem in two dimensions is simply a diagonal matrix with diagonal entries M_x and M_y.

One of the advantages of using the Riesz-Feller formulation of the space-fractional operator in two dimensions is the fact that this definition naturally handles anisotropy. In fact, $M\mathcal{R}^{\alpha}_{\Omega}$ simply becomes

$$M_x \mathcal{R}^{\alpha}_{x,L_x} + M_y \mathcal{R}^{\alpha}_{y,L_y}, \tag{6.10}$$

where M_x and M_y are the different conductivities in the x and the y directions. Moreover, in this case we could think of using different values of the fractional order in each spatial direction and hence consider the more general formulation

$$M_x \mathcal{R}^{\alpha_x}_{x,L_x} + M_y \mathcal{R}^{\alpha_y}_{y,L_y}. \tag{6.11}$$

As a result, the non-negative set of eigenvalues to be used in the spectral decomposition of the solution to the fractional problem becomes

$$M_x \left(\frac{j\pi}{L_x}\right)^{\alpha_x} + M_y \left(\frac{i\pi}{L_y}\right)^{\alpha_y} \quad \text{for } j, i = 0, 1, 2, \ldots, \tag{6.12}$$

while the eigenfunctions of the problem remain unchanged.

On the other hand, in order to incorporate the anisotropic assumption in the spectral definition of the two-dimensional fractional Laplacian as a whole, we consider the operator in the form

$$(-\nabla \cdot (M\nabla))^{\alpha/2}, \tag{6.13}$$

that in the case of a diagonal tensor M results in the set of eigenvalues

$$\left[M_x \left(\frac{j\pi}{L_x} \right)^2 + M_y \left(\frac{i\pi}{L_y} \right)^2 \right]^{\alpha/2} \quad \text{for } j, i = 0, 1, 2, \ldots. \tag{6.14}$$

We observe that with definition (6.13), in order to preserve the correct units in the solution of the problem and allow the comparison with the solution of a model involving the anisotropic fractional operator (6.11), each eigenvalue must be multiplied by a scaling factor with units $(\mathrm{mS}\cdot\mathrm{cm}^{-1})^{1-\alpha/2}$. We also notice that, as it is, the formulation of the operator given by (6.13) only allows us to consider one fractional order α that will affect the solution in both spatial dimensions indistinctly.

We conclude this section by pointing out that the speculation on the two-dimensional extension of the reflection idea and the corresponding definition of $(-\Delta)^{\alpha/2}$ as a whole is here reasonable and possible thanks to the fact that the considered spatial domain is a rectangle. For more general and possibly irregular geometries, analytic expressions of the eigenvalues and eigenfunctions of the continuous standard two-dimensional Laplacian are not available. In fact, in many cases, only estimates of the eigenvalues are possible and therefore, the implementation of a spectral method as proposed in this thesis becomes questionable.

On the other hand, the Riesz-Feller formulation once again offers some additional flexibility and thanks to the essential separation between the two spatial dimensions, handling non-rectangular shapes (or simple irregular ones) might be possible and not too difficult to implement. For example, on a convex domain Ω, one could think of building the approximation of the frac-

tional operator at a given internal point P by separately using the reflection strategy along the two dimensions on two spatial intervals $[x_a(P), x_b(P)]$ and $[y_a(P), y_b(P)]$ with ends (and hence length) depending on the position of P in the domain Ω, as shown by Figure 6.8.

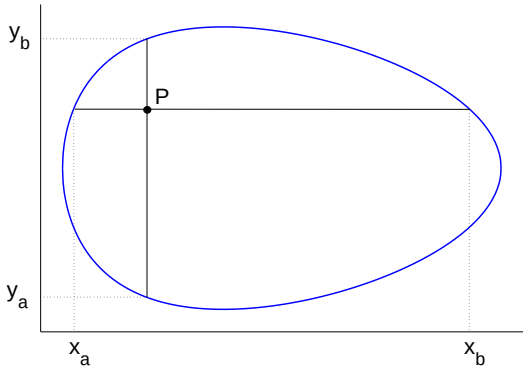

Figure 6.8: *Point dependent intervals that could be used for the implementation of the fractional two-dimensional Riesz-Feller operator on simple convex domains.*

6.5 Numerical simulations of space-fractional excitable media models in 2D

In this section we present a set of results for some simulations of two-dimensional excitable media models. Due to the similar qualitative behaviour observed for the two cell models considered in one spatial dimension (that is, FHN and BR), fundamentally differing in the characteristic shape of the action pulse generated by a sufficiently strong applied current, we decide here to only focus on one of these ionic models, namely the BR model, and to investigate the effect produced by the introduction of a non-local operator in space on the solution of the standard two-dimensional monodomain BR model.

We hence start by considering for $t > 0$ and for all points (x, y) of a given

insulated domain $\Omega = [0, L_x] \times [0, L_y]$, the following system:

$$\begin{cases} \dfrac{\partial v}{\partial t} &= \dfrac{1}{\chi}\dfrac{\lambda}{1+\lambda}\left[M_x \mathcal{R}^{\alpha_x}_{x,L_x} + M_y \mathcal{R}^{\alpha_y}_{y,L_y}\right] v - I_{\text{ion}}(v, \mathbf{z}) + \dfrac{1}{\chi} I^{(\text{vol})} \\ \dfrac{d\mathbf{z}}{dt} &= \mathbf{f}(v, \mathbf{z}), \end{cases} \tag{6.15}$$

where I_{ion}, the vector $\mathbf{z}$ and the functional form of $\mathbf{f}$ are given by the BR ionic model, and the non-locality in space is introduced via the Riesz-Feller operator with possibly different fractional orders along the two spatial dimensions, according to the discussion presented in Section 6.4.

Given our interest in studying how the fractional order affects the solution of the standard model, in the set of presented results we consider the conductivities M_x and M_y to be fixed parameters of the model so that we can simply ignore the contribution given to the solution behaviour by modified diffusivity coefficients. In particular, throughout the section we assume that the components of the diagonal diffusion tensor are $M_x = M_y = 1\,\text{mS}\cdot\text{cm}^{-1}$. Observe that with this choice of M_x and M_y the solution produced in the standard case will always be isotropic. However, in the fractional case we still expect to be able to introduce anisotropy in our simulations by using different values of the fractional orders α_x and α_y in the interval of interest $(1, 2]$.

6.5.1 Solution strategy

For a given choice of α_x and α_y, the solution of system (6.15) is computed via the spectral modification of Whiteley's method as done in Section 6.3 for the one-dimensional simulations. This time the spectral expansion of the solution has the form

$$v(x, y, t) = \sum_{i=0}^{\infty} \sum_{j=0}^{\infty} \hat{v}_{ji}(t) \varphi_j(x) \phi_i(y), \tag{6.16}$$

where $\varphi_j(x)$ and $\phi_i(y)$ are the eigenfunctions defined in equation (6.7) and equation (6.8), respectively.

Let D be the coefficient $D := \frac{1}{\chi}\frac{\lambda}{1+\lambda}$. After introducing a uniform temporal grid with time step Δt and using the semi-implicit Euler method for the temporal discretisation of the PDE governing the spatio-temporal evolution of the transmembrane potential v, thanks to the orthonormality of the considered eigenfunctions, we can compute each of the coefficients $\hat{v}_{ji}^k$ in equation (6.16) independently, as follows:

$$\hat{v}_{ji}^{k+1} = \frac{1}{1 + \Delta t\, D \left(M_x \lambda_j^{\alpha_x/2} + M_y \mu_i^{\alpha_y/2} \right)} \Big[\hat{v}_{ji}^k + \Delta t\, \hat{g}_{ji}(v^k) \Big], \tag{6.17}$$

where for $j, i = 0, 1, 2, \ldots,$

$$\lambda_j^{\alpha_x/2} = \left(\frac{j\pi}{L_x} \right)^{\alpha_x} \quad \text{and} \quad \mu_i^{\alpha_y/2} = \left(\frac{i\pi}{L_y} \right)^{\alpha_y},$$

are the eigenvalues of the considered non-local operator,

$$\hat{v}_{ji}^k = \int_0^{L_y} \int_0^{L_x} v(x, y, t_k) \varphi_j(x) \phi_i(y)\, dx\, dy,$$

and $\hat{g}_{ji}(v^k)$ is the Fourier coefficient of the source term of the PDE in system (6.16), that is, $g(v) := -I_{\text{ion}}(v, \mathbf{z}) + \frac{1}{\chi} I^{(\text{vol})}$, evaluated at v^k and corresponding to the pair of indices ji.

For practical reasons the numerical solution is approximated by considering a finite number of eigenfunctions in the expansion (6.16) and by approximating at each time step the value of the integrals $\hat{v}_{ji}^k$ and $\hat{g}_{ji}(v^k)$ via the trapezoidal rule applied to both dimensions. Let $N_x + 1$ and $N_y + 1$ be the number of nodes for the spatial discretisation of $[0, L_x]$ and $[0, L_y]$, respectively. Then in the numerical solution we use a total number of eigenfunctions equal to $(N_x+1)\times(N_y+1)$ by considering φ_j for $j = 0, 1, \ldots, N_x$ and $\phi_i = 0, 1, \ldots, N_y$.

6.5.2 Numerical results in 2D

Let us consider the square domain $\Omega = [0, 2\,\text{cm}] \times [0, 2\,\text{cm}]$. Despite the advantage given by the orthogonality of the considered eigenfunctions, it is immediate to see that a fine mesh in both spatial dimensions will result in high computational costs due to the fact that the total number of nodes is now $O(N^2)$. In one spatial dimension, we saw that in order to avoid oscillations in the numerical solution, as α decreases we must consider an increasing number of nodes. In particular, for values of $\alpha \in [1.5, 2]$, in order to be able to obtain good spatial resolutions in the solution, we chose to use a mesh size $h_x = 0.004\,\text{cm}$. This mesh size in the two-dimensional case would result in a total of 251001 nodes for the considered domain Ω. However, if we choose a representative value of the fractional order equal to $\alpha = 1.9$, a mesh size of $h_x = 0.01\,\text{cm}$ is already sufficient to produce oscillation-free numerical results.

Therefore, in order to reduce the computational costs for the two-dimensional simulations, we consider for both spatial dimensions the mesh size $h_x = h_y = 0.01\,\text{cm}$ (resulting in a total of 40401 nodes) and use the value $\alpha = 1.9$ when considering the solution in the non-standard case. The temporal step adopted to compute the solution is $\Delta t = 0.01\,\text{msec}$.

Let us assume that the parameter λ in the monodomain formulation is $\lambda = 1$ and the surface to volume ratio is $\chi = 2000\,\text{cm}^{-1}$ (resulting in $D = \frac{1}{\chi}\frac{\lambda}{1+\lambda} = \frac{1}{4000}\,\text{cm}^{-1}$). Furthermore, let us consider an electrical stimulus $I^{(\text{vol})} = 10^5\,\mu\text{A}\cdot\text{cm}^{-3}$ applied at $t = 10\,\text{msec}$ for five consecutive milliseconds to the square region $[0, \bar{x}] \times [0, \bar{y}]$ surrounding the origin, with $\bar{x} = \bar{y} = 0.1\,\text{cm}$.

Figure 6.9(a) depicts the solution surface for the transmembrane potential v at $t = 60\,\text{msec}$ produced on the two-dimensional grid by solving system (6.15) in the standard case, that is, with $\alpha_x = \alpha_y = 2$.

In order to facilitate the visualisation of the pulse front, in Figure 6.9(b) we provide the projection of the surface of Figure 6.9(a) onto the xy-plane, where

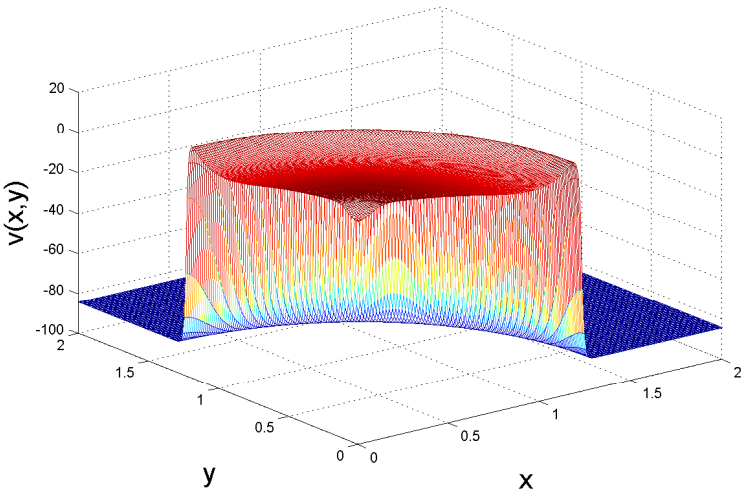

(a) Solution surface in 3D

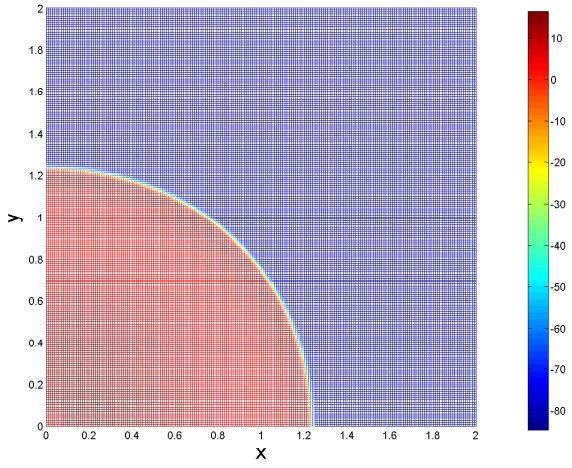

(b) Surface projection onto xy-plane

Figure 6.9: *Two-dimensional solution of the monodomain BR model (6.15) in the standard case ($\alpha_x = \alpha_y = 2$). The solution is computed via the spectral modification of Whiteley's method with a uniform time grid of $\Delta t = 0.01$ on $\Omega = [0, 2] \times [0, 2]$ and plotted at $t = 60$. The mesh size used in both spatial directions is $h_x = h_y = 0.01$.*

the colour of each node represents the corresponding value of the solution according to the colour bar.

Clearly, as seen in one spatial dimension, due to the width of the BR pulse and the restricted spatial domain considered, we are not able to visualise the entire excitation wave generated by the applied stimulus. However, we can still make some preliminary considerations by looking at the shape of the pulse front corresponding to the quick depolarization phase and represented by the narrow transition region between nodes at rest (blue) and depolarized nodes (red).

In Figure 6.10 we report the solution surface and the corresponding projection onto the xy-plane of the transmembrane potential obtained always at $t = 60$ by solving system (6.15) on the same temporal and spatial grid used in the standard case, this time with $\alpha_x = \alpha_y = 1.9$.

If we compare Figure 6.9 and Figure 6.10, similarly to the one-dimensional case, we see that the solution produced by the same electrical stimulus in the purely fractional case is still a travelling pulse moving in time away from the stimulation site but with speed equally reduced along both axes.

On the other hand, if we assume that $\alpha_x = 2$ and $\alpha_y = 1.9$, at $t = 60\,\text{msec}$, the solution surface for v and its projection onto the xy-plane are as in Figure 6.11.

As expected, we see that by using a different order along the x and the y directions results in the moving pulse advancing faster along the direction characterised by a higher value of the fractional exponent, namely the x direction in this case. In order to compare better the pulses generated by these three combinations of α_x and α_y, once again we use the traditional approach and follow the transmembrane potential changes at fixed points in the domain for all time steps in a given temporal interval $[0, t_f]$.

In Figure 6.12, we consider the points $P_1(1, 0)$, $P_2(0, 1)$ and $P_3(1, 1)$ and report the value of the solution v at these points as a function of time for $t \in [0, 500]$, computed for the indicated choices of the pair (α_x, α_y).

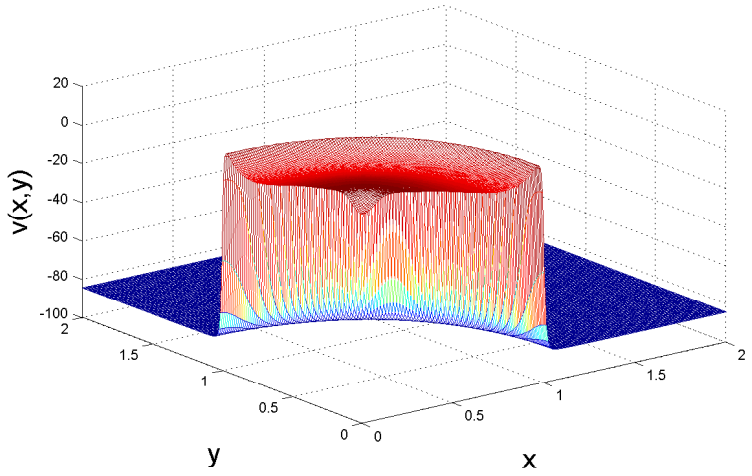

(a) Solution surface in 3D

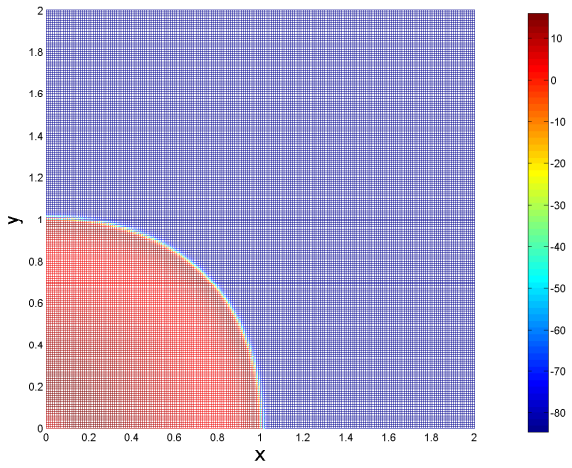

(b) Surface projection onto xy-plane

Figure 6.10: *Two-dimensional solution of the monodomain BR fractional model (6.15) with* $\alpha_x = \alpha_y = 1.9$. *The solution is computed via the spectral modification of Whiteley's method with a uniform time grid of* $\Delta t = 0.01$ *on* $\Omega = [0, 2] \times [0, 2]$ *and plotted at* $t = 60$. *The mesh size used in both spatial directions is* $h_x = h_y = 0.01$.

In all three simulations the transmembrane potential at the considered points goes through an entire action potential. However, as anticipated by looking

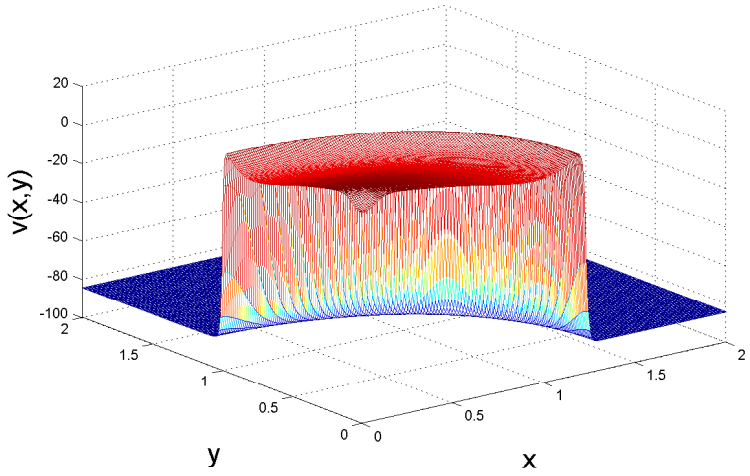

(a) Solution surface in 3D

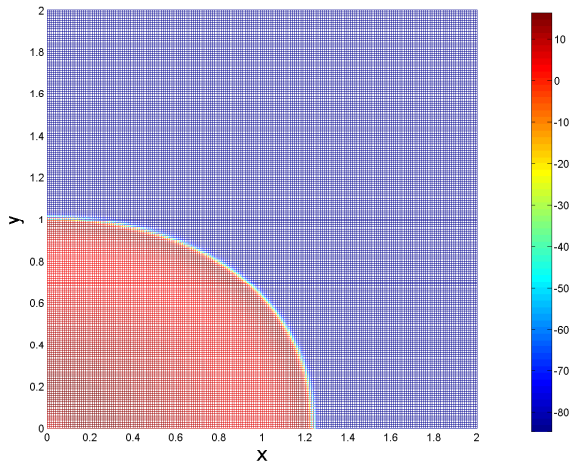

(b) Surface projection onto xy-plane

Figure 6.11: *Two-dimensional solution of the monodomain BR fractional model (6.15) with* $\alpha_x = 2$ *and* $\alpha_y = 1.9$. *The solution is computed via the spectral modification of Whiteley's method with a uniform time grid of* $\Delta t = 0.01$ *on* $\Omega = [0, 2] \times [0, 2]$ *and plotted at* $t = 60$. *The mesh size used in both spatial directions is* $h_x = h_y = 0.01$.

at the previous figures in the section, there are visible differences in the activation time of the same point for different simulations. For example, the

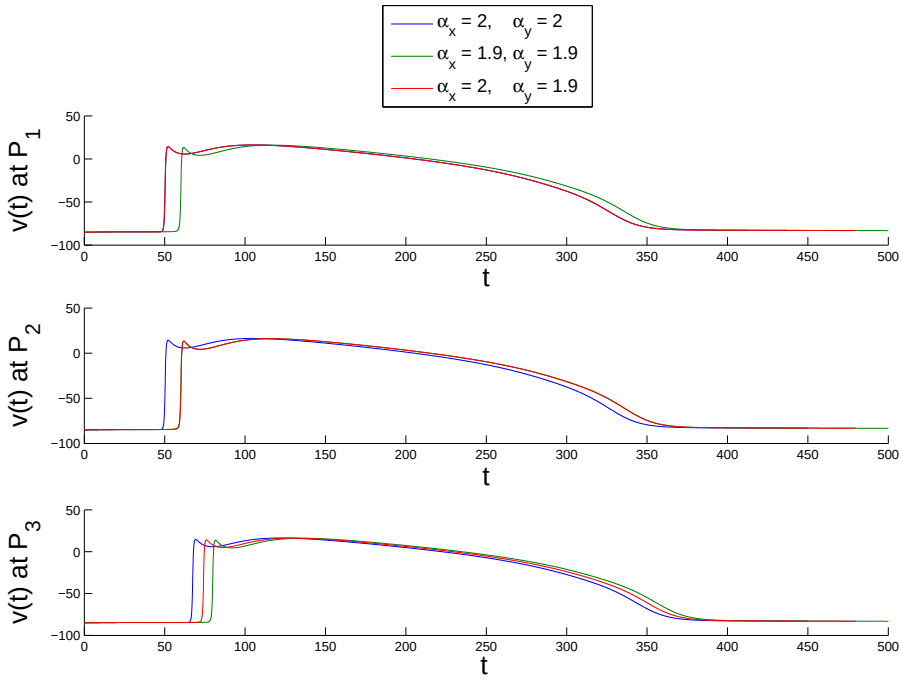

Figure 6.12: *Transmembrane potential changes recorded in the time interval* $[0, 500]$ *at the points* $P_1(1, 0)$, $P_2(0, 1)$ *and* $P_3(1, 1)$ *for the solution of system (6.15) with three different combinations of* α_x *and* α_y. *Note that at* P_1, *the two action potential profiles corresponding to* $\alpha_x = 2$ *(blue and red lines) are almost indistinguishable. Similarly, when considering* P_2, *the two action potential profiles corresponding to* $\alpha_y = 1.9$ *(green and red lines) are overlapping. However, the effect of both fractional orders is combined as we move away from the two axes and as a result, if we consider* P_3 *on the main diagonal, the thee combinations of* α_x *and* α_y *considered generate three distinct action potential profiles.*

activation time of P_1 when $\alpha_x = 1.9$ is significantly delayed, whereas in the other two simulations, having $\alpha_x = 2$ results in action potentials for P_1 that are almost indistinguishable. Similarly, the choices made for α_y result in an earlier depolarization of P_2 in the first simulation (when $\alpha_y = 2$), while a later activation time is observed for the same point in the two simulations with $\alpha_y = 1.9$ (this time the green and the red lines are almost indistinguishable). However, if we consider P_3, we see that the one-dimensional effect along the x-axis and the y-axis is added resulting in three different depolarization times:

the earliest corresponding to the standard case, the latest corresponding to the purely fractional case and the intermediate one resulting from the use of different fractional orders in the two directions.

Additional information on the pulse propagation throughout the domain can be obtained by looking at the activation time of multiple points along different directions in the two-dimensional domain. For this reason, we define the coarse grid of Figure 6.13 for the square domain $[0, 2] \times [0, 2]$ and for each simulation we store the computed values of the solution at the twenty-four nodes highlighted in blue. In particular, we choose eight equally spaced nodes along each axis and eight equally spaced nodes along the main diagonal of the square indicated by the dashed line (always excluding the origin, falling in the area where the electrical stimulus is applied).

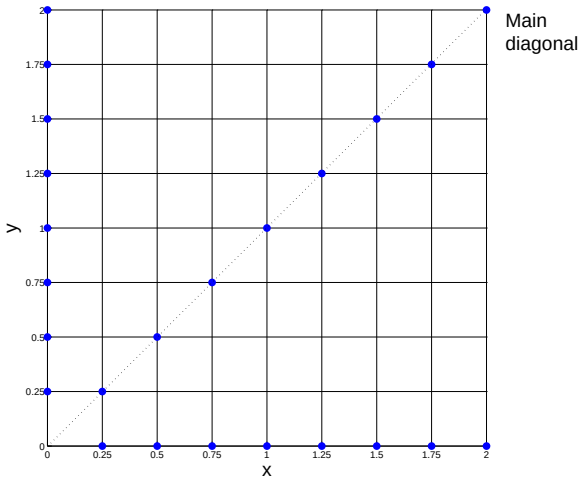

Figure 6.13: *The highlighted nodes (blue dots) of this coarse grid are the twenty-four representative nodes used to measure some quantities of interest for a given computed solution and to compare the solutions obtained from different simulations.*

The obtained activation times for the three considered simulations at the highlighted nodes of the grid are shown in Figure 6.14 and exhibit a linear

advancing of the front in each spatial direction, with steeper gradient when corresponding to a reduced fractional order (hence indicating a lower conduction velocity along that particular direction). Once again, on the main diagonal the differences between all three simulations are well evident, whereas along the two axes the activation time seems to be dependent essentially on the fractional order considered for that particular direction.

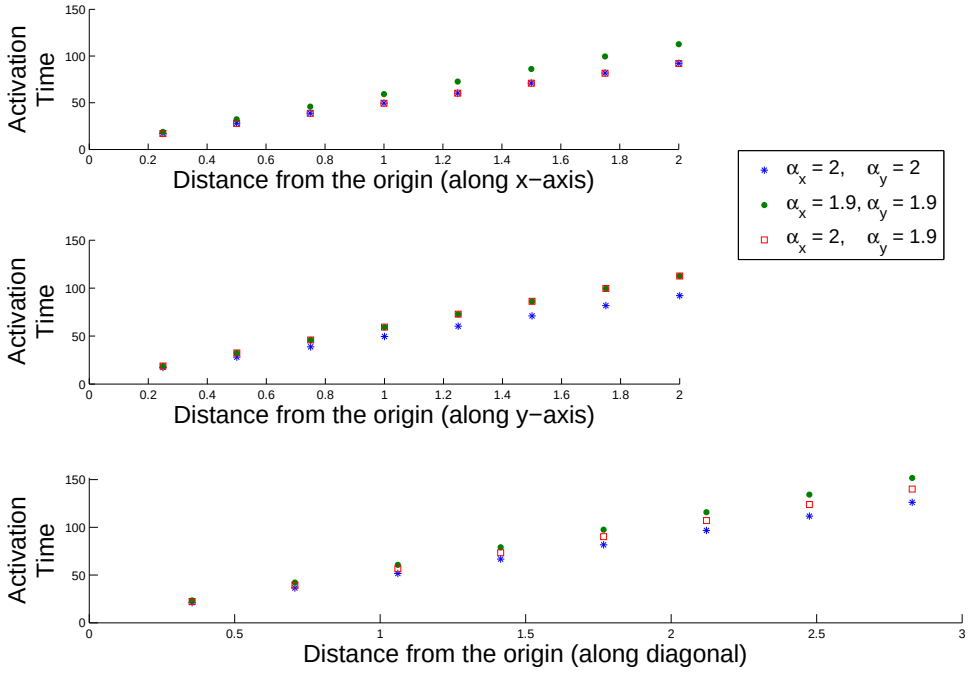

Figure 6.14: *The activation time of the points highlighted in blue in the grid of Figure 6.13 computed for the solution of system (6.15) for three different combinations of α_x and α_y. In the top diagram we plot the activation times of the eight equally spaced nodes with coordinate $y = 0$, in the following diagram we consider the nodes with coordinate $x = 0$, and in the bottom diagram we consider the eight points on the main diagonal (with coordinates $x = y$).*

The final result for the proposed set of simulations concerns the APD dispersion. Similar conclusions to those drawn for the one-dimensional case can be made here. In fact, the reduction in APD duration observed as the repo-

larization phase of the excitation wave advances towards the boundaries of the considered domain becomes more pronounced as the fractional order is reduced. Hence, if we measure the dispersion of APD across the domain in a particular direction, we observe that it is essentially related to the degree of non-locality characterising diffusion along the given direction.

Therefore, if we compare the three considered simulations (that is, the standard case $\alpha_x = \alpha_y = 2$, the purely fractional case $\alpha_x = \alpha_y = 1.9$, and the mixed case $\alpha_x = 2$, $\alpha_y = 1.9$) along the main diagonal, we obtain the result depicted in Figure 6.15.

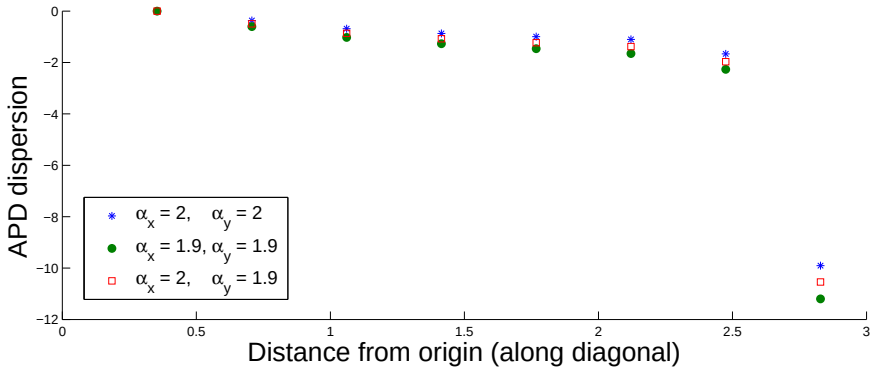

Figure 6.15: *Dispersion of APD calculated for the solution of system (6.15) with three different combinations of α_x and α_y at the eight equally spaced nodes on the main diagonal of the grid in Figure 6.13.*

As expected, the ΔAPD is stronger in the purely fractional case, followed by the mixed case and finally by the one computed for the standard model and the differences between the three simulations become more pronounced as we move closer to the boundary of the domain.

The results shown so far are all obtained with the Riesz-Feller formulation of the non-local operator in space. If in system (6.15) we substitute the space-fractional term with the operator given by equation (6.13), defined in the

previous section via its spectral expansion, we obtain the system

$$\begin{cases} \dfrac{\partial v}{\partial t} &= -\dfrac{1}{\chi}\dfrac{\lambda}{1+\lambda}(-\nabla\cdot(M\nabla))^{\alpha/2}v - I_{\text{ion}}(v,\mathbf{z}) + \dfrac{1}{\chi}I^{(\text{vol})} \\ \dfrac{d\mathbf{z}}{dt} &= \mathbf{f}(v,\mathbf{z}). \end{cases} \tag{6.18}$$

As observed in Section 6.4, with this definition of the operator we can only consider a single value of the fractional order α.

However, if we use the two-dimensional spectral definition of the fractional Laplacian on a rectangular insulated domain Ω and we compare (results not shown) the solution of the purely fractional case $\alpha < 2$ with the one obtained in the standard case[7], we find the same qualitative behaviour observed when making the comparison while using the Riesz-Feller operator. In fact, a sufficiently strong electrical stimulus applied to the system with a reduced value of α still produces an excitation wave moving in time across the spatial domain away from the stimulus site, but with a reduced conduction velocity. Moreover, as α decreases, the activation times of nodes along a given direction are delayed and a stronger ΔAPD is observed as we move away from the stimulus site and get closer to the insulated boundaries of the domain.

For both the Riesz-Feller operator and the considered spectral definition of the two-dimensional fractional Laplacian, we expect to see that as the fractional order decreases, the effects of the non-locality assumption become more pronounced. Furthermore, along any given direction, we expect to see similar behaviour as observed for different values of α in the one-dimensional simulations. However, it would be interesting to see for a given value of $\alpha_x = \alpha_y = \alpha < 2$, how different is the solution computed for system (6.15) from the one computed for system (6.18), when all modelling and simulation parameters remain fixed.

[7] Actually identical to the one computed with the Riesz-Feller operator with fractional orders $\alpha_x = \alpha_y = 2$.

Lemma 6. *For all $a, b \geq 0$ and for all $\alpha \in (1, 2]$, the following relationship holds:*

$$(a+b)^{\alpha/2} \leq a^{\alpha/2} + b^{\alpha/2}. \tag{6.19}$$

Proof. Clearly the above relationship is trivial if a or b (or both) are zero. Therefore we can assume that both are strictly positive. Without loss of generality we can assume that $b \leq a$ and hence $\frac{b}{a} \leq 1$. Using the series expansion given by the binomial theorem for non-integer exponents we find

$$\begin{aligned}
(a+b)^{\alpha/2} &= \sum_{k=0}^{\infty} \binom{\alpha/2}{k} a^{\alpha/2-k}\, b^k \\
&= a^{\alpha/2} + b^{\alpha/2} \sum_{k=1}^{\infty} \binom{\alpha/2}{k} \left(\frac{b}{a}\right)^{k-\alpha/2} \\
&\leq a^{\alpha/2} + b^{\alpha/2} \sum_{k=1}^{\infty} \binom{\alpha/2}{k}.
\end{aligned}$$

Using that

$$\sum_{k=1}^{\infty} \binom{\alpha/2}{k} = \sum_{k=0}^{\infty} \binom{\alpha/2}{k} - 1 = 2^{\alpha/2} - 1,$$

and that the fractional order $\alpha \in (1, 2]$, that is, $\alpha/2 \in (0.5, 1]$, we finally obtain

$$(a+b)^{\alpha/2} \leq a^{\alpha/2} + b^{\alpha/2}(2^{\alpha/2} - 1) \leq a^{\alpha/2} + b^{\alpha/2}.$$

□

If we consider as a and b the eigenvalues of the standard one-dimensional Laplacian on $[0, L_x]$ and on $[0, L_y]$ coupled with homogeneous Neumann boundary conditions, then from (6.19) we obtain that each eigenvalue in the spectrum of the two-dimensional fractional Laplacian is smaller than or equal to the corresponding eigenvalue of the two-dimensional Riesz-Feller operator. Hence, we expect the effect of non-locality to be stronger in the case of the fractional Laplacian and the difference between the two approaches to become more evident as the considered fractional order decreases.

This is indeed the case. In Figure 6.16 we provide the projection onto the

xy-plane of the solution of system (6.15) (in Figure 6.16(a)) and of system (6.18) (in Figure 6.16(b)) at $t = 120\,\text{msec}$, generated by the stimulus $I^{(\text{vol})} = 10^5\,\mu\text{A}\cdot\text{cm}^{-3}$ applied to the region $[0, 0.1\,\text{cm}] \times [0, 0.1\,\text{cm}]$ surrounding the origin at $t = 10\,\text{msec}$ for five consecutive milliseconds when $\alpha = \alpha_x = \alpha_y = 1.5$. In order to avoid oscillations in the solution we reduce the uniform mesh size in both directions to $h_x = h_y = 0.004\,\text{cm}$ but also reduce the size of the square domain to $\Omega = [0, 1\,\text{cm}] \times [0, 1\,\text{cm}]$ in order to reduce the computational cost of producing the two numerical solutions.

As we can see that the solution produced by the two fractional models at the same time point differs fundamentally in the wavefront shape. In fact, the position reached by the propagating pulse advancing along the two axes is almost identical. However, as we move away from the boundaries, the stronger non-locality effect of the two-dimensional fractional Laplacian (essentially contained in the eigenvalues of its spectral expansion) results in a more uniform and smaller curvature of the pulse front and the consequent slower depolarization of the points along the main diagonal of the considered square domain.

6.6 Discussion

In this chapter we have focused our attention on the effect produced on the solution of some standard excitable media models by the introduction in the model of a fractional component in space. We are aware of the fact that in the simulation study proposed many simplifying assumptions were made (such as the choice of the monodomain formulation over the bidomain model, or ignoring rotational effects in the definition of the diffusive tensor) and that the quantitative results obtained are strongly related to the particular sets of parameter values used in the simulations (such as the value of the surface to volume ratio, the conductivity values, and - probably the most important of all - the strength, duration and region to which the electrical stimulus was applied). Moreover, dictated by numerical requirements and in order to avoid high computational costs, only a certain subset of values of the

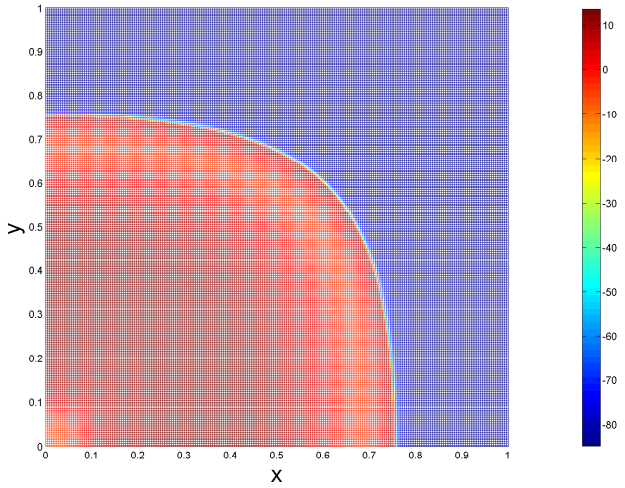

(a) Riesz-Feller

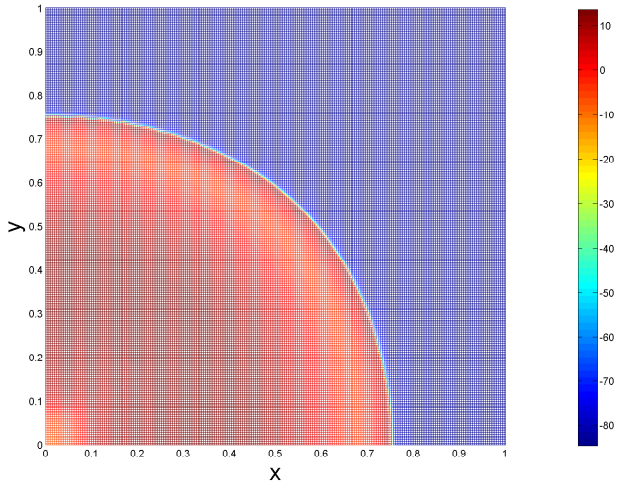

(b) 2D fractional Laplacian

Figure 6.16: *Projection onto the xy-plane of the solution of system (6.15) with* $\alpha_x = \alpha_y = 1.5$ *and of the solution of system (6.18) with* $\alpha = 1.5$ *at* $t = 120\,\text{msec}$. *The solution is computed via the spectral modification of Whiteley's method with a uniform time grid of* $\Delta t = 0.01$ *on* $\Omega = [0,1]\times[0,1]$. *The mesh size used in both spatial directions is* $h_x = h_y = 0.004$.

fractional parameters were considered.

However, the simulations performed and the results proposed allowed us to make important and valuable qualitative considerations on the space-fractional modification of the excitable media models studied and to isolate the effect of a reduced fractional order from other possible causes of modified signal propagation. We were also able to identify strengths and weaknesses of the spectral decomposition method proposed, which certainly requires additional work in order to be improved and made more flexible before this strategy can be adopted for the solution of large scale models.

Finally, the two-dimensional case served as an important point of discussion due to the challenges that one faces when aiming to extend the concept of non-local fractional operators on finite domains (with non-trivial boundary conditions) in more than one spatial dimension.

As for the cell migration application considered in Chapter 5, one of the main objectives and future extensions of this work will be the development of excitable media models with variable fractional order, in the attempt of characterising different levels of heterogeneity with different values of α and using these models to capture the anomalous behaviour of electrical propagation through excitable tissue observed in some pathological cases.

Before doing so it is however important that all modelling and implementation aspects of purely fractional excitable media models are investigated in greater detail so that all the interactions between modelling and simulation parameters are clearly understood and accounted for.

Chapter 7

Conclusions

The main theoretical goal of this thesis was to correctly formalise on insulated spatial domains the space-fractional modification of some standard models of interest describing different examples of transport phenomena (in biology and electrophysiology). These modifications were made under the assumption that the structures in which the observed transport processes took place were characterised by non-negligible levels of heterogeneity and complexity. In particular, we considered the Fisher–Kolmogoroff equation as example of cell migration model and the monodomain Fitzhugh–Nagumo and the monodomain Beeler–Reuter models as examples describing electrical pulse propagation in excitable media. We then considered various implementation aspects for the computation of the solution of the non-local version of these models and specifically focused on the spectral decomposition method. Finally, we compared the results of space-fractional simulations with the results typically obtained for the considered models in the standard case.

In this chapter we restate the specific objectives of the thesis (identified in Chapter 1), discuss how each of these objectives was addressed, summarise our findings and discuss strengths and weaknesses of our approach. In Section 7.2, we present possible future directions of research for the improvement and extension of the work presented here. Section 7.3 provides a list of the papers obtained as outcome of this thesis.

7.1 Addressing the main objectives

Derivation of a matrix representation of the space-fractional operator obtained from the finite-difference Grünwald–Letnikov approach and embedding reflecting boundary conditions.

By interpreting one-dimensional insulating boundary conditions as elastic walls reflecting the parabolic trajectories of an ensemble of particles performing symmetric α-stable Lévy flights, Krepysheva et al. [45] and Néel et al. [65] arrived at a formulation of the continuous non-local operator on the insulated interval $[0, L]$ embedding in its definition reflecting boundary conditions (in this thesis denoted by $\mathcal{R}^{\alpha}_{x,L}$).

In Chapter 4, we followed the steps made by these authors, building successive modifications of the generalised master equation, and reformulated their final result by introducing the sawtooth function $[x]^L_0$. We then introduced a spatial discretisation grid and used a modification of the shifted Grünwald–Letnikov approach accounting for reflections to define the discrete approximation A_α of the operator $-\mathcal{R}^{\alpha}_{x,L}$, providing the explicit expression for all entries of this matrix. In fact, thanks to the introduction of the sawtooth function in our reformulation, we were able to find the specific link between the nodes of the spatial grid of the finite domain and the weights in the approximation given by the shifted Grünwald–Letnikov approach.

Investigation and clarification of the relationship between the discrete reflection operator and the discrete operator obtained via the matrix transfer technique when standard homogeneous Neumann boundary conditions are considered.

The matrix transfer technique is essentially a method based on the definition of a discrete non-local operator on a finite domain via its spectral decomposition. In Theorem 1 of Chapter 4, we provided the analytic expression for the spectrum of the discrete reflection operator A_α derived in Section 4.2 as a function of the fractional order α and the size N of the operator (corresponding to the number of nodes used to discretise the interval $[0, L]$). We

observed that the eigenfunctions of A_α do not depend on the fractional order and that the N eigenvalues can be written as products of two factors, $\lambda_j^{\alpha/2}$ and q_α in Section 4.4.

In particular, $\lambda_j^{\alpha/2}$ is the fractional power of the j-th eigenvalue of the discrete standard Laplacian obtained using the finite-difference method on the considered spatial grid when a second order approximation is used at both boundaries and homogeneous Neumann boundary conditions are assumed. We hence saw that the $\lambda_j^{\alpha/2}$, for $j = 0, 1, \ldots, N-1$, were the N eigenvalues of the operator B_α of size N obtained with the matrix transfer technique with homogeneous Neumann boundary conditions and second order approximation at both ends of $[0, L]$. Therefore, we can draw the following conclusions:

- The eigenvectors of A_α and B_α coincide $\forall \alpha \in (1, 2]$.
- When $\alpha = 2$, $A_\alpha = B_\alpha$ and hence also the set of N eigenvalues of the two operators coincide.
- When $\alpha < 2$, the two operators are different. There is in fact a discrepancy between the eigenvalues of A_α and B_α that can be precisely quantified for each eigenvalue as the factor q_α defined in equation (4.53). Note that $q_\alpha \neq 1$ when $\alpha < 2$, and its expression also depends on the index j, that is, q_α is different for all eigenvalues.

Suitable formulation of the restriction of the fractional Laplacian operator on an insulated finite one-dimensional domain $[0, L]$.

We saw that when $\alpha < 2$ the discrete operators A_α and B_α are different and hence we expect the solution to the same space-fractional problem computed with the method of lines using these two operators to be in principle different as well. However, from the practical point of view we are interested in considering the limiting case $N \to \infty$, or equivalently $h \to 0$, where h is the uniform size used in the spatial discretisation mesh. In Section 4.4 we found that the eigenpairs of both operators converge to the same limit as N approaches infinity, and this limit was used to provide a spectral definition of the continuous fractional Laplacian on the insulated interval $[0, L]$. In particular,

the eigenfunctions of the limiting operator were equal to the eigenfunctions of the continuous standard Laplacian on $[0, L]$ coupled with homogeneous Neumann boundary conditions and the eigenvalues were fractional powers (with exponent $\alpha/2$) of the eigenvalues of the same continuous standard operator. Therefore, when formulating the space-fractional modification of a given reaction-diffusion problem on an insulated domain $[0, L]$, we simply substituted the standard diffusive operator $-\frac{\partial^2}{\partial x^2}$ with the one-dimensional fractional Laplacian $(-\Delta)^{\alpha/2}$ embedding reflecting boundary conditions and defined via its spectral expansion as the limiting case of A_α for $N \to \infty$.

The observations made on the asymptotic case not only implied that if the number of spatial nodes used in the discretisation of $[0, L]$ is sufficiently large, then the solution approximations computed either with A_α or B_α are practically equivalent, but also suggested a different implementation strategy for the solution of space fractional problems on insulated domains. In fact, having at our disposal the exact spectral expansion of the non-local operator, we decided to use the spectral decomposition method instead of introducing a discrete approximation of the operator (such as A_α or B_α), so that, at least in principle, we were able to avoid the introduction of the numerical errors due to the spatial discretisation of the continuous operator and obtain a more accurate representation of the solution. However, as we saw for the practical applications of interest, there were still a number of approximations that had to be considered in the actual computation of the solution for a generic space-fractional reaction-diffusion problem.

Formulation and solution of the space-fractional modification of the Fisher–Kolmogoroff equation on an insulated finite interval using the spectral decomposition method.

Chapter 5 was dedicated to the study of the space-fractional modification on an insulated finite interval $[0, L]$ of the Fisher–Kolmogoroff equation, probably the simplest reaction-diffusion equation used in biology to describe cell migration phenomena. We formulated the fractional FK equation by using the one-dimensional fractional Laplacian embedding reflecting boundary

conditions and compute the solution of the model for $\alpha \in (1, 2]$ with the spectral decomposition method. In particular, for practical reasons, we must truncate the series expansion of the solution and introduce a suitable integration scheme for the update of the solution in time, due to the presence of a reaction term in the equation of the model. We decided to introduce a semi-implicit Euler method for time discretisation of the problem, and truncated the infinite series expansion of the solution after a number of terms equal to the number of points in space at which we wanted the value of the final solution to be provided. Clearly, in order for the error due to the truncation of these sums to be negligible, we had to ensure that the number of terms considered in the series was sufficiently high and we did so by computing the solution on a fine spatial grid. Having chosen an initial condition with exponential decay for $x \to \infty$, when $\alpha = 2$ we obtained the expected travelling wave solution profile advancing in the spatial interval with constant shape and speed. In the fractional case however, the travelling wave nature of the solution was lost and a quick acceleration towards the stable steady state of the system, $u = 1$, was observed.

By introducing the concept of level sets (see Chapter 5 for details) we were able to quantify this acceleration of the solution profiles as an exponential advancing of the level sets in time, clearly different from the linear advancing observed for the solution in the standard case. This result is in agreement with the asymptotic result proposed by Cabré and Roquejoffre [15] on the infinite domain. However, in the case of a finite domain, not being able to follow the solution profile after the boundary $x = L$ is reached, we did not recover the exact exponential profile of the asymptotic prediction, but only a more generic (and truncated) exponential behaviour (see Figure 5.4(b)).

Inspired by the experimental observations made by Druckenbrod and Epstein [24] on the migration of neural crest-derived cells in the gut of mice embryos *in vivo*, in which differences in the migrating pattern are observed as the advancing cell population reaches different regions of the gut, we then wanted to see whether it was possible to develop a fractional modification

of the FK model accounting for the qualitative differences in the migration patter observed. In particular, wanting to characterise different spatial subregions of the domain with different values of α, we focused on the possibility of implementing a space-fractional modification of the FK equation with variable fractional order. Specifically, we considered a piecewise constant function $\alpha(x)$ (assuming two different values on the insulated interval $[0, 2L]$), and aimed at providing a definition of $(-\Delta)^{\alpha(x)/2}$ on the considered domain. We realised that the probably more intuitive approach of splitting the domain into two subregions corresponding to the different values of $\alpha(x)$ and solving the problem on the two separated domains with some additional matching conditions at the interface, was not the best choice. In fact, this approach would have required the introduction of additional boundary conditions at the interface for the non-local operator to be defined in both subregions. However, neither homogeneous Dirichlet nor reflecting boundary conditions would have been suitable for the considered model since they would have added additional restrictions to the solution that were not part of the problem.

Perhaps some alternative approach could be found by suitably modelling different types of boundary conditions (not necessarily homogeneous Dirichlet nor reflecting conditions) but to our knowledge, rigorous theories providing the definition of the fractional Laplacian on finite domains in the presence of these other boundary conditions have not been developed yet. We hence decided to look for a different approach so that the interval $[0, 2L]$ could be treated as a whole, and reflecting conditions only at $x = 0$ and $x = 2L$ were introduced. Being unable to define the spectrum of $(-\Delta)^{\alpha(x)/2}$ on $[0, 2L]$, nor provide an alternative continuous definition of this operator, we chose to go back to the discrete approach and formulate a discrete approximation of the variable order operator that could be used to compute the solution with the method of lines, instead of the spectral method. We hence built the discrete operator $A_{\alpha(x)}$ of equation (5.6), by suitably combining the reflection matrices corresponding to the two values assumed by $\alpha(x)$. We then computed the numerical solution of the variable order fractional FK model with $\alpha(x) =$

1.5 on $[0, L]$ and $\alpha(x) = 2$ on $(L, 2L]$ and obtained the desired effect on the solution. In fact, by looking at the solution profile (Figure 5.5) and at the level sets (Figure 5.6) corresponding to a specific $s \in (0, 1)$, we found that the solution initially behaved similarly to that observed in the purely fractional case but in the second half of the spatial interval, the character of the solution changed and its profile eventually evolved to a travelling wave solution advancing in time with constant shape and speed.

Formulation and solution of the space-fractional modification of the Fitzhugh-Nagumo and Beeler-Reuter monodomain models on an insulated finite interval and on an insulated rectangular domain via the spectral decomposition method.

In Chapter 6 we focused on the second application object of study in this thesis, that is, excitable media models in electrophysiology. In particular, we chose two simple cell models reproducing the main features of the action potential observed for two different types of excitable cells (namely the FHN model for neural cells and the BR model for cardiac muscle cells), coupled them with the monodomain formulation providing a simplified description of signal propagation in excitable tissue, and finally considered the space-fractional modification of these excitable media models by introducing a suitable non-local operator.

We started by considering the one-dimensional case and by formulating the problem on the insulated interval $[0, L]$ by using once again the one-dimensional fractional Laplacian embedding reflecting boundary conditions. Excitable media models in the monodomain formulation typically involve a PDE governing the spatial and temporal evolution of the variable of interest (the transmembrane potential) and a system of stiff ODEs describing the evolution in time of the additional gating varibles and concentrations involved in the ionic model considered. The space-fractional modification of the resulting system of differential equations formally affects only the diffusive component of the PDE. Therefore, in order to compute the solution in the fractional case, we adopted the spectral decomposition method to solve

the fractional PDE, but still used Whiteley's approach [83] to update the entire system in time. By simulating the application of a sufficiently strong electrical stimulus in the system, in the standard case we were able to trigger an excitation wave that moves in time away from the stimulus site, causing all points of the spatial domain to undergo an action potential with particular shape and size dictated by the cell model considered. The same applied current still generated an excitation wave in the case of $\alpha < 2$. However, as α decreased, the conduction velocity of the advancing wave in both models decreased and the action potential recorded at a given point in space exhibited a later activation in time, a slight reduction of the action potential height for both cell models, a slightly more pronounced early depolarization phase for the BR case, and finally an increasingly large dispersion of action potential duration as we moved away from the site where the stimulus was applied.

The second half of Chapter 6 was dedicated to possible two-dimensional extensions of these non-local models, their implementation and comparison. Specifically, we considered the case of a rectangular insulated domain $\Omega = [0, L_x] \times [0, L_y]$ and proposed two different definitions of space-fractional operators on Ω. The first option essentially defined the non-local operator as the direct sum of two one-dimensional fractional Laplacian operators embedding reflecting boundary conditions in the x and y directions, and can hence be seen as the restriction of the two-dimensional Riesz-Feller operator (defined as in equation (2.55) with $n = 2$) on the finite domain Ω. On the other hand, the second definition was not based on any theoretical result but rather was a speculation on what we expected to be the result of generalising the concept of reflections to two spatial dimensions. Both definitions were given in terms of the spectral expansion of these operators and differed only in the set of eigenvalues. We provided extensions of these definitions to the more general case in which different conductivity values are assumed in each spatial direction (however, ignoring rotational effects in the conductivity tensor), and also observed that in the Riesz-Feller definition we have the additional freedom of choosing different fractional orders (α_x and α_y) for each of the two one-dimensional fractional operators involved.

The numerical strategy was easily generalised to the two-dimensional case thanks to the explicit knowledge of the eigenpairs of the considered operators. We provided essentially two sets of results on an insulated square domain. In the first case we stimulated a small region of Ω surrounding the corner in the origin (that is, a small region $[0, \bar{x}] \times [0, \bar{y}]$) and compared the solution obtained for a given applied current in three different cases:

- standard case (obtained when the Riesz-Feller operator was used with $\alpha_x = \alpha_y = 2$);
- Riesz-Feller approach with two equal fractional orders ($\alpha_x = \alpha_y = 1.9$);
- Riesz-Feller approach with a combination of different fractional orders ($\alpha_x = 2$, $\alpha_y = 1.9$).

We observed that when the same order was used in both directions, the excitation wave advanced symmetrically with respect to the main diagonal of the square and as the fractional order was reduced we essentially observed the same effect seen in the one-dimensional case in both spatial directions: later depolarization, reduced conduction velocity and more pronounced dispersion of action potential duration as we moved away from the stimulation site. When a combination of two different fractional orders was used, the advancing of the front along each axis was dictated by the particular order used in that direction and as a result, the two-dimensional front was not symmetric anymore but rather moved faster along the direction with the higher fractional exponent. On the other hand, the advancing of the front at points not located along the two main spatial directions received the contribution of both fractional orders, and hence by observing the characteristics of the action potential at points located along the main diagonal of the square domain, a clear difference between the three options considered was evident.

In the second and final sets of results in the chapter, we compared the solution obtained with the Riesz-Feller approach (when a single fractional order was considered in both dimensions) and the one computed with the second definition of non-local operator, with equal fractional order. We found that

the advancing of the travelling pulse triggered by the same applied stimulus in the two cases was equal along the two axes but differed substantially in the curvature as we moved away from these axes. This discrepancy could be justified by looking at the spectrum of both operators and observing that each eigenvalue in the spectrum of the two-dimensional fractional Laplacian as a whole is smaller than the corresponding eigenvalue in the spectrum of the Riesz-Feller operator (see Lemma 6 in Chapter 6 and following considerations). The reduction in the eigenvalues can be in fact interpreted as an indicator of a higher level of non-locality being introduced in the space-fractional modification of the considered standard model and hence further reducing the advance of the excitation wave in the domain.

7.2 Future directions of research

To conclude the thesis, in this Section we discuss possible improvements and extensions of the proposed work, suggesting some directions for future research. In particular, we classify the areas of future research into three big categories related to the three fundamental components considered in this work: models, numerical schemes and applications.

Models

As presented in Chapter 1, and then reiterated throughout the rest of the thesis, restricting the definition of non-local operators to finite domains for practical applications is a challenging task and still presents a large number of open questions. For example, in the one-dimensional case, it is still unclear how to properly model non-local problems on a finite domain with more general boundary conditions, that is, not necessarily homogeneous Dirichlet or reflecting conditions. In this thesis we clarified the particular case of insulating boundary conditions for one-dimensional finite domains, however, we recognize that their generalisation to more than one spatial dimension requires further investigation. Nevertheless, we were able to provide two alternative definitions for the particular case of a regular rectangular domain

$\Omega = [0, L_x] \times [0, L_y]$. The restriction of the Riesz-Feller definition was a natural choice, extending the results obtained on the one-dimensional reflection operator to the intervals $[0, L_x]$ and $[0, L_y]$ in the definition of Ω. On the other hand, the spectral definition of the two-dimensional fractional Laplacian as a whole, was essentially possible because on a rectangular domain the spectrum of the continuous standard two-dimensional Laplacian is known. However, we stress once again that this second option requires the development of a firmer theoretical framework (so that its definition could be justified more rigorously from the mathematical point of view) and clearly the case of non-rectangular domains (or more generally, irregular domains) is an important topic that will have to be addressed next.

Furthermore, from the practical point of view, of particular interest is the development of models of variable fractional order. In fact, one of the ultimate goals is to see whether it is possible to use different fractional orders in different subregions of a given domain in order to capture mathematically different levels of heterogeneity that might be observed experimentally in a considered spatial structure. The discrete operator of variable order $A_{\alpha(x)}$ in Chapter 5 was defined in order to address an issue of this type. However, even in the relatively simple example proposed, the definition of the operator was not the result of a rigorous theoretical framework but it was rather an operational definition made to satisfy the particular requirements of the problem of interest. Therefore, the study of the operator $(-\Delta)^{\alpha(x)/2}$, especially for more generic functional forms of $\alpha(x)$, deserves additional attention and we do not exclude that different (possibly better) implementation strategies for the variable order problem considered in Chapter 5 might be discovered.

Numerical schemes

In this thesis we focused on the spectral decomposition method for the computation of the solution of the space-fractional modifications of the two applications of interest. This method allowed us to obtain the analytic solution in the case of the fractional diffusion equation in Chapter 4, and to compute a satisfactory approximation of the solution of the fractional FK model in

Chapter 5 in just a fraction of a second.

The computational cost required to compute the solution of fractional excitable media models was significantly higher compared to the fractional FK equation and the reason for this is to be seen in the higher complexity of the system that has to be solved (which distinguishes the two models even in the standard case). However, in our simulations we encountered some additional issues related to the particular strategy used to approximate the Fourier coefficients in the truncated series expansion of the solution. Due to the simplicity of implementation, we chose in fact to use the trapezoidal rule for the approximation of the integrals $\hat{v}_j^k$ and $\hat{g}_j(v^k, \mathbf{z}^k)$ in equation (6.3). The trapezoidal rule is an example of polynomial approximation typically of the second order in the mesh size used to discretise the spatial variable. However, for highly oscillatory integrands, polynomial approximations do not work unless a very high number of spatial nodes is used, and alternative strategies (such as Filon-type approximations) might offer a much better approximation of the consider integral. The use of the trapezoidal rule in the FK case is not an issue, however, in our simulations of fractional excitable media models, it imposed the use of a very fine spatial mesh, especially as the considered fractional order decreased.

We believe that the main reason for this restriction is the poor approximation of the integral coefficients in the spectral expansion of the source term $g(v, \mathbf{z})$. In fact, for the FK equation $g(u) = u(1-u)$, whereas for our excitable media models $g(v, \mathbf{z}) = -I_{\text{ion}}(v, \mathbf{z}) + \frac{1}{\chi} I^{(\text{vol})}$. Therefore, other than having a much more complex functional form (given by the ionic current term), the source term of our excitable media models also involves the applied stimulus, which is a significant perturbation of the system during the temporal interval when $I^{(\text{vol})} \neq 0$. Thanks to the full diagonalisation of the solution strategy in the spectral method, requiring the computation of the solution at a very high number of spatial nodes simply required longer times for the solution to be provided. We hence decided for the simulations proposed in the chapter to preserve the simplicity of implementation of the solution strategy given by

the trapezoidal rule and simply compute the numerical solution on a very fine spatial grid to avoid oscillations in the final result. However, we recognize that this is a considerable limitation of the strategy proposed, especially if we consider possible extensions to more complex ionic models or larger scale simulations. The strength of a spectral decomposition method is to provide higher accuracy in the solution with less computational effort (due to the fully diagonal formulation of the problem). Therefore, it is important to ensure that all components of this strategy are optimised so that the spectral method can be more effective.

The choice of using the semi-implicit Euler method for temporal integration of the space-fractional PDE is another aspect of the numerical implementation that could be further investigated. The temporal discretisation used is in fact first order accurate in time and we believe that one could significantly benefit from a higher order integration scheme such as a higher order exponential method in which the source term $g(v, \mathbf{z})$ is possibly linearised. Some additional effort might be required in general to obtain an explicit formulation (or a suitable approximation) of the Jacobian of the source term but this has to be done only once at the beginning of the computation. After that, the advantage of having a higher order method in time can be exploited and larger time steps can be used, allowing a much faster computation of the solution approximation.

Applications

The final consideration we make here is related to the practical applications of interest. In fact, the space-fractional modification of the cell migration models in biology and the excitable media models in electrophysiology were developed not only from a purely theoretical perspective but also inspired by specific applications in which the transport phenomena observed presented characteristics that could not be reproduced with simple reaction-diffusion models. Our space-fractional modifications of the considered models presented good qualitative agreement with the behaviour observed for the specific applications studied. These results strengthened the idea that space-

fractional models might offer significant and useful insight into transport processes that are sensibly affected by the heterogeneity of the structure in which they take place. However, due to the relative simplicity of the models used (simplified domain structure and simplified assumptions) and the lack of detailed experimental data, it was not possible to validate our models quantitatively. When dealing with models for practical applications, validation is a very important component of the work. Therefore, if one of the future aims of the study presented here is to use these fractional models (or variations of them with possibly variable fractional order) to obtain useful information or predictions in a clinical setting, it will be vital to gain access to a significant amount of experimental and clinical data for the particular applications considered so that not only qualitative but also quantitative validation of these models will be possible.

7.3 Publications

The papers obtained as outcome of this thesis are as follows:

- N. Cusimano, K. Burrage and P. Burrage, *Fractional models for the migration of biological cells in complex spatial domains*, ANZIAM Journal E (2013), 54, C250-C270.

- D. Kay, N. Cusimano, K. Burrage and I.W. Turner, *Reflecting boundary conditions for space-fractional equations on insulated finite domains and the discrete reflection operator*, to be submitted at the beginning of 2015.

- N. Cusimano, K. Burrage, P. Burrage and I.W. Turner, *Computationally efficient methods for the solution of space-fractional reaction-diffusion equations on one-dimensional insulated bounded domains: The spectral approach with exponential integration in time*, journal article in preparation.

- N. Cusimano, K. Burrage, P. Burrage and I.W. Turner, *Space-fractional*

operators on finite insulated rectangular domains in 2D and their application in electrophysiology, journal article in preparation.

Bibliography

[1] A.S. Ackleh, E.J. Allen, R.B. Kearfott and P. Seshaiyer, *Classical and modern numerical analysis. Theory, methods and practice*, Chapman & Hall/CRC (2009).

[2] I.J. Allan and D.F. Newgreen, *The origin and differentiation of enteric neurons of the intestine of the fowl embryo*, The American Journal of Anatomy (1980), 157, 137-154.

[3] H. Anton and C. Rorres, *Elementary linear algebra: Applications version*, Wiley (2010), Tenth Edition.

[4] U.M. Ascher, S.J. Ruuth and B.T.R. Wetton, *Implicit-explicit methods for time-dependent partial differential equations*, SIAM Journal on Numerical Analysis (1995), 32 (3), 797-823.

[5] D.A. Benson, S.W. Wheatcraft and M.M. Meerschaert, *Application of a fractional advection-dispersion equation*, Water Resources Research (2000), 36 (6), 1403-1412.

[6] G.W. Beeler and H. Reuter, *Reconstruction of the action potential of ventricular myocardial fibres*, Journal of Physiology (1977), 268, 177-210.

[7] B.J. Binder, K.A. Landman, M.J. Simpson, M. Mariani and D.F. Newgreen, *Modeling proliferative tissue growth: A general approach and an avian case study*, Physical Review E (2008), 78 (3), 1-13.

[8] Y. Bourgault and C. Pierre, *Comparing the bidomain and monodomain models in electro-cardiology through convergence analysis*, HAL Archives-Ouvertes (2010), <hal-00545888v1>.

[9] J.P. Boyd, *Chebyshev and Fourier spectral methods*, Dover Publications (2001), Second Edition (Revised).

[10] M.A. Breau, A. Dahmani, F. Broders–Bondon, J.P. Thiery and S. Dufour, *β1 integrins are required for the invasion of the caecum and proximal hindgut by enteric neural crest cells*, Development (2009), 136, 2791-2801.

[11] A. Bueno–Orovio, D. Kay and K. Burrage, *Fourier spectral methods for fractional-in-space reaction-diffusion equations*, BIT Numerical Mathematics (2014).

[12] A. Bueno–Orovio, D. Kay, V. Grau, B. Rodriguez and K. Burrage, *Fractional diffusion models of cardiac electrical propagation: Role of structural heterogeneity in dispersion of repolarization*, Journal of the Royal Society Interface (2014), 11 (97), 20140352.

[13] J.C. Butcher, *Numerical methods for ordinary differential equations*, Wiley (2003).

[14] K. Burrage, N. Hale and D. Kay, *An efficient implementation of an implicit FEM scheme for fractional-in-space reaction-diffusion equations*, SIAM Journal on Scientific Computing (2012), 34, A2145-A2172.

[15] X. Cabré and J.M. Roquejoffre, *The influence of fractional diffusion in Fisher-KPP equations*, Communications in Mathematical Physics (2013), 320, 679-722.

[16] J.M. Carcione, F.J. Sanchez–Sesma, F. Luzón and J.J. Perez Gavilán, *Theory and simulation of time-fractional fluid diffusion in porous media*, Journal of Physics A (2013), 46, 345501.

[17] H. Chen, *On the summation of subseries in closed form*, International Journal of Mathematical Education in Science and Technology (2010), 41 (4), 538-547.

[18] E.M. Cherry and F.H. Fenton, *Effects of boundaries and geometry on the spatial distribution of action potential duration in cardiac tissue*, Journal of Theoretical Biology (2011), 285 (1), 164-176.

[19] R.H. Clayton, O. Bernus, E.M. Cherry, H. Dierckx, F.H. Fenton, L. Mirabella, A.V. Panfilov, F.B. Sachse, G. Seeman and H. Zhang, *Models of cardiac tissue electrophysiology: Progress, challenges and open questions*, Progress in Biophysics and Molecular Biology (2011), 104 (1-3), 22-48.

[20] A. Compte, *Stochastic foundations of fractional dynamics*, Physical Review E (1996), 53 (4), 4191-4193.

[21] N. Cusimano, K. Burrage and P. Burrage, *Fractional models for the migration of biological cells in complex spatial domains*, ANZIAM Journal E (2013), 54, C250-C270.

[22] D. del–Castillo–Negrete, B.A. Carreras and V.E. Lynch, *Front dynamics in reaction-diffusion systems with Lévy flights: A fractional diffusion approach*, Physical Review Letters (2003), 91 (1), 018302.

[23] D. del–Castillo–Negrete, *Truncation effects in superdiffusive front propagation with Lévy flights*, Physical Review E (2009), 79, 031120.

[24] N.R. Druckenbrod and M.L. Epstein, *The pattern of neural crest advance in the cecum and colon*, Developmental Biology (2005), 287, 125-133.

[25] N.R. Druckenbrod and M.L. Epstein, *Behaviour of enteric neural crest-derived cells varies with respect to the migratory wavefront*, Developmental Dynamics (2007), 236, 84-92.

[26] H. Engler, *On the speed of spread for fractional reaction-diffusion equations*, International Journal of Differential Equations (2010), 31542, 1-16.

[27] G. Erochenkova and R. Lima, *A fractional diffusion equation for a marker in porous media*, Chaos (2001), 11 (3), 495-499.

[28] R.A. Fisher, *The wave of advance of advantageous genes*, Annals of Eugenics (1937), 7, 353369.

[29] R. Gorenflo and F. Mainardi, *Random walk models for space-fractional diffusion processes*, Fractional Calculus and Applied Analysis (1998), 1, 167-191.

[30] B.I. Henry and T.A.M. Langlands, *Fractional cable models for spiny neuronal dendrites*, Physical Review Letters (2008), 100 (12), 128103.

[31] A.L. Hodgkin and A.F. Huxley, *A quantitative description of membrane current and its application to conduction and excitation in nerve*, Journal of Physiology (1952), 117, 500-544.

[32] U. Hornung, *Homogenization and porous media*, Springer-Verlag (1997).

[33] V. Hutson, J.S. Pym and M.J. Cloud, *Applications of functional analysis and operator theory*, Elsevier (2005), Second Edition.

[34] M. Ilić, F. Liu, I.W. Turner and V. Anh, *Numerical approximation of a fractional-in-space diffusion equation (I)*, Fractional Calculus and Applied Analysis (2005), 8, 323-341.

[35] M. Ilić, F. Liu, I.W. Turner and V. Anh, *Numerical approximation of a fractional-in-space diffusion equation (II) - with nonhomogeneous boundary conditions*, Fractional Calculus and Applied Analysis (2006), 9, 333-349.

[36] M. Ilić, I.W. Turner, F. Liu and V Anh, *Analytical and numerical solutions of a one-dimensional fractional-in-space diffusion equation in*

a composite medium, Applied Mathematics and Computation (2010), 216, 2248-2262.

[37] A. Iserles, *On the numerical quadrature of highly-oscillating integrals I: Fourier transforms*, IMA Journal of Numerical Analysis (2004), 24, 365-391.

[38] A. Iserles, *A first course in the numerical analysis of differential equations*, Cambridge University Press (2009), Second Edition.

[39] J. Keener and J. Sneyd, *Mathematical Physiology. I: Cellular Physiology*, Springer Science+Business Media (2009), Second Edition.

[40] J. Keener and J. Sneyd, *Mathematical Physiology. II: Systems Physiology*, Springer Science+Business Media (2009), Second Edition.

[41] A. Kharab and R.B. Guenther, *An introduction to numerical methods. A MATLAB® approach*, Chapman & Hall/CRC (2006), Second Edition.

[42] A.A. Kilbas, H.M Srivastava and J.J. Trujillo, *Theory and applications of fractional differential equations*, Elsevier (2006).

[43] J. Klafter, M.F. Shlesinger and G. Zumofen, *Beyond Brownian motion*, Physics Today (1996), 49 (2), 33-39.

[44] A. Kolmogoroff, I. Petrovsky and N. Piscounoff, *Étude de l'équation de la diffusion avec croissance de la quantitè de matiére et son application à un probléme biologique*, Moscow University Mathematics Bulletin (1937), 1, 1-25.

[45] N. Krepysheva, L. Di Pietro and M.C. Néel, *Space-fractional advection-diffusion and reflective boundary condition*, Physical Review E (2006), 73, 021104.

[46] K.A. Landman, G.J. Pettet and D.F. Newgreen, *Mathematical models of cell colonization of uniformly growing domains*, Bulletin of Mathematical Biology (2003), 65, 235-262.

[47] K.A. Landman, M.J. Simpson, J.L. Slater and D.F. Newgreen, *Diffusive and chemotactic cellular migration: Smooth and discontinuous traveling wave solutions*, SIAM Journal of Applied Mathematics (2005), 65 (4), 1420-1442.

[48] R. Lin, F. Liu, V. Anh and I.W. Turner, *Stability and convergence of a new explicit finite-difference approximation for the variable-order nonlinear fractional diffusion equation*, Applied Mathematics and Computation (2009), 212, 243-445.

[49] K. Logvinova and M.C. Néel, *A fractional equation for anomalous diffusion in a randomly heterogeneous porous medium*, Chaos (2004), 14, 982-987.

[50] J.T. Machado, V. Kiryakova and F. Mainardi, *Recent history of fractional calculus*, Communications in Nonlinear Science and Numerical Simulations (2011), 16, 1140-1153.

[51] R. Magin, X. Feng and D. Baleanu, *Solving the fractional order Bloch equation*, Concepts in Magnetic Resonance Part A (2009), 34A, 16-23.

[52] P.K. Maini, D.L.S. McElwain and D.I. Leavesley, *Travelling waves in a wound healing assay*, Applied Mathematics Letters (2004), 17 (5), 575-580.

[53] P.K. Maini, D.L.S. McElwain and D.I. Leavesley, *Traveling wave model to interpret a wound-healing cell migration assay for human peritoneal mesothelial cells*, Tissue Engineering (2004), 10 (3-4), 475-482.

[54] R. McLennan, L. Dyson, K.W. Prather, J.A. Morrison, R.E. Baker, P.K. Maini and P.M. Kulesa, *Multiscale mechanisms of cell migration during development: Theory and experiment*, Development (2012), 139, 2935-2944.

[55] M.M. Meerschaert and C. Tadjeran, *Finite difference approximations for fractional advection-dispersion flow equations*, Journal of Computational and Applied Mathematics (2004), 172, 65-77.

[56] M.M. Meerschaert and E. Scalas, *Coupled continuous time random walks in finance*, Physica A (2006), 370, 114-118

[57] F.C. Meral, T.J. Royston and R. Magin, *Fractional calculus in viscoelasticity: An experimental study*, Communications in Nonlinear Science and Numerical Simulations (2010), 15, 939-945.

[58] R. Metzler and J. Klafter, *The random walk's guide to anomalous diffusion: A fractional dynamical approach*, Physics Reports (2000), 339, 1-77.

[59] R. Metzler, J. Klafter and I.M. Sokolov, *Anomalous transport in external fields: Continuous time random walks and fractional diffusion equations extended*, Physical Review E (1998), 58 (2), 1621-1633.

[60] R. Metzler and T.F. Nonnenmacher, *Space- and time-fractional diffusion and wave equations, fractional Fokker-Planck equations, and physical motivation*, Chemical Physics (2002), 284, 67-90.

[61] T.J. Moroney and Q. Yang, *A banded preconditioner for the two-sided, nonlinear space-fractional diffusion equation*, Computers & Mathematics with Applications (2013), 66 (5), 659-667.

[62] J.D. Murray, *Mathematical Biology. I: An Introduction*, Springer-Verlag (2003), Third Edition.

[63] J.D. Murray, *Mathematical Biology. II: Spatial Models and Biomedical Applications*, Springer-Verlag (2003), Third Edition.

[64] M.J. Nelson, C. Bosch, L. Venance and P. Pouget, *Microscale inhomogeneity of brain tissue distorts electrical signal propagation*, Journal of Neuroscience (2013), 33 (7), 2821-2827.

[65] M.C. Néel, L. Di Pietro and N. Krepysheva, *Enhanced diffusion in a bounded domain*, Proceedings of the 2nd IFAC Workshop on Fractional Differentiation and its Applications (2006), Porto, Portugal, July 19-21.

[66] P. Pathmanathan, M.O. Bernabeu, R. Bordas, J. Cooper, A. Garny, J.M. Pitt–Francis, J.P. Whiteley and D.J. Gavaghan, *A numerical guide to the solution of the bidomain equations of cardiac electrophysiology*, Progress in Biophysics and Molecular Biology (2010), 102, 136-155.

[67] L.F. Pavarino and S. Scacchi, *Parallel multilevel Schwarz and block preconditioners for the bidomain parabolic-parabolic and parabolic-elliptic formulations*, SIAM Journal on Scientific Computing (2011), 33 (4), 1897-1919.

[68] I. Podlubny, *Fractional differential equations. An introduction to fractional derivatives, fractional differential equations, some methods of their solution and some of their applications*, Academic Press (1998).

[69] M. Riesz, *L'intégrale de Riemann-Liouville et le problème de Cauchy*, Acta Matematica (1949), 81 (1), 1-222.

[70] B. Ross, *A brief history and exposition of the fundamental theory of fractional calculus*, Fractional Calculus and its Applications (1975), Springer lecture notes in Mathematics, 57, 1-36.

[71] A.I. Saichev and G.M. Zaslavsky, *Fractional kinetic equations: Solutions and applications*, Chaos (1997), 7 (4), 753-764.

[72] S.G. Samko, A.A. Kilbas and O.I. Marichev, *Fractional integrals and derivatives. Theory and applications*, Gordon and Breach (1993).

[73] J.M. Sancho, A.M. Lacasta, K. Lindenberg, I.M. Sokolov and A.H. Romero, *Diffusion on a solid surface: Anomalous is normal*, Physical Review Letters (2004), 92, 250601.

[74] E. Scalas, R. Gorenflo and F. Mainardi, *Fractional calculus and continuous-time finance*, Physica A (2000), 284, 376-384.

[75] E. Schumacher, *Ordinary and fractional diffusion in simple biological models*, Masters Thesis Université catholique de Louvain (2010).

[76] M.J. Simpson, K.A. Landman and D.F. Newgreen, *Chemotactic and diffusive migration on a nonuniformly growing domain: Numerical algorithm development and applications*, Journal of Computational and Applied Mathematics (2006), 192, 282-300.

[77] M.J. Simpson, K.A. Landman, B.D. Hughes and D.F. Newgreen, *Looking inside an invasion wave of cells using continuum models: Proliferation is the key*, Journal of Theoretical Biology (2006), 243, 343-360.

[78] M.J. Simpson, D.C. Zhang, M. Mariani, K.A. Landman and D.F. Newgreen, *Cell proliferation drives neural crest cell invasion of the intestine*, Developmental Biology (2007), 302, 553-568.

[79] J. Sundnes, G.T. Lines, X. Cai, B.F. Nielsen, K.A. Mardal and A. Tveito, *Computing the electrical activity in the heart*, Springer-Verlag (2006).

[80] E. Tadmor, *A review of numerical methods for nonlinear partial differential equations*, Bulletin of the American Mathematical Society (2012), 49 (4), 507-554.

[81] A.J. Trewenack and K.A. Landman, *A traveling wave model for invasion by precursor and differentiated cells*, Bulletin of Mathematical Biology (2009), 71, 291-317.

[82] B.P. van Milligen, I. Calvo and R. Sánchez, *Continuous time random walks in finite domains and general boundary conditions: some formal considerations*, Journal of Physics A: Mathematical and Theoretical (2008), 41, 215004.

[83] J.P. Whiteley, *An efficient numerical technique for the solution of the monodomain and bidomain equations*, IEEE Transactions on Biomedical Engineering (2006), 53, 2139-2147.

[84] Q. Yang, *Novel analytical and numerical methods for solving fractional dynamical systems*, PhD Thesis Queensland University of Technology (2010).

[85] Q. Yang, T. Moroney, K. Burrage, I.W. Turner and F. Liu, *Novel numerical methods for time-space fractional reaction diffusion equations in two dimensions*, ANZIAM Journal (2011), 52 (CTAC2010), C395-C409.

[86] Q. Yang, I.W. Turner, F. Liu and M. Ilić, *Novel numerical methods for solving the time-space fractional diffusion equation in two dimensions*, SIAM Journal on Scientific Computing (2011), 33, 1159-1180.

[87] Q. Yang, T. Moroney, F. Liu and I.W. Turner, *Computationally efficient methods for solving time-variable-order time-space fractional reaction-diffusion equation*, Proceedings of the 5th IFAC Symposium on Fractional Differentiation and its Applications (2012), Hohai University, Nanjing, China, May 14-17.

[88] H.M. Young, A.J. Bergner, R.B. Anderson, H. Enomoto, J. Milbrandt, D.F. Newgreen and P.M. Whitington, *Dynamics of neural crest-derived cell migration in the embryonic mouse gut*, Developmental Biology (2004), 270, 455-473.

[89] A. Zoia, A. Rosso and M. Kardar, *Fractional Laplacian in bounded domains*, Physical Review E (2007), 76, 021116.